CRANFIELD UNIVERSITY

Nathalie ALEGRE

Full-Scale Runback Ice: Accretion and Aerodynamic Study

SCHOOL OF ENGINEERING
Department of Power and Propulsion - Icing Group

PhD THESIS

Initial registration : February the 11th 2008

Supervisor : Dr. D. Hammond

December 2010

CRANFIELD UNIVERSITY

SCHOOL OF ENGINEERING
Department of Power and Propulsion - Icing Group

PhD THESIS

Initial registration : February the 11th 2008

Nathalie ALEGRE

Full-Scale Runback Ice: Accretion and Aerodynamic Study

Supervisor : Dr. D. Hammond

December 2010

This thesis is submitted in partial fulfilment of the requirements for the degree of Doctor of Philosophy

Abstract

The runback ice phenomenon is well-known for anti-icing or de-icing systems when the system is not evaporating 100% of the water impinging the surface. The water runs back to the point where the added heat no longer raises the surface temperature above freezing. The water freezes behind this limit. No runback ice is tolerated for some flight configurations, but not for all. Then for off-design cases, some runback ice may grow on the wings surface. However, data from full-scale realistic runback ice is not very well-known by aircraft manufacturers and they are not sure what thickness is allowed before the effect of the ice on the flow becomes too adverse.

To better understand full-scale high-fidelity runback ice growth and how it can be simulated with simplistic shapes, test campaigns and CFD studies were undertaken. First of all, tests in the Cranfield icing tunnel were performed. In this work, full-scale runback ice shapes were grown on a model with a full-scale leading edge equiped with an electrical heating system. An innovative moulding and casting technique has been introduced which allowed the production of 3D planarised full-scale realistic runback ice castings. In parallel to the icing tunnel tests, a mass and energy balance has been computed on Excel. This energy and mass balance can predict the heat and mass fluxes involved in the runback ice accretion mechanism. Following this, aerodynamic tests of the ice castings were lead in one of the low speed wind tunnels at Cranfield University. The aerodynamics of simplistic shapes such as geometrical shapes or ballotini layers were also studied. The effects of the ice castings on the flow were compared to the effects of the simplistic shapes. The tests were done on a flat surface and not on an airfoil due to technical complications. The boundary layer displacement thickness was the parameter used to quantify the effect of the shapes on the flow. 2D CFD simulations were performed as a support to the testing but as well to compare with the experimental data. The CFD simulations were for steady or unsteady flow.

It has been possible to grow full-scale ice shapes in a relatively small icing tunnel. The shapes have been successfuly moulded and cast using silicone and plaster mixed with polymer. A catalogue of runback ice shapes for different liquid water content, heat inputs and positions along the chord has been recorded. Following the wind tunnel tests, it has been possible to find a relationship between the real ice and the simplistic shapes. Thin runback ice shapes (4 mm) has a similar effect on the flow as a layer of 1 mm ballotini. It was found that thicker ice shapes, of the order of 1 cm, is equivalent to a rectangle with rounded corner, associated with 1mm ballotini. The triangle shape which is usually used to simulate runback ice by the aircraft manufacturers, was found to be the most aerodynamically penalising simplisitc shape that has been investigated in this PhD project. It was found that rounded corners greatly improve the representativeness of the simplistic shapes, such as triangle or rectangle.

Acknowledgements

I would like to thank my supervisor, Doctor David Hammond, for his support, encouragements and availability throughout this project. This project would have never been a success without his continuous guidance.

Thank you to Nick Dart, my industrial supervisor from Airbus UK, whose guidance was much appreciated and essential for the succes of this project.

A special thanks is directed to Brian Stapleton, for his advice, patience and optimism during the icing tunnel tests. For the wind tunnel tests, I would like to thank Jenny Holt and Professor Kevin Garry for their help and support.

I would like to thank as well my co-supervisors, Mark Savill and Chris Thompson for their advice on the CFD part of my project.

Thank you to Roger Gent from AeroTex for his precious advice.

This project has been a colaboration with MSc students: Jorge Sancho and Kathrin Dittmar. I would like to thank them for their contribution to the project, their critical view and their friendship.

My Cranfield experience has not been only professional. It has been a very important part of my personal life. I met people from all over the world with who I shared lots of laugh. A special thank to the people from the icing group, to the bunch of people I used to share my lunch and to my house mates who makes my life much more fun during these 3 years of hard work.

A special thanks to my parents who always gave me the freedom to make my choices and who actively supported me. I am deeply grateful to my sister for her great support. At least but not last, I would like to thank my boyfriend for his support and patience during all these years. Thanks to my boyfriend's family for their encouragements.

Contents

List of Figures

List of Tables

List of symbols

Roman letters

a Length between the front of the ridge and the ice shape, m

A Area of the control volume used in the analytical tool, m^2

AOA Angle of attack

b Length of the runback ice ridge, m

B Global catch efficiency

c Chord length, m

C Speed of sound, ms^{-1}

c_i Specific capacity heat of ice, $Jkg^{-1}K-1$

c_p Specific capacity heat of air for constant pressure, $Jkg^{-1}K-1$

CV_i Control volume i

c_w Specific capacity heat of water, $Jkg^{-1}K-1$

C_d Drag coefficient

$C_{d_{min}}$ Minimum drag coefficient

C_l Lift coefficient

$C_{l_{max}}$ Maximum lift coefficient

d Maximum thickness of the runback ice ridge, m

D Distance between the end of the protected region and the runback ice shape

D_w Diffusion coefficient of water vapour in air, $m^2 s^{-1}$

d_y Ordinates difference of droplets diameter free stream for the calculation of the global catch efficiency, m

e_s Water vapour pressure on a surface, Nm^{-2}

e_∞ Water vapour pressure free stream, Nm^{-2}

h Local convective heat transfer coefficient, $Wm^{-2}K^{-2}$

H Ordinates difference of the last hitting trajectories impacting the model, m

i Ice thickness, mm

k Turbulent kinetic energy, $m^2 s^{-2}$

k_a Air thermal condictivity, $Wm^{-1}K^{-1}$

k_s Roughness height, m

K Factor in the uncertainties propagation formula

Le Lewis Number

L_f Latent heat of fusion, $kj\ kg^{-1}$

L_s Latent heat of sublimation, $kj\ kg^{-1}$

L_v Latent heat of vaporisation, $kj\ kg^{-1}$

M Mach number

M''_{evap} Water evaporative mass flux, $kg\, m^{-2} s^{-1}$

M''_{imp} Impinging water mass flux, $kg\, m^{-2} s^{-1}$

M''_{freeze} Freezing water mass flux, $kg\, m^{-2} s^{-1}$

M_{in} Water mass flux running in CV_i, $kg\, s^{-1}$

M_{out} Water mass flux running out CV_i, $kg\, s^{-1}$

n, Number of samples

P Static pressure, Pa

P_a Air pressure in the CIT, psi

P_d Local dynamic pressure, Pa

$P_{d\,\infty}$ Dynamic pressure free stream, Pa

P_l Local pressure, Pa

Pr Prandtl number

P_s Surface pressure, Pa

P_t Total pressure, Pa

P_w Pressure in the CIT, psi

$\dot{Q}_{aero\,heating}$" Energy flux from the aerodynami heating, Wm^{-2}

$\dot{Q}_{anti}$" Energy flux from the anti-icing systems, Wm^{-2}

$\dot{Q}_{conv}$" Energy flux from the convection, Wm^{-2}

$\dot{Q}_{drop\,kin\,energy}$" Energy flux from the droplets kinetic energy, Wm^{-2}

$\dot{Q}''_{drop\,warm}$ Energy flux from the droplets warming, Wm^{-2}

$\dot{Q}''_{evap}$ Energy flux from the evaporation, Wm^{-2}

$\dot{Q}''_{freeze}$ Energy flux from the droplets freezing, Wm^{-2}

$\dot{Q}''_{sub}$ Energy flux from the sublimation, Wm^{-2}

r recovery factor

R Gaz constant, $m^2s^{-2}K^{-2}$

Re Reynolds number

Re_x Reynolds number at the position x

$R_u = \dfrac{u}{U_\infty}$, Ratio of local speed to free stream speed

S_l Lower surface impingement limit, m

S_u Upper surface impingement limit, m

St Stanton number

t Time,s

T_r Recovery temperature, °C

T_s Static temperature, °C

T_S Surface temperature, °C

T_t Total temperature, °C

T_∞ Static free stream temperature, °C

u Velocity in the boundary layer, $m.s^{-1}$

$u(y)$ Velocity in the boundary layer in the y direction, $m.s^{-1}$

u_{CFD} Velocity from CFD simulation, $m.s^{-1}$

u_{exp} Velocity measured during the experiments, $m.s^{-1}$

u_i Field of velocity, $m.s^{-1}$

$U(x)$ Velocity outside the boundary layer in the x direction, $m.s^{-1}$

U_e Velocity on the edge of the boundary layer, $m.s^{-1}$

U_∞ Free stream velocity, $m.s^{-1}$

x Position along the chord, m

x/c Chordal position, %

$\bar{x}$ Average of x

x' Fluctuation of x

y ordinates axis, m

y^+ Size of the first cell of the boundary layer (CFD), m

Greek letters

α Angle between the front of the ridge and the normal to the surface

β Local catch efficiency

β_i Mono-dispersed catch efficiency

$\beta_{poly-dispersed}$ Poly-dispersed catch efficiency

δ Boundary layer thickness, m

δ^* Displacement thickness, m

δ_x Random error of x

δ_y Ordinates difference of the last hitting trajectories free stream, m

Δ_y Ordinates difference between two impinging droplets, m

Δ_x Abscissa difference between two impinging particles, m

ϵ Turbulent dissipation rate, $m^2 s^{-3}$

ϵ_x Total error on x

θ Momentum thickness, m

μ Dynamic viscosity, $N m^{-2} s$

μ Turbulent dynamic viscosity, $N m^{-2} s$

ν Kinematic viscosity, $m^2 s^{-1}$

γ Ratio of specific heat

Φ Scalar in Fluent

ρ Density, $kg\, m^{-3}$

ρ_{air} Air density, $kg\, m^{-3}$

ρ_i Ice density, $kg\, m^{-3}$

ρ_s Saturated vapour density over surface, $kg\, m^{-3}$

ρ_∞ Saturated vapour density free stream, $kg\, m^{-3}$

σ_x Standard deviation of x

$\sigma_{mean} = \frac{\sigma_x}{\sqrt{n}}$ Standard deviation of the sampled mean

τ Shear stress, Pa

ω Specific dissipation rate, $m^2 s{-}3$

Acronyms

AMIL Anti-Icing Materials International Laboratory

CFD Computational Fluid Dynamic

CIT Cranfield icing tunnel

CIRA Centro Italiano Ricerche Aerospaziali

DPM Discrete Phase Model

EASA European Aviation Safety Agency

FAA Federal Aviation Administration

FAR Federal Aviation Regulations

FS Free stream

LWC Liquid water content, $g.m^{-3}$

MAC Mean aerodynamic chord, m

MVD Mediam volumetric diameter, μm

OAT Outside air temperature, °C

RANS Reynolds Averaged Navier Stokes

S-A Spalart-Allmaras turbulence model

SLD Supercooled large droplets

SST Shear Stress Transport

T Tunnel

Chapter 1

Introduction

1.1 General Introduction

It is well-known that the meteorological conditions are a key parameter in aircraft safety and economics. Aircraft are exposed to all kind of weather conditions when flying all over the world (sand cloud, volcano ashes, strong wind, turbulence, icing, etc). During spring 2010, when one of the Iceland volcano erupted, the all Europe flights were stopped or delayed causing an unprecedent crisis in Europe. Hopefully, no accident was recorded. Another example, is the closure of the London airports in December 2009, because of heavy snow falls. Thus for safety and economics reasons, aircraft manufacturers are continuously investing in research in order to build aircraft which are all the more relible to cope with adverse weather conditions.

1.2 Atmoshperic conditions

The aircraft protection againt icing, in flight or on the ground, is one of the challenge that the aircraft manufacturers have to face. This study main interest is in flight icing due to supercooled water droplets. Supercooled water is metastable where water remains liquid below its freezing point. A disturbance of a certain magnitude such as the presence of a nucleus is required to provide enough disruption for the droplets to freeze (Hobbs (1974)). Droplets of supercooled water often exist in stratus (flat, featureless) and cumulus (puffy appearance) clouds. Hence, aircraft flying through such clouds can be subject to ice formation on critical aerodynamic surfaces (engine, wing, tail, etc). These surfaces will act as the disturbance required to make the water freeze. Ice formation on aircraft surfaces is a function of aircraft configuration, air flow and icing conditions (LWC, MVD and air temperature). Typically, ice

accretions result from small supercooled droplets, usually 10 μm to 50 μm in diameter with ambient temperature not below -20°C, which can freeze upon impact with the aircraft surface.

For the purpose of aircraft icing systems design and certification, the FAA, defined envelopes conditions within stratus (continuous conditions) and cumulus clouds (intermittent conditions) in a document named Appendix C of FAA FAR Part 25 (see Appendix A). The continuous conditions are related to lower LWC for a longer distance exposure in comparison with the intermittent conditions. The document is based on flight data collected in the 1940s and it defines limits of LWC, altitude, temperature and MVD . This document has been adopted as an engineering standard. For icing certification, aircraft manufacturers must demonstrate to the FAA or the EASA that airplanes intended for operation in known icing conditions must be capable of operating safely in all icing conditions described in the Appendix C icing envelope. However those conditions are incomplete. Conditions have been found beyond the Appendix C (Gelder et al. (1953), Mason (1971), Jentink (2001)). For instance, droplets with diameter above 50 μm (SLD) or icing conditions at altitudes above 22000 ft and temperature lower than -40°C are outside the Appendix C conditions. Thus, further studies are being conducted (Cober and Isaac (2006)) to try to improve the Appendix C. However it is difficult to know about all of the adverse conditions in which an aircraft might go through. Hence, pilot training and awareness is a key factor to reduce the risk of icing aircraft. For instance, continuous climb or descent though supercooled layers reduce icing on the critical surfaces (Korolev et al. (2006)).

1.3 Icing Aircraft

1.3.1 Background

The major part of the accidents due to icing is mainly due to technology weakness or icing phenomena which are not part of the aircraft certification (Green (2006)). The consequences of icing on aircraft are loss of handling performance, decrease of lift and stall AOA and increase of drag (Almendaroglu et al. (1997)). A well-known accident is the one that happened in 1994, October the 31st, near Roselawn, Indiana to an ATR-72 (Papadakis et al. (2004a)).

Two conditions are necessary for the formation of ice on aircraft surfaces during flight (Al-Khalil et al. (1993)):

- The aircraft must be flying through visible water, such as rain or cloud droplets .
- The surface temperature of the airframe must be below freezing.

The level of ice accretion on wing surfaces depends mainly on how well-protected these surfaces are, on the icing conditions (LWC, MVD, OAT), on the flight speed, on the wing design and on the spanwise position along the chord. If the wings are un-protected, leading edge ice shapes may grow. These ice shapes often include complex roughness features, horns and scallops. For a protected surface with anti-icing or de-icing systems, small ice shapes and roughness can form behind protected areas. It is the runback ice.

Before going further in the study of aircraft icing, some background related to the different sorts of ice found on the wings is explored. Two main types of ice can develop on wings (Politovich (2000) and Vargas et al. (2007)) depending on the atmospheric and flight conditions: rime ice and glaze ice (Figure 1.1)

(a) Rime ice (b) Glaze ice

Figure 1.1: *Ice shapes from the CIT*

- Rime ice or dry ice is white ice that forms when all of the supercooled water droplets impinging the critical surfaces of the aircraft, freezes. It means that the droplets are able to lose the latent heat of fusion rapidly and so they freeze in place. The conditions that favour rime are: low temperature, low air speed, low LWC and low MVD.

- Glaze ice or wet ice occurs when not all of the water is frozen straight away. A water film remains on the ice. This phenomenon can lead to typical ice shape such as horns. Glaze ice is almost transparent. Conversely to rime ice, glaze ice occurs for higher temperature, higher air speed, higher LWC and higher MVD.

Nevertheless it would be a mistake to assume that these types of ice are the only ones. A mixed growth (glaze and rime ice see) is often observed. It is important to note that the nature if ice growth is of importance in the aircraft icing context as the shape, roughness characteristics and other properties of each kind of ice is totally different.

1.3.2 Ice protection systems

To avoid aerodynamic performance loss due to icing, ice protection systems exist. There are different strategies in terms of ice protection. The easiest one is the avoidance. Some aircraft may have the ability to tolerate a bit of ice. Then there is the ice protection systems. The use of ice protection systems for the critical surfaces has been explored since the fifties. Thanks to experimental data and simulation results, ice shapes and ice behaviour can be roughly predicted and these results help engineers to design ice protection systems with more accuracy in terms of energy cost and de-icing or anti- icing effectiveness. On an aircraft, the main critical surfaces where the protection systems are applied to, are: engine nacelles, wings and tail surfaces. The extent of the ice protection systems is typically between 7-10% of the chord for the wing and tail (Papadakis et al. (2004b) and Lima da Silva et al. (2007a)). However, this limit is really dependant on the nature of the application (helicopters, aircraft, etc), the airfoil geometry and the spanwise position along the chord. For instance, the outboard of the wing is more protected than the inboard part. Icing protection is a complex problem as it has to be a compromise between safety, performance and energy limitations.

There are 2 main strategies for the ice protection systems: anti-icing systems and de-icing systems. Anti-icing strategy deals with the prevention or minimization of ice growth on protected surface whereas de-icing strategy is concerned with ice removal after and during ice growth. Usually the anti-icing systems are thermal systems. Mechanical (pneumatic boots) or heating means are used for de-icing systems. In the case of thermal systems several sources of energy, to provide the heat requirement, exist. Bleed air from engines can be one of these sources (Figure 1.2) (Al-Khalil et al. (1990), Al-Khalil et al. (1993) and Wright (2004)).

For turbofans aircrafts, bleed air anti-icing system is very popular. It is based on the so-called "Piccolo tube" (Figure 1.3) commonly used on regional and long-range jets (Croce et al. (2002) and Wright (2004)). The hot-air provided by the high-pressure engine compressor, impinges from a series of small holes onto the internal wall of the wing leading edge or the engine nacelle.

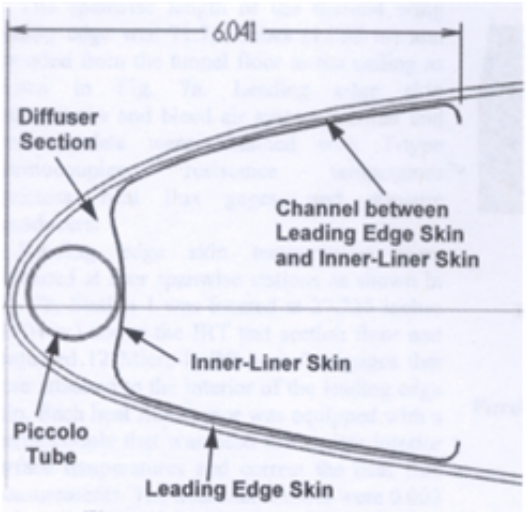

Figure 1.2: *Bleed air system details Papadakis et al. (2008)*

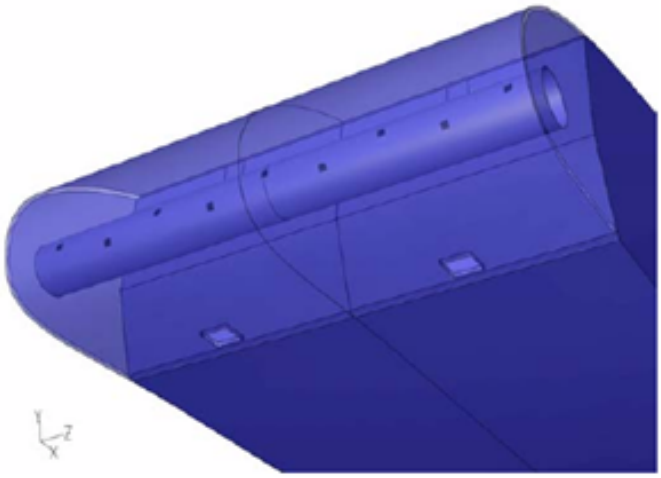

Figure 1.3: *Leading edge anti-icing Piccolo tube Hua et al. (2007)*

The thermal anti-icing systems can have two regimes of action:

- Evaporative systems that provide enough heat to evaporate the impinging water on the critical surfaces.

- Wet systems (Lima da Silva et al., 2005) where the energy provided is just enough to maintain the temperature of the critical areas above freezing. Thus the evaporation is limited. Some water will runback and freeze on the part of the surface which is below the freezing point. This is runback ice.

A thermal anti-icing system is not calibrated to be either one of these two regimes. Actually, a system may be evaporating for certain icing conditions and wet for more critical icing conditions. It may depend as well on the engine regime. For turboprop aircrafts, such as ATR 72 or ATR 42, the most usual system is de-icing system with pneumatic boots. These are inflated cyclically and require a very small amount of energy. For effective ice removal the ice must have a minimum thickness.

For modern high bypass turbofans the amount of available bleed air is rather limited and therefore the aircraft manufacturers try to reduce the extent of the protected region as far as possible. What's more the new aircraft wings are made in composite which have an influence on the choice of the ice protection system. Another constraint involved in the design of icing protection systems is the energy cost (Gelder et al. (1953)). Thermal systems using bleed air from the engine reduces engine performance and more particularly during critical phase of flight such as take-off and landing. It also increases the fuel consumption and the weight (Gray and Von Glahn (1953)). Thus, lots of efforts are put in research to find an alternative to bleed air systems: Electrical heating associated with wet de-icing or anti-icing, tolerance of runback on the wing, etc. For instance, GKN Aerospace has developed an electrical heating de-icing systems for the new Boeing, the B787 Dreamliner. Enhanced knowledge is required by the authorities about runback and intercycle ice if such types of ice are to be tolerated on the airfoil surface. An alternative to anti-icing or de-icing system could be a hybrid one. The NASA researchers have explored such possibility (STI[1]) and they gave birth to the Cox Low Power Ice Protection System which combines elements from both thermal anti-icing and mechanical de-icing systems. This system has been certified by the FAA. It is supposed to reduce energy and operating costs.

However, despite ice protection systems some incidents remain, most of the time because of meteorological conditions unknown so far or because of pilot miss-training. A sadly famous one, is the crash of an ATR 72 in Roselawn in October 1994 (NTSB (1996)). The commuter aircraft crashed in Indiana with

[1]NASA Scientific and Technical Information

the loss of all the passengers and the crew despite its icing protection systems. The accident was attributed to freezing drizzle droplets striking downstream of the protected region and forming a ridge which disrupted the aerodynamic flow over the ailerons. In the official report of the accident (NTSB (1996)), it is written that the probable causes of the accident were loss of control attributed to a "sudden and unexpected aileron hinge moment reversal that occured after a ridge of ice accreted beyond the de-icer boots" (Figure 1.4).

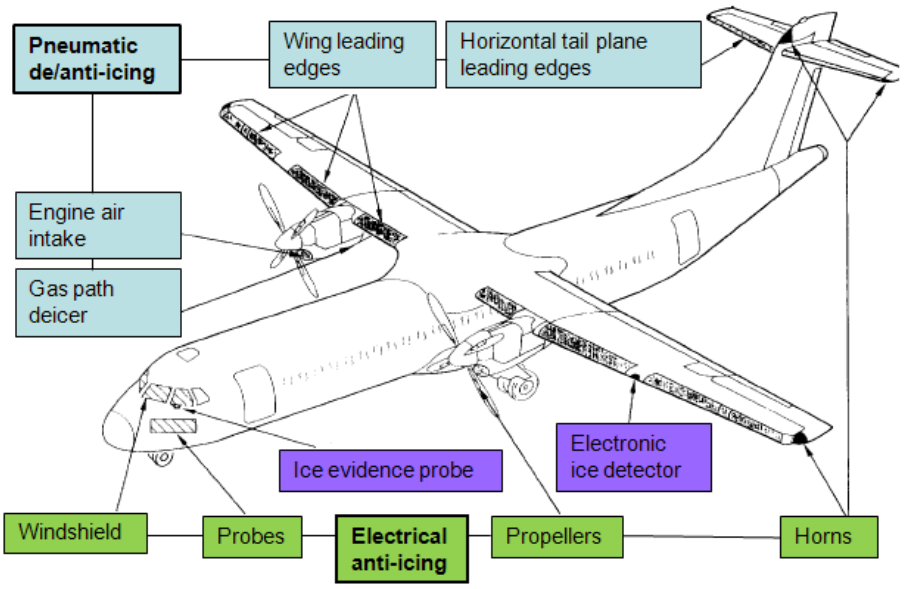

Figure 1.4: *ATR 72 icing protection systems NTSB (1996)*

1.3.3 Runback ice

The runback ice phenomenon is well-known for anti-icing and de-icing systems when the protective system is not evaporating 100% of the water impinging the surface. The water runs back beyond the point where the added heat no longer raises the surface temperature above freezing. The water begins to freeze, developing into a ridge and leaving the leading edge clean (Figure 1.5 and Figure 1.6).

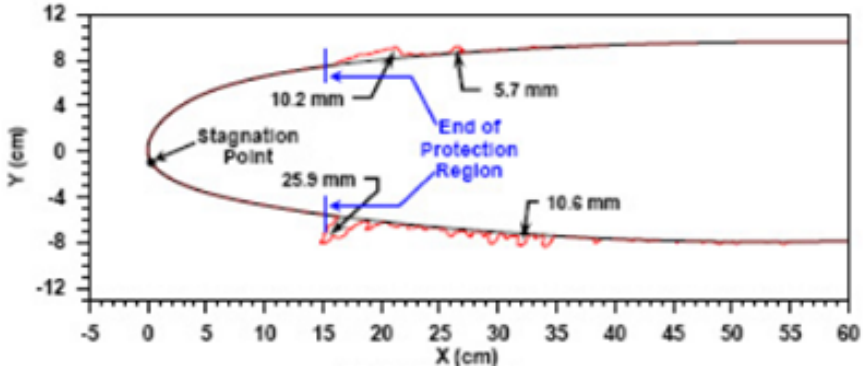

Figure 1.5: *Runback ice profile (Whalen et al. (2005))*

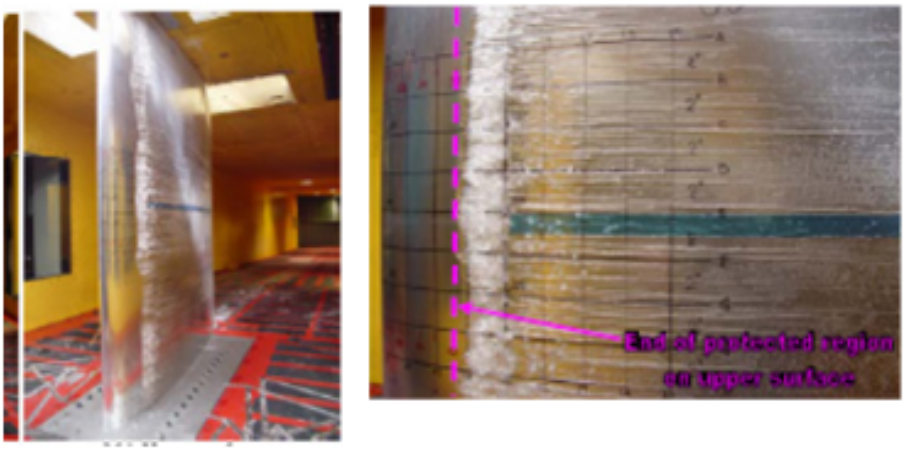

Figure 1.6: *Runback ice shape on a upper surface of a wing (Whalen et al. (2005))*

1.4 Relevance of the study

Nowadays, there is an increase in demand for all-weather flight capabilities (Almendaroglu et al. (1997)). There are several reasons for that. The first one is that there is an increase in air-traffic which increases the holding time and thus the exposure time to adverse conditions. The hold phase of flight is very critical for icing because it takes place at a critical altitude. The altitude does not have a direct impact on the rate of ice accretion (Gent et al. (2000)). However it may have an indirect impact on the severity of icing. First of all the altitude is linked with the likely occurrence of icing. The largest LWCs

generally occur in the altitude range between 5000 ft and 15000 ft (Almendaroglu et al. (1997)) and the size of the supercooled water droplets decreased when the altitude is increased. Second of all, as the air density is changed with the altitude, this change may affect the heat transfer balance that occurs on a protected surface exposed to icing conditions. Third of all, for thermal anti-icing systems using bleed air from the engines, the bleed air is reduced with the altitude. Another reason for the increase in demand for all-weather flight capabilities, is the change in the engine design which reduce the amount of heat available for heating system. Finally, a third reason for the increase of demands for all-weather flight capabilities is the development of new military aircraft.

For all of these reasons, aircraft icing is a large topic of research with three main tracks:

- Meteorological
- Details of ice accretion
- Effects of performance degradation

This thesis is dealing with the study of runback ice. It is focus on the details of the ice accretion and on the effects of performance degradation due to runback ice. The current sitution concerning the runback ice is relatively unclear:

- If anti-icing power is reduced beyond a certain level, runback ice can grow on wings downstream the protected area.
- There is very little information about the shape and texture of runback iceformation on full-scale aircraft geometries.
- Runback ice is defined by many aircraft manufacturers by shapes which are much worst for the flow (conservative) than the real runback ice.

From the present situation some problems occur:

- Runback ice may grow for off-design cases or when thermal de-icing systems are used. Can we tolerate some? Which ice thickness limit is then acceptable in terms of aerodynamic?

- Runback ice testing on sub-scale wind tunnel models uses very conservative shapes to simulate the aerodynamic effect of runback ice on the air flow in the vicinity of an airfoil. How close to the aerodynamic of real runback ice those shapes are? In addition, too much conservatism in the simulation of runback ice affects the design of ice protection systems, introducing an unnecessary amount of system power.

1.5 Aim and objectives

In regards to these problems the aim of the PhD is to improve the knowledge of full-scale runback ice growth and find a relationship between simplistic shapes and real ice shapes in terms of aerodynamic performance loss, in order to improve the runback ice aerodynamic study. To complete the main aim it was necessary to deliver the following objectives:

- Study the thermodynamic aspect of runback ice accretion growth by developing a simple tool to quantify the energy and mass fluxes involved in the runback ice process
- Study the geometrical aspects (shape, roughness) of full-scale runback ice shapes by growing full-scale high-fidelity runback ice shapes in the Cranfield Icing Tunnel
- Capture the ice shapes from the icing tunnel using innovative moulding and casting techniques
- Make a selection of simplistic shapes which are likely to have similar aerodynamic effects on the air flow as the full-scale runback ice shapes
- Study the aerodynamic of the runback ice castings and of the selected simplistic shapes
- Find a relationship between runback ice castings and simplistic shapes in terms of aerodynamic performance loss.

According with Airbus, only the upper surface ice accretions are studied, as they are more penalising for the flow than the lower surface ice accretions. The project is based mainly on experiments. The CFD tool was used all along the project as support to the experiments.

Chapter 2

Literature review

2.1 Ice accretion mechanism

The analysis of the ice accretion process is governed by a balance of the energy and mass fluxes at the studied surface. The first approach is the Messinger model (Messinger (1953) and Hansman Jr and Turnock (1989)) which has been used in several icing codes. It consists of an energy balance on a control volume. The second approach (Myers and Hammond (2004) and Myers and Charpin (2004)), introduce a more complete mathematical model which takes into account the time dependence and the conduction through the ice and water layer. In order to understand the phenomenon of ice accretion, it is essential to investigate the interaction between the water surface behavior, the collection efficiency, and the surface convective heat transfer coefficient so that the energy balance may be determined locally on the surface where ice may grow.

2.1.1 The water surface behavior

The water surface behavior is governing the way the impinging water is distrubuted to a surface. It is involved in the heat transfer coefficient between the water and the air because of its impact on the surface roughness. The water behaviour depends on the relative strength of the surface tension, the aerodynamic forces, the water/air surface interface and the body forces on the fluid. These body forces can generally be neglected compared to the aerodynamic forces on an aircraft.

The water can behave as a film, beads or rivulets. The main parameter which is used to describe the water surface behaviour is the wetness factor. The wetness factor is defined by Al-Khalil et al. (1990) as "the fraction of the surface

that is wetted by runback water at a particular downstream location". A lot of work is reported about the water behaviour and more especially concerning the factors which influence the transition of water film to rivulets.

Hansman Jr and Turnock (1989), studies the water surface behavior during glaze ice accretion. Their study was based on experimental investigations on a cylinder. The authors defined 3 zones:

- Water film in the stagnation region.
- Water beads downstream the water film region for cold surface temperature.
- Water running back as rivulets for warmer surface temperature.

The definition of these 3 zones is based on the study of the contact angle between the fluid and the substrate. For glaze ice accretion the substrate is the ice. Depending on the size of this angle and on the flow conditions the water behaves differently. For high flow rates and small contact angle, the water is supposed to behave as a water film. For lower flow rate and higher contact angles the water should break-up into beads or rivulets. The authors highlighted that the contact angle was strongly dependent on the substrate temperature distribution and that the change in the surface temperature was changing the ice shapes. Thus, the authors proved that the water surface behavior has an influence on the final ice shapes, at least for leading edge ice accretion.

At the beginning of the nineties, Al-Khalil et al. (1990) developed a numerical model for wet anti-icing system. They did not compare their numerical results with experiments because of the complexity of the problem. In their model, the water behaves as a film in the impingement zone. Thus, the water breaks-up into rivulets for a certain water film thickness and operating conditions. To predict the water film break-up, the authors took into account the surface tension that was observed in the experiments of Hansman Jr and Turnock (1989). For a certain thickness, the water film is breaking-up due to the surface tension.

Al-Khalil et al. (1993), improved the precedent model by taking into account the heat transfer through the water rivulets and through a multi-layers solid wall which can be heated. Thus the heat transfer coefficient is considered as 2D. Once again their study is based on a numerical model and no comparison

with experiments is made. However, the authors assessed the numerical results as accurate. Based on the critical film thickness developed by Al-Khalil et al. (1990), the authors claimed that the break-up of the water film should occur at the impingement limit. This is a very convenient conclusion, because once the impingement is known, no more analysis is required to find the water surface behavior. This transition between the water film and the rivulets at the limit of the impingement has been observed during the icing tunnel experiments. This water behaviour seems to have been adopted by the icing community and it is used in many icing codes (Gent (1990)):

- Uniform film in the impingement zone. The wetness factor is one.
- Rivulets in the region downstream the impingement zone. The wetness factor is less than unity.

2.1.2 Collection efficiency

The collection efficiency is a key parameter for any calculation in icing. It refers to the ratio of impinging droplets mass flux on the surface, to the mass flux that would occur on the surface if droplets were not deflected by the air stream (Wright (1995)). Thus, it is droplet trajectories in front of the leading edge that control the collection efficiency. The determination of the catch efficiency can be done using experimental results or CFD simulation. For CFD simulation two ways of calculation exist: the Eulerian method (Wirogo and Srirambhatla (2003)and Milanez and Naterer (2005)) or the Lagrangian method. Droplets trajectories modelling using a Lagrangian approach has been developed in many icing codes (Gent (1990) and Wright (1995)). With the Lagrangian approach a force balance is made for each droplets. One expression of the catch efficiency for a 2D model using a Lagrangian method is shown in Figure 2.1 (Almendaroglu et al. (1997)). The Lagrangian method in the CFD software Fluent is considered as a relatively simple and accurate way to find the local catch efficiency.

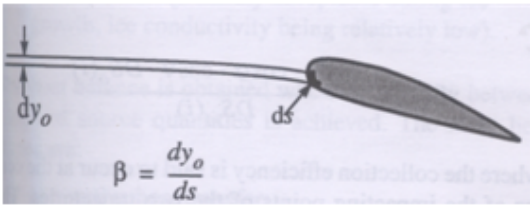

Figure 2.1: *Local catch efficiency using a Lagrangian method (Almendaroglu et al. (1997))*

The main parameters which influence droplets trajectories and thus the catch efficiency are the droplets drag, the gravity, the MVD, the air flow temperature and turbulence and the shape of the impinging body (Gent et al. (2000)). Noll and Pilat (1970), Hansman Jr (1985) and Kollar et al. (2005) found that the effect of gravity decreases as the air stream velocity is increased and as the droplets diameter decreases. In the context of icing aircraft, the air speed is high and the droplets diameter is relativaly low, at least for the range of droplets diameters included in the Appendix C of FAA FAR 25, so the gravity can be neglected. For droplet diameters above 50 μm (SLD) further investigations are needed. Most of the time, the collection efficiency is calculated using the drag definition of Lagmuir and Blodgett (Hansman Jr (1985)) in which the droplet deformation (flattening, coalescence, etc) is neglected. This hypothesis is all the more remote from the reality in the case of SLD. In the context of icing, a Median Volumetric Diameter is used instead of a diameter. The MVD represents the diameter "above and below which half of the mass of water is contained" (Gent et al. (2000)). The catch efficiency can be approximated to a mono-dispersed analysis or handled as poly-dispersed. For the mono-dispersed catch efficiency, the MVD is used as a single diameter. In the case of the poly-dispersed catch efficiency, diameters distribution corresponding to a real cloud is used. Then by summing each catch efficiency weighted by its corresponding volume fraction in the distribution, it is possible to get a poly-dispersed catch efficiency (Wright (1995)). However, the mono-dispersed analysis shows good accuracy and the main improvement using a poly-dispersed analysis is for the impingement limits which are enhanced by the largest droplet of the distribution (Gent (1990)).

2.1.3 The heat transfer coefficient

The main fluxes responsible for the heat loss on airfoil surface (convection and evaporation/sublimation) are strongly linked to the local heat transfer coefficient. It means that the ice accretion rate and the runback water are affected by the heat transfer coefficient. The heat transfer coefficient is strongly dependent on the nature of the flow (laminar or turbulent), the surface curvature, the pressure gradient and the surface roughness (Crawford et al. (2005)).

The nature of the flow on a contaminated airfoil is quite a difficult matter and it has not been investigated deeply in this study. It depends mainly on the speed, the surface roughness and the surface geometry. Li et al. (2003)) measured the local heat transfer coefficient and surface static pressure around an assymetric airfoil for 5 AOA and 3 Reynolds numbers. The experiments took place in the closed circuit wind tunnel at the university of Cincinnati. The

authors obesrved a peak in the heat transfer coefficient curve at the transition and then the heat transfer coefficient is slowly decreasing with the boundary layer thickness increasing. In the present study, it is considered that the boundary layer is fully turbulent from the leading edge mainly because of the water running back on the surface which might trigger the transition very early on the airfoil.

Wang and Simon (1987) studied the effect of curvature and free stream turbulence on momentum and heat transfer, in a boundary layer undergoing transition. The authors observed a 5 to 10% decrease of the heat transfer coefficient due to the convex curvature in the early turbulent region. Ozalp and Umur (2003) lead an experimental study about the combined effect of pressure gradient and wall curvature on the boundary layer development and heat transfer coefficient. They found that a convex surface stabilised the flow and decreased the heat transfer. They observed a 25% decrease in heat transfer over a convex surface in a turbulent boundary layer in comparison with a flat plate. An adverse pressure gradient (or deceleration) caused the Stanton number to decrease of 29% on a convex surface in turbulent flow. Thus, the authors concluded that a convex curvature and an adverse pressure gradient produce thicker boundary layer which corresponds to a lower heat transfer. Finally, they found that a favourable pressure gradient (accelerating flow) caused the heat transfer to increase of 24% on convex surface in turbulent flow.

Achenbach (1977) studied the effect of surface roughness on the heat transfer from a circular cylinder. He found that the convective heat transfer was strongly related to the surface roughness and was enhanced with the roughness. Hence, in the context of icing, a wrong roughness estimate can lead to major error in the final ice shape. The ice roughness or the water roughness are crutial parameters for icing. However, it is very difficult to calculate or measure. The roughness depends on the conditions for which the ice is growing. So it depends on the LWC, the temperature, the free stream speed, the droplets size, the droplets distribution and the free stream turbulence. Moreover, as the water behavior is changing with time, the roughness is time dependent.
Many studies were done on the water behavior (see 2.1.1) and its roughness in order to improve ice shape simulation and more particulary, icing code accuracy. Hansman Jr and Turnock (1989) were one of the first authors to investigate the surface roughness depending on the water surface behaviour for glaze ice accretion on a cylinder. Their study was focused on the roughness of the water which is not evaporated once impacting the model. Water has

been observed to have a distinct roughness zone depending on its behaviour:

- Smooth wet zone in the stagnation zone where a water film is formed. This zone is considered as having no roughness.
- Rough zone made of water beads. In this zone the roughness is estimated to be 1 mm.
- Rough zone made with rivulets. The roughness of the rivulets has not been estimated.

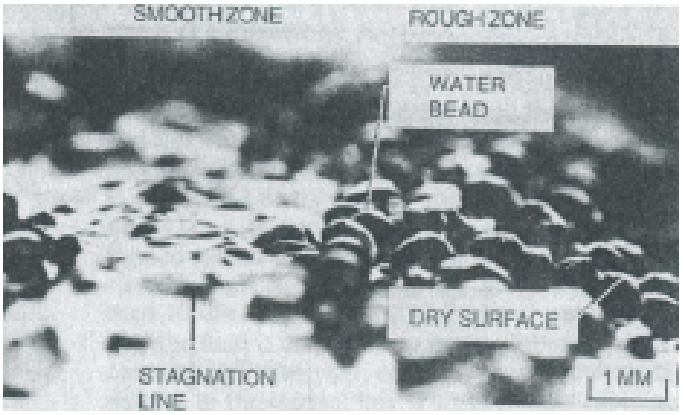

Figure 2.2: *Picture of beads in the rough zone (Hansman Jr and Turnock (1989))*

This model has been improved for anti-icing application by Al-Khalil et al. (1990) and Al-Khalil et al. (1993). Even if their study was more focused on the water surface behavior than on the roughness, some of their conclusions are directly releated to roughness. First of all, they concluded that the limit, between the smooth zone and the rough zone, was the limit of the impingement. Then they suggested that some roughness could be granted to the water film due to waveness at the surface. No value of these roughness was proposed by the authors.
Shin (1996) studied the ice roughness associated with leading edge ice accretion, in glaze ice conditions. He measured the surface roughness on a NACA 0012 airfoil in the Icing Research Tunnel at NASA Lewis Research Center, using optical imaging technique in order not to alter the surface conditions during the acquisition process. Hemispherical elements were measured with heights from 0.57 mm to 0.79 mm and center to center spacing from 1.02 mm to 1.71 mm. The author found that once the roughness has reached a critical level, it remains constant. Shin concluded that the height of roughness

elements was dependent on the total temperature and LWC. The roughness increases when the total temperature and the LWC are increased. On another end, he found that the speed has little effect on the roughness. Shin (1996) compared these trends with the equivalent surface roughness computed in the LEWICE icing code (Ruff and Berkowitz (1990)). In the code the roughness is calculated using an empirical relationship based on the main parameters which are influencing the roughness: the LWC, the temperature and the speed. The results between Shin (1996) and Ruff and Berkowitz (1990) give the same trend for the LWC and the temperature dependence. However, the authors don't agree concerning the influence of the speed on the roughness growth. For Shin (1996) the air speed has little effect on the roughness whereas Ruff and Berkowitz (1990) consider that the roughness is increasing with the air speed. Ruff and Berkowitz (1990) recommend further experimental study in order to validate other empirical relationship between the roughness and parameters such as the droplet dimaters, the droplets distribution and the free stream turbulence.
In 1996, Bragg et al. (1996) enhanced Shin (1996) study by measuring the heat transfer on an airfoil with simulated ice roughness. The roughness was not real roughness from icing tunnel tests. It comes from a previous study from Bragg et al. (1995) where the roughness was simulated using hemispherical elements with heights of 0.35 mm and 0.75 mm and spacing from center to center of 1.3 mm and 1.9 mm. This range of roughness height and density is close to the one of Shin (1996). Bragg et al. (1996) found that the heat transfer downstream the roughness was increased by 2.5 in regards to the heat transfer value from the laminar boundary layer with no roughness.

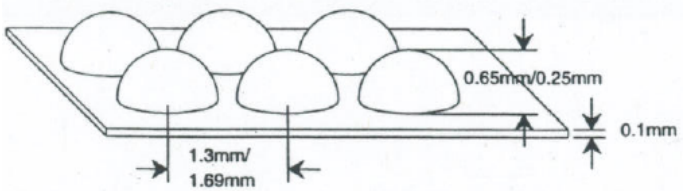

Figure 2.3: *Distributed rougness (Bragg et al. (1996))*

There exists a different method from the empirical approach depending on the icing conditions (Ruff and Berkowitz (1990) and Shin (1996)) to evaluate the surface roughness. Louchez et al. (1998) presents an ice accretion thermophysical model developped by the University of Quebec and CIRA[1]. The evalution of the beads roughness is made using a force balance on the bead.

[1]Italian Aerospace Research Center who owns the biggest icing tunnel in Europe

The height of the bead is considered as being the surface roughness. For the water film it is unclear. A mass and energy balance is made to evaluate the thickness of the film but it seems that no roughness is given to the water film. Fortin et al. (2006) presented a similar roughness approach for an icing code developped by AMIL[2] and CIRA. It is based on a force balance, however the approach has been improved as the roughness for the water film and for the rivulets is evaluated. The bead roughness is equal to the height the bead reaches before moving, the rivulets roughness is equal to the rivulets height which is assumed to be the bead height just before moving, and the roughness of the water film is equal to the wave height at the film surface. Fortin et al. (2006) have eveluated their method by comparing their ice shapes with other works and experiments and they have found a good accuracy. They have in particulary compared their ice shapes with the one produced by the LEWICE icing code which uses an empirical approach to calculate the roughness (Ruff and Berkowitz (1990).
However, whatever the approach to calculate the roughness, only an uniform roughness is taken into account. Dukhan et al. (2003) investigated the difference between randomly spaced roughness, which is close to the reality, and uniform roughness simulated by hemispherical elements. To do so, the authors study the heat transfer around aluminium casts of 2 types wet leading edge ice accretion: middly rough glaze and rough glaze with horns (Figure 2.4). He concluded that the heat transfer coefficients calculated for the uniform roughness were underestimated compared to the heat transfer coefficient calculated with the castings. The roughness distribution is still the focus of research works.
Despite the efforts of the icing community to get a value of roughness size, the roughness characteristics (height, density and location) is still not well known in the icing context. There exists 2 main approaches, one based on an empirical evaluation of the roughness and one based on an analytical approach using a force balance. Both methods seem to give results of similar accuracy. However, many unknowns remain in the calculation or evaluation of the ice or water roughness in icing aircraft context. The main track of investigation is maybe to find a non uniform roughness law. Nowadays a rule of thumb is used to evaluate the roughness of the rivulets in the case of runback ice. A constant value of 25 μm is usually used.

[2]Anti-Icing Materials International Laboratory

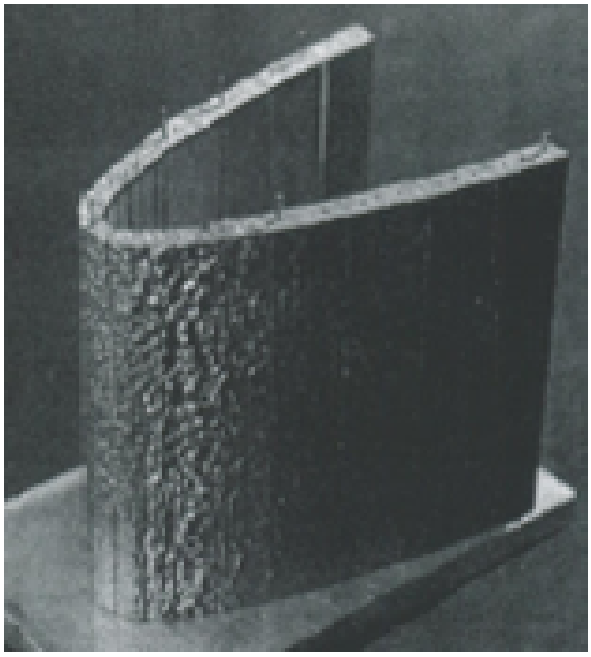

(a) Middly rough glaze ice

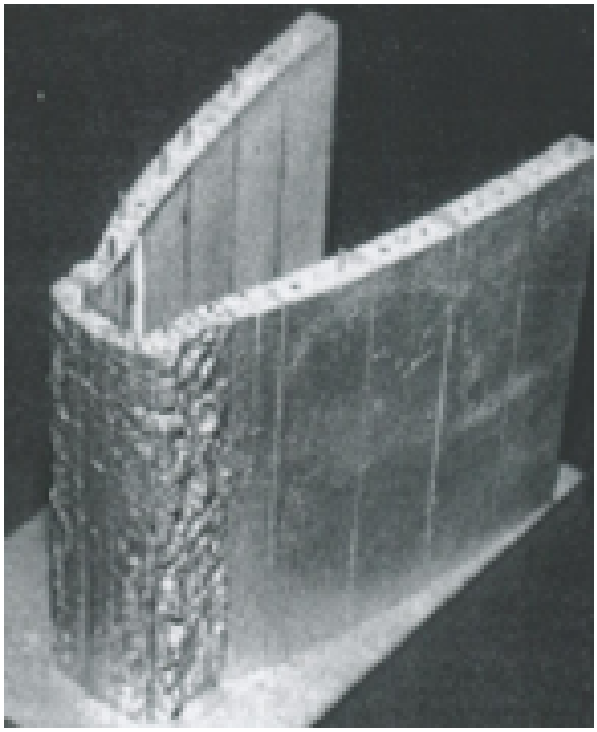

(b) Rough glaze ice with horns

Figure 2.4: *Aluminium castings for a NACA 0012 leading edge(Dukhan et al. (2003))*

Turner et al. (2000) carried out experiments in order to measure the heat transfer coefficient over a curved and roughed surface using the lower surface of a wind tunnel. The upper surface of the tunnel could be flexed in order to control the streamise pressure gradient. The roughness was simulated using pyramidal elements of 1 mm, 0.75 mm and 5 mm. The authors found that an acceleration in the flow increased the heat transfer up to 18%. The curvature caused an increase of the heat transfer of 2 to 3% compared with the straight section. The roughness elements increased the heat transfer by 70%. They concluded that the effect of the pressure gradient and curvature on the heat transfer coefficient was small compared to the effect of the roughness.

Following this literature review about the heat transfer coefficient, it seems that the heat transfer is tricky to evaluate as it is influenced by the nature of the flow, surface curvature, pressure gradient and surface roughness. Then, in the context of icing, the surface roughness of the substrate (airfoil, ice or water) is going to have a major impact on the heat transfer coefficient and then on the ice accretion rate.

2.1.4 The Messinger model

A very popular model used to quantify the energy and mass fluxes over a surface in the context of icing aircraft, is the Messinger model (Messinger (1953)). This is a one-dimensional equilibrium energy balance on a control volume to analyze wet or dry surface, for surface temperature below 0°C, equal to 0°C or above 0°C (Figure 2.5).

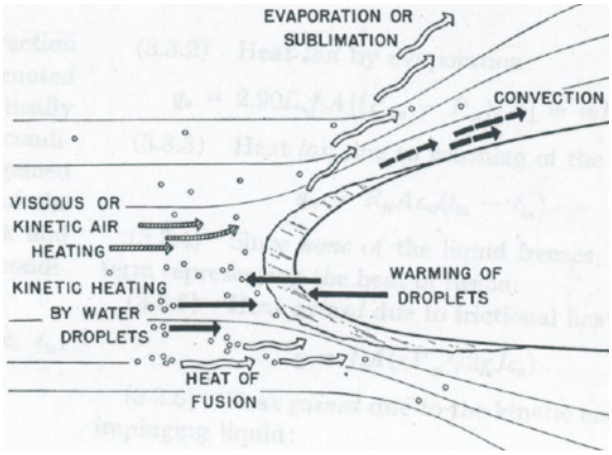

Figure 2.5: *Energy balance on a non heated airfoil leading edge with a surface temperature below 0°C (Messinger (1953))*

Messinger introduced the notion of freezing fraction which "denotes the proportion of the impinging liquid which freezes in the impingement region". Then the freezing fraction is changing from 1 to a value below zero when switching from rime ice to glaze ice. In the Messinger model, the switch is immediate. The surface is considered as non heated. In the context of runback ice, the water is impinging on a surface with a temperature above 0°C. The energy fluxes involved in water droplets impinging a surface above 0°C, following the Messinger model, are:

- Energy entering the control volume:
  - Aerodynamic heat
  - Kinetic energy of the droplets impacting the surface
- Energy leaving the control volume:
  - Convective heat
  - Evaporation heat
  - Droplet warming

It is important to note that following the Messinger model from 1953, as it is for a non heated surface, there is no heat flux allowed for a heating system. What's more the Messinger model does not take into account the heat loss by radiation and the conduction through the water, the ice or the substrate.

This energy balance has been improved, by adding the heat input from an anti-icing system and the heat loss by conduction through the substrate (Ruff and Berkowitz (1990)). Moreover, it has been associated with a mass balance as illustrated in Hansman Jr and Turnock (1989). Gent et al. (2000) explained that the energy balance has been modified a few years before to cope with compressible flow. They combined the air kinetic heating and the convection, and they changed the expression of the heat loss by evaporation (O'Rourke (2006)). The new expression "allows for the effect of pressure distribution around the airfoil on the local water vapor concentration".

Myers (2001) proposed to improve the limitaions of the Messinger model, knowing the freezing fraction switch between rime and glaze ice and the conduction within the water and ice sublayers. Both, the freezing fraction and the conduction through the ice and water, are time dependent. In reality, the conduction at the water/ice interface tends to cool down the system. It leads to an increase in the ice accretion rate. The author succeeded to get

ice growth as a function of the time in taking into account the conduction through the water and ice sublayers. Myers was able to get temperature profiles inside the water and ice sublayers which may improve the heat transfer calculation. He found a formula to predict at which ice thickness the glaze ice is going to form. Finally he was able to predict a smooth transiton of the freezing fraction. This new model has been compared to experimental data. It showed better agreement than the Messiger model, especially in glaze ice accretion. The Messinger model tends to underpredict ice accretion in these conditions. This new mathematical model has been implemented in the Icecremo code (O'Rourke (2006)).

2.2 Simulation of runback ice for aerodynamic performance loss study

According to the literature, the aerodynamic performance of an airfoil or a wing can be dramatically changed due to ice accretion. The problem is very complex as it is a function of:

- The airfoil/wing geometry
- The chordwise position of the ice shape
- The phase of flight
- The atmospheric conditions.

Several studies have been carried out to evaluate the importance of these parameters on the aerodynamic performance of an airfoil under icing conditions using in-flight data, experiments or numerical models. However, many studies based on sub-scale shapes at sub-scale Reynolds and Mach number have been done but very few results of full-scale high-fidelity aerodynamic runback ice study exist in the open literature.

In the early fifties, Gray and Von Glahn (1953) led experiments on the influence of high-fidelity 3D runback ice on the drag of a NACA 65-212 airfoil (c=2.43 m) equipped with hot-air anti-icing system, in the NASA Lewis icing tunnel. The authors's objective was to see if it was possible to tolerate runback ice without losing too much of the clean wing aerodynamic performance. Tolerated runback ice on the airfoil would have meant reducing the heat input from the system and saving some energy. The maximum speed investigated was 116m/s, with a droplet range from 10 μm to 16 μm, a LWC from 0.25 $g.m^{-3}$to 1.4 $g.m^{-3}$, outside air temperature from -34°C to -1.1°C and an AOA from 2°to 8°. The drag was directly measured during the ice growth, thanks to an electrically heated pressure rake. The authors highlighted that the runback ice shape and location were highly dependent on the catch efficiency, heating system input and air temperature. A noticeable increase in the drag occurs for glaze ice condition (either primary or runback) especially at high AOA. For 2°AOA, the drag increases of 29% in 20 minutes of icing whereas at 8°AOA, the drag is increased by 10% within the first 2 minutes of icing. For rime ice conditions, the drag increase was very small. The runback ice on the lower surface was proved to play a negligible role in the drag increase. However, even though the authors studied full-scale runback ice, no moulding and casting of the ice was done because the aerodynamic testing were led

directly in the icing tunnel. More over, as the flow in an icing tunnel is a lot more turbulent than in a wind tunnel, it makes the meaning of the aerodynamic measurements uncertain. This last remark highlighted the crutial need of high-fidelity runback ice castings in order to have releavant aerodynamic measurements from an aerodynamic wind tunnel where the turbulence level remains low.

Calay et al. (1997) led a series of wind-tunnel tests on a NACA 0012 airfoil (c=1 m) to simulate the aerodynamic effects of 2D runback ice, on a subscale model, at low speed and using simplistic ice shapes for different chordwise positions (see Figure 2.6). Hence, no comparison between the aerodynamics of the simplistic shapes and the real shapes was done. The simplistic shapes were triangles with sharp edges and different angles between the front surface of the shape and the normal to the surface.

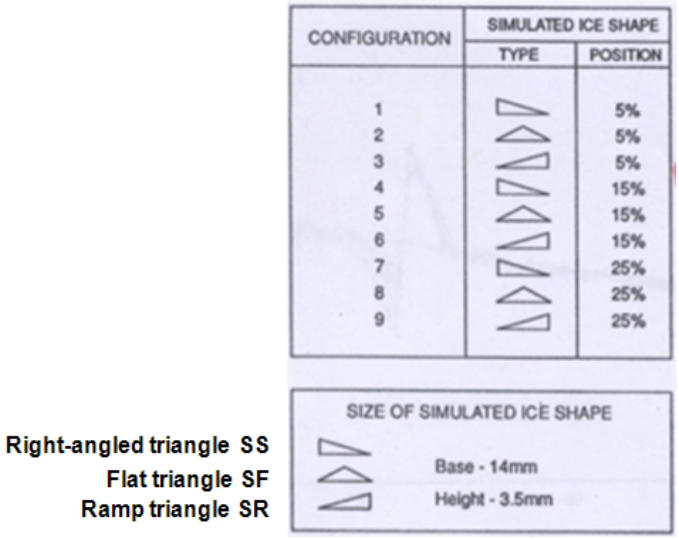

Figure 2.6: *Test figure configuration (Calay et al. (1997))*

The simplistic shapes were chosen based on the most critical ice shapes approach. This approach is widely used by the aircraft manufacturers. It consists on considering the triangle shape as the most critical shape in terms of aerodynamic performance loss (the most conservative) to simulate runback ice shapes. This approach is based on icing code, experimental results and flight tests data. The tunnel speed was 30m/s with a Reynolds number of $1.23 * 10^6$. The authors highlighted that (Figure 2.7):

- The ramp triangle is the least adverse for the flow in terms of drag coefficient and lift coefficient whatever the chordwise positions

- The right-angled triangle is the worst shape for the flow in terms of lift coefficient whatever the chordwise positions

- The flat shape is the worst for the flow considering the drag coefficient for the first and last position positions on the airfoil. For the middle position the right-angled triangle is slightly worst.

They found that the contaminated airfoil has a greater $C_{l_{max}}$ than the clean airfoil, for the positions 15% and 25% of the chord.

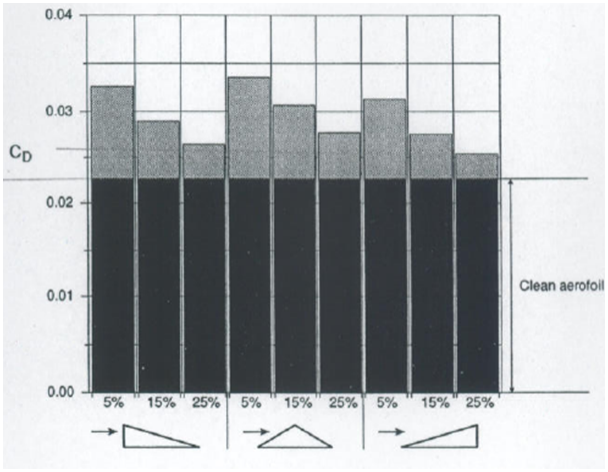

(a) Drag coefficient

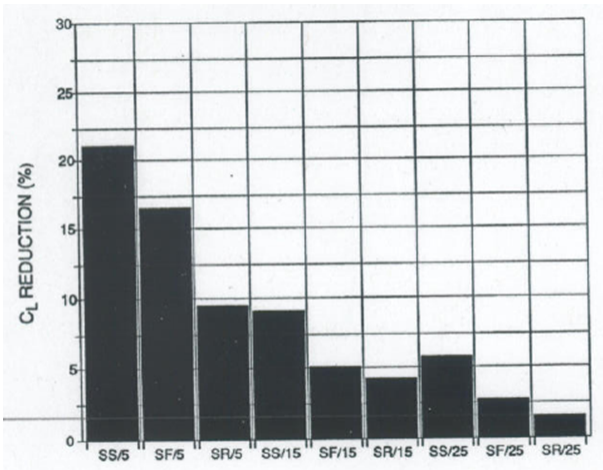

(b) Lift coefficient

Figure 2.7: *Comparison of aerodynamic coefficients for various ice shapes at different chordal positions and the clean airfoil (Calay et al. (1997))*

Lee and Bragg (1999) and Lee et al. (2000) investigated the ice shapes which grew downstream of the protected surface of a de-icing system, forming a ridge. Even if they argue that these kinds of shapes are generally a consequence of SLD conditions, it is possible to make an analogy between runback ice due to wet thermal systems and such ice accretions. They investigated 2D simple geometry such as quarter round or ramp on a NACA 23012 and NLF 0414 airfoils for $Re = 1.8 * 10^6$. Figure 2.8 shows these simplistic shapes.

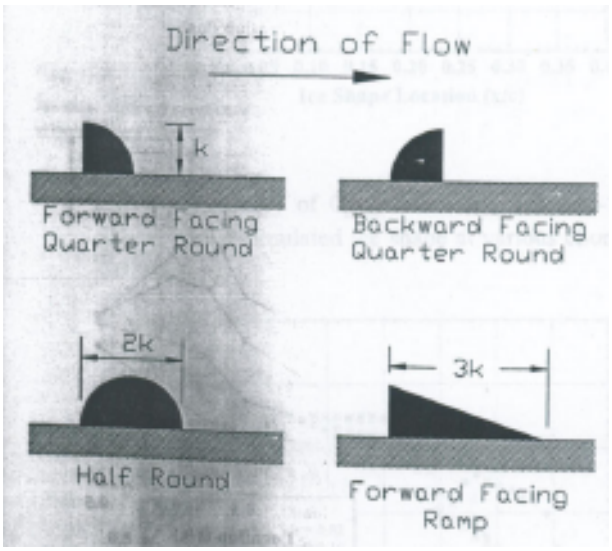

Figure 2.8: *Ice shapes simulation geometry (Lee and Bragg (1999))*

The tests are based only on simplistic shapes with no comparison with realistic shapes and on a subscale airfoil at low speed. The ratio of the investigated shapes thickness to the airfoil chord was from d/c=0.0056 to d/c=0.0139. They concluded that the effect of the simulated ice shapes is highly dependent on the airfoil geometry, on the chordal position of the ice shapes and on the ice shapes geometry. The half-rounded shape has the greater increase in the maximum lift coefficient and for the shapes with the most blunt forward faces (forward facing quarter round and forward facing ramp), the backward face has very small influence on the aerodynamic of the shapes. Another point that the authors highlighted is that the Reynolds number has very little influence on the $C_{l_{max}}$ loss beyond a critical value. The critical Reynolds number, beyond which there is no influence on the $C_{l_{max}}$, decreases when the ice shape is increasing. For instance for a leading edge roughness with d/c=0.0009, the critical Reynolds number is $0.1 * 10^6$.

Papadakis et al. (2004b) enhanced the aerodynamic study of 2D ridge ice shapes by performing similar experiments on a swept wing instead of an airfoil. A subscale swept finite wing representative of a modern business and regional jet aircraft was used. The wing consisted of an 8.7% thick airfoil section, which remained constant from root to tip, a leading edge sweep of 28°and a trailing edge sweep of 15.6°(Figure 2.9).

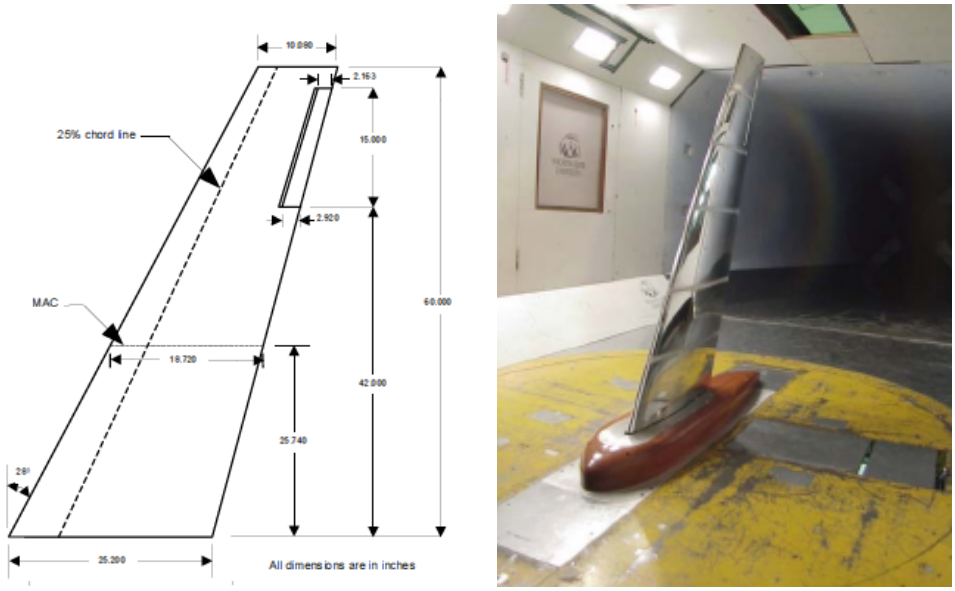

(a) Drawing (b) The swept wing in the WSU

Figure 2.9: *The swept wing used by Papadakis et al. (2004a)*

The experimental investigation was conducted in the Wichita State University (WSU) Beech Memorial Low- Speed Wind Tunnel with a Reynolds Number of $1.46 * 10^6$ per foot, an AOA from -8°to 20°and M=0.185. The simplistic ice shapes tested are triangles, squares and quater rounds (Figure 2.10). All ice shapes remained constant with spanwise distance. In non-dimensional terms the height of the simulated ice shapes ranged from 1.07% to 2.67% of the mean aerodynamic chord. The shapes geometry was chosen in order to be similar to previous experimental studies on 2D airfoils (Lee and Bragg (1999)). The shapes were located at different chordwise positions to study the influence of the ice shape location on the aerodynamic results. The authors found that the wing aerodynamic performance is very sensitivity to ice shapes geometry and chordwise position. Though, it is difficult to get clear trends of which shape is definitely the worst for the flow. If we consider that for a commercial jet equiped with an anti-icing system, the limit of the protected region is up

to 10% of the chord, only the positions at 10% and 15% of the chord are interesting in the context of the runback ice. The positions at 20% and 30% of the chord are considered to be too remote from the end of the theoretical heated region to be contaminated by runback ice. The position at 2.5% and 5% of the chord are considered to be in the heated region.

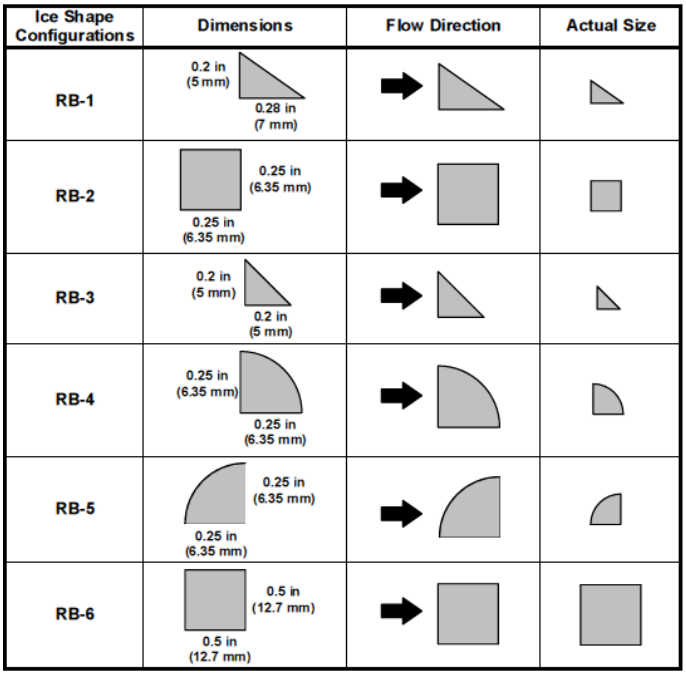

Figure 2.10: *Simplistic shapes geometry (Papadakis et al. (2004a))*

In Figure 2.11 the $C_{l_{max}}$ is reported for all the shapes at the different chordwise positions. The shapes RB4 and RB6 have a $C_{l_{max}}$ which is increased as the position is moved further downstream. The shapes RB1 and RB2 have a $C_{l_{max}}$ which is decreased as the position is moved further downstream. The shapes RB3 and RB5 have a $C_{l_{max}}$ which remains constant as the position is moved further downstream. Finally, it is found that $C_{l_{max}}$ of the contaminated airfoil is always greater than $C_{l_{max}}$ of the clean airfoil, except for shape RB6 at 10% of the chord.

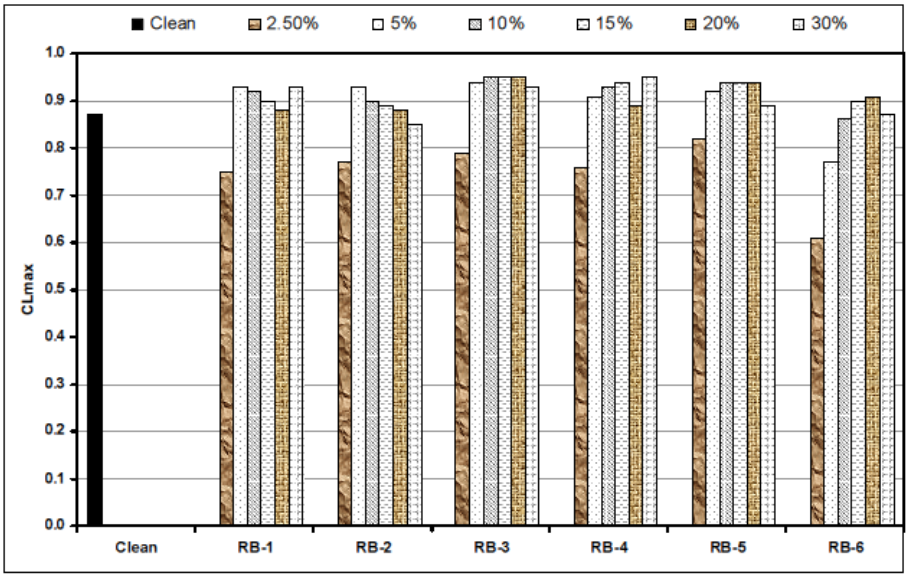

Figure 2.11: *Ice shapes geometry (Papadakis et al. (2004a))*

Whalen et al. (2005) and Whalen et al. (2006) went further than the previous authors in the study of the runback ice aerodynamic. They first grew thermodynamically scaled runback ice shapes on a full-scale typical business jet 3D wing section equiped with a hot-air ice protection system for different phases of flight (Table 2.1), in the NASA Glenn IRT (Figure 2.12). The wing had a span of 1.82 m, a root chord of 1.7 m and a tip chord of 1.4 m. The purpose of the thermodynamic scaling was to take into account the altitude which changes the heat and mass transfer in the external flow. They made high-fidelity ice casting of the collected ice shapes. They concluded that full-scale ice shapes were required to compared with the thermodynamically scaled ones in order to assess the thermodynamically scaling method. Following that, they conducted aerodynamic testing in the Illinois 3 by 4 foot subsonic wind tunnel. Due to wind tunnel and financial limitations, they did not used the high-fidelity ice castings. Instead, they tested geometrically-scaled

(ratio to the chord) and boundary-layer scaled (ratio to the local boundary layer thickness) simplistic 2D shapes (square or rectangular cross section) and 3D artificial runback ice shapes (multiple substrate layers and non uniform roughness) on a NACA 23012 and a NACA 3415 for a Reynolds number of $1.8 * 10^6$ and a Mach number of 0.18. They compared the results for the clean airfoils with the same Mach number and Reynolds number. They found that geometry scaled shapes enhance the aerodynamic performance of the airfoil when the size of the local boundary layer thickness is of the same order as the ice height. The boundary layer scaled ice shapes never enhanced the aerodynamic performance of the airfoil. The authors recommend further studies in the field of ice shapes scaling methods and aerodynamic full-scale testing (airfoil, Reynolds and Mach number).

Conditions	U∞ (m/s)	T∞ (°C)	LWC (g/m^3)	MVD (µm)	Altitude (ft)
Warm hold	105	-6.6	0.50	20	15000
Cold hold	100	-30.0	0.15	20	15000
Descent	128	-20.0	0.15	20	10000

Table 2.1: *Icing conditions for the phases of flight investigated by Whalen et al. (2005))*

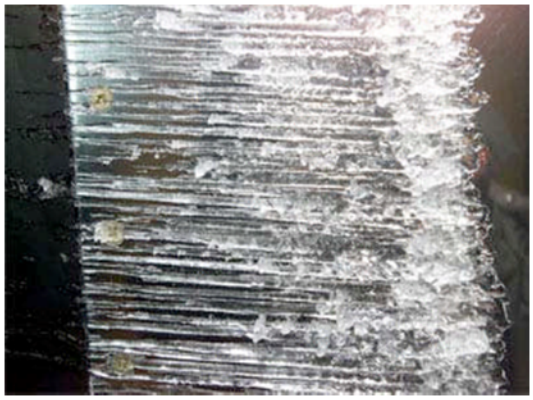

Figure 2.12: *Close-up picture of a upper surface warm hold ice accretion after 22.5 minutes accretion, T_t=-5° C, $U\infty$=59 $m.s^{-1}$, LWC=0.87 $g.m^{-3}$ and MVD=29 µm (Whalen et al. (2005) and Whalen et al. (2006))*

For this reason a wide program of research is led by NASA, Onera and the University of Illinois on airfoil ice accretion aerodynamic simulation (Bragg et al. (2007)). The autors investigated several type of ice, including runback

ice. The objective of the programme is to validate sub-scale simulation methods by comparing these methods to full-scale high-fidelity ice accretion data. The programme is based on 6 phases:

- Phase1: Classification of the ice shapes based on their aerodynamic effect on the flow in the vicinity of an airfoil (Bragg et al. (2005), Figure 2.13): roughness, horn ice, streamwise ice and spanwise ridge. The runback ice shape belongs to the spanwise ridge type of ice.
- Phase 2: Ice accretion in the NASA IRT on a sub-scale model (NACA 23012, c=0.457 m). The objective is to get ice accretions which have the same geometric features as in phase 1. The ice shapes are recorded using numerous pictures, tracings and 3D castings.
- Phase 3: Aerodynamic tests of the previous sub-scale ice accretions were led in the University of Illinois wind tunnel. In additon to the 3D high-fidelity castings, 2D smooth shapes based on smooth profiles from ice tracings and simple geometric shapes (rectangles, etc) were tested as well (Broeren et al. (2007)). The authors concluded that the best match with the 3D casting was the 2D smooth shape and that the addition of grit roughness on the 2D shapes didn't improve the simulation.

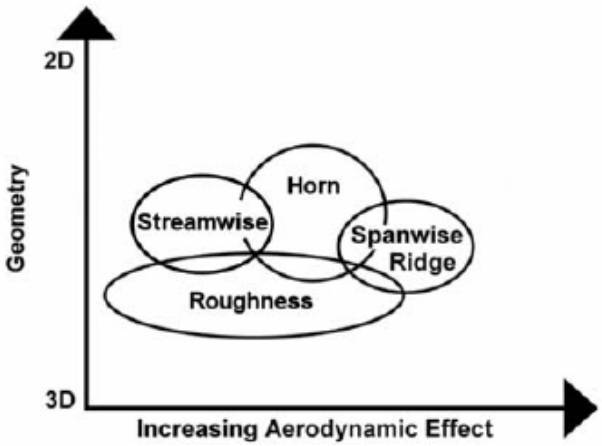

Figure 2.13: *Classification of the different types of ice shapes depending on their aerodynamic effect (Bragg et al. (2005))*

- Phase 4: Full-scale ice accretion testing in the NASA IRT on a NACA 23012, c=1.828m. The objective is to get ice accretions which have the same geometric features as in phase 1. The ice shapes are recorded using numerous pictures, tracings and 3D castings. Figure 2.14 shows the tracing and a picture of full-scale spanwise ridge accretion for U_∞ =77 $m.s^{-1}$, AOA=1.5°, MVD=20 μm, LWC=0.81 $g.m^{-3}$, $T_t = -6.7$°C, $T_s = -9.6$°C and for a time of accretion of 15 min. The spanwise ridge accretion, is the closest shape to runback ice.

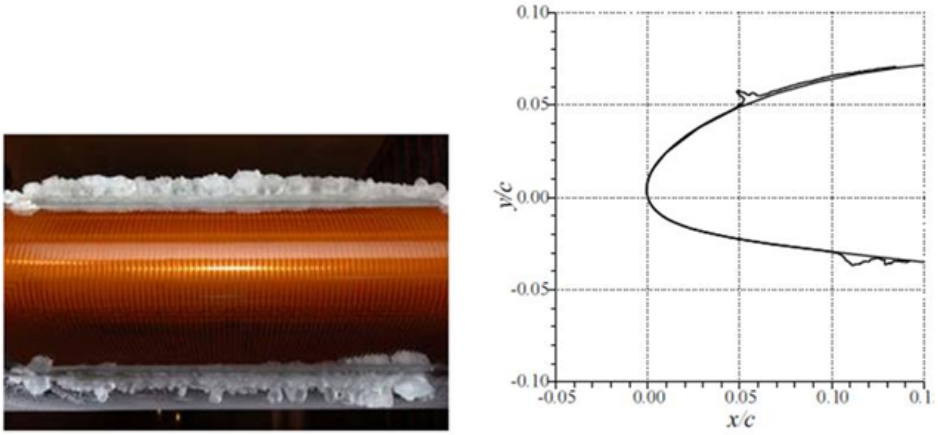

(a) Runback ice picture (b) Runback ice tracing

Figure 2.14: *Picture and tracing of full-scale spanwise ridge ice shape for* U_∞ *=77* $m.s^{-1}$ *, AOA=1.5°, MVD=20* μm*, LWC=0.81* $g.m^{-3}$*,* $T_T = -6.7°C$*,* $T_S = -9.6°C$ *and for a time of accretion of 15 min (Bragg et al. (2007))*

- Phase 5: Aerodynamic tests of the previous full-scale 3D castings were led in the Onera F1 pressurized wind tunnel on a NACA 23012, c=1.828 m. Some runback ice castings (NG0671 and NG0662) from another icing tests in the NASA IRT where tested as well in phase 5 (Figure 2.15). These castings are supposed to be "representative of flight in holding conditions for a full-scale aircraft equiped with a bleed-air, thermal ice protection system" (Broeren et al. (2010c)). These two runback ice shapes were grown for the same typical hold conditions: U_∞ =72 $m.s^{-1}$, AOA=1.1°, MVD=28 μm, LWC=0.91 $g.m^{-3}$, $T_t = -5.05$°C, $T_s = -7.66$°C and for a time of accretion of 22.5 min.

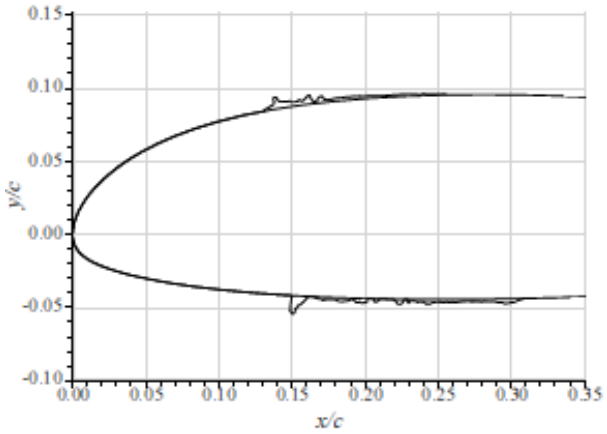

(a) NG0662

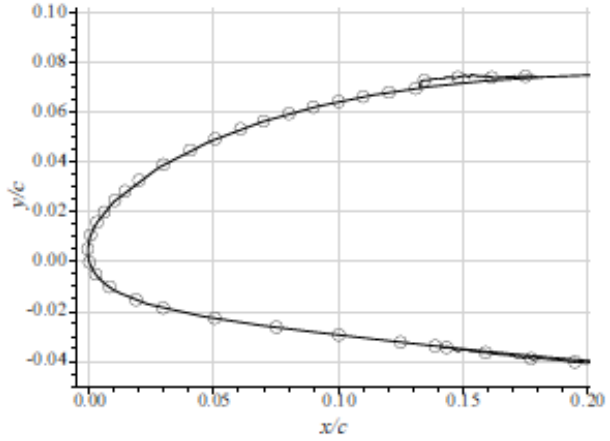

(b) NG0671

Figure 2.15: *Tracings of full-scale runback ice accretion on a NACA 23012 leading edge for* U_∞ *=72* $m.s^{-1}$*, AOA=1.1°, MVD=28* μm*, LWC=0.91* $g.m^{-3}$*,* $T_T = -5.05°C$*,* $T_S = -7.66°C$ *and for a time of accretion of 22.5 min (Broeren et al. (2010c))*

The only difference between both accretions is the amount of heat from the system. The results of these tests are presented by Broeren et al. (2010a), Broeren et al. (2010c) and Cassou De Salle et al. (2009) for a Reynolds number range from $4.5 * 10^6$ to $16 * 10^6$ and a Mach number range from 0.10 to 0.28. Even though, no full-scale simplistic shapes were tested because of a lack of time in the wind tunnel, these results are the only results available in the open literature for aerodynamic study of full-scale high-fidelity runback ice shapes. For the runback ice shape NG0671 compared to the clean airfoil, the loss in Cl_{max} is evaluated

at 17%, the stall AOA is decreased by 17% and the Cd_{min} is increased by a factor of 2. For the spanwise ridge (Figure 2.14) the aerodynamic performance loss are much more dramatic. The authors found that the shape lead to a decrease of Cl_{max} of 70% compared to the clean airfoil, the stall AOA is decreased by 69% and the minimum drag coefficient is at least four times the one of the clean airfoil. Moreover, the authors found that the contaminated airfoil performance does not change much for the range of Mach number and Reynolds number investigated in the study.

- Phase 6: To close the study, the previous full-scale high-fidelity ice shapes are 2D geometrically scaled, simplified and compared to the results of phase 5. Only the results for the runback ice shape NG0671 are reported here as this is the most important shape in relation to this PhD work. The simplistic shapes associated with the shape NG0671 are rectangular ridges associated with roughness or rivulets applied on the upper surface only, or on the upper and lower surface (Figure 2.18). The simplistic shapes were tesed in the wind tunnel of the University of Illinois on a NACA 23012, c=0.457m, with M=0.18 and Re=$1.8 * 10^6$ (Broeren et al. (2010c)). The authors found that the lift curve slope for the simple geometry on the upper surface only was slightly lower than the airfoil with the NG0671 casting full-scale for higher Reynolds number (Re=$16 * 10^6$ and M=0.20). However the Cl_{max} and the stall AOA are pretty much the same between the sub-scale simplistic shape and the full-scale casting. The drag of the simple geometry is smaller than for the casting.

  Adding a simple geometry on the lower surface of the airfoil didn't change the lift performance but it makes the drag coefficient closer to the casting. Adding some roughness on the simplistic shape on the lower and upper surface of the airfoil makes the values of the lift coefficient, stall angle of attack and drag coefficicient to diverge from the casting. Instead of adding roughness, some rivulets were added to the lower and upper surface to see if a more complex simulation would improve the results. Broeren et al. (2010c) found that the aerodynamic perforamance was closer to the casting when using rivulets than with the roughness. However, the closest results with the casting were obtained for the simple geometry on the upper and lower surface.

  None of the simplistic shapes tested, lead to the same stall character-

istics as the casting. The authors reported that the Cl_{max} and the stall AOA where slightly greater for the slimplistic shape on the upper surface than for the clean airfoil for the same scaled Reynolds number (Re=$1.8*10^6$) and Mach number (M=0.18). These results are similar to Calay et al. (1997), Papadakis et al. (2004b) and Whalen et al. (2005). These authors didn't really justify their findings by lack of full-scale data. However, they mentionned that one of the reason for a gain in aerodynamic performance due to geometrically scaled ice shape could come from the fact that the shapes where the same height as local boundary layer thickness for AOA near stall. Thus, the ice shape in such cases would energize the boundary layer. In regards to the full-scale study, Broeren et al. (2010c) justify these results by the fact that there is a reduction in clean airfoil lift performance for low Reynolds number. Then, the ice shape might act like a low Reynolds number lift enhancement device.

To sum-up, the study of the aerodynamic of runback ice shapes is a very complex problem for several reasons. High-fidelity runback ice is highly dependent on the atmospheric conditions and on the heating systems. Morever, the study of the aerodynamic performance loss of runback ice is highly dependent on the airfoil geometry and on the chordwise position of the shape. Then, the aerodynamic study of runback ice needs further investigation in different fields. The 2 main tracks of investigation are:

- Study of the ice shapes scaling: Different methods of scaling have been investigated so far but none has been validated. The thermodynamic scaling to grow runback ice need to be checked with full-scale runback ice shapes. Concerning the geometry scaling of the shapes, it is has been tried to scale a shape in comparison to the chord length or to the boundary layer height. Some studies of geometrically scaled runback ice highlighted that the iced airfoil has greater aerodynamic performance loss than the clean airfoil. This kind of result is not found when the ice shapes are scaled to the boundary layer. An explanation for this result could be the difference in aerodynamic performance between the clean model full-scale for high Reynolds number and sub-scale for low Reynolds number.

- Enhancement of the data base of full-scale realistic runback ice shapes and comparison with full-scale simplistic shapes: So far very few people have studied full-scale runback ice shapes because it is difficult to put in place. Only one aerodynamic study has been done for full-scale high-fidelity runback ice shapes. However these shapes have not been

compared to full-scale simplistic shapes. It has only been compared to sub-scale simplistic shapes

Some of the results of this literature review about the aerodynamics of runback ice, are going to be widely used in the present study, either to take decisions concerning the set-up for the tests or to compare with my experimental results:

- Because of the high turbulence level in an icing tunnel and because of the complexity of insulating measuring device against the cold and the water, two sets of experiments are required to study the aerodynamic of high-fidelity runback ice: one set in an icing tunnel to get high-fidelity runback ice shapes and a second set in an aerodynamic wind tunnel to get good aerodynamic meassurements (Gray and Von Glahn (1953)).

- As the aerodynamic performance loss of the runback ice is highly related to the airfoil geometry, it is impossible to find results which are true for all airfoils. Then the choice of the model for the wind tunnel tests has to be chosen with care, keeping in mind that the results might change with another model (Lee and Bragg (1999) and Lee et al. (2000)).

- Above a certain limit, the Reynolds number and Mach number have a small influence on the aerodynamic performance of an iced contaminated airfoil (Lee et al. (2000) and Broeren et al. (2010a)). Then, the results from aerodynamic testsing a low speed wind tunnel are maybe not that remote from the reality.

- The simplistic shapes based on the most simple design lead to the results the closest to casting (Broeren et al. (2010c)).

- Roughness on the simplistic shapes have a large influence on the aerodynamic performance of the airfoil (Broeren et al. (2010c)).

- Bragg et al. (2007) presents conditions to grow full-scale runback ice shapes typical of hold configuration on a NACA 23012 with c=1.828 m: U_∞ =72 $m.s^{-1}$, AOA=1.1°, MVD=28 μm, LWC=0.91 $g.m^{-3}$, T_t = -5.05°C, $T_s = -7.66$°C, time of accretion 22.5 min.

- Broeren et al. (2010c) has reported full-scale high-fidelity runback ice tracings which can be compared to the results of my icing tunnel experiments.

2.3 Capturing runback ice shapes geometry

Reehorst and Richter (1987) describe an alternative to the usual wax and plaster used for 3D high fidelity ice shapes. Wax and plaster have some drawbacks which could be avoided if more modern materials are used. For instance, Reehorst and Richter (1987) reported that using wax, means using an airfoil with a removable leading edge in order to soak the leading edge with the ice in a bath of wax. Moreover, when it comes to casting from a wax mould, the mould can be used once as it has to be destroyed to remove the casting inside. The plaster has the inconvenience of being brittle which is not so convenient if the casting has to be tested in a wind tunnel. The authors recommend using silicone for moulding and epoxy or urethane for casting. It is important to mention, that the study of Reehorst and Richter (1987) is mainly focus on leading edge ice accretion which is different from runback ice shapes.

Calay et al. (1997), Lee and Bragg (1999), Papadakis et al. (2004b) and Bragg et al. (2005) based their aerodynamic study of runback ice on 2D simplistic shapes. Very simple geometry such as triangle or rectangle are used to imitate the main features of the ice accretion. This is the easiest way to simulate ice shape.

Whalen et al. (2005) studied 2D and 3D shapes based on quantitative observations (build-up approach) from the icing tunnel tests . The method to manufacture the 2D and 3D shapes consists in using a wood substrate covered with sandpaper grit to simulate the roughness (see Figure 2.16). The 2D shapes had uniform roughness whereas some periodic accumulations of roughness were made on the surface of the 3D shapes. The height of the shapes, based on the average height of the accretion heights, were scaled to the chord length or the boundary layer thickness.

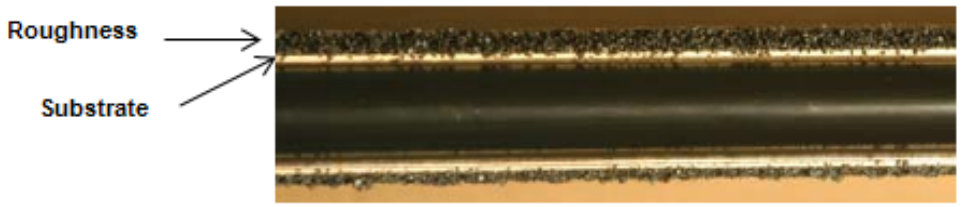

Figure 2.16: *Front view of the leading edge with installed artificial runback accretions (Whalen et al. (2005) and Whalen et al. (2006))*

Broeren et al. (2010c) used a 3D casting method to capture full-scale high-fidelity runback ice shape. The casting matarial was polyurethane of very low viscosity in order "to flow into the intricate details of the ice molds" (Broeren et al. (2010b)). The authors did not indicate what kind of material was used for the moulding. This casting method gives very good results as it captures nearly all of the 3D features and details of original ice accretion. Broeren et al. (2010c) considered the 3D casting as the benchmark for the other types of simulation method in terms of aerodynamic study.

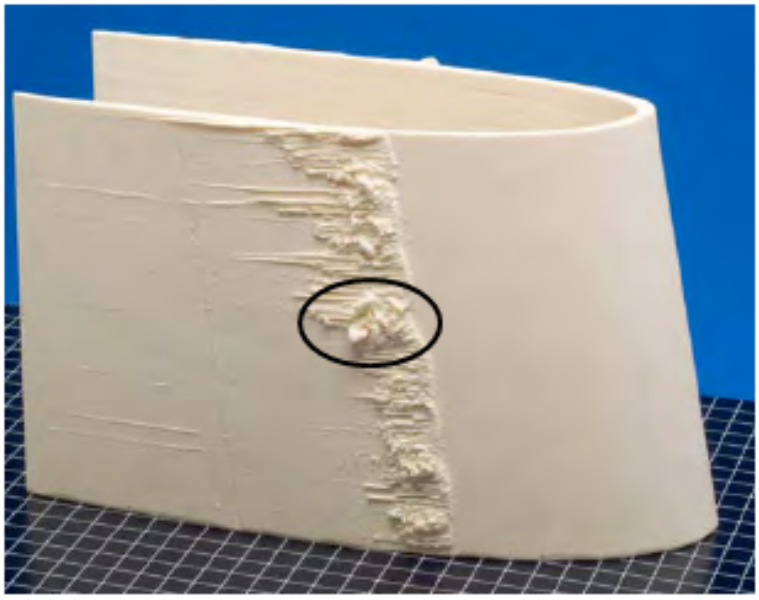

Figure 2.17: *3D high-fidelity full-scale runback ice casting NG0671 (Broeren et al. (2010c))*

Broeren et al. (2010c) study sub-scale simplistic 2D runback ice shapes. These shapes are based on a build-up approach and on the observations of the castings and of the 2D profiles. They are rectangular ridges associated with roughness or rivulets applied on the upper surface, or on the upper and lower surface (Figure 2.18). The location of the simplistic shapes on the airfoil is the same as for the real ice accretion, the height of the simplistic shapes corresponds to a scaling of the maximum height of the full-scale shape and the length of the simplistic shape corresponds to the length of the ridge and the rivulets on the tracing of Figure 2.15.

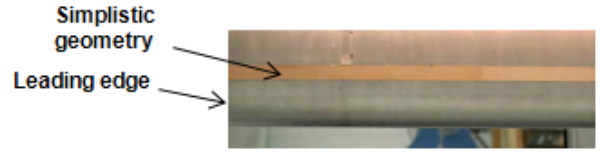

(a) SG-US: Single Geometry on the Upper Surface with height d/c=0.0028 at x/c=0.13 and chorwise extent of 0.047 to the chord

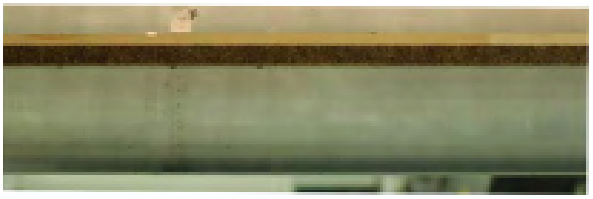

(b) SG+R-US: Single Geometry on the Upper Surface with some roughness element of k_s/c=0.0008

(c) SG+Riv-US: Single Geometry on the Upper Surface associated with simulated frozen rivulets with a height of d/c=0.0017 and density of 18 rivulets per inch-span

Figure 2.18: *Sub-scale simplistic shapes corresponding to the full-scale runback ice shape NG0671 (Figure 2.15, Broeren et al. (2010c))*

So far, it appears that there are two main approaches to simulate runback ice: 3D casting or 2D simplistic geometry which consists on a substrate such as rectangle, triangle or hemishperical shapes, with the possibility to add some

roughness on the top. In the context of this work, we are interested in both methods. The 3D casting is going to play the role of benchmark.

2.4 Ice shapes CFD study

This section is focused on a CFD aerodynamic study of iced airfoils. CFD represents the most cost effective method to study the aerodynamic aspects of icing aircraft. The other methods are flight test and wind/icing tunnel experiments. Several CFD studies have been done to predict aerodynamic performance loss due to aircraft icing. However most of the work has been done for leading edge ice accretions (protuberant horns) (Chung and Addy (2000), Chi et al. (2002), Zhu et al. (2002), Zhu et al. (2003) and Chi et al. (2005)). It was found that in the case where there are large horns and feathers, the prediction can be significantly different from the experiments. The studies addressing runback ice include spanwise ridge which are typical upper surface ice accretions under SLD conditions. Until now, no CFD studies have been encountered in the literature to simulate high-fidelity 2D or 3D full scale runback ice. The strategy used for the grid generation and flowfield calculation on leading edge and upper surface accretion may be re-used (partially) for runback ice study. Several types of grid (structured, unstructured, structured/unstructured, single block, multi block) have been investigated in the literature in order to assess which type is best to model ice features. This is a very complex problem as it is highly linked with the ice shape and the main characteristics of the flow (adverse pressure gradient, detachment, turbulence intensity, etc).

Dunn et al. (1999) studied spanwise step ice shapes ($d/c = 0.0083$ and $d/c = 0.0139$) located at 5% chordal position of a NACA 23012 at M=0.3 and $Re = 3{*}10^6$. It is not exactly the same as runback ice but it is typical of upper surface ice accretions. The spanwise step is studied using a high resolution single block unstructured grid associated with the NSU2D[3] code. It is a 2D RANS solver for single and multi-elements airfoils using unstructured grid. A grid refinement was performed to ensure very fine grid in the vicinity of the ice step. The Spalart-Allmaras turbulence model was used. The results are for a steady flow. The results show good agreement with experiments in terms of lift, drag and (pitching and hinge) moments predicted for iced and non-iced airfoil especially before stall. The results are all the more close to the experimental results when the detached zone is small. The authors concluded that the reason for this is due to unsteadiness which are likely to

[3]The NSU2D code is a code by the Scientific Simulations LLC, www.scientific-sims.com

appear in the flow for large detached bubble. Only an unsteady simulation could catch the unsteadiness. The study shows that single block unstructured grid is able to generate good results for aerodynamics simulation, at least for simple upper surface ice accretion, before flow detachment.

Chung and Addy (2000) tried to evaluate the performance of CFD against experimental data in the case of a NLF-0414 airfoil with leading edge icing. Two ice accretions were investigated: one, with large horns in the front and another one, smaller without any horns, but with lots of little surface details (Figure 2.23).

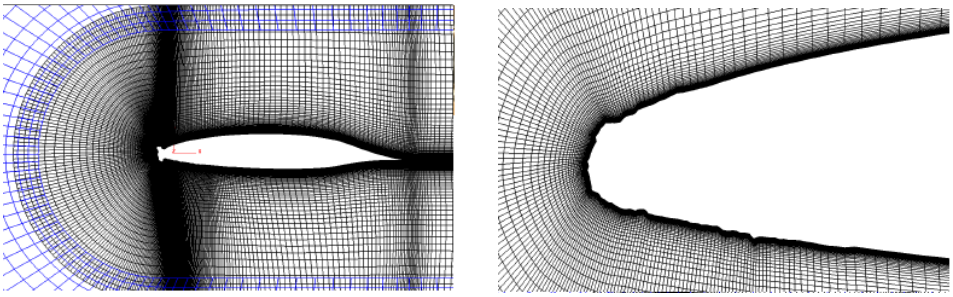

(a) Ice shape with large horns (b) Ice shape without any horns

Figure 2.19: *Mesh around the ice shapes studied by Chung and Addy (2000)*

Only 2D cases were numerically simulated, but 2D and 3D castings were tested in a wind tunnel. A multi-block structured grid was generated with a y^+ below one. The Spalart-Allmaras and SST k-ω turbulence model were used. The Gridgen[4] software was used for the grid generation and WIND[5] for the flow calculation. The authors reported that the Spalart-Allmaras turbulence model proved to be the best for the ice shape with the horn, whereas the SST k-ω turbulence model was the best for the smoother shape and for the clean airfoil. The SST k-ω turbulence model overestimated the effect of the complex shape of the flow. The authors recommend further study to get more results concerning the choice of the turbulence model.

Chi et al. (2002) investigated high-quality single/multi- block structured grids for predominant leading edge ice accretions (horns). The authors tend to implement a method for high-quality single/multi block grids (Figure 2.20).

[4]Gridgen is a meshing sofware developed by the Pointwise company, www.pointwise.com

[5]WIND is a CFD made up of the NASA Glenn Research Center and the U.S. Air Force Arnold Engineering Development Center

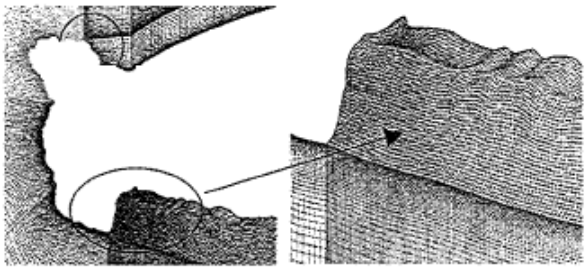

Figure 2.20: *A multi-block grid with highly clusterd grid into the domain and allong the wall Chi et al. (2002)*

They found that there is a good agreement between CFD simulation and experimental data when the ice shape does not protrude too much. In the case where there are large horns and feathers, the predictions can be significantly different from experiments. The authors raised the hypothesis of a meshing problems. The authors observed the creation of streaks and clustered grids next to wall with very high aspect ratio that can degrade the accuracy of the simulation. To solve this problem, Chi et al. (2002) recommend to divide the single grid in one inner and one outer part. In the inner part the grid lines close to the ice shape are regenerated creating sub-blocks. It allows to ovoid streaks. To avoid high aspect ratio grids close to the wall, the authors suggested the creation of a thick wrap-around grid (Figure 2.21). The thickness of this layer is made so that the grid spacing from contiguous blocks will be comparable in size at all block boundaries. The CFD was compared with experiments considering the lift coefficient for different values of AOA. They used the WIND solver, with the SST k-ω turbulence model and second-order formulas. For the clean airfoil the agreement is excellent between CFD and experiments before stall. After stall the numerical simulation does not match the experiments. For the contaminated airfoil the CFD results match the experiments at low AOA and predict well the stall AOA. However the lift coefficient is over-estimated compared to the experimental results.

Pan et al. (2003) studied steady numerical simulation of upper surface quarer-round ridge on NACA 23012, NLF-0414 and NACA 3415 airfoils using the WIND package. The grid is a single block structured grid generated from the airfoil surface to 20 chords length away in all directions, $y^+ = 1$ (Figure 2.23).

The software used to generate the grid is Gridgen. The Spalart-Allmaras turbulence model was chosen because of the good performance of the model compared to experiments and because of the work done by Dunn et al. (1999). Different ice shape sizes and locations were investigated. The simulation

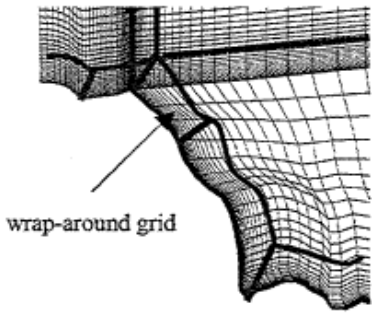

Figure 2.21: *Wrap around grid as presented by Chi et al. (2002)*

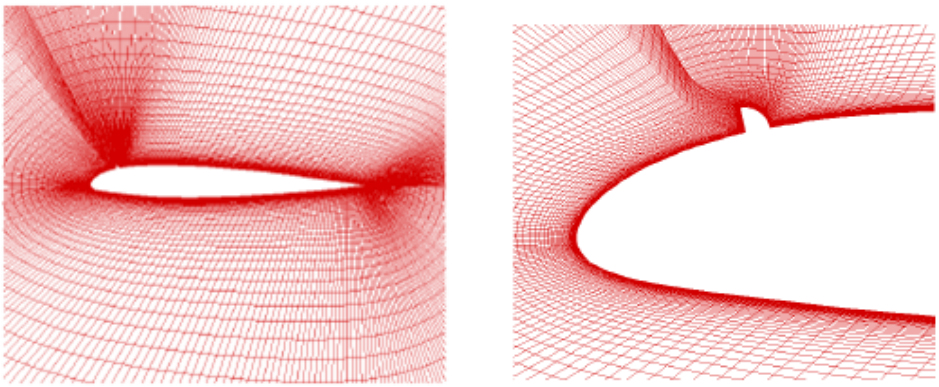

(a) Grid far-field (b) Close-up grid

Figure 2.22: *Grid for NACA 2312 with a ridge on the upper surface Pan et al. (2003)*

shows good agreement with experiments before stall. As Dunn et al. (1999), the authors concluded that when large flow detachment occurs, for instance near stall, a steady RANS simulation won't predict accurate results because of the flow unsteadiness which can't be calculated with such turbulent models. Pan et al. (2003) suggested that more sophisticated turbulence models (unsteady, non RANS), such as Large Eddy Simulation or Detached Eddy Simulation, should be investigated.

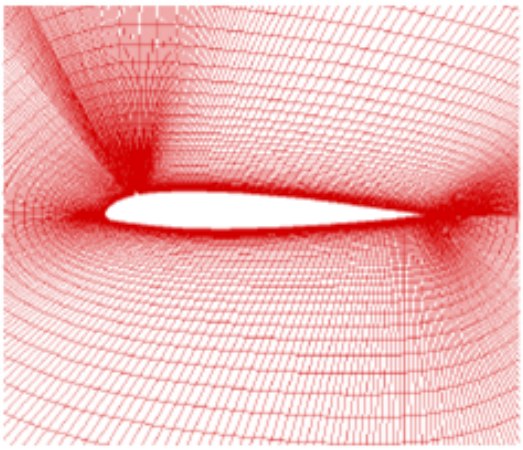

Figure 2.23: *Grid for NACA 2312 farfield view Pan et al. (2003)*

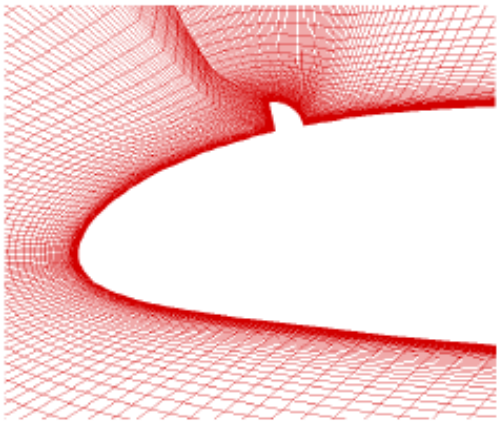

Figure 2.24: *Grid for NACA 2312 close-up view Pan et al. (2003)*

Chapter 3

1D model of runback ice

3.1 Introduction

To be able to grow full-scale runback ice in the CIT, it was vital to fully understand the runback water/ice process. It was as well interesting to have a usefull indication of the heat and mass fluxes values which are associated with the ice growth mechanism with a wet anti-icing system. The value of the anti-icing system heat flux was of major importance in order to design the heating system that would be tested to get runback ice accretion in the CIT. For all of these reasons, a 1D runback ice model, based on the Messinger model (Messinger (1953) and Hansman Jr and Turnock (1989)), has been computed on Excel. The model allows the calculation of the heat and mass fluxes involved in the runback ice growth over an airfoil surface. The accuracy of the model was assessed by comparing the model results with the literature (present section) and with experimental results (see 5.6).

3.2 Details of the 1D model

3.2.1 Model methodology

The mechanism of the model is shown in Figure 3.1. From the airfoil geometry, four steps are required to get all the heat and mass fluxes over the surface. This study is focused on the heat flux from the heating system and on the runback water flux.

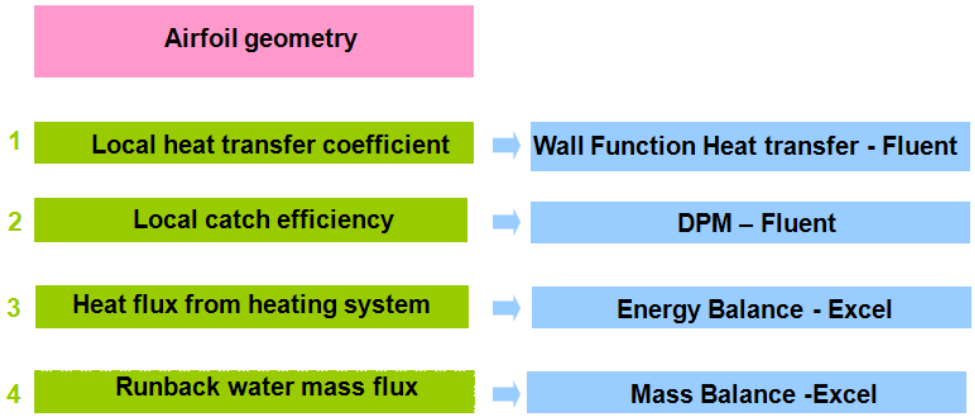

Figure 3.1: *Anti-icing 1D model methodology*

Step 1 and step 2 are the calculation of the convective heat transfer coefficient and the local catch efficiency on the airfoil surface. These two parameters are essential in the context of icing aircraft as they are part of the main energy and mass fluxes which control the ice accretion. They have been calculated by Fluent and then exported to the 1D model. Step 3 is the computation of the heat fluxes by doing an energy balance. It allows the calculation of the mass of runback water which is evaporated. Step 4 allows the calculation of the water running back mass flux thanks to a mass balance. The mass and energy balances are made on control volumes, CV_i $(1 \leq i \leq n)$, of 10^{-3} m length each, along the upper surface of the airfoil.

The energy and mass balance (Figure 3.2) has been inspired by the Messinger model in which the heat loss by conduction in the substrate and in the water and ice layer is neglected (Messinger (1953), Hansman Jr and Turnock (1989), Louchez et al. (1998) and Fortin et al. (2006)). The break-up of the water film into rivulets has been taken into account. A consequence of this is the insertion of a wetness factor into the evaporative and convective flux. The wetness factor was set to 1 in the impingement region and to 0.3 downstream the impingement region. This last value come from the study of Gelder and Lewis (1951). It was also suggested by engineers at Airbus. The wetness factor downstream of the impingement limit is in reality not constant as the water is evaporated. However a constant value was chosen in order to simplify the study.

The energy terms which are included in the system are (red arrows in Figure 3.2):

- Aerodynamic heating due to the viscous heating in the boundary layer (Wm^{-2}, flux number 1 in Figure 3.2) :

$$\dot{Q}''_{\text{aero heating}}$$

- Kinetic energy of the droplet impacting the surface (Wm^{-2}, flux number 2 in Figure 3.2):

$$\dot{Q}''_{\text{drop kinetic energy}}$$

- Heat from the anti-icing system (Wm^{-2}, flux number 3 in Figure 3.2) :

$$\dot{Q}''_{anti}$$

- Latent heat of fusion released as the droplets freeze (Wm^{-2}, flux number 4 in Figure 3.2) :

$$\dot{Q}''_{freezing}$$

The energy terms which are removed from the system are (blue arrows in Figure 3.2):

- Convection heat (Wm^{-2}, flux number 5 in Figure 3.2):

$$\dot{Q}''_{conv}$$

- Evaporation/sublimation heat (Wm^{-2}, flux number 6 in Figure 3.2) :

$$\dot{Q}''_{evap}$$

- Heat absorbed from the surface as supercooled water droplets impinge and warm up to 0°C (Wm^{-2}, flux number 7 in Figure 3.2):

$$\dot{Q}''_{\text{drop warming}}$$

The mass fluxes in the control volumes of Figure 3.2 correspond to the black arrows: the water evaporative mass flux (M''_{evap}), the impinging water mass flux (M''_{imp}), the water mass fluxes entering (M_{in}) and coming out (M_{out}) of CV_i and the freezing water mass flux (M''_{freeze}).

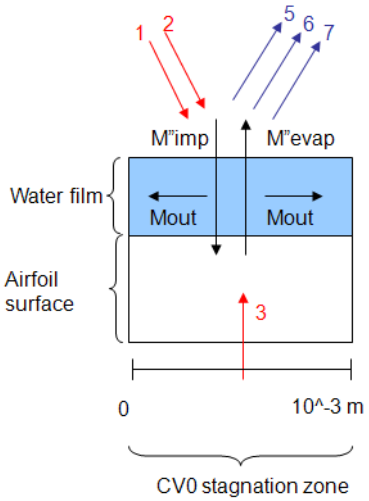

(a) Stagnation point

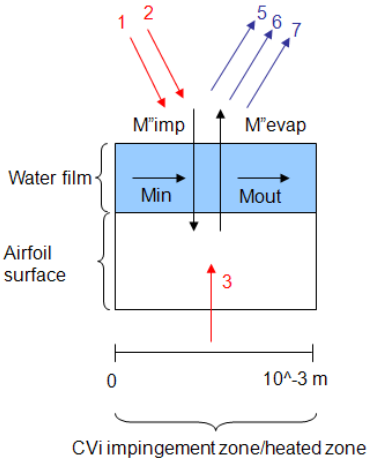

(b) Heated zone in the impingement region

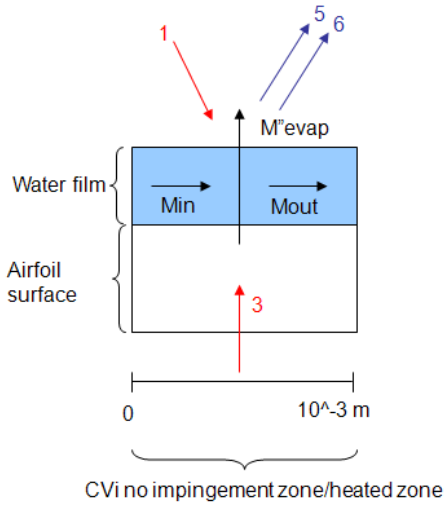

(c) Heated zone downstream the impingement region

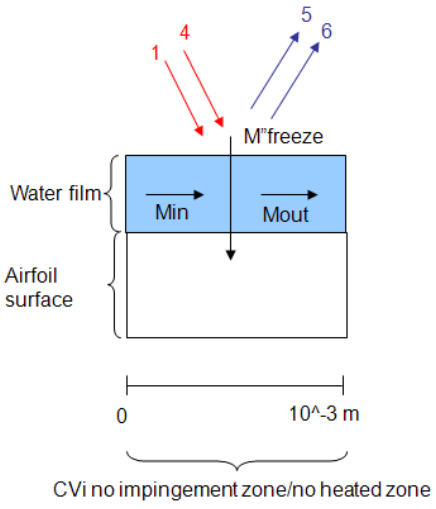

(d) Non heated zone

Figure 3.2: *Energy and mass balance on control volume*

The choice of formulation for the heat loss by evaporation remains a key point in the calculation of the runback water flux and of the power density required for the heating system, as it is a predominant term in the energy balance. For this reason two evaporative flux formulations were used and compared: the one used by Hansman Jr and Turnock (1989), equation (3.2.1) and the ones used in the icing code Icecremo (O'Rourke (2006), equation (3.2.2)):

$$\dot{Q}''_{evap} = \frac{hD_w L_v}{k_a}(\rho_{vsurf} - \rho_{v\infty}) = M_{evap} L_v \tag{3.2.1}$$

$$\dot{Q}''_{evap} = \frac{0.622 h L_v}{c_p P_t L_e^{2/3}} \left(e_s \frac{T_t}{T_S} \left(\frac{P_l}{P_t} \right)^{-\frac{1}{\gamma}} - R_h e_\infty \frac{P_t}{P_\infty} \right) = M_{evap} L_v \tag{3.2.2}$$

The evaporative flux used by Hansman Jr and Turnock (1989) is similar to the one introduced by Messinger (1953) in his energy balance. The evaporative flux developped for the Icecremo code is an improvement of the evaporative flux used by Messinger (1953). It takes into account the flow compressibility in order to "allow for the effect of pressure distribution around the airfoil on the local water vapour concentration" (Gent et al. (2000)). All the equations involved in the calculation of the heat and mass fluxes are presented into details in Appendix B.

In the 1D runback ice model, some idealisations were made following literature findings related to the Messinger model:

- The surface temperature is constant with time and position
- The heat transfer coefficient is calculated for a dry surface
- The runback water leaving the CV_i is equal to the water entering the CV_{i+1}
- No water enters the first control volume except the impinging water
- No energy loss by radiation
- No conduction in the substrate or in the water/ice sublayers

3.2.2 The heat transfer coefficient

The heat transfer is calculated between a dry surface and the ambient air. The calculation is based on the wall function approach (Fluent). The heat transfer coefficient is highly dependant on the surface roughness (see 2.1.3) and on the nature of the flow (Crawford et al. (2005)). Some time was allowed to decide which surface roughness was going to be applied and the nature of the flow. According to the Airbus engineers' expertise, it was decided that the flow was turbulent from the leading edge. The roughness was to account for the waviness due to the water film/rivulets on the surface. The runback water film is assumed to breakdown into rivulets downstream of the impingement limit. It has been chosen to neglect the roughness of the water film but to take into account the rivulets roughness. In most of the literature the roughness determination requires empirical input (Ruff and Berkowitz (1990), Broeren et al. (2010c)). The size of the roughness was defined as follows using the literature (Louchez et al. (1998)) and the Airbus engineers' expertise:

- Impingement zone: Water film, no roughness.
- Downstream the impingement zone: Rivulets: k_s=25 μm.

3.2.3 The catch efficiency

Water droplet trajectories were computed using the DPM method (Fluent). The global and local catch efficiencies were then calculated by extracting the droplets trajectories to a spreadsheet. The DPM is a common way to compute local and global catch efficiency especially for 2D simple geometry. It allows simulating a discrete 2^{nd} phase. The DPM follows the Euler-Lagrange approach where the 1^{st} phase is treated as a continuum and solved with the Navier-Stokes equations, while the 2^{nd} phase is solved by applying a force balance on each particle through the flow-field. In the present work, the continuous 1^{st} phase is the air and the 2^{nd} phase is spherical water droplets. The forces which apply to the droplets are mainly the drag, the lift and the gravity. The lift and the gravity have a minor effect on the droplet trajectories, especially when a droplet is considered as a rigid sphere with a diameter below 50 μm. The drag can be calculated by different formulas depending mainly on the Reynolds number of the droplets and on their shape. One of the limitations of the DPM is that the dispersed phase "occupies a low volume fraction, even though high mass loading is acceptable" (Fluent). The boundary conditions applied to the DPM was the escape one. It means that the particle is lost from the calculation at the point where it impacts the

boundary.

The trajectories were computed from 5-7 times the chord length, ahead the airfoil (Gent (1990)). The start point of the computation depended on the chord of the airfoil and on the computation time. For a small chord, it is possible to start the calculation $7 * c$ ahead. For longer chord, a smaller distance of the model was used to reduce the computation time. In this study, the limits of the impingement for the global and local catch efficiency are the last hitting trajectories. The last hitting trajectories are relatively easy to extract from Fluent. This is a bit different from what is usually done for the calculation of the catch efficiency with Lagrangian method in the icing codes (Gent (1990), Almendaroglu et al. (1997) and Da Silveira et al. (2003)). Usually the tangential missing trajectories are used instead of the last hitting trajectories. However it should not affect the result significantly. The following definitions were used for the calculation of the global catch efficiency, B and the local catch efficiency, β (equation (3.2.3), Figure 3.3 and Figure 3.4):

$$B = \frac{dy}{H},\ \beta = \frac{\delta y}{\delta s} \tag{3.2.3}$$

with $\delta s = \sqrt{\Delta y^2 + \Delta x^2}$.

The local and global catch efficiencies are related as follow (Ruff and Berkowitz (1990)):

$$B = \frac{1}{H} \int_{S_l}^{S_u} \beta \, \mathrm{d}s \tag{3.2.4}$$

with S_u and S_l the upper and lower surface impingement limits, respectively.

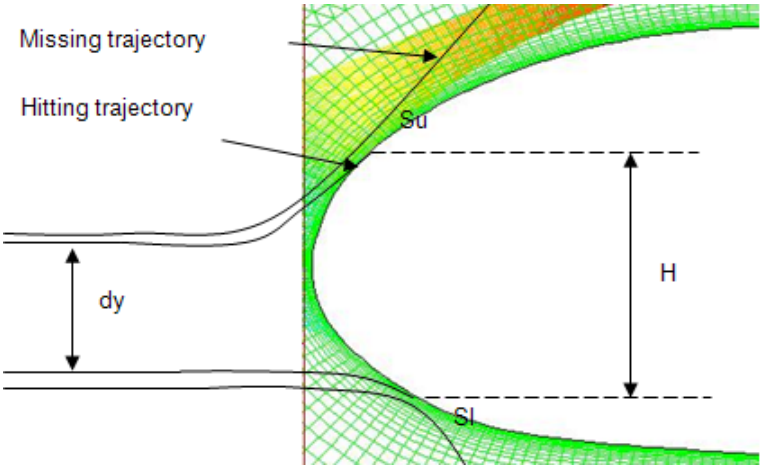

Figure 3.3: *Definition of the overall catch efficiency as calcultaed with Fluent*

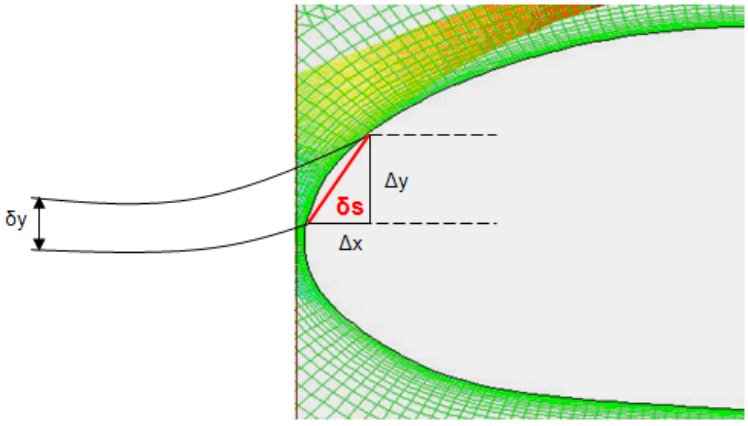

Figure 3.4: *Definition of the local catch efficiency as calculated with Fluent*

3.3 Accuracy of the 1D runback ice model

The objective of this section is to assess the accuracy of the 1D runback ice model in predicting the runback water mass flux, M_{out}, and the heat flux from an anti-icing system, $\dot{Q}''_{anti}$. To do so, the results of the 1D model are compared to the work of Lima da Silva et al. (2005), Lima da Silva et al. (2007a) and Lima da Silva et al. (2007b) who developed a new mathematical model for an electro-thermal anti-icing system. The parameters which have the biggest influence in the heat and mass fluxes calculation are the local heat transfer coefficient and the local catch efficiency. Both of these parameters are Fluent outputs in the present 1D runback ice model. Hence, the calculation of the heat transfer coefficient and of the local catch efficiency in the 1D runback ice model is compared with the work of Lima da Silva et al. (2007b).

3.3.1 The energy and mass balance for a wet anti-icing system from Lima da Silva *et al.*

Lima da Silva et al. (2005), Lima da Silva et al. (2007a) and Lima da Silva et al. (2007b) developed a new mathematical model for an electro-thermal anti-icing system. The heat transfer coefficient is calculated using a boundary layer integral method over heated airfoil with non isothermal and relatively smooth surface. The conduction through the water film is neglected but the authors considered the coupling between the convective heat transfer between the wall and the air and the convective heat transfer between the water film and the air. The authors used a NACA 0012 airfoil, with a chord of 0.914 m and a Reynolds number of $8.5 * 10^6$. The running wet case, 67B, studied by Lima da Silva has been used to assess the outputs of the present 1D model results. The authors used the ONERA2D code to calculate the external flow and the droplet trajectories. Their model has been validated using Al-Khalil *et al.* work on the ANTICE code (Lima da Silva et al. (2007a)).

The heating system configuration used by Lima da Silva et al. (2007b) is presented in Figure 3.5 and in Table 3.1. In Figure 3.6 and Figure 3.7 the results from Lima da Silva et al. (2005) and Lima da Silva et al. (2007b) are presented.

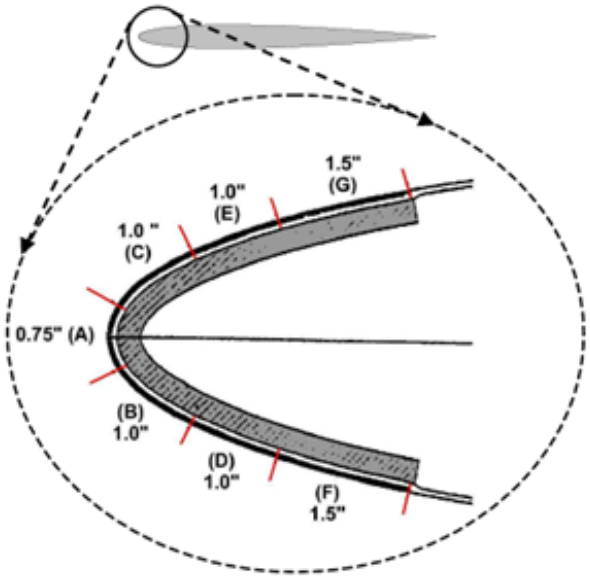

Figure 3.5: *Electrical heaters configuration of the NACA 0012 Lima da Silva et al. (2007b)*

Heater Element	Case 67A [kW/m^2]	Case 67B [kW/m^2]
F	20.15	8.37
D	21.70	11.94
B	32.55	10.85
A	43.40	15.19
C	26.35	9.92
E	18.60	12.87
G	18.60	8.68

(a) Heat density

Heater Element	s/c position	
	start	end
F	-0.1024	-0.0607
D	-0.0607	-0.0329
B	-0.0329	-0.0051
A	-0.0051	0.0157
C	0.0157	0.0435
E	0.0435	0.0713
G	0.0713	0.1129

(b) Heat distribution

Table 3.1: *Details of the heating system for case 67B Lima da Silva et al. (2007b)*

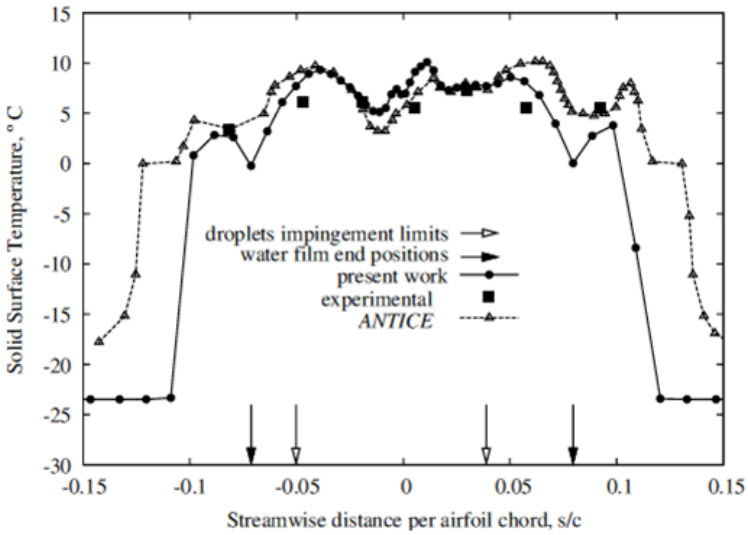

Figure 3.6: *Temperature distributions for case 67B Lima da Silva et al. (2007b)*

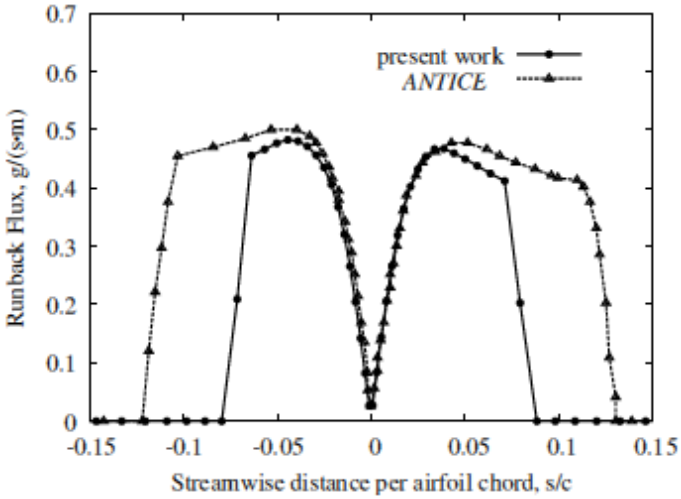

Figure 3.7: *Runback and impingement mass fluxes for case 67B Lima da Silva et al. (2007b)*

In Figure 3.6 and Figure 3.7 the "present work" curve refers to the work of Lima da Silva et al. (2007b) and the experimental and ANTICE results refer to the work of Al-Khalil *et al.* (Lima da Silva et al. (2007a)).

3.3.2 Accuracy of the 1D model output

Three cases have been used to assess the results of the 1D runback ice model (Table 3.2).

Cases	Energy and mass balance	Airfoil	Chord (m)	Catch efficiency	Heat transfer coefficient (W/m^2K)
case 1	Da Silva et al	NACA 0012	0.914	Antice	Da Silva et al
case 2	Present work	NACA 0012	1	Fluent - DPM	Fluent - Wall Function
case 3	Present work	NACA 0012	1	Antice	Fluent - Wall Function

Table 3.2: *Cases used to assess the result of the 1D model*

Case 1 represents the results from Lima da Silva et al. (2007b) for their case 67B which has been presented in section 3.3.1. This is the reference case. Case 2 represents the results of the energy and mass balance calculated by the present model with the catch efficiency and the heat transfer coefficient computed with Fluent. Case 3 represents the energy and mass balance calculated with the 1D model but using the catch efficiency used by Lima da Silva et al. (2007b). The conditions used to do the comparison are presented in Table 3.3.

Icing conditions	
Velocity (m/s)	89
LWC (g/m^3)	0.55
Droplet diameter (microns)	20
T∞ (°C)	-18

Table 3.3: *Conditions used to compare the 1D model results with case 67B of Lima da Silva et al. (2005) and Lima da Silva et al. (2007b)*

The runback water fluxes and the impinging water fluxes from the literature and from the 1D model are presented in Figure 3.8.

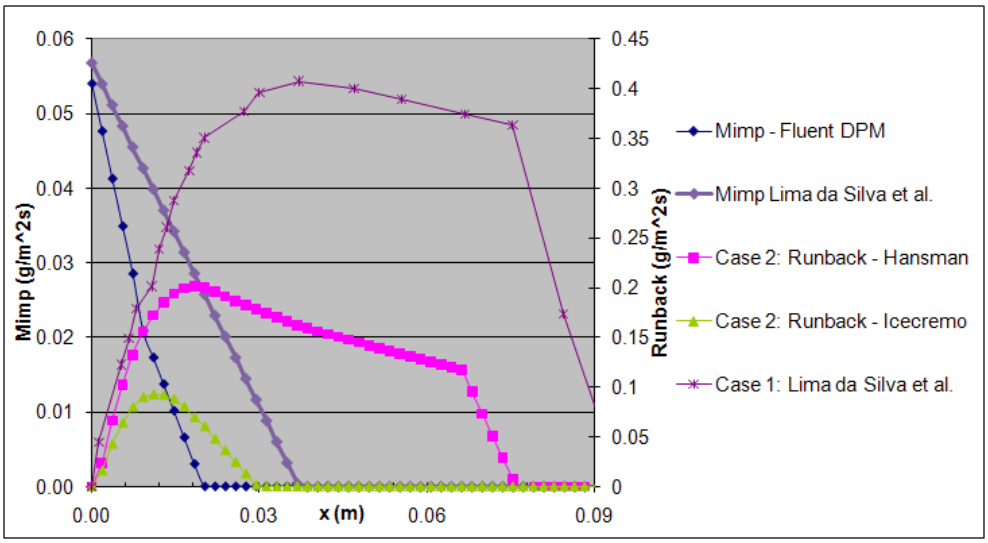

Figure 3.8: *Runback water mass fluxes and impinging water mass fluxes for case 1 and 2*

It is clear from Figure 3.8 that whatever the evaporative flux formulation used, the runback water flux calculated by the 1D model (green and pink curves) is underestimated in regards to the reference case (purple curve). Using the evaporative formulation from the Icecremo code (green curve), leads to a dry system as all the running back water is evaporated before the end of the heated zone. The runback water mass flux using the evaporative formulation from Hansman Jr and Turnock (1989) gives a running back water mass flux closer to the reference case. With the evaporative formulation from Hansman Jr and Turnock (1989), not all of the water is evaporated before the end of the protected region. From Figure 3.8 it appears from the impinging water mass fluxes, that the impingement zone is wider for the reference case than for the 1D model. Hence, there is less water running back according to the 1D model in regards to the reference case. It is likely that the discrepancy between the catch efficiency of the 1D model and of the one for the reference case (see 3.3.4), is a reason for such a difference in the impinging water mass fluxes. However, the difference in impinging water mass fluxes may not be the only reason why there is such a difference between the 1D model and the reference case for the runback water mass flux. The heat transfer coefficient (see 3.3.3) or one of the physical approximations in the model (nature of the flow, water behaviour, etc) could be a source of difference.

In case 3, the runback water mass flux calculated by the 1D model and using the same local catch efficiency as Lima da Silva et al. (2007b), is compared to

the reference case, case 1. This result is highlighted in Figure 3.9. It looks like the runback water mass flux calculated with 1D model using the Hansman evaporative model is getting very close to the one calculated by Lima da Silva et al. (2007b). Actually, the Hansman runback water mass flux is similar to the one calculated by Al-Khalil *et al.* and which was used as reference by Lima da Silva et al. (2007b) to validate their anti-icing model. The runback water flux calculated with the 1D model using the Icecremo evaporative flux is underestimated compared to Lima da Silva et al. (2007b). The reason for that is still unclear.

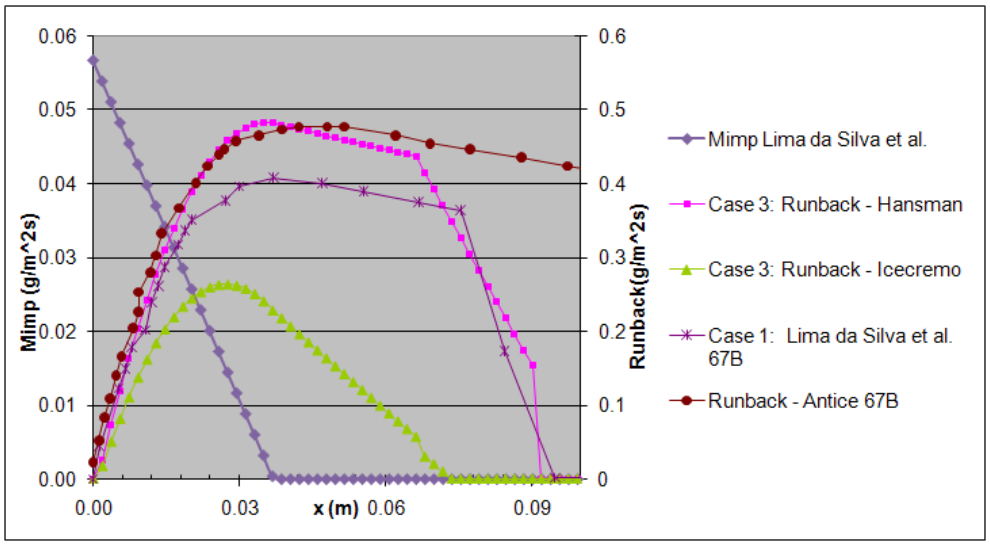

Figure 3.9: *Catch efficiency for the NACA 0012 calculated with Fluent and calculated by Lima da Silva et al. (2007b) using Onera 2D*

To complete the study, the heat fluxes from the anti-icing system calculated by the 1D model and computed by Lima da Silva et al. (2007b) are presented in Figure 3.10. The heat input $\dot{Q}''_{anti}$ was calculated using the 1D model with the inputs of case 3 and the Hansman evaporative model. Before the end of the impingement zone, the heat flux from the heating system is over-estimated in the present study whereas $\dot{Q}''_{anti}$ is underestimated by comparison to the literature downstream the end of the impingement zone. However, when considering the area underneath both curves, they look very similar. Using a trapezoidal integration in Excel, the difference between the area underneath the curves of Figure 3.10 is found to be 4.5 %. Hence, even though the heat distribution is different, the total heat input calculated by the 1D model gives results close to the literature if the 1D model uses an

improved catch efficiency (case 3) and if the evaporative model from Hansman is used. This result was very useful to design the heating system for the present icing tunnel tests. The objective was to have a rough idea of the heat input required to build a wet system that allowed for some flexibility in the heat input distribution. Then even if the total heat input predicted by the 1D is not perfect it doesn't affect the results as a wet heating system is targeted. Another study concerning the area underneath the heat input curves is done when the 1D model outputs are compared to the present icing tunnel experimental results (see section 5.6).

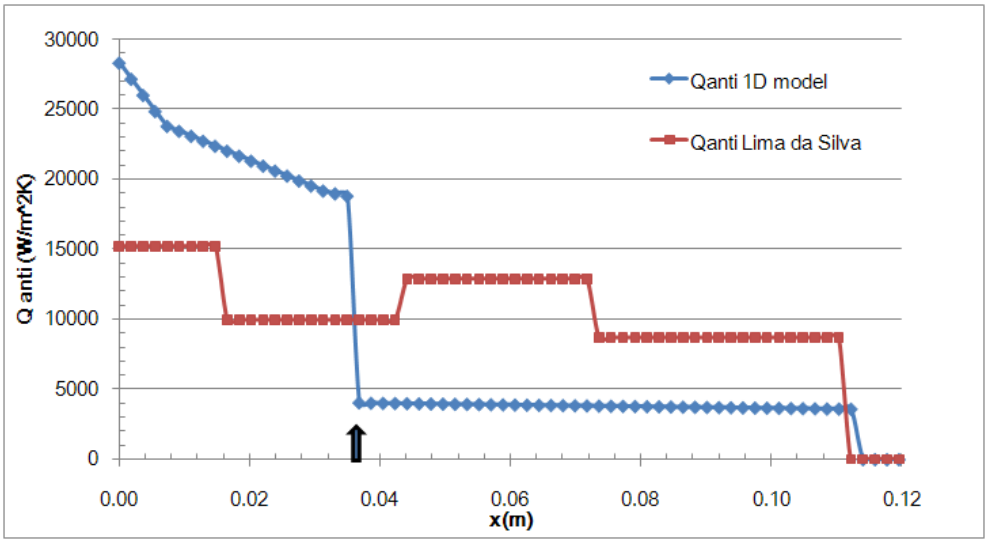

Figure 3.10: $\dot{Q}''_{anti}$ *calculated with the present model and calculated by Lima da Silva et al. (2007b) (the black arrow represents the end of the impingement zone)*

There are some differences in the method used to calculate h and β between Lima da Silva's work and the 1D runback ice model. These differences are highlighted in the next 2 sections.

3.3.3 The local convective heat transfer coefficient

In case 67B, the local convective heat transfer coefficient is calculated by a new thermodynamic solver developepd by Lima da Silva et al. (2003) which was validated using the work of Al-Khalil et al. (1997). It takes into account the convection between the airfoil surface and the water and the convection between the water film and the air. In this new thermodynamic solver the

flow is laminar at the leading edge and the transition occurs downstream in a region defined statistically. In the present work it is assumed that the flow is fully turbulent from the leading edge and the heat transfer coefficient is calculated for a dry surface. Hence, it is likely that some differences are going to arise for the value of the local convective heat transfer coefficient. However it is very difficult to quantify these differences.

3.3.4 The local catch efficiency

The local catch efficiency was calculated by Lima da Silva et al. (2007b) using the Onera 2D solver. This results has been validated using the local catch efficiency calculated with ANTICE from LEWICE. In order to assess the catch efficiency value calculated by Fluent, it was compared to the local catch efficiency calculated with ANTICE, which has proved to give reliable results in terms of local catch efficiency calculations, especially with droplets of MVD=20 μm (Papadakis et al. (2004a) and Wright (2005)). Both, Fluent and ANTICE, use a Lagrangian approach. The particles are represented as rigid spheres and the splashing of the droplet is not taken into account. The main force is the drag. The droplet trajectories have no influence on the flow calculation in ANTICE (Wright (2005)) nor in Fluent if the one-way-coupling option is used. In LEWICE the air flow is solved using a panel method whereas Fluent uses a Navier Stokes solver. This difference does not influence the trajectory calculation much. The main difference between both codes is that ANTICE uses a distribution of droplet sizes centred on the MVD whereas Fluent uses a single droplet size (Wright (1995) and Papadakis et al. (2004a)). ANTICE uses the Langmuir D distribution (Wright (1995)). The Langmuir D distribution comes from the work of Langmuir and Blodgett in 1846 on droplet trajectories. It associates the droplets diameter proportion present in a cloud considering a certain MVD. By calculating the catch efficiency for the different droplet diameters, and then by summing each catch efficiency weighted by its corresponding volume fraction in the distribution, it is possible to get a poly-dispersed catch efficiency as illustrated in equation (3.3.1) (Wright (1995)):

$$\beta_{polydispersed} = \sum_{i=0}^{n} \%Volume\beta_i \tag{3.3.1}$$

Where the % Volume represents the contribution of a certain droplet size and β_i represents the local catch efficiency for this droplet size. The Langmuir D distribution gives good results and it is widely used in the icing codes. Table 5 gives an example of an approximation of the Langumir D distribution for MVD=20.36 μm. Seven droplets size were considered.

Diameter (microns)	Mass(%)
6.31	5
10.58	10
14.46	20
20.36	30
27.89	20
35.42	10
45.19	5

Table 3.4: *Langmuir D distribution used for* $MVD = 20.36\,\mu m$ *(Bragg and Khodadoust (1995))*

The poly-dispersed catch efficiency can be calculated in Fluent by using a similar method of weighted catch efficicency. Hence, mono-dispersed and the poly-dispersed local catch efficiency are computed by Fluent and compared with ANTICE results. The Langmuir D distribution and the CIT distribution for $MVD = 20\,\mu m$, are used for the computation of the poly-dispersed local catch efficiency. This result will allow us to assess the discrepancy between the Langmuir D ditribution and the CIT distribution. The reference case used to compare Fluent results with ANTICE is the one used by Da Silveira et al. (2003). They used a NACA 0012 airfoil with a chord of 0.914 m, 0°AOA, a free stream velocity of 44.5 $m.s^{-1}$, a static free stream temperature of -7.5°C and with a MVD of 20 μm.

First, Fluent determined the mono-dispersed local catch efficiency using a droplet size of 20 μm is compared to ANTICE results (Figure 3.11). The maximum peak is off the same order for both numerical methods. However the impingement limits for the local mono-dispersed catch efficiency computed with Fluent are underestimated by a factor of 2 in regards to the ones computed with ANTICE. Second, the poly-dispersed methodology was applied to the local catch efficiency calculation using Fluent. Both, the CIT measured distribution (Figure 3.13 and Table 3.5) and the one from Langmuir were used for $MVD = 20\,\mu m$. The poly-dispersed catch efficiency using the CIT distribution remains almost the same as the mono-dispersed catch efficiency, except that the impingement limits are getting close to the ANTICE and experimental results (Figure 3.12). This result is encouraging, however the DPM still under-estimates the local catch efficiency.

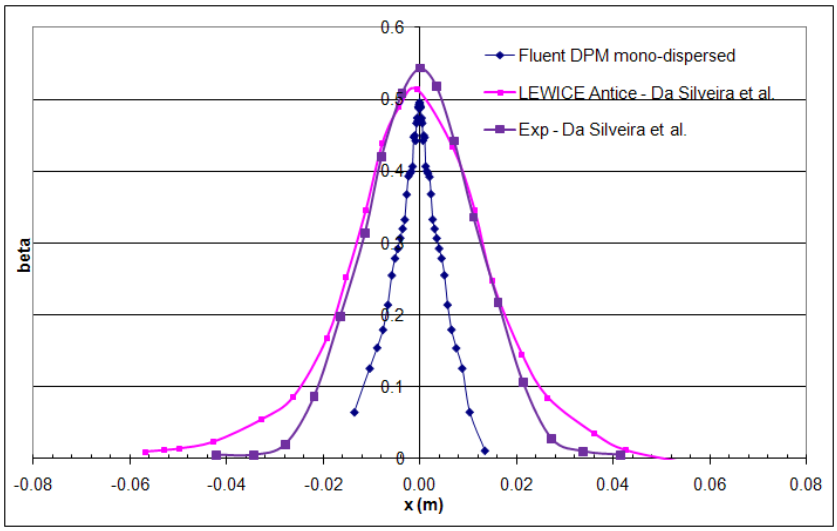

Figure 3.11: *Local catch efficiency for 1m long NACA 0012 airfoil, 0° AOA, $U\infty$=44.5 $m.s^{-1}$, $T_S = -7.5°$, $MVD = 20\ \mu m$ (Fluent mono-dispersed and Antice poly-dispersed)*

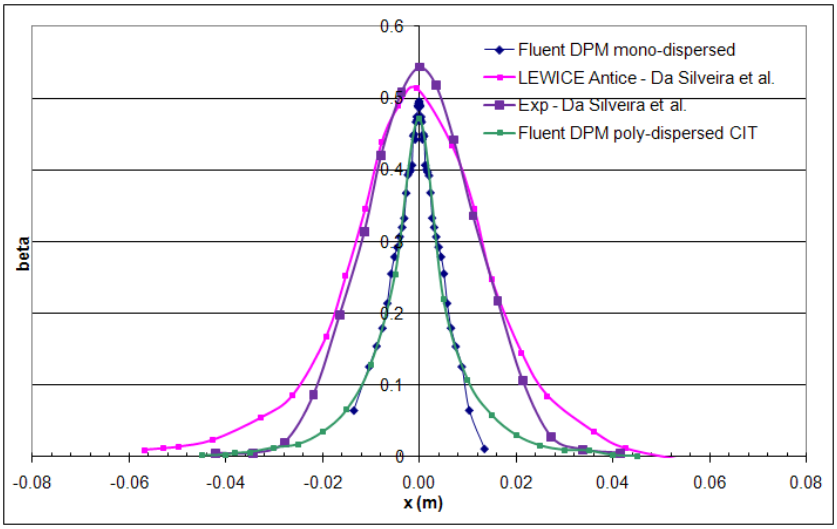

Figure 3.12: *Local catch efficiency (Fluent mono-dispersed and poly-dispersed methods are compared to ANTICE and experimental value) for 1m long NACA0012 airfoil, 0° AOA, U∞=44.5 m.s^{-1} , $T_S = -7.5°$, $D = 20\ \mu m$*

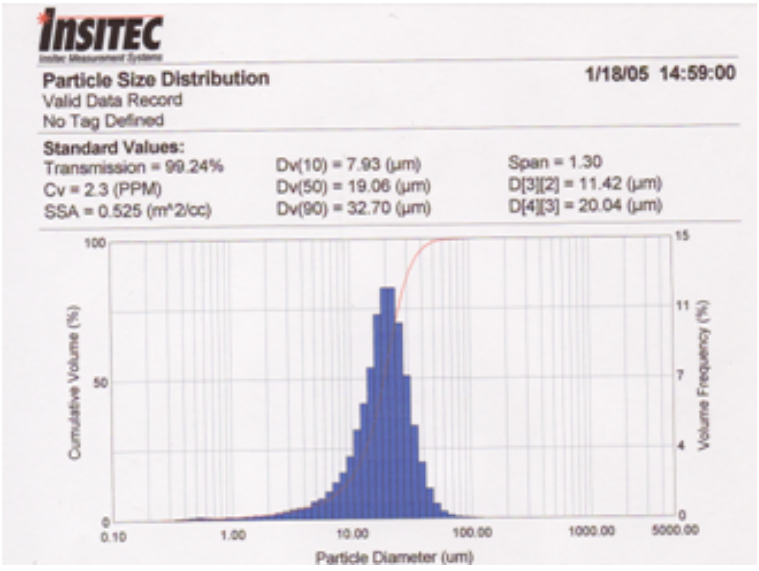

Figure 3.13: *Particule size distribution in the CIT with, $MVD = 19.06\ \mu m$*

Diameter (µm)	Cumulative volume (%)	Individual volume (%)
10	14.00	14.00
15	40.00	26.00
19	50.00	10.00
20	57.00	7.00
21	64.80	7.80
25	78.88	14.08
30	88.00	9.12
35	93.00	5.00
40	96.40	3.40
45	99.30	2.90

Table 3.5: *Volume in percent of the different droplet for a* $MVD = 19.06\,\mu m$ *distribution in the CIT*

Using the Langumir D distribution instead of the one measured in the CIT, doesn't really change the results (Figure 3.14). It slightly increases the local catch efficiency but the maximum peak and the impingement limits remain of the same order.

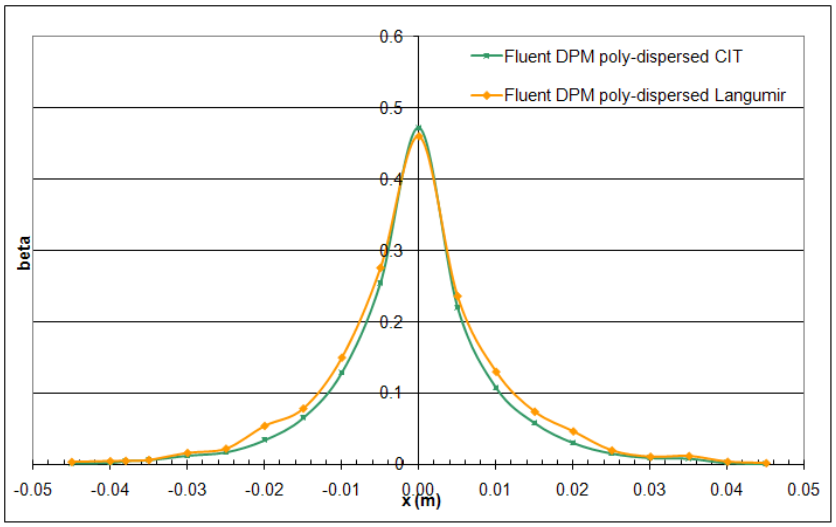

Figure 3.14: *Local catch efficiency from Fluent with poly-dispersed using the Langmuir D and CIT distribution for 1m long NACA0012 airfoil, 0° AOA,* $U\infty$*=44.5* $m.s^{-1}$ *,* $T_S = -7.5°$*,* $D = 20\,\mu m$

To sum-up, the local catch efficiency calculated by Fluent using the DPM, has a similar peak height as the one from the literature but its width is underestimated for both mono-dispersed and poly-dispersed distribution. The

limits of the impingement are greatly improved for a poly-dispersed catch efficiency than for a mono-dispersed catch efficiency.

3.3.5 Conclusions

It seems that the 1D model built with Excel, in order to calculate the runback water flux and the heat input from an anti-icing system, gives results which need further investigation:

- The catch efficiency computed by Fluent is under-estimated compared to the literature for both mono-dispersed and poly-dispersed distribution
- The 1D runback ice model calculates runback water flux of the same order as the literature, if the evaporative formulation from Hansman Jr and Turnock (1989) is used combined with an improved local catch efficiency
- The value obtained for the anti-icing heat flux is encouraging. The average of the $\dot{Q}''_{anti}$ along the chord is approximately the same for both the present work and the literature. However, the heat flux distribution is not very well predicted. The heat flux is largely overstimated before the end of the impingement zone, whereas it is largely underestimated downstream the impingement zone. This is further discussed in section 5.6.

It is decided to use a mono-dispersed distribution when it comes to the catch efficiency for the 1D runback ice model, as a poly-dispersed distribution is time consuming and it does not improve significantly the catch efficiency. Even though, the catch efficiency calculated by Fluent shows some discrepencies with the one from the literature, the level of accuracy is enough to use the 1D runback ice model as a preliminary tool to study runback ice accretion and to calibrate the heating system for the icing tunnel experiments.

Chapter 4

The Hybrid airfoil

The objective of the icing tunnel test campaign is to get nearly full-scale runback ice shapes which can be moulded and cast to reproduce the real ice shapes with good accuracy, to compare with simplistic shapes. However, before growing ice shapes, a preliminary study is required. First, the airfoil which is used in the icing tunnel has been designed. Second, the aerodynamic and icing conditions to grow full-scale ice shapes according to the authorities requirements are found, based on a CFD study.

4.1 The design of the Hybrid airfoil

One of the objectives of the study is to grow full-scale runback ice shapes. Then, the design of the airfoil to be tested in the icing tunnel is a compromise between the experimental requirements to get full-scale ice shapes, and the size and speed restrictions of the tunnel. As the ice accretion scaling is not well understood, several authors used the concept of a truncated airfoil, which would create full-scale ice accretion. Saeed et al. (1997) and Saeed et al. (1998) validated the concept of the hybrid airfoil that allows to grow full-scale ice shapes on a truncated airfoil. This concept is based on the fact that the ice accretion on the truncated airfoil (the first 10-20 % of the chord of an airfoil) is going to remain the same as on the full-scale airfoil if the velocity distribution in the vicinity of the leading edge (Mach number, stagnation point and local flow-field velocity), the water impingement (local and global catch efficiency) and the model surface thermodynamics (surface heat transfer coefficient) are the same between the two airfoils. To validate the hybrid airfoil concept Saeed et al. (1998) used a modern business jet airfoil (c=0.9 m) that they truncated after the 15% of the chord in order to have a hybrid airfoil with a chord of 0.45 m (Figure 4.1). In Figure 4.1, the angles highlighted that

there was a difference in geometry between the model that had been designed (full line) and the manufactured model (dashed line). Then they compared leading edge ice shapes for the two airfoils (Figure 4.2) in the conditions cited in Table 4.1. The results from the authors were encouraging. However they found that the Hybrid airfoil was sensitive to flow separation for quite low AOA.

	U∞ (m/s)	T∞ (°C)	Re	M	α (°)	LWC (g/m^3)	MVD (µm)
Full-scale	90	-5.3	6 * 10^6	0	6	0.54	20
Hybrid	90	-5.3	6 * 10^6	0	6	0.54	20

Table 4.1: *Aerodynamic and icing conditions for the hybrid airfoil validation from Saeed et al. (1998)*

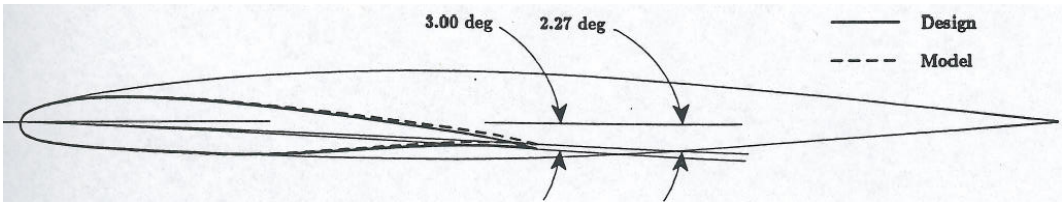

Figure 4.1: *The full-scale airfoil and its corresponding hybrid airfoil (Saeed et al. (1998))*

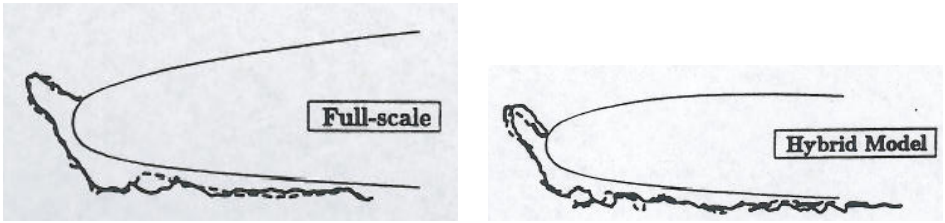

(a) Rime ice (b) Glaze ice

Figure 4.2: *Leading edge ice shapes comparion between the full-scale airfoil and the hybrid airfoil (Saeed et al. (1998))*

The design of the airfoil was part of a MSc project (Sancho (2008)). Sancho (2008) applied the hybrid airfoil concept to design the airfoil for the present project. An airfoil has been designed, based on a 4 m long B737/700 airfoil. Airbus were preparing to release a section of their wing but agreed that the available B737/700 section would be sufficiently close, and that since the coordiantes are already in the public domain (UIUC), it would be easier to publish our results. The leading edge of the B737/700 airfoil has been kept

full scale up to 9.25% (0.37 m) of the chord of the 4 m airfoil (Figure 4.3 and Figure 4.4). The aft of the airfoil has been designed in order to be suitable for the icing tunnel (Figure 4.5). It results in an airfoil with a chord of 1 m. The full-scale leading edge is 1 cm thick and made of aluminium. The after body has a wood skeleton with an aluminium skin.

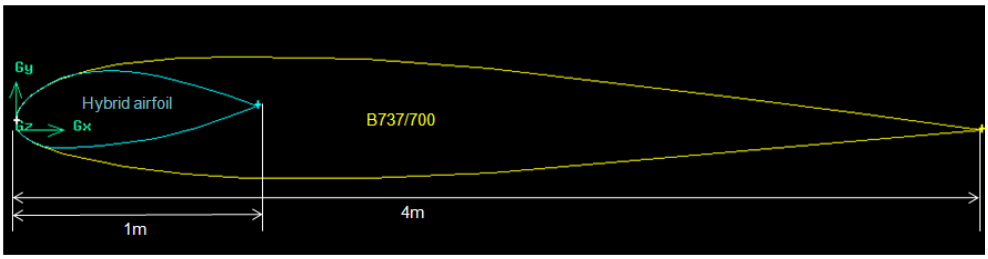

Figure 4.3: *The Hybrid model: full-scale leading edge associated with an adapted after body*

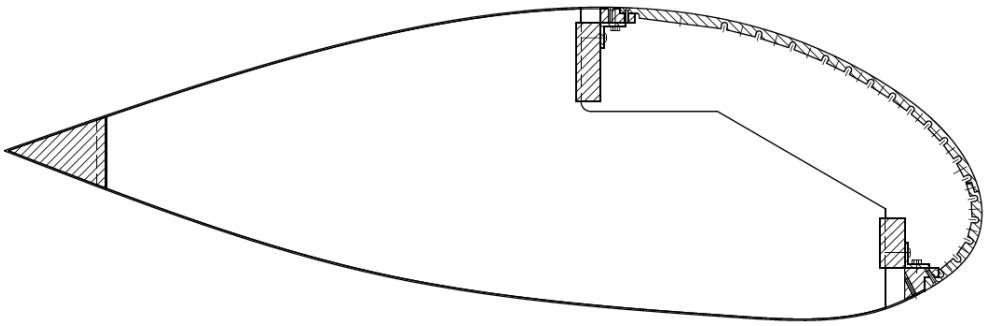

Figure 4.4: *Industrial drawing of the Hybrid airfoil*

There are two reasons for choosing this particular limit for the extent of the full-scale leading edge. First of all, a protected region in the range of 7-10% of the chord is typical for large jet transport wing. However this range may change along the span. In theory, the extent of the protected region is smaller close to the root. The presence of a high-lift device may reduce the extent of the protected zone as well. Second of all, the size of the model was limited due to a small test section.

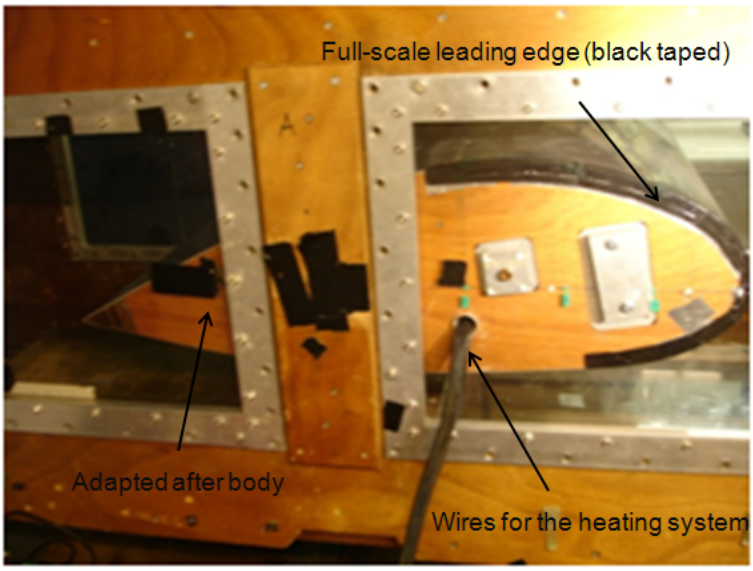

Figure 4.5: *Hybrid model in position in the icing tunnel*

4.2 The worst icing conditions

4.2.1 Introduction

This 2D CFD study is a complement to the one done by Sancho (2008) as part of his thesis. It consists of an analysis to support the choice of the aerodynamic conditions (speed, AOA) and of the icing conditions (MVD, LWC) which are going to grow full-scale runback ice in the CIT. Following Saeed et al. (1997) and Saeed et al. (1998) study, the leading edge velocity, the droplets impingement and the thermodynamics of the leading edge surface must match between the full-scale airfoil and the hybrid airfoil. Then the similarity parameters that have to be matched to get full-scale runback ice on the Hybrid airfoil are:

- The Mach number, the static surface pressure, the surface shear stress and the stagnation point in order to compare the leading edge flow field
- The local and global catch efficiency in order to compare the droplets impingement
- The Stanton number in order to compare the surface heat transfer coefficient.

According to the authorities, the worst icing conditions are the conditions which result in the maximum mass of ice. A reference case, based on the

B737/700 airfoil, is defined using requirements in terms of icing and aerodynamic conditions for the worst icing conditions. The similarity parameters introduced above are going to be compared to the Hybrid airfoil in a free stream context and in taking into account the icing tunnel walls.

4.2.2 The reference case

The worst icing conditions used by Airbus following the EASA requirements is the 45 minutes hold case in continuous maximum icing, at an altitude of 17000 ft, a calibrated speed of 118 $m.s^{-1}$ and a static temperature of -9°C. These conditions were adapted to cope with the limitations due to the facilities (mainly size of the tunnel and speed limitation) and with the objectives of this project.

In order to match a hold flight configuration, the sponsor suggested that the lift coefficient was in a range between 0.4 and 0.6 and that the stagnation zone was on the airfoil lower surface. Several AOA were tested for the B737/700 using CFD and an AOA of 3° was chosen as it is representative of hold flight configuration. The continuous maximum icing represents the highest combination of global catch efficiency and LWC as function of the droplet diameter. The total catch efficiency is increased but the LWC is reduced while the droplet diameter is increased. Thus, the continuous maximum icing is found by determining which droplet diameter corresponds to the maximum value of $LWC * B$. The LWC as a function of the droplet diameter for the B737/700 has been determined using the Appendix C of FAA FAR part 25 (Appendix A) for an outside air temperature of -9°C and a speed of 118 $m.s^{-1}$. For the maximum continuous icing, MVD=20 μm and LWC=0.45 $g.m^{-3}$ were chosen. The maximum intermittent icing conditions were defined with MVD=20 μm and LWC=2.23 $g.m^{-3}$. As the icing tunnel is not pressurised, the altitude has not been taken into account. However, as mentioned in section 1.4, the altitude has not a direct influence on the ice growth rate. The runs timing was decided with Airbus to depend on the ice thickness.

So, the reference case is the B737/700 airfoil associated with the worst icing conditions, defined by the EASA and taking into account the above mentionned simplifications. It has been decided also to do a few runs for the maximum intermittent icing conditions to study the runback ice shape for higher LWC but during a shorter period of time. The reference conditions for the B737/700 are presented in Table 4.2.

These conditions are different from the conditions used by Bragg et al. (2007) who grew full-scale runback ice shapes for hold configuration on a NACA 23012 (c=1.828 m) in the NASA icing tunnel. However, it is likely that the icing is similar for both cases as the lower speed from Bragg et al. (2007) is compensated by higher LWC and MVD.

	Aerodynamic conditions		Icing conditions				
Airfoil	AOA (°)	Speed (m/s)	T∞ (°C)	Conditions	Time exposure (min)	LWC (g/m^3)	Droplet diameter (µm)
B737/700 c=4 m	3	118	-9	continuous	NA	0.45	20
	3	118	-9	intermittent	NA	2.23	20
NACA 23012 c=1.828 m	1.1	72	-7.66	continuous	22.5	0.81	28

Table 4.2: *Conditions to grow full-scale runback ice shapes for the reference case and for Bragg et al. (2007)*

4.3 Meshing and numerical set-up

Three different cases were studied. One for the B737/700 in free stream, one for the Hybrid airfoil in free stream and one for the Hybrid airfoil in the CIT. The three meshes are all unstructured with $30 \leq y^+ \leq 300$ (Figure 4.6, Figure 4.7, Figure 4.8 and Figure 4.9). The free stream meshes have an envelope 10 times the chord length away from the airfoil. For the Hybrid model in the tunnel, the test section is 10 times the chord of the model forward and backward. The turbulence model used was the standard k-ϵ model associated with the standard "wall function". A second order discretization was used with a single precision solver. The simulations were considered as converged once the darg coefficient remained unchanged between two iterations low residuals reasonably low and constant.

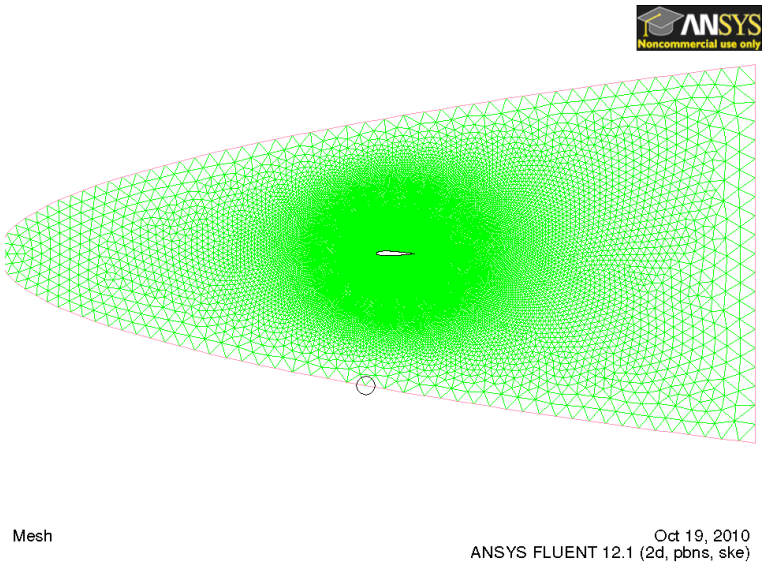

Figure 4.6: *Mesh for the B737/700*

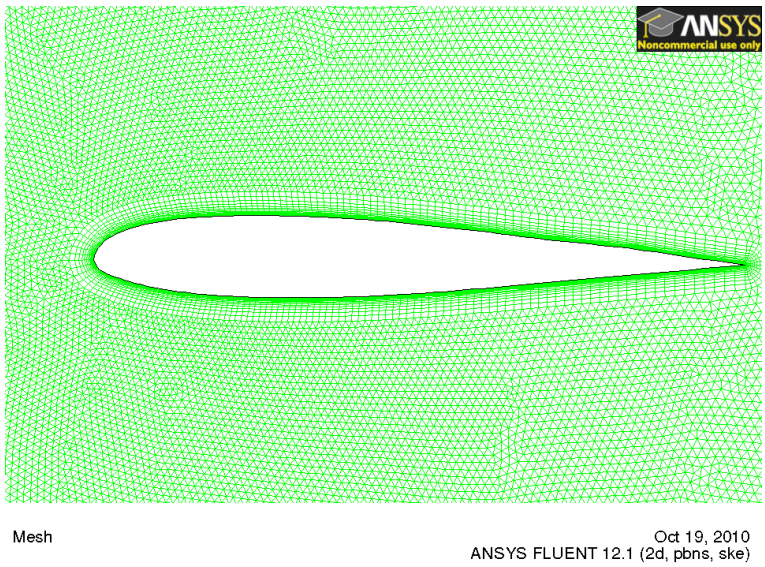

Figure 4.7: *Close-up view of the B737/700 mesh*

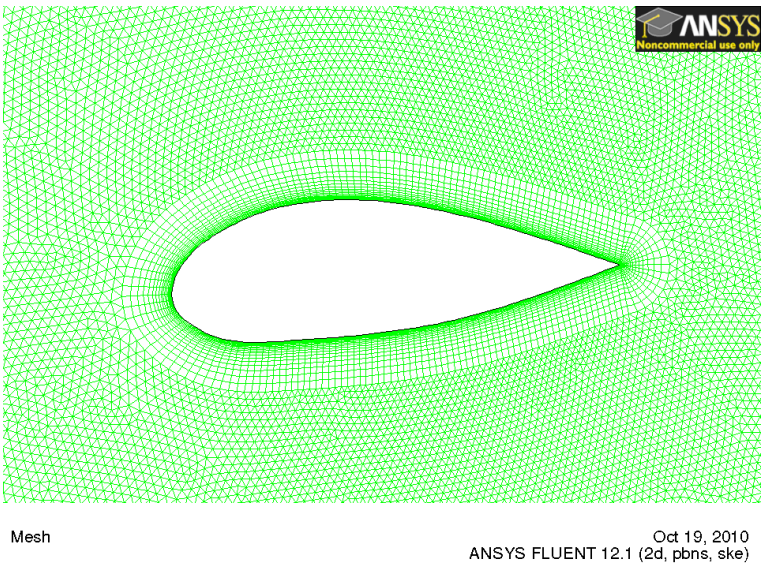

Figure 4.8: *Close-up view of the Hybrid airfoil mesh in free stream*

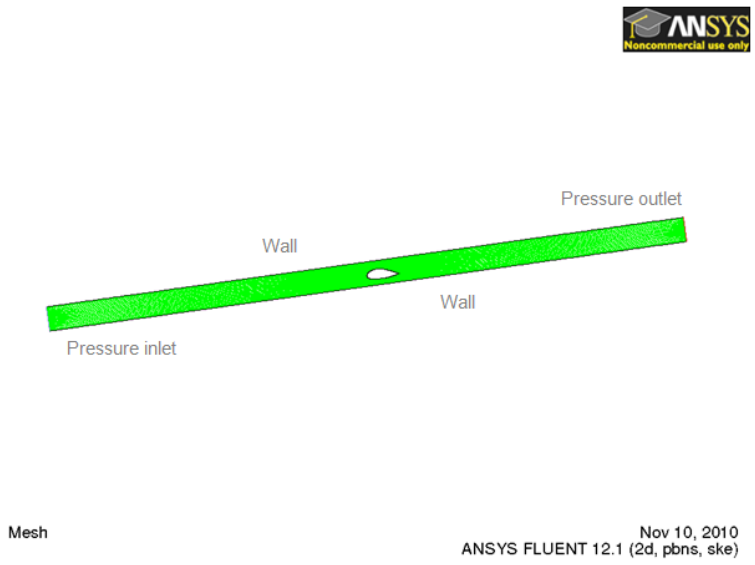

(a) Global view

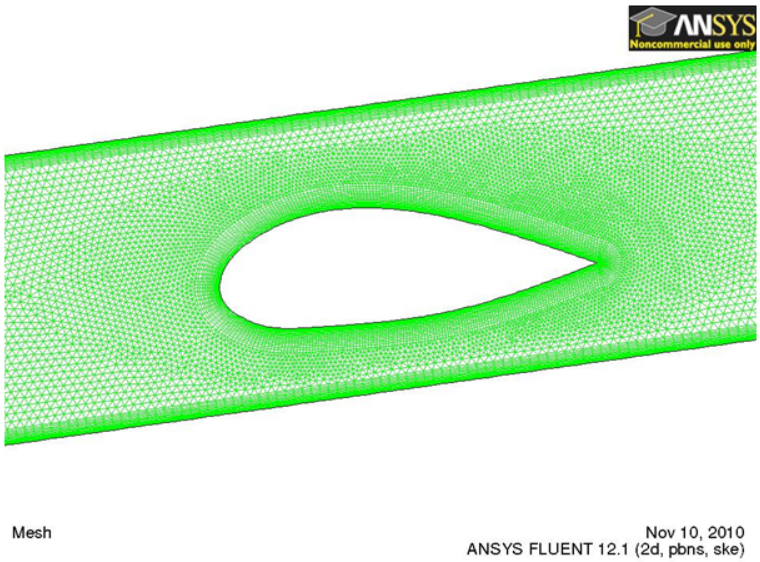

(b) Close-up view

Figure 4.9: *Views of the grid for the Hybrid airfoil in the CIT*

The discretization errors were examined by doing a grid independence study for the B737/700 in free stream and the Hybrid airfoil in the tunnel (Table 4.3 and Table 4.4). No grid independance study was done for the Hybrid airfoil in free stream as the meshing strategy was the same as for the B737/700 airfoil. The mid sized meshes were chosen for each case as they allowed the solution to reach asymptotic values of the drag coefficient.

	coarse	mid	fine
number of cells	23505	69313	246134
Cd	0.018	0.021	0.022

Table 4.3: *Grid independance study for the B737/700 airfoil in free stream*

	coarse	mid	fine
number of cells	18214	50340	93028
Cd	0.114	0.120	0.122

Table 4.4: *Grid independance study for the Hybrid airfoil in the tunnel*

A "pressure farfield" bounday condition was used for the free stream simulations. For the case inside the tunnel, "pressure inlet" and "pressure outlet" boundary conditions were applied. The perfect gas law was used to model the air. The total pressure (equation (4.3.1)) and total temperature (equation (4.3.2)) at the input of the domain were calculated as follow:

$$P_t = P\left(1 + \frac{\gamma - 1}{2}M^2\right)^{\frac{\gamma}{\gamma - 1}} \tag{4.3.1}$$

$$T_t = T_s\left(1 + \frac{\gamma - 1}{2}M^2\right) \tag{4.3.2}$$

with the Mach number calculated as follow:

$$M = \frac{U_\infty}{C}, C = \sqrt{\gamma R T_\infty} \tag{4.3.3}$$

R represents the gas constant.

The heat transfer was calculated for a dry surface with T_S=10°C. The local and global catch efficiency are calculated using mono-dispersed droplets distributions. A roughness of 25μm was applied to the airfoil surface to simulate the water waviness on the surface. This roughness value is commonly used in this context as explained in section 3.2.2.

4.4 Study of the reference case

The reference case corresponds to the icing and flight reference conditions (Table 4.2) applied to the B737/700 in order to determine a benchmark of the required aerodynamic parameters (surface static pressure, surface shear stress) and icing parameters (heat transfer coefficient and catch efficiency). The Stanton number (equation (4.4.1)) has been chosen to make a comparison of the heat transfer coefficient between the airfoil surface and the air free stream:

$$St = \frac{h}{c_p \rho U_\infty} \tag{4.4.1}$$

The calculated static pressure, shear stress, heat transfer coefficient, Stanton number and global catch efficiency for the B737/700 are presented in Figure 4.10 to Figure 4.14. The study is focused on the upper surface as only the upper surface icing is considered.

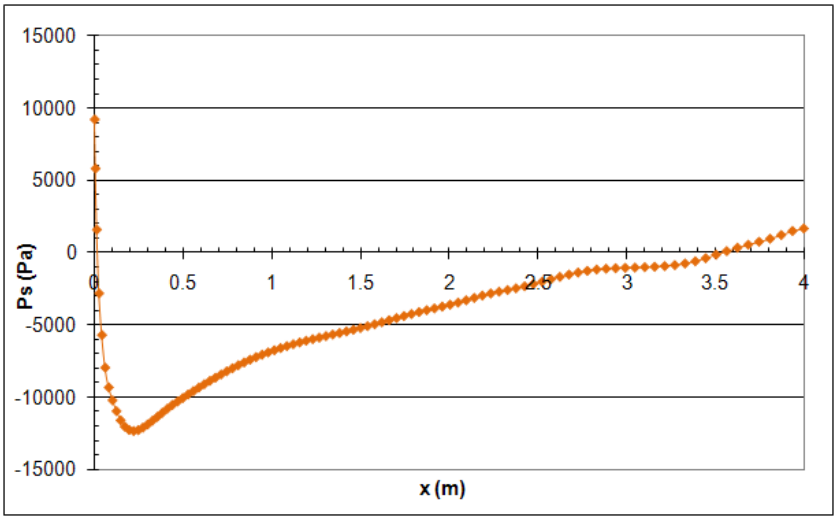

Figure 4.10: *Upper surface static pressure for the reference case*

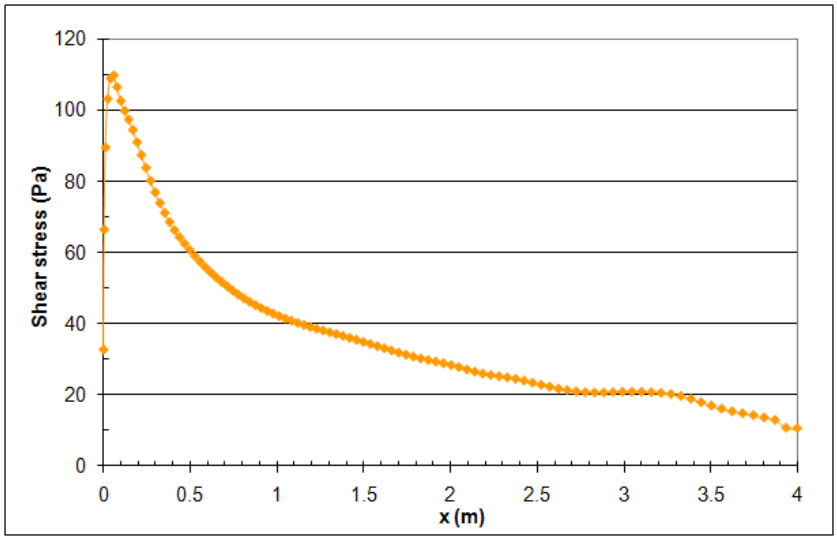

Figure 4.11: *Upper surface shear stress for the reference case*

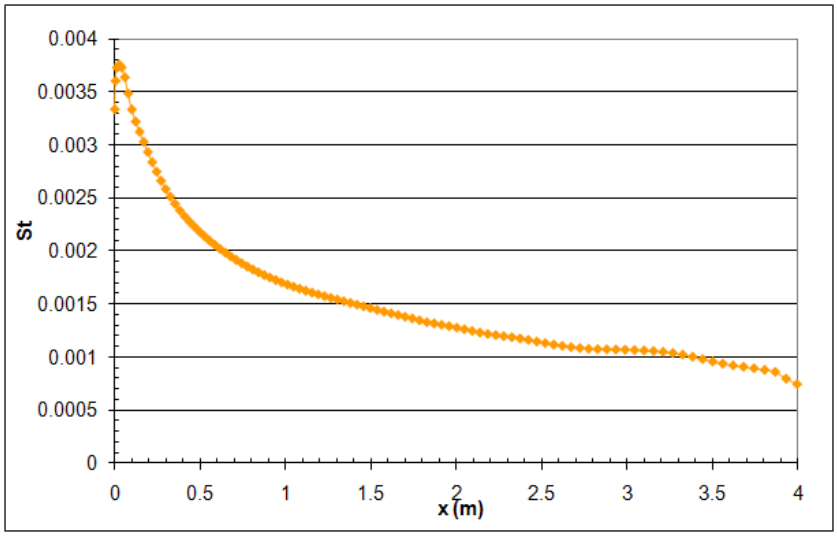

Figure 4.12: *Upper surface Stanton number for the reference case*

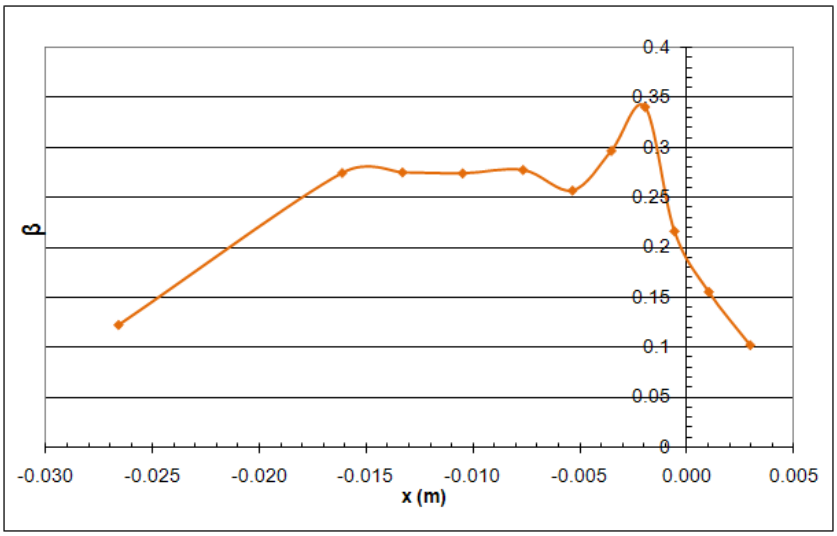

Figure 4.13: *Local catch efficiency for the reference case*

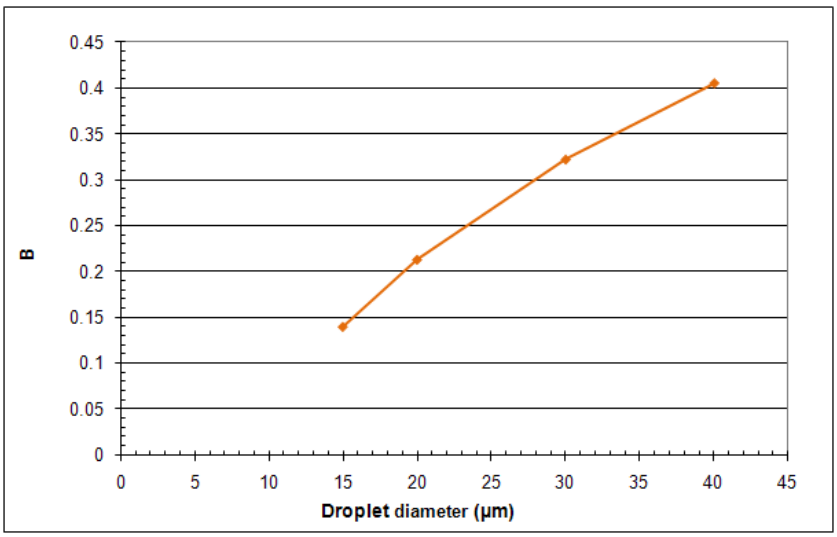

Figure 4.14: *Global catch efficiency for the reference case*

4.5 Analysis of the Hybrid airfoil

4.5.1 Aerodynamic parameters in free stream

Even though the leading edge of the Hybrid airfoil is full-scale, the overall Hybrid airfoil has a shape different from the B737/700. Thus, a change in speed and AOA is expected to get a similar icing as on the B737/700. The full-scale leading edge is maintained up to 0.37 m chordwise. The runback ice is intended to be studied up to this limit. The aerodynamic parameters are also studied up to this limit and minimum attention is retained for what happens downstream this zone.

Firstly, the free stream speed used for the Hybrid airfoil has been reduced compared to the B737/700. As the Hybrid airfoil has a very bluff shape, a large blockage effect is going to have to be dealt with during the icing tunnel tests. It means that the flow in the vicinity of the model is going to be accelerated in the icing tunnel. For this reason, it was likely that a speed of 118 $m.s^{-1}$ during the experiments would involved very high speed close to the model and vibrations of the tunnel walls. Therefore, the CFD study of the Hybrid airfoil was done with a speed of 100 $m.s^{-1}$ instead, even for the free stream case. In Figure 4.15 and Figure 4.16 the contours of Mach numbers are plotted.

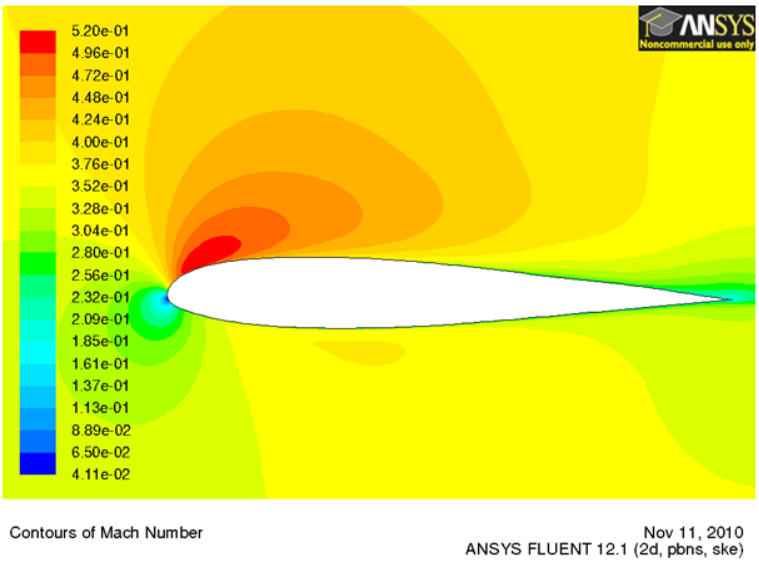

Figure 4.15: *Mach number distribution for the reference case (3° AOA)*

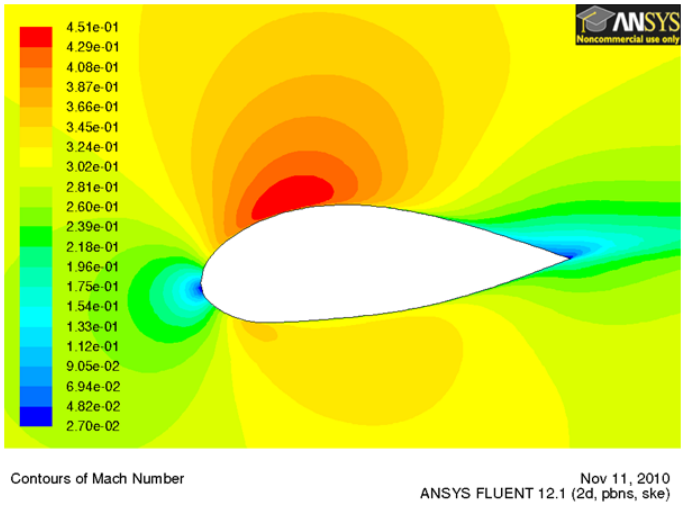

Figure 4.16: *Mach number distribution for the Hybrid airfoil (8° AOA)*

As expected, we can see that the flow is deccelerated along the leading edge of the Hybrid airfoil with respect to the reference case, because of the free stream speed reduction. This speed reduction is expected to be compensated for, once the airfoil is installed in the tunnel.

Secondly, it has been decided that the AOA representative of the hold case for the B737/700 airfoil is 3°. Because of the chord difference between the reference case and the Hybrid airfoil, the lift coefficient for the Hybrid airfoil should be roughly 4 times the one of the B737/700 if the same lift force is to be expected on the Hybrid airfoil compared to the B737/700. This was not achievable because of the non aerodynamic shape of the Hybrid airfoil. The stall would be reached before getting such high lift coefficient. So, it was decided to choose a reasonably high AOA (before massive flow detachment occurs at the full-scale leading edge) which would allow having the stagnation point on the lower surface with a positive lift and a reasonable match between the surface pressure and shear stress distribution on the studied zone. However it was necessary to keep the leading edge of the airfoil in the central zone of the test section of the icing tunnel, as this is the position where the cloud is the most uniform. Though there was an upper limit in the choice of the AOA. Then several angles of attack were tested in Fluent and 8° was chosen for the Hybrid airfoil as it gives the stagnation point slightly on the lower surface (Figure 4.16) and it keep the leading edge of the airfoil in the central zone of the test section.

Given these changes in the aerodynamic parameters, the surface pressure is greater and shear stress is smaller in comparison with the reference case (Figure 4.17 and Figure 4.18). However, these differences were expected for the free stream cases. Once in the tunnel, the blockage effect will result in a decrease of P_s and an increase τ which will make them closer to the reference case.

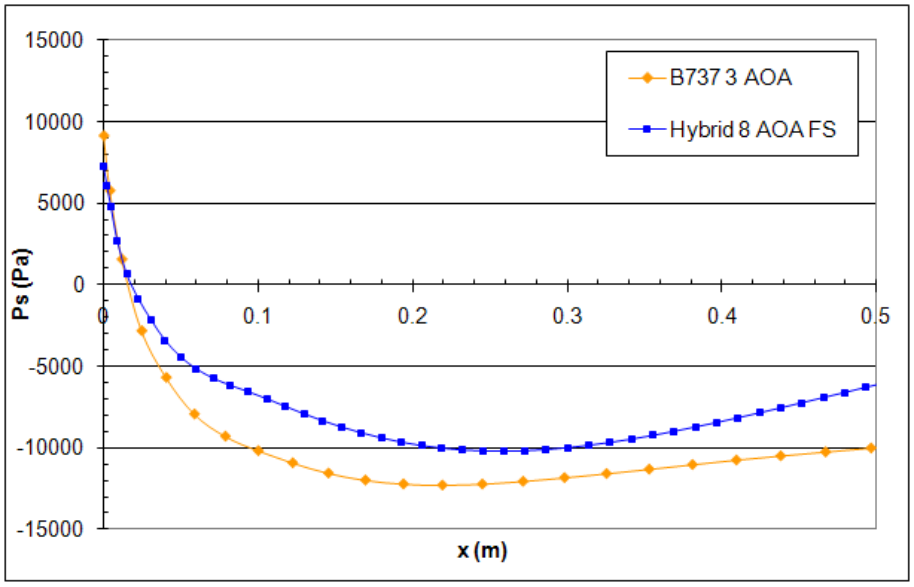

Figure 4.17: *Upper surface static pressure comparison for the Hybrid airfoil (8° AOA) and the B737/700 (3° AOA)*

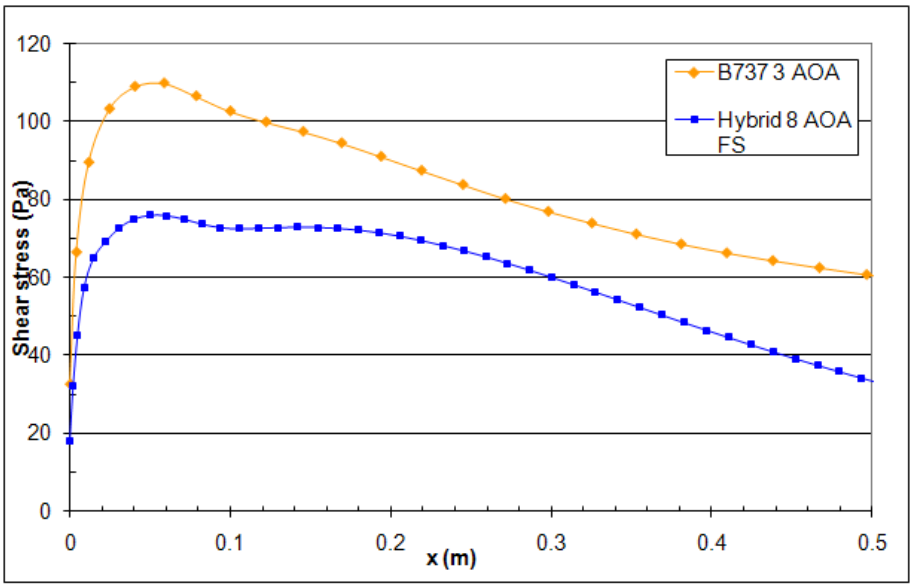

Figure 4.18: *Upper surface shear stress comparison for the Hybrid airfoil (8°AOA) and the B737/700 (3°AOA)*

4.5.2 Icing parameters in free stream

According to Gent et al. (2000), the catch efficiency is increased when the speed is increased but it is decreased when the length of the airfoil is increased. Between the reference case and the Hybrid airfoil in free stream, the speed and the length of the airfoil are changed. For the Hybrid airfoil, the far stream velocity is 15% less than for the reference case. The chord length of the Hybrid airfoil is 1/4 the size of the B737/700 chord. These changes should have an opposite effect on the catch efficiency: the decrease in speed should decrease the catch efficiency but the decrease in chord length should increase it. As the the change in the chord length is the biggest change, it is likely that the catch efficiency is going to be increased for the Hybrid airfoil in free stream in comparison with the reference case. When looking at the global catch efficiency as function of the droplet diameter for both airfoils, this trend is clear, except for the 15μm droplet diameter case (Figure 4.19). The calculation of the mono-dispersed local catch efficiency for a droplet diameter of 20 μm also confirmed this trend, especially for the upper impingement limit (Figure 4.20). The upper impingement limit of the Hybrid airfoil is 1.5 times greater compared with the reference case.

The impingement peak remains of the same order for both cases. As the blockage effect is going to enhance the droplet impingement, it is likely that the MVD will be adapted for the airfoil mounted in the tunnel.

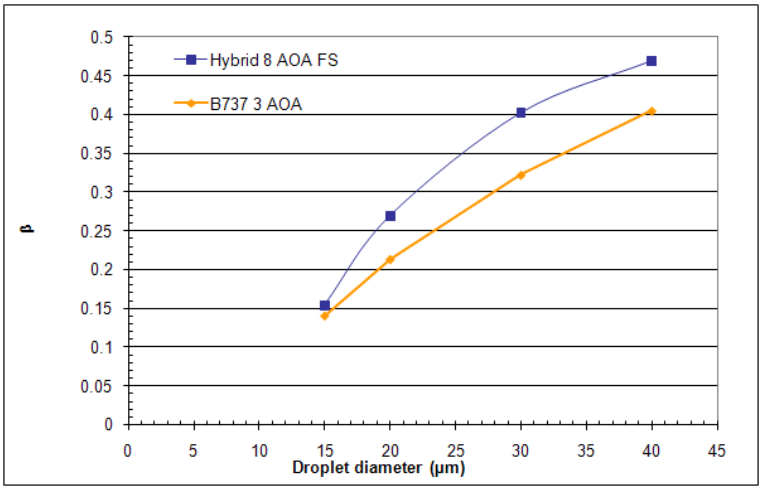

Figure 4.19: *Global catch efficiency comparison between the Hybrid airfoil and the B737/700 in free stream*

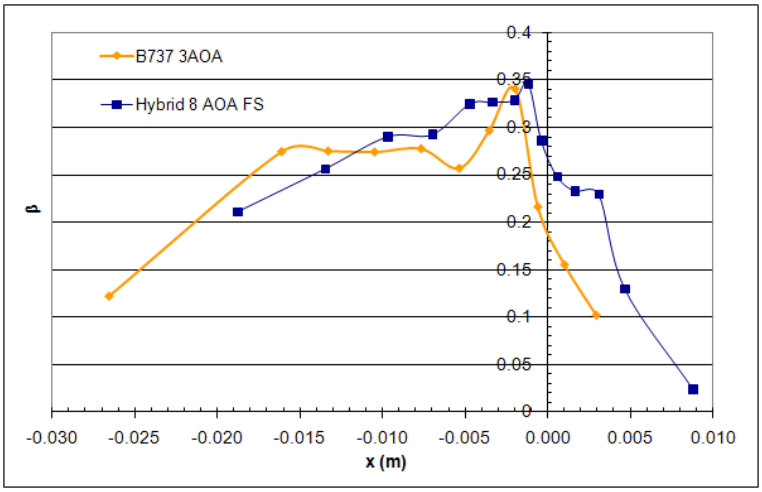

Figure 4.20: *Mono-dispersed local catch efficiency comparison between the Hybrid airfoil and the B737/700 in free stream (20 µm)*

Concerning the heat transfer coefficient, as the free stream speed, the pressure gradient and the airfoil curvature are changed for the Hybrid airfoil, it is expected that this will influence the heat transfer along the airfoil. The surface curvature of the Hybrid airfoil, is changed at the position were the full-scale leading edge is connected to the after body. It has been highlighted in the literature review (see 2.1.3) that a change in the surface curvature or in the pressure gradient, influences the heat transfer coefficient (Wang and Simon (1987), Turner et al. (2000) and Ozalp and Umur (2003)). An increase in the surface curvature lead to an increase in the heat transfer coefficient. In Figure 4.21, we can see that the stanton number in the leading edge region is increased for the Hybrid airfoil in regards to the B737/700 airfoil.

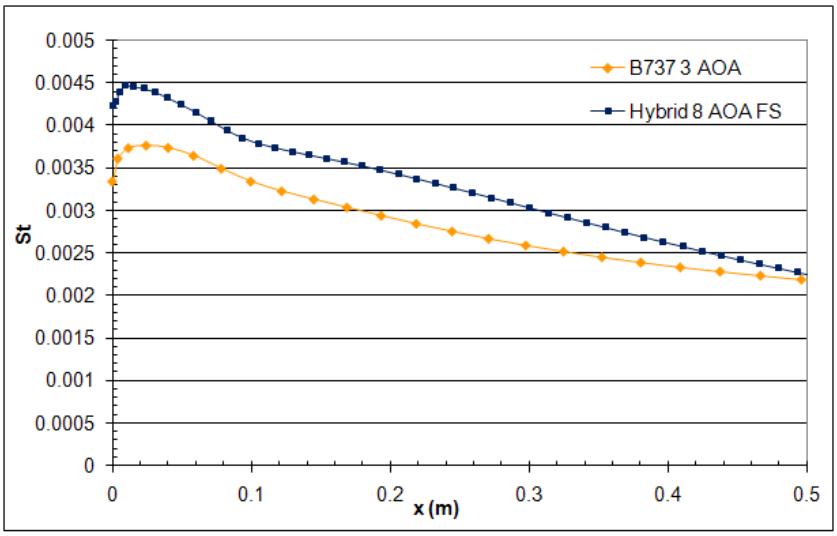

Figure 4.21: *Upper surface heat transfer comparison between the Hybrid airfoil and the B737/700*

4.5.3 Wall effects in the icing tunnel

The tunnel walls have an effect on the aerodynamics of the flow in the vicinity of the airfoil and thus on the ice accretion. This effect is all the more present with the Hybrid airfoil which is big compared to the icing tunnel. It is likely that some corrections will have to be made in some parameter values (AOA, velocity, LWC, MVD, etc) to take into account the tunnel walls effect on the experiments.

Following the simulation results including the tunnel walls (Figure 4.22), a speed of 100 $m.s^{-1}$ should not trigger any shock waves in the CIT. When looking at the Mach number contours of the Hybrid airfoil in the tunnel (Figure 4.22) and for the B737/700 (Figure 4.15), we can see that both leading edges are in the same range of velocity. As expected the blockage effect has compensated for the speed decrease in the vicinity of the Hybrid airfoil that was observed in the free stream case in comparison with the reference case. However the Mach number at this position is quite high ($M = 0.53$) and there is a risk that the turbulence may produce huge vibrations and somehow limit the use of the tunnel in this range of velocity.

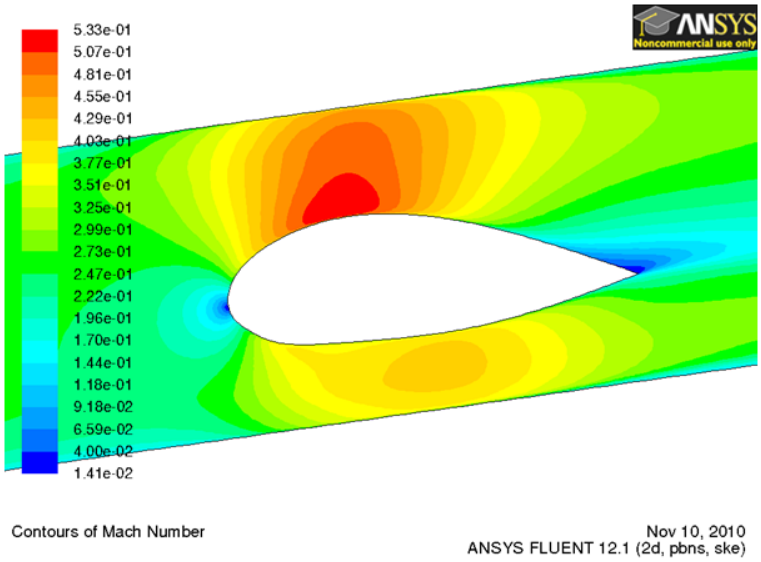

Figure 4.22: *Mach number distribution in the vicinity of the Hybrid airfoil in the tunnel (8° AOA)*

The tunnel walls have an influence on the surface pressure and shear stress distribution, especially in the vicinity of the suction peak (Figure 4.23 and

Figure 4.24). The static pressure is decreased by 39% and the shear stress is increased by 11% at the suction peak in the tunnel compared to the reference case. However, the zone we are interested in is just upstream of the suction peak where the tunnel walls have less influence. P_s and τ are the forces which affect the water film and rivulet speed. It is difficult to discuss the influence of these 2 parameters on the surface water behavior without any experimental results. Further work should be done on this particular matter. From the literature it seems that the shear stress has no significant effect on the water temperature distribution and wetness factor (Al-Khalil et al. (1993)).

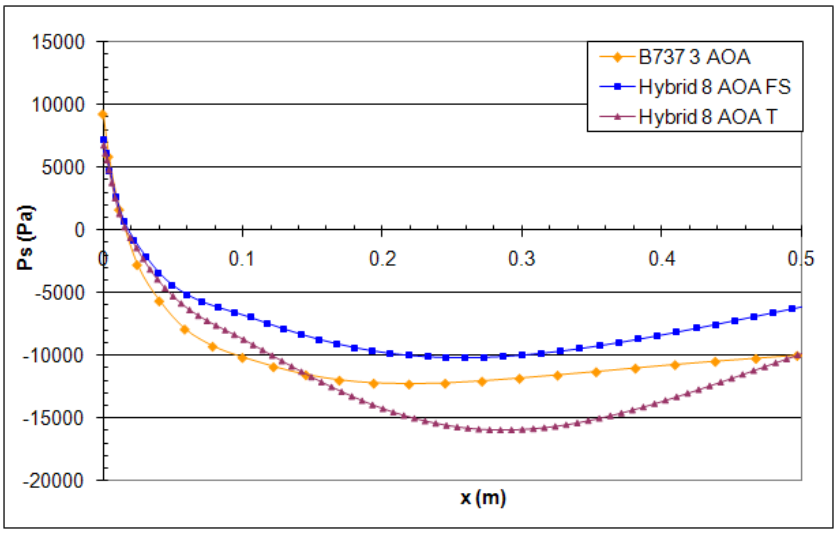

Figure 4.23: *Upper surface static pressure comparison between the Hybrid airfoil in the tunel and in free stream and the B737/700 in free stream*

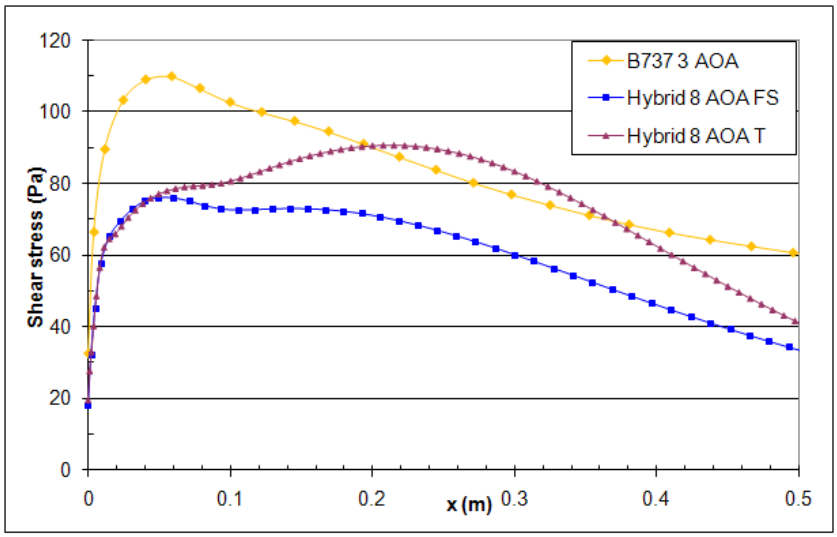

Figure 4.24: *Upper surface shear stress comparison between the Hybrid airfoil in the tunel and in free stream and the B737/700 in free stream*

The Stanton number is increased due to the influence of the tunnel walls (Figure 4.25). The main reason is that the heat transfer coefficient is highly linked with the surface pressure gradient and then with the flow acceleration or deceleration over a surface. The flow is accelerated on the leading edge of the Hybrid airfoil in the tunnel compared to the airfoil in free stream. Then it was expected to have an increase of the heat transfer in the tunnel (Turner et al. (2000) and Ozalp and Umur (2003)).

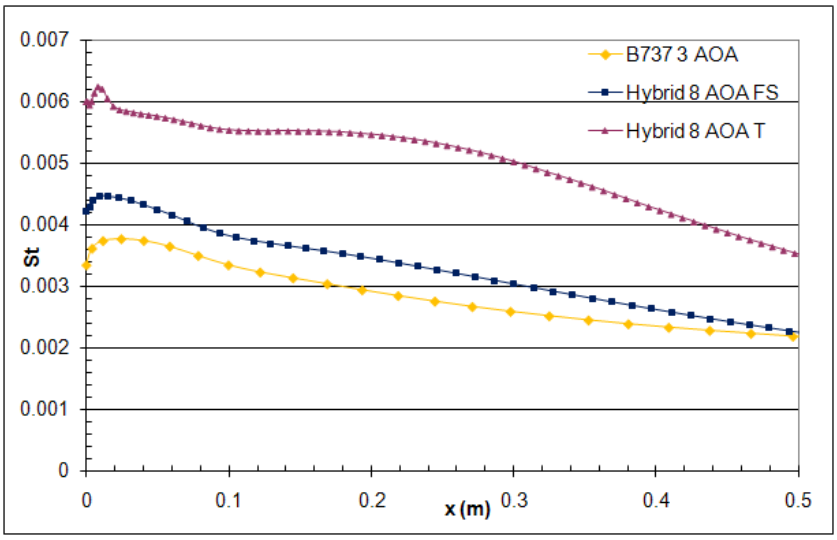

Figure 4.25: *Upper surface heat transfer comparison between the Hybrid airfoil in the tunel and in free stream and the B737/700 in free stream*

Concerning the wall effects on the droplet impingement, Bragg and Wells (1994) found that the effect was minor when the size of the tunnel divided by the chord length was between 1 and 3. However, for this study, this ratio (0.76) is smaller than the range explored by Bragg and Wells (1994). From the CFD simulation, it seems that the impingement for the Hybrid airfoil in the tunnel is increased compared to the Hybrid airfoil in free stream, for droplets diameter of 20 μm:

- The global catch efficiency is increased by 30% between the free stream and the tunnel conditions (Figure 4.26 a)).
- The local catch efficiency is as well largely influenced by the tunnel walls. Its peak is increased by 76% and the upper impingement limit is almost multiplied by 2 for the Hybrid model between free stream and tunnel conditions (Figure 4.26 b)).

These results were expected due to the flow acceleration in the vicinity of the Hybrid airfoil.

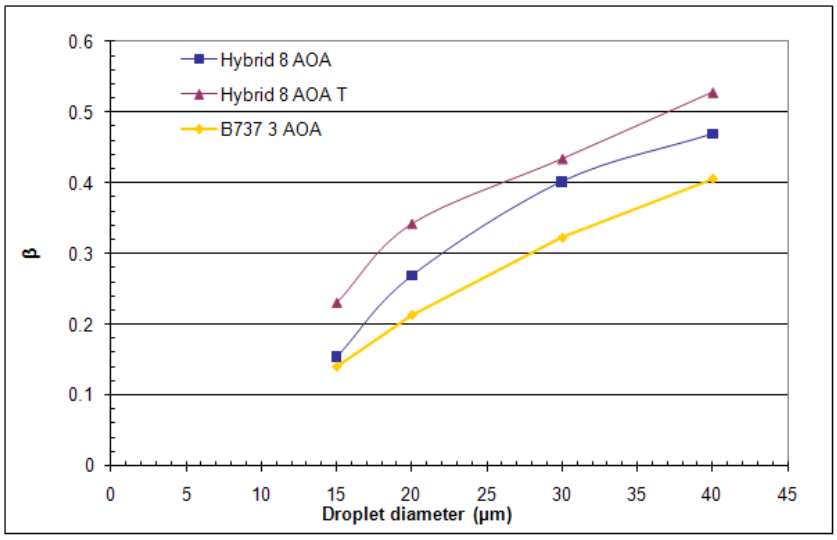

(a) Global catch efficiency

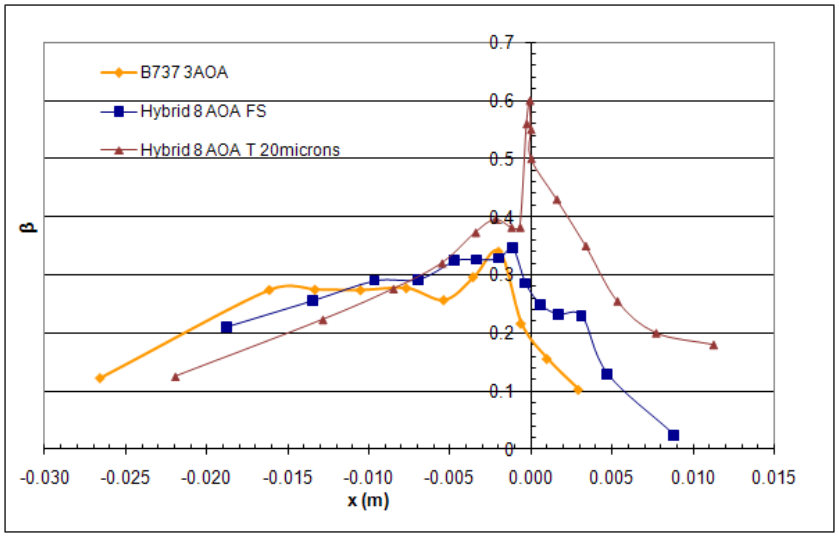

(b) Local catch efficiency

Figure 4.26: *Impingement comparison between the Hybrid airfoil in free stream and in the tunnel and the B737/700 in free stream, for droplets diameter 20 μm*

In order to reduce the effect of the walls and to keep the local catch efficiency as close as possible to the one of the reference case, β was calculated for a smaller droplet diameter (Figure 4.27). With a droplet diameter of 17 μm in the tunnel, the upper limit of the impingement and the peak value of the local catch efficiency are relatively close to the reference case. However, the upper limit impingement is predicted to be slightly larger compared to the reference case.

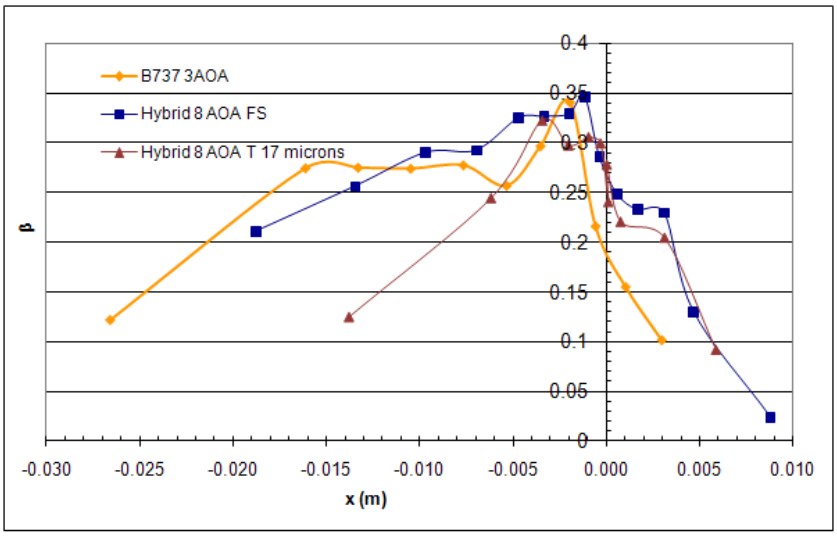

Figure 4.27: *Local catch efficiency comparison between the Hybrid airfoil in free stream (20 μm) and in the tunnel (17 μm) and the B737/700 in free stream (20 μm)*

4.5.4 Conclusions

Testing the Hybrid airfoil in the CIT induces some differences in the air flow in the vicinity of the leading edge compared to the reference case. It is difficult to quantify how these differences are going to affect the ice shapes growth. However, these differences remain relatively small.

Some changes to the reference conditions were made in order to decrease the differences between the reference case and the Hybrid airfoil in the CIT in terms of droplet impingement, surface pressure, surface shear stress and heat transfer:

- The droplets diameter during the icing tunnel testing is reduced from 20 μm to 17 μm
- The AOA of the Hybrid airfoil is increased from 3° to 8°
- The speed in the tunnel is going to be reduced. The speed has been reduced from 118 $m.s^{-1}$ to 100 $m.s^{-1}$ in the CFD study. This speed is still quite large for the icing tunnel with such a big airfoil inside. It is likely that it will trigger some vibrations and the air cooling might not be achieved correctly. With this in mind it has been decided to reduce the speed during the test to 85 $m.s^{-1}$.

Even though some changes to the conditions are necessary, there is no geometry scaling. For this reason, we can say that full-scale runback ice is going to grow on the Hybrid airfoil leading edge. Finally, in order to be sure that the worst icing conditions are considered, it was decided to test intermittent conditions as well. Table 4.5 summarizes the aerodynamic and icing conditions that are going to be used to get full-scale ice accretion on the Hybrid airfoil in the CIT.

Aerodynamic conditions		Icing conditions				
AOA (°)	Speed (m/s)	T∞(°C)	Conditions	Time of exposure (min)	LWC(g/m^3)	Droplet diamter (µm)
8	85	-9	continuous	NA	0.45	17
8	85	-9	intermittent	NA	2.23	17

Table 4.5: *Conditions for the Hybrid airfoil in the CIT following the CFD study*

4.6 Validation of Fluent results

4.6.1 Introduction

The aerodynamic and icing conditions which are going to be used for the full scale ice accretion experiments were chosen in the previous section using CFD simulation. No validation has been done so far. In this section the stagnation zone, the speed distribution and the droplet trajectories in the vicinity of the Hybrid airfoil are validated with experimental data.

4.6.2 Speed distribution

Fluent is considered to be a robust tool to calculate speed around an airfoil. However, the Hybrid airfoil in the tunnel is subject to a big pressure gradient due to the blockage effect which might not be well captured by Fluent. The speed distribution has been measured for two sets of positions in the vicinity of the airfoil using a Pitot static tube: one above the airfoil close to the suction peak, x=0.333 from the most front point of the airfoil, and the other one, in front of the airfoil. The Pitot tube was moved from the top wall to the surface of the airfoil and from the position y=0 and x=-0.177 to the top wall of the tunnel, respectively (Figure 4.28).

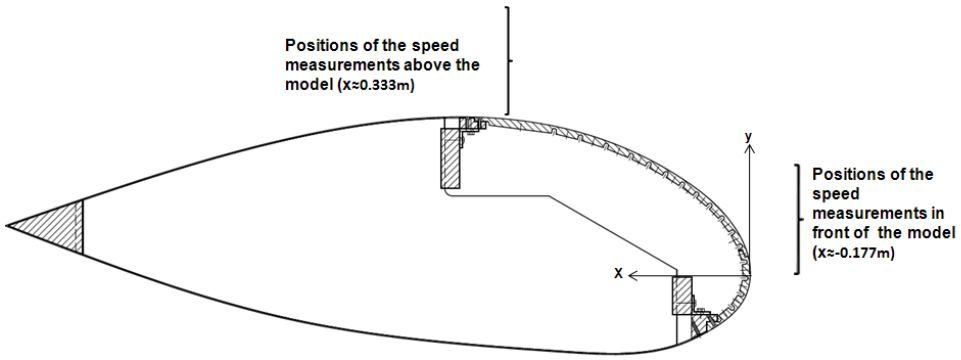

Figure 4.28: *Positions of the speed measurements in front and above the tunnel in the CIT*

By placing the Pitot tube directly into the flow and by connecting the device to a manometer, the operator can easily read the dynamic pressure. Once the dynamic pressure is known, the speed is found using the Bernouilli equation:

$$U(x) = \sqrt{\frac{2P_d}{\rho_{air}}} \tag{4.6.1}$$

The velocity profiles in the vicinity of the airfoil measured in the tunnel (U_∞=85 $m.s^{-1}$) have been compared with the velocity profiles computed by Fluent at the same position for the Hybrid airfoil in the tunnel (U_∞=100 $m.s^{-1}$). To quantify the difference between numerical and experimental data the velocity profiles have been linearly approximated. Then the difference of the experimental data in regards to the Fluent data has been computed as follow:

$$\Delta U(x) = \frac{(U(x)_{CFD} - U(x)_{exp})}{U(x)_{exp}} * 100 \tag{4.6.2}$$

For the velocity distribution above the airfoil, the results are presented in Figure 4.29. The difference between the Fluent simulation and the experimental measurements is increased close to the tunnel wall. One of the reasons for this may be a less fine grid density in this area. However the difference between both cases remains quite small, below 6%. Though, Fluent underestimates the flow speed in the vicinity of the airfoil as with a tunnel speed of 85 $m.s^{-1}$ the velocity distribution is almost the same as in Fluent with a speed of 100 $m.s^{-1}$.

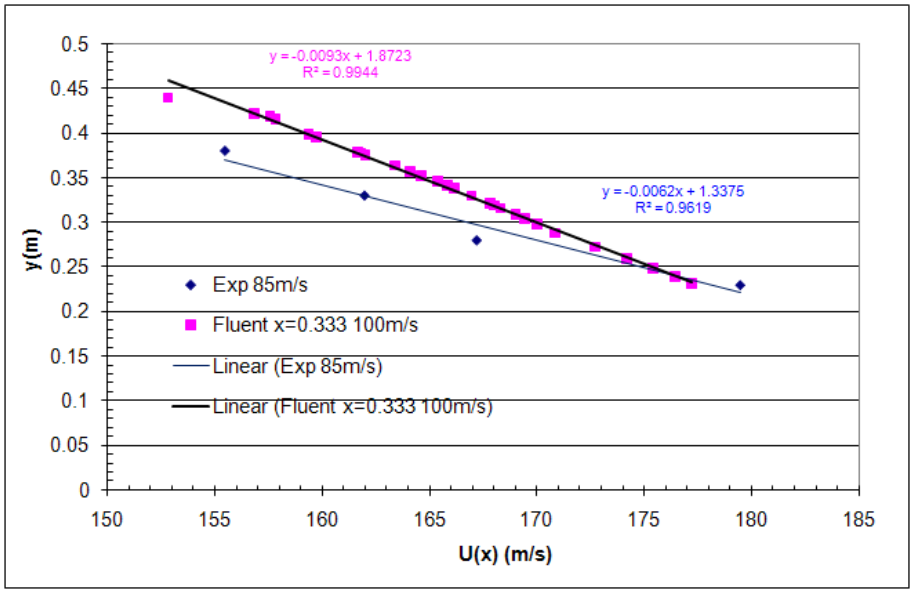

Figure 4.29: *Velocity profile comparison between the experiments and Fluent above the airfoil*

The same analysis was conducted for the position in front of the airfoil (Figure 4.30). Once again, the velocity distributions are quite close.

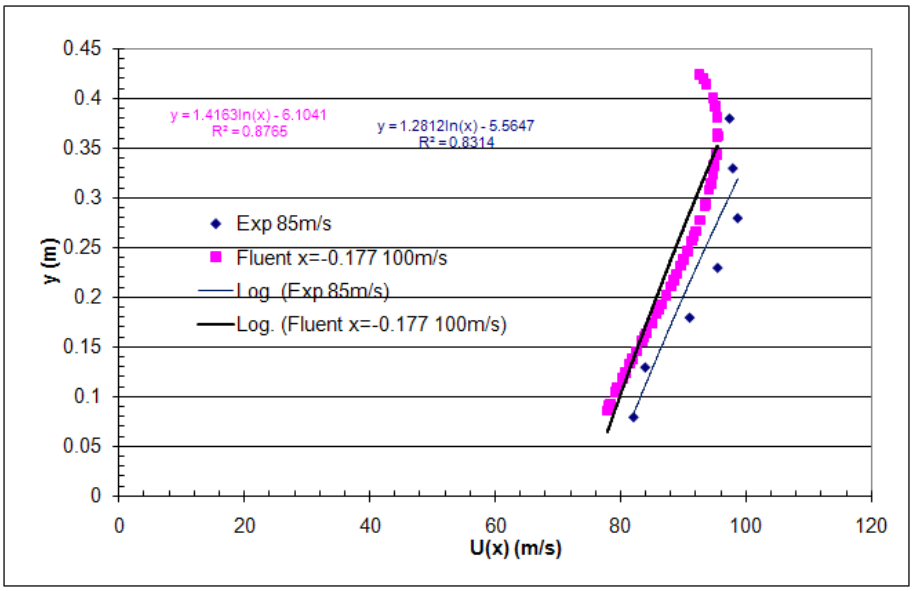

Figure 4.30: *Velocity profile comparison between the experiments and Fluent in front the airfoil*

To conclude, a tunnel speed of 85 $m.s^{-1}$ is found to give similar result as the Fluent simulation for the Hybrid model with in the tunnel with a speed of 100 $m.s^{-1}$. This is very encouraging as it seems that the speed reduction from 100 $m.s^{-1}$ in Fluent to 85 $m.s^{-1}$ during the experiments does not change much the speed distribution in the vicinity of the airfoil. Increasing the tunnel speed above 85 $m.s^{-1}$ during the experiments would involve the design of a hump to modify the wall shape in order to reduce the turbulence and the vibrations in the test section. This solution was suggested by J.Sancho in his thesis (Sancho (2008)). Hence, it is acceptable to keep a tunnel speed of $85m.s^{-1}$ as it is underneath the tunnel limitations and the air flow with this speed is close to the Fluent simulations which were used to define the AOA and MVD for the icing tunnel tests. In practice, the airfolw at 85 $m.s^{-1}$ did give rise to noticeable vibration but it was at a level thought acceptable.

4.6.3 Impingement limit and stagnation point

Even if the stagnation zone is difficult to visualise, by spraying warm water on the surface it is possible to distinguish a zone from where the water film is circulating toward the upper surface and the lower surface. The error of visualising the stagnation zone is ±0.5 cm. It looks to be situated just below the upper surface limit which corresponds to the Fluent simulation.

The impingement limits were measured using rime ice and a 2D ice tracing technique. Rime ice is used because it does not allow any water film on the surface. The water which is impinging on the airfoil at a certain location is freezing at the same location. The 2D ice tracing technique works as follows: once some ice has grown on the surface, a cardboard template is applied to the leading edge and a pencil is used to draw the ice shape 2D profile. The error of drawing by hand the ice profile is estimated to be ±1mm. Previously, a hot metal plate has been applied to the surface to remove a slice of ice to allow the cardboard to be applied to the airfoil surface (Figure 5.1). This technique is commonly used in the icing community (Wright (1999) and Broeren and Bragg (2002)). The following conditions were used to generate the cloud which is used to calculate the impingement limit: T_s=-15°C, U_∞=85 $m.s^{-1}$, time of accretion 7.5 min, 16 μm≤MVD≤18 μm and LWC=0.42 $g.m^{-3}$. The measurements were made for the spanwise positions 3.5 and 4.0 (Figure 4.32 and Figure 4.33 respectively). The red arrow on the ice profile pictures represents the observed upper limit of impingement.

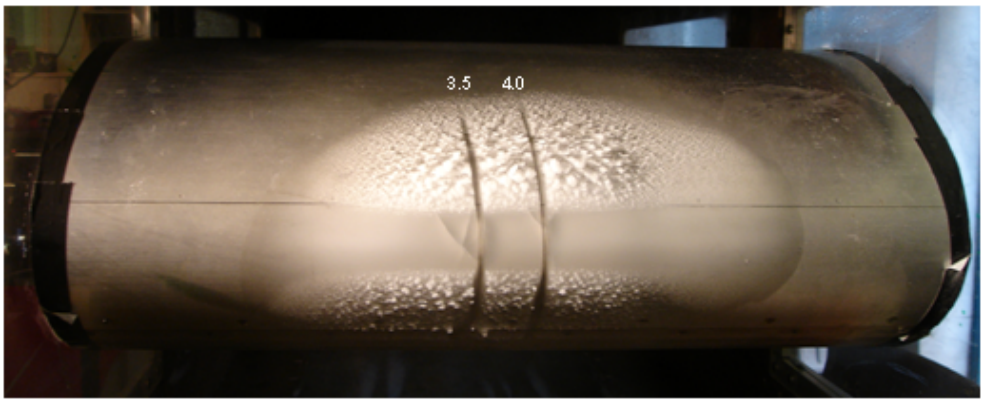

Figure 4.31: *Position of the ice profiles measurements*

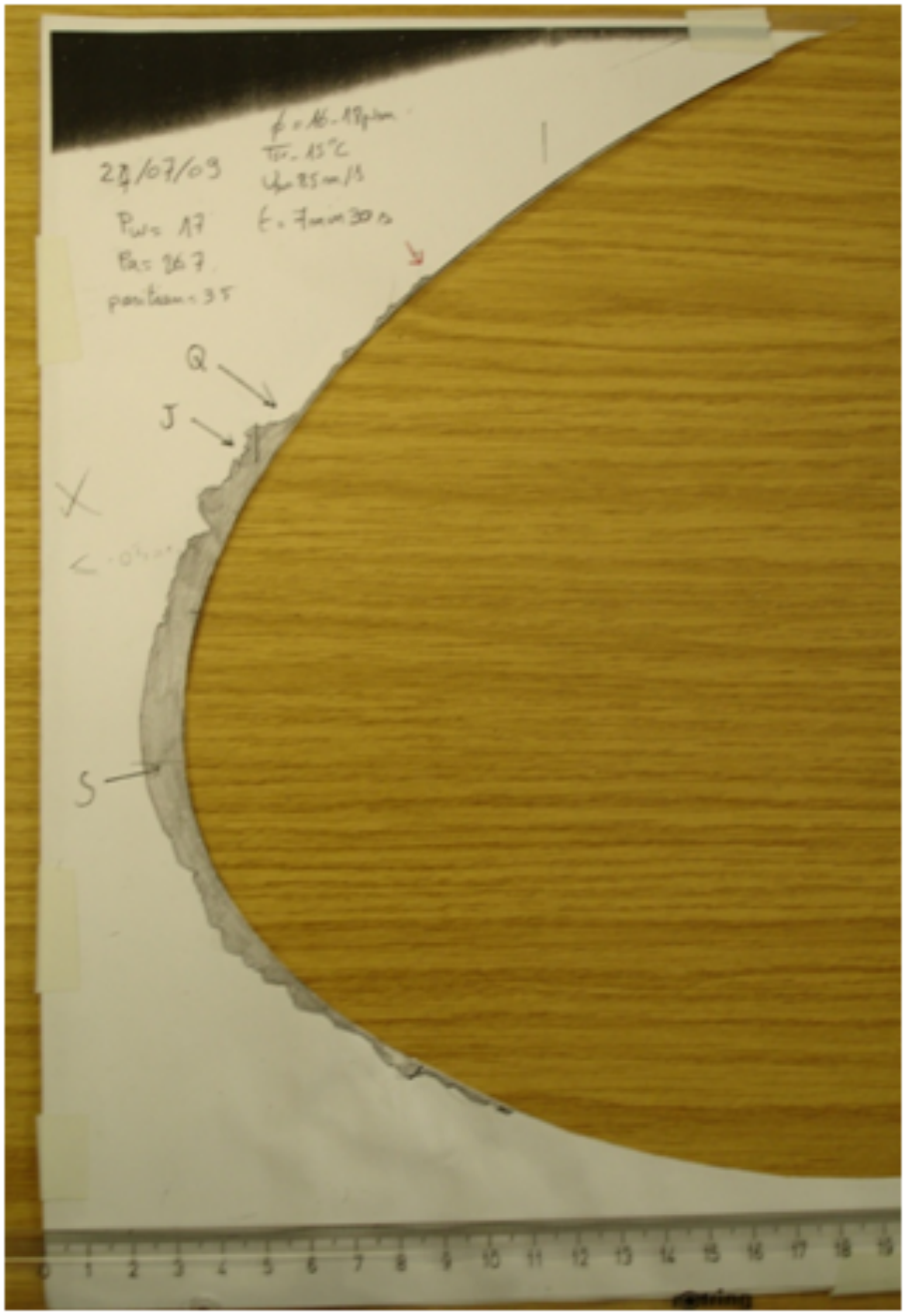

Figure 4.32: *Ice thickness profile at position3.5*

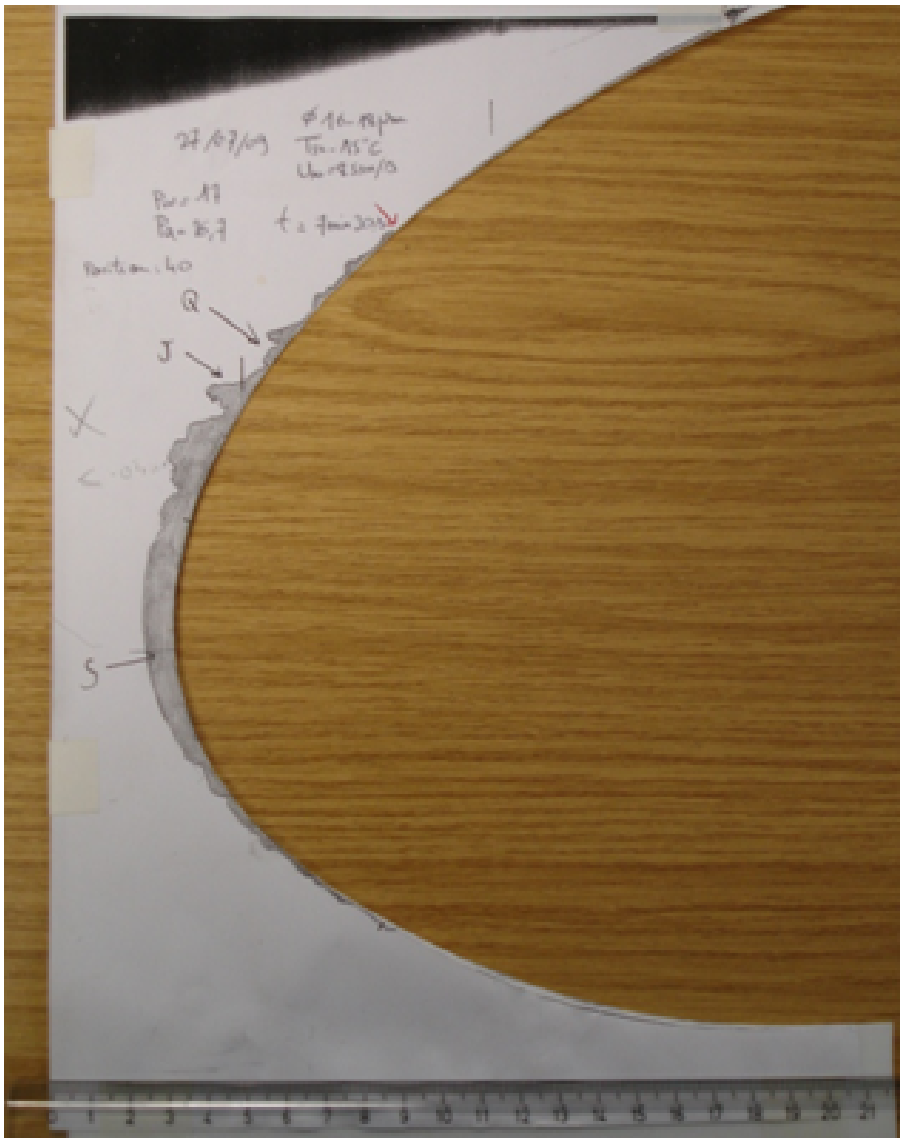

Figure 4.33: *Ice thickness profile at position4.0*

The upper surface impingement limit measured on the ice profile was compared to the impingement limit that has been calculated with Fluent using mono-dispersed (Figure 4.27) and poly-dispersed droplets distribution for the Hybrid airfoil in the tunnel (Table 4.7). The droplets size distribution used for the poly-dispersed numerical simulation is MVD=16.36 μm (Table 4.6) and the diameter used for the mono-dispersed simulation is 17 μm.

Diameter (microns)	Cumulative Volume (%)	Individual Volume (%)
16	50	50
18	53.52	3.52
20	59.15	5.63
30	71.12	11.97
40	86.6	15.48
60	95.77	9.17

Table 4.6: *Volume fraction of the droplet diameters for MVD=16.36μm in the CIT*

	Fluent mono-dispersed 17 µm	Fluent poly-dispersed MVD=16.36 µm	Experiments 16 µm<MVD<18 µm
Upper impingement limit (m)	0.007	0.07	0.06

Table 4.7: *Impingement limits*

The upper limit of the impingement is underestimated by Fluent using a mono-dispersed calculation. This result has already been highlighted in section 3.3.4. Using a poly-dispersed calculation the upper limit impingement of the Hybrid airfoil in the tunnel calculated with Fluent is close to the one reported during the experiments. The difference that remains between the experiments and Fluent in terms of impingement limits can be explained by several reasons. First of all, the cloud defined in Fluent is perfectly uniform whereas in the tunnel it is not. Second of all, the calculation of the impinging droplets trajectories is calculated by considering a clean airfoil in Fluent. This is also different from what happens in the icing tunnel. The impingement can be modified as function of the time because of the ice accretion on the surface of the airfoil which disturbs the flow. It may expand the impingement limits. Another reason is that the Fluent simulation is 2D. It is likely that because of the influence of the tunnel walls and because of non uniformity of the cloud spanwise, the impingement is modified.

Chapter 5

Icing tunnel experiments

5.1 Objective of the experiments

The main objective of the icing tunnel experiments is to capture 3D full-scale high-fidelity runback ice shapes using an anti-icing system, for use in the aerodynamic test campaign in a wind tunnel. The geometric features of these ice shapes are going to be studied as a function of LWC, heat input and the limit of the heated zone in order to compare and to rank them. The secondary objective of the experiments was to grow runback ice using the system in a de-icing mode. However the set-up required for a de-icing system is more complex than anti-icing system and the amount of heat per square meter required by the system is greater especially at the stagnation zone. For these reasons the runback ice from the system in de-icing was not explored extensively.

5.2 Test methods

To fulfil these objectives several methods of capturing the ice shapes were employed. Firstly numerous pictures of the ice shapes were taken. Secondly, 2D ice profiles were captured, in the middle of the span (35 cm from the near side of the model), using 2D tracing on a cardboard as presented in section 4.6.3. They have been used extensively in this study to probe runback ice shapes so as to help target those cases most worth moulding. As an aid to compare and rank the 2D shapes, characteristic parameters were defined from a typical runback ice shape profile (Figure 5.1):

- a the length between the front of the shape and the ridge
- b the length of the ridge

- d the peak height
- α the angle between the normal to the surface and the line between front of the shape and the front of the ridge
- D the length between the end of the heated zone and the front position of the shape.

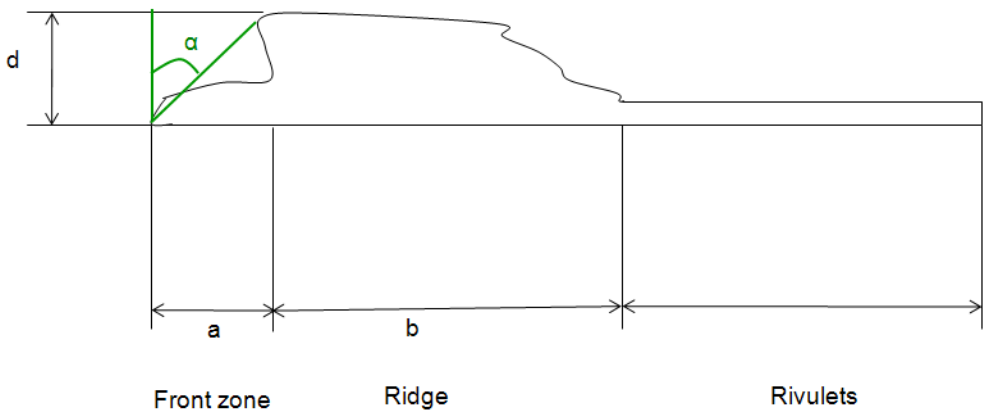

Figure 5.1: *Ice tracing technique*

Thirdly, 3D full scale high-fidelity runback ice shapes were captured using an innovative moulding and casting technique. Making high-fidelity ice shapes mouldings and castings is not as easy. The main problem for moulding is to find a material that can cure in a reasonable time at temperatures below freezing. The search of a casting material is less complicated as the temperature limitation is removed. The main characteristic for casting material is to be stiff enough to be used for wind tunnel testing. Reehorst and Richter (1987) led experiments in order to find new moulding and casting materials. Before them, wax and plaster were used for moulding and casting respectively. They proposed to use silicone and epoxy or urethane instead. The silicone is a very powerful material in this context as it can cure at a temperature below freezing. It can be poured over the ice without damaging it, and the mould so made can be re-used to make multiple castings. It also allows the making of the moulding directly onto the model. Neither the ice nor the leading edge have to be removed from the tunnel in order to make the moulding. This is very useful for small ice shapes. The main drawback of the silicone is its time of cure: at -9°C it may not even cure and remain liquid. For this reason the silicone was mixed with catalysts to reduce its cure time: 5 hours at -9°C. The

silicone rubber T20[1] was used with the T6[2] catalyst and the TW[3] catalyst booster. The weighing of the silicone and catalysts was done using a high quality digital scale as different mixtures of the components would change the time of cure of the silicone rubber. A specially made wooden box has been used to contain the silicone on the airfoil surface (the moulding box). A metallic arm allows the box to be secured while the tunnel is running at 20-25 $m.s^{-1}$ to keep the temperature below zero (Fig. 5.2).

During the experiments the operators follow this method:

1) Place the silicone and catalysts in the freezer before the tests to cool down the material to below the freezing point of water.

2) While the ice is growing onto the model, prepare the mixture.

3) Once it is ready put it back to the freezer to rest for 10 minutes to allow the larger air bubbles to float to the surface.

4) While the mixture is resting and when the cloud is switched off at the end of the run, cool down the tunnel to the minimum temperature allowed by the refrigeration plant. This allows the operator to access the inside of the tunnel without increasing the temperature above zero.

5) Take pictures of the runback ice shapes.

6) Remove two slices of ice using a hot plate to leave some clean airfoil surface so that the moulding box can seal against the model.

7) Put the moulding box onto the airfoil surface, centered on the ice.

8) Pour the mixture inside the box.

9) Close the box and put in place the metallic arm.

10) Start the tunnel and keep it running at 20-25 $m.s^{-1}$ during 5 hours at -9°C static. After one hour, some heating can be applied using the anti-icing system to raise the surface temparature to -6°C.

[1]The T20 silicone is easily pourable and medium soft. It can be used for making block moulds or skin moulds. T20 is suitable for the casting of plaster (www.tiranti.co.uk).

[2]Standard catalyst for the T20 silicone. It is used of the ratio of 5% (www.tiranti.co.uk).

[3]A separate additive which, when mixed with T6 catalyst, will give T20 silicone rubber a much quicker cure (www.tiranti.co.uk)

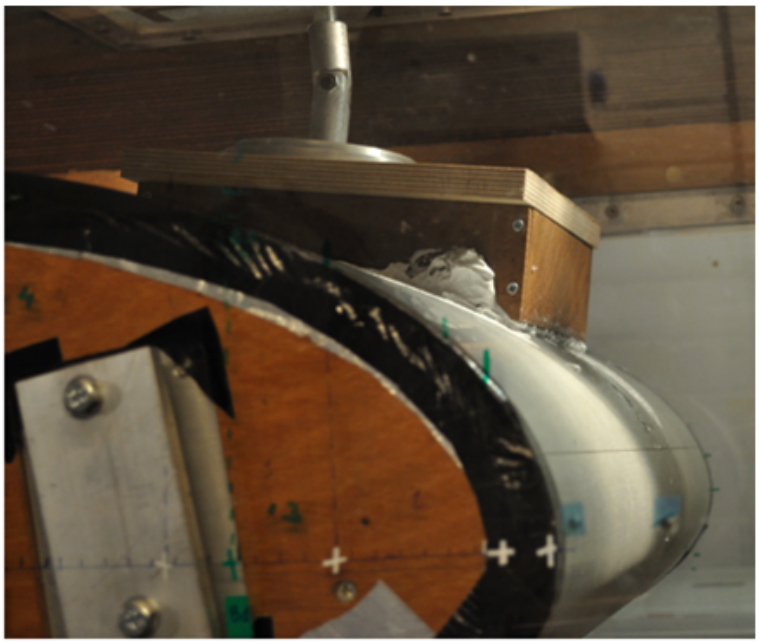

Figure 5.2: *Hybrid model in the CIT with the "moulding box" on the upper surface*

For the casting material it has been possible to avoid using more toxic materials such as epoxy or urethane. Plaster has been chosen. As pure plaster is quite brittle, the plaster has been mixed with polymer instead of water (www.tiranti.co.uk). This allows us to capture the rivulets more easily and to use the casting in wind tunnel. The plaster mixed with polymer cures in a few minutes at room temperature. One tricky point was to produce a flat casting and not curved as it is on the airfoil because a flat surface is going to be used for the wind tunnel test campaign. To do so, another box has been made with the reverse curvature of the section were the Silicone mould is placed. Then the plaster is poured into the mould. Once the casting is set, it is removed from the silicone moulding and the underneath surface is polished by hand to get it as flat as possible. (Figure 5.3).

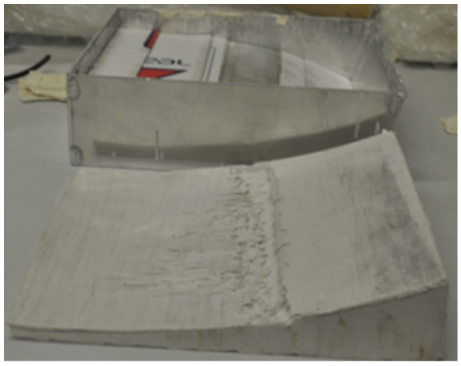

(a) Moulding with the reverse curvature box

(b) Flat casting

Figure 5.3: *Moulding and casting of a typical runback ice shape for maximum continuous icing conditions*

5.3 Instrumentation

The heating system was designed on the basis of the predictited requirements for heat fluxes and that the heating should be as flexible as possible to control the heat input distribution. The heaters are attached to the inner skin of the aluminium leading edge. The skin is 1cm thick. The heaters are composed by 16 rows of resistors (Figure 5.4 and Figure 5.5). From row 1 to 6 there are 16.6 Ω per row and from row 7 to 16, 20 Ω are available per row. Between each row a gap has been introduced into the skin to minimise heat flow by conduction chordwise. Each row is plugged to a power supply. Two different power supply arrangements have been tested. A fixed 160 V 10 kW power supply was connected to each row of circuits. The second arrangement used three identical variable power suppliers which can reach 100 V each. The method is to connect the rows in series or in parallel by zone and then to monitor the heat input to each zone independently.

The surface temperature of the leading edge was monitored using an array of 37 thermocouples (K type). This type of thermocouple was chosen because it is readily available, compact, inexpensive and accurate enough without individual calibration. The error of measurements is ±1°. The thermocouples are positioned in small holes along the inner skin. Figure 5.6 is a scheme of the resistors (green cells) arranged by row in the inner skin of the Hybrid airfoil. The thermocouples positions are represented by white cells with the

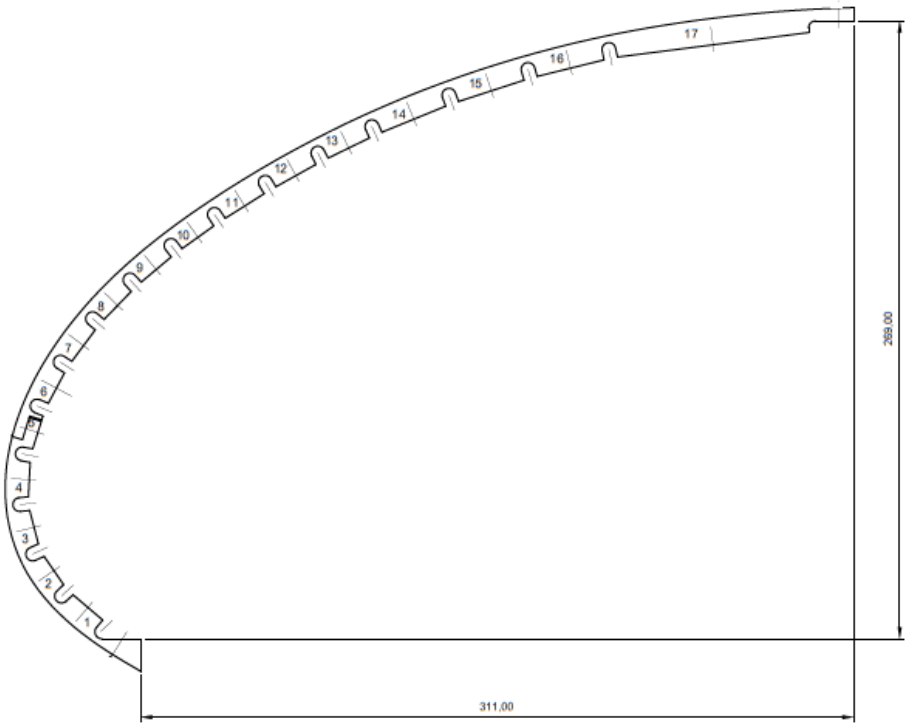

Figure 5.4: *Sketch of the leading edge skin*

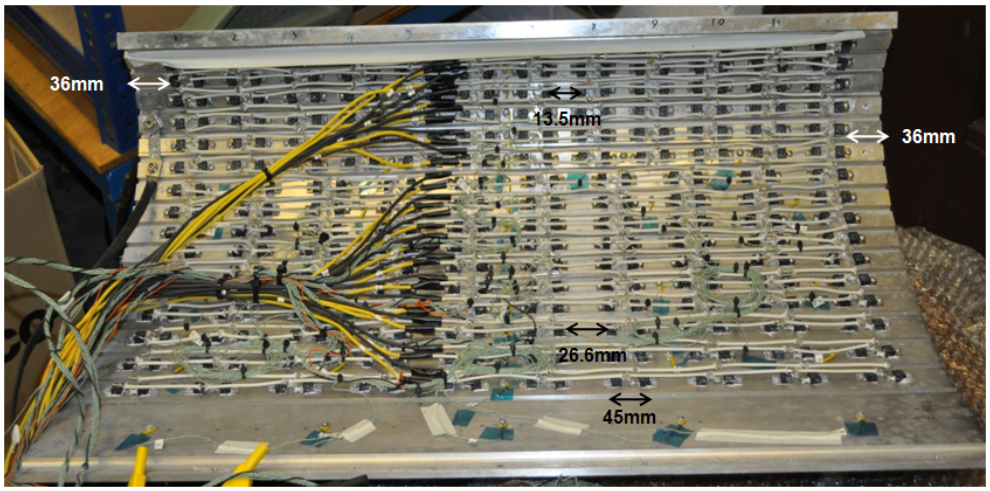

Figure 5.5: *Leading edge inner skin wiring*

thermocouple name on it.

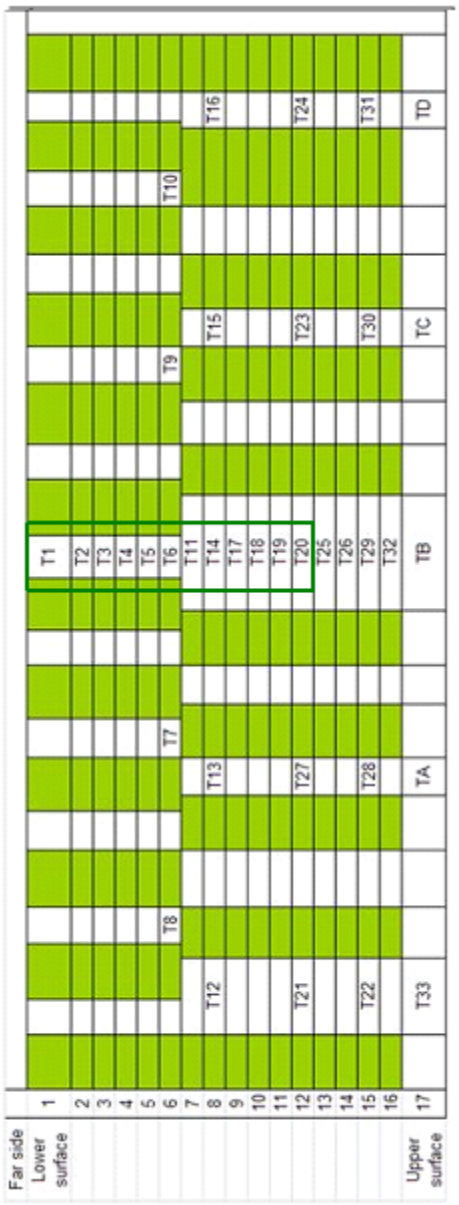

Figure 5.6: *Map of thermocouples embedded in the inner skin of the leading edge of the Hybrid model*

5.4 Range of conditions

The fixed conditions used for each run are presented in the Table 5.1:

Hybrid airfoil AOA (°)	U∞(m/s)	T∞(°C)	MVD (µm)
8	85	-9	17

Table 5.1: *Fixed conditions in the icing tunnel*

Two LWC values have been tested: 0.42 $g.m^{-3}$for the maximum continuous conditions and 1.2g $g.m^{-3}$for the maximum intermittent conditions. The time of accretion for each run was dependant on what ice thickness was targeted. Airbus main interest is in ice shape thickness between 3 and 6 mm.

Concerning the anti-icing system inputs, the experiments have been focused on 9 heat input configurations (Figure 5.7 and Table 5.2). The green squares represent rows of resistors plugged in series, the blue squares represent the rows in parallel and the grey ones are the inactive rows. The first four configurations are different but they all use the home made fixed voltage power supply which means that no high temperature gradient can be reached. Then, H5, H6, H7 and H8 are identical to the first four configurations but with the last heated zone removed to change the limit of the heated zone. Finally the last configuration H9 is plugged to the three GEN-100-15 power suppliers. The last configuration provides a high temperature gradient. In Figure 5.7 the chordwise position of the limit of the heated zone is given for each configuration. The heat input for H1 has been firstly estimated using the 1D runback ice model. The average surface temperature distributions in the heated zone for all the configurations have been calculated using the average temperature of the thermocouples in the central zone during the time of accretion. An example of the thermocouples taken into account for H1 is in the green zone in Figure 5.6.

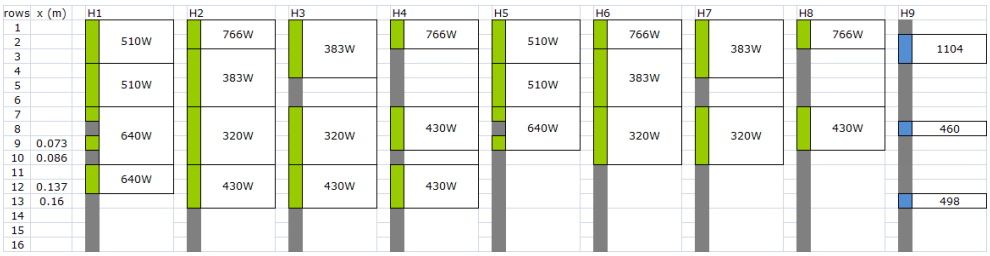

Figure 5.7: *Heating system configuration*

Heat input configuration	Limit of the heated zone (m)	Total heat input (kW)	Wet Ts (°C) (LWC=0.45g/m^3)	Dry Ts (°C)
H1	0.137	2.30	20.10	33.30
H2	0.160	1.90	12.10	21.40
H3	0.160	0.70	7.10	11.80
H4	0.160	1.20	10.20	18.70
H5	0.073	1.66	20.10	33.80
H6	0.086	1.47	12.90	25.10
H7	0.086	1.13	5.70	11.20
H8	0.073	1.63	8.70	18.70

Table 5.2: *Details of the heating system configuration*

The average wet surface temperature distribution for the heat input configurations H1, H2, H3, H4 and H9 are presented in Figure 5.8. These temperature distributions are different from temperature distributions from icing code. The configuration H9 is the one which gives a temperature distrubution the closest to the distribution given by Trajice. However, after the end of the heated zone ($x/c = 0.15$ for Trajice and $x/c = 0.16$ for H9), the temperatures in the present work decrease more slowly with distance (1deg per cm) than for the Trajice case. It is likely that in the icing code the temperature drop to zero exactly at the end of the heated zone. It seems that in a real case heat loss by conduction through the leading edge skin will give a temperature gradient at the end of the heated zone less strong than in the icing code. It has not been possible to compare the present temperature distribution with experimental data. Hence it is difficult to assess how close to the reality are the temperature distributions used in the present work.

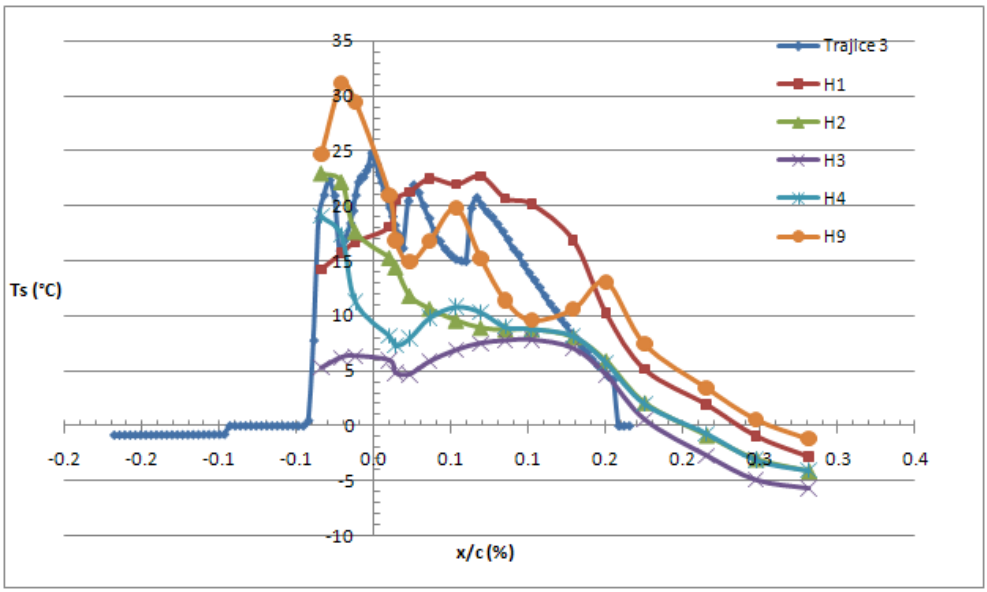

Figure 5.8: *Comparison between the surface temperature distribution for H1, H2, H3, H4 and H9 and a typical distribution from Airbus*

Concerning the de-icing mode of operation, 6 heat input configurations were tested (Table 5.3). H10, H11 and H12 have no continuous heat at the stagnation zone whereas with H13, H14 and H15, the stagnation zone is continuously heated. Three GEN-100-15 power suppliers were used with rows mounted in parallel. This study presents results only from H12 and H13 configurations (Figure 5.46 and Figure 5.47 respectively).

Heat input configuration	Limit of the heated zone (x/c%)	Total heat input (kW)	Time for 1 cycle
H10	0.086	2.70	2min 24s
H11	0.053	3.27	2min 24s
H12	0.053	3.27	2min 29s
H13	0.109	2.60	2min 26s
H14	0.109	2.60	1min 50s
H15	0.073	2.60	2min 26s

Table 5.3: *Details of the heat input configurations used for the de-icing system*

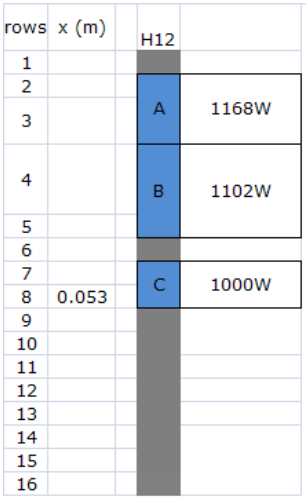

(a) Row arrangement

Heated zone	A	B	C	off
Time (s)	18	15	20	96

(b) Cycle sequence

Figure 5.9: *Details of H12 heat configuration for de-icing system*

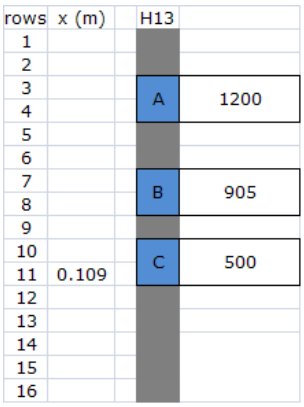

(a) Row arrangement

Heated zone	A	B	C	off
Time (s)	on	15	20	96

(b) Cycle sequence (continuous heat at the stagnation zone

Figure 5.10: *Details of H13 heat configuration for de-icing system*

5.5 Repeatability and uncertainties

The consideration of repeatability and uncertainties for this study is based on the guidance of the British Measurement and testing Association (Birch (2001) and Bell (2001)). The repeatability in temperature measurements and in the characteristic dimensions of the runback ice shapes are based on the run 6 which has been repeated four times on the same day (Table 5.4). The run 6 is for a LWC of 0.42 $g.m^{-3}$using the H7 configuration of heat input (anti-icing mode, total heat input 0.7 kW, limit of the heated zone x=0.086 m). The best estimate values are based on the average for the four runs. The standard deviation is multiples by a factor of 2.58 to get a confidence level of 99%. The surface temperature study takes into account all the central thermocouples which are likely to be on the heated surface (Figure 5.6).

Characteristic dimensions	Best estimate	Standard deviation (±)	Relative standard deviation (±%)
a (m)	0.0060	0.0018	30
b (m)	0.0460	0.0142	31
d (m)	0.0093	0.0012	13
α (°)	51	5	10
m (kg)	0.1604	0.0143	9
D (m)	0.0058	0.0004	6
Wet Ts (°C) (LWC=0.45g/m^3)	4.8	1.1	22
Dry Ts (°C)	9.9	1.6	16

Table 5.4: *Uncertainties with a confidence level of 99% for the characteristic dimensions of the runback ice shape in the case of run 6 repeated four times*

This repeatability scatter is above the usual ±10%. This is not surprising in the context of icing. It is very difficult to keep the LWC, droplets diameters and tunnel temperature perfectly constant in the icing tunnel. It has been highlighted in a previous part (C.3) that the uncertainties in the LWC are ± 0.11 $g.m^{-3}$for a confidence level of 99% and that the uncertainties in the droplets diameter for a LWC of 0.42 $g.m^{-3}$are ±2.2 μm and ±3.2 μm for a LWC of 1.2 $g.m^{-3}$. The free stream temperature uncertainty range is ±0.5°C. The ice accretion is very sensitive to a change in any of these conditions. Even a slight change in the surface temperature between two runs may affect the water film thickness and the heat transfer at the surface a lot (Whalen et al. (2005)).

The ice tracing for each of the repeated runs are display in Figure 5.11. The origin has been set the same for all the shapes. However, D, the difference in the chordwise location of each shape noted in Table 5.4 is very small. The height of the ridge remains more or less the same for each run. The front of the ridge is also similar for each run except for run 6.4. This horn phenomenon will be explained in section 5.7.3 and section 5.7.4 . The length of the shape is changing between each runs.

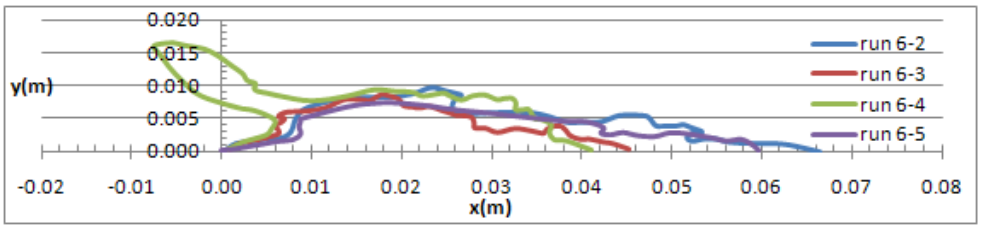

Figure 5.11: *Ice tracing for run 6 repeated four times*

5.6 1D runback ice model predictions vs experiments

The heat input of the anti-icing system used to maintain a certain surface temperature, calculated with the spreadsheet, has been compared with the experimental results. The objective is to see if the 1D runback ice model can predict correctly the heat intensity of an anti-icing system for certain icing conditions in regards to the experiments. A simialr study was undertaken in a section 3.3, however it was based on data from the open literature.

Two cases have been studied for wetted surfaces. One for an average wet surface temperature of 5°C (Figure 5.12) and one for an average wet surface temperature of 20°C (Figure 5.13). In both cases the outside temperature was -9°C, LWC=0.42 $g.m^{-3}$and U_{∞}=85 $m.s^{-1}$. In the model the surface temperature is an input and the heat from the heating system is the output. The surafce temperature is constant in the spreadsheet.

For the case with an average wet surface temperature of 5°C, the heat input from the 1D model is overestimated in the impingement zone (black arrow) and it is underestimated downstream that zone (Figure 5.12 b)). To quantify the difference between the 1D model and the experimental data, the areas underneath the heat flux curves were computed using a trapezoidal integration on Excel. The area underneath the curve from the 1D model is $\approx$ 13%

lower than the area underneath the experimental curve. It means that total heat input from the 1D model is underestimated by 13% in regards to the experiments. This result is encouraging. It means that the 1D runback ice model can predict with reasonable accuracy the heat input of an anti-icing system.

A similar analysis was done for an average wet surface temperature of 20°C (Figure 5.13). The trend is the same as for the 5°C case. The 1D model is underestimated, the heat input from the heating system before the end of the impingement zone and downstream that zone the heat is underpredicted. The trends remain the same when comparing the % difference in the areas, below the heat flux curves, between the model and the experimental. The difference is of $\approx 25\%$.

It is not surprising that there are some differences between the analytical outputs and the experimental data. Many assumptions were made in the spreadsheet (wetness factor, roughness of the water film/rivulets, heat transfer coefficient, temperature distribution, etc). Moreover, it was prouved that the amount of water impinging the model was underestimated in the model. Hence, we could excpect, that an improvement in the catch efficiency calculation would improve the accuracy of the 1D model, to predict heat flux.

However, even if it is not perfectly accurate, the 1D model is able to give a clue on the input for a heating system in certain icing conditions. It seems that the overall output from the 1D model are underestimated compared to the experiments. The difference between both does not exceed 25%. The 1D model remains very usefull when a heating system needs to be calibrated using a simple mean.

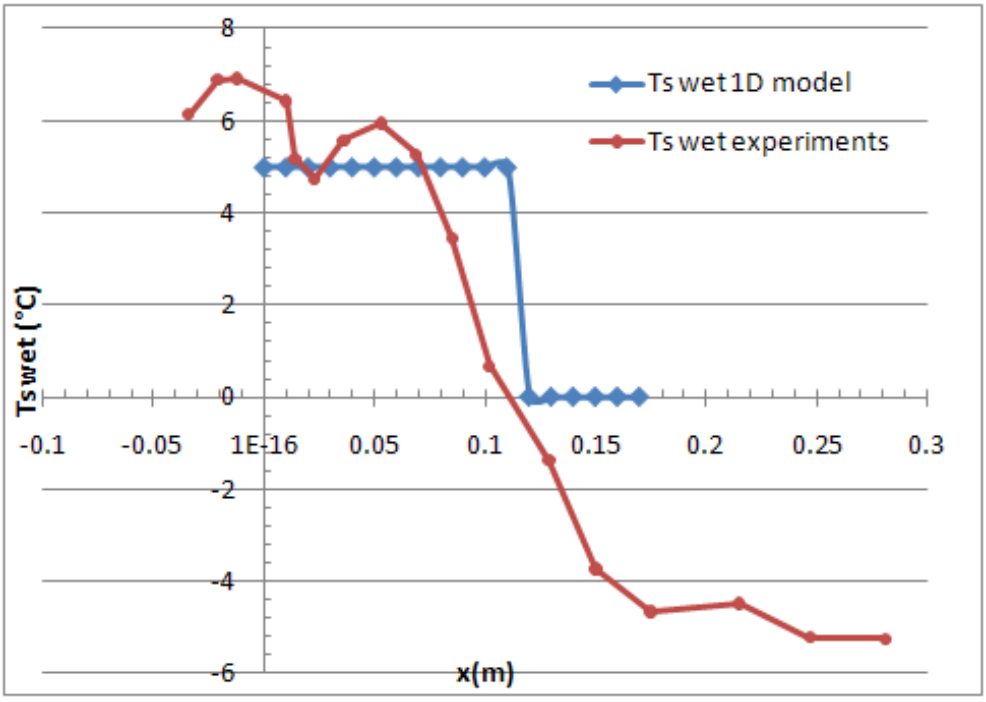

(a) Average surface temperature

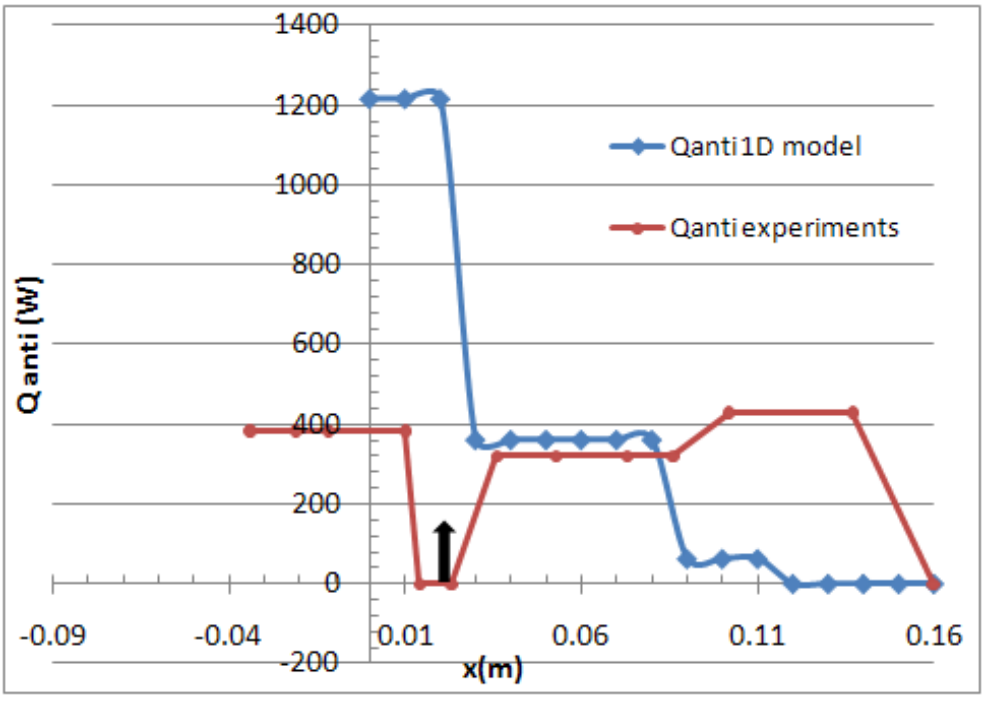

(b) Heat intensity from the anti-icing system

Figure 5.12: *Comparison between the 1D model and the experiments in terms of heat intensity for the anti-icing system for an avarage wet surface temperature of 5° C.*

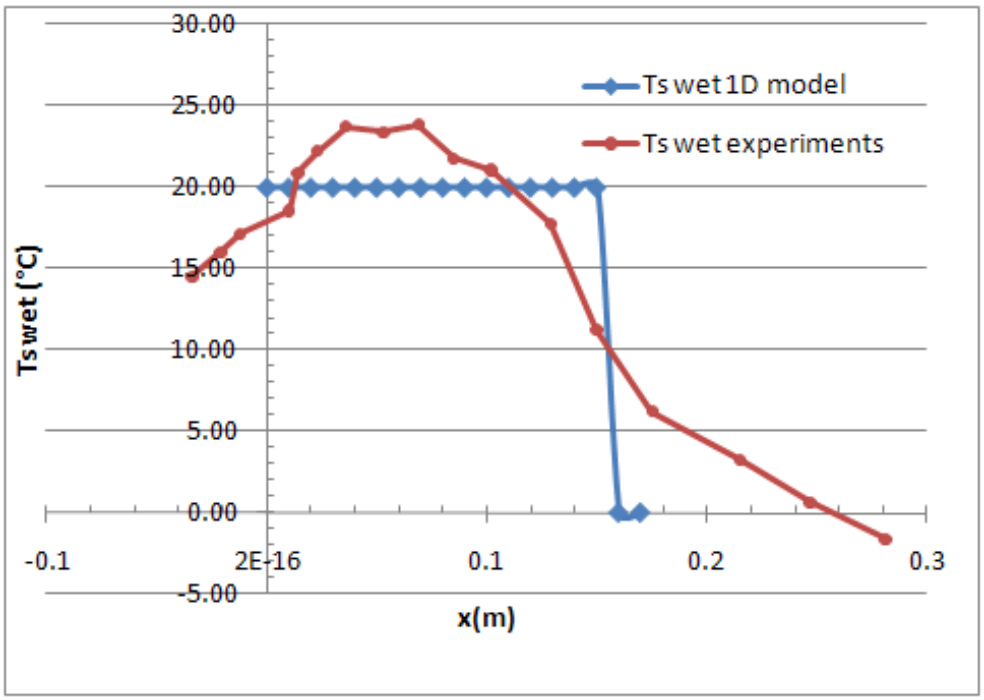

(a) Average surface temperature

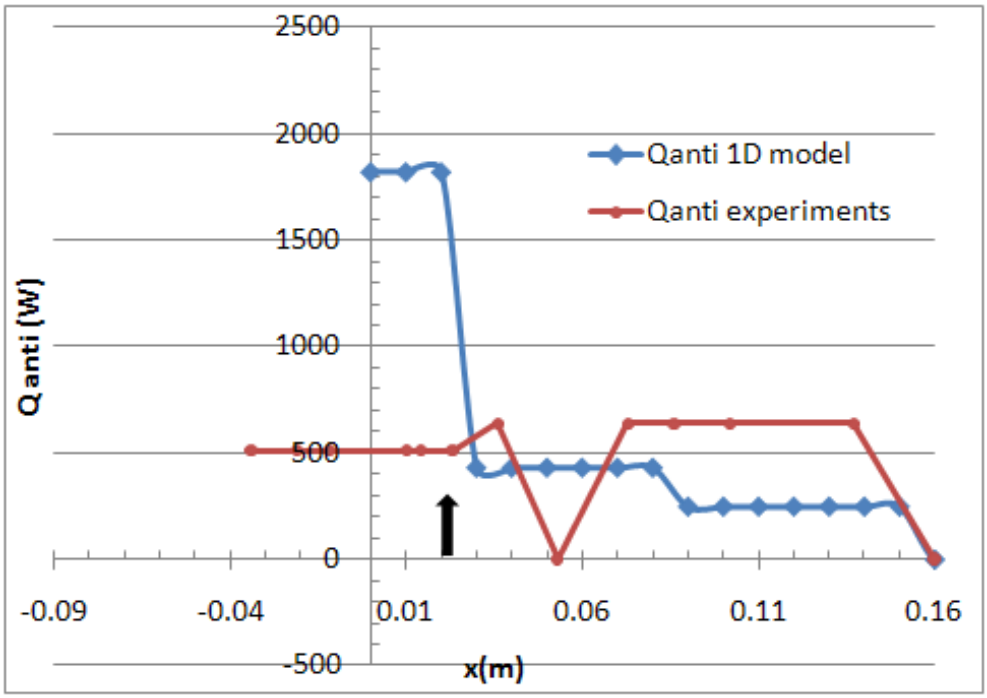

(b) Heat intensity from the anti-icing system

Figure 5.13: *Comparison between the 1D model and the experiments in terms of heat intensity for the anti-icing system for an avarage wet surface temperature of 20° C.*

5.7 Runback ice growth with anti-icing system: results

The list of the run details are presented in Appendix E.

5.7.1 Observation of the ice build-up

Some general observations concerning the ice build-up can be made using the run 2b-3 (Figure 5.14) which is a typical run for continuous maximum icing.

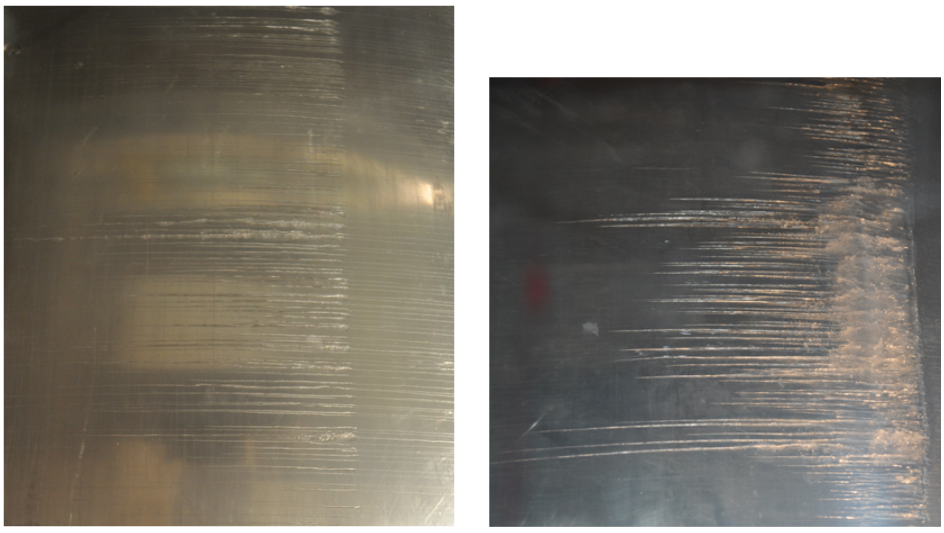

(a) t=30 s (b) t=5 min

(c) t=10 min (d) t=20 min

Figure 5.14: *Ice build-up as function of the time for continuous maximum icing conditions (run 2b-3, LWC=0.42 g.m^{-3}, MVD=17 μm, U_∞=85 m.s^{-1} , T_∞=-9° C)*

During the first seconds of accretion ($\approx$ 2 or 3 s), the rivulets which are running back downstream of the the heated zone freeze. They are quite dense but they don't cover all of the surface. The limit where the rivulets start to freeze can be seen in Figure 5.14 after 30 s of accretion. This limit is moving upstream with time as the surface temperature is cooling down due to the runback water and the runback ice growth. Figure 5.15 represents wet and dry temperature distributions on the airfoil surface for run 2b-3 at different time during the accretion. On Figure 5.15, the red arrow represents the end of the heated zone and the blue arrow represents the position of the front of the ice shape after 20 min accretion.

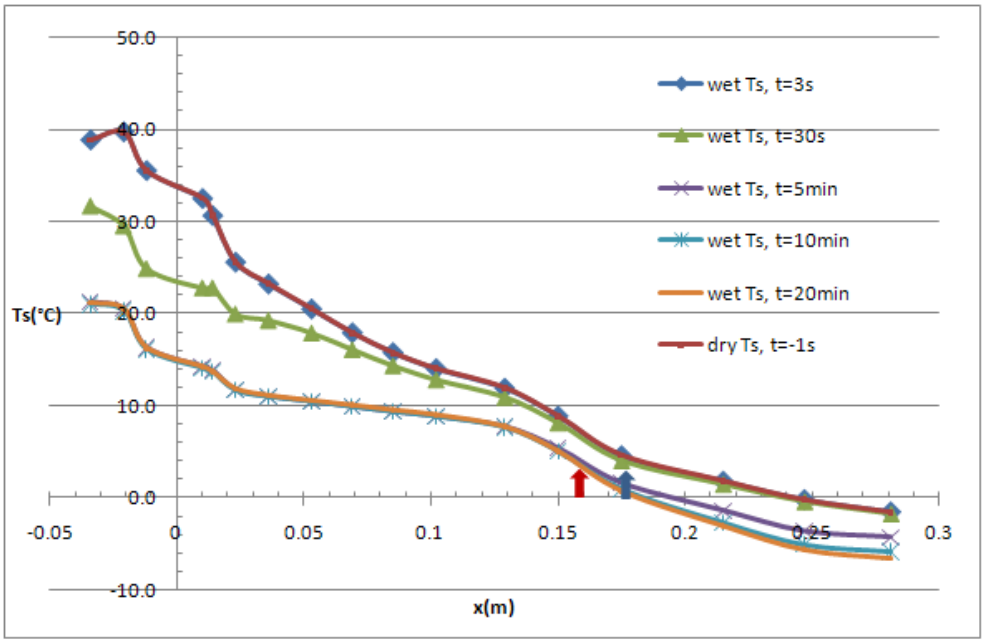

Figure 5.15: *Comparison of wet and dry surface temperatures at different times during the 20 min accretion for run 2b-3*

It is clear from Figure 5.15 that the position of the limit of the zone where the temperature is below 0°C is moving $\approx$ 6 cm upstream during the 20 min of accretion. During the first second of accretion, the part of the airfoil where the water is impinging, has a surface temperature which is droping quickly compared to the zone where the ice is growing. The zone where the ice is growing has a surface temperature which is decreasing until the 10th minute of accretion. After 10 min of accretion, the all leading edge reaches a steady temperature. Hence, it seems that the surface temperature distribution is reaching a steady level after 10 min of accretion.

After ≈1 min, a ridge, starts to form in front of the rivulets, leaving large liquid beads in front of the ridge (Figure 5.16 a)). The ridge has a curved front face (Figure 5.16 b)), it has the pattern of frozen rivulets superimposed and its back looks like sawtooth with spikes (Figure 5.16 c)). The runback water does not freeze entirely as soon as it reaches the ridge. It runs back along the ridge while it freezes partially. It seems that the liquid water rivulets either freeze totally when reaching the end of the ridge or the remaining unfrozen water is going back to the flow. Little by little the ridge increases in size. Frozen rivulets cover almost all of the surface just downstream the ridge. After 1 cm or 2, the rivulets are less dense. As soon as the ridge is forming, there are no more rivulets freezing downstream the ridge. The frozen rivulets which are grown during the first second of accretion, tends to be removed to the surface due to the aerodynamic forces.

The total length of the runback ice shape ridge depends on the amount of water running back (heat input and local liquid water content). The rivulets zone size is between 5 to 10 cm in length. This description of the runback ice shape growth is very close to the description of thermodynamically scaled runback ice on a full scale airfoil, given by Whalen et al. (2005).

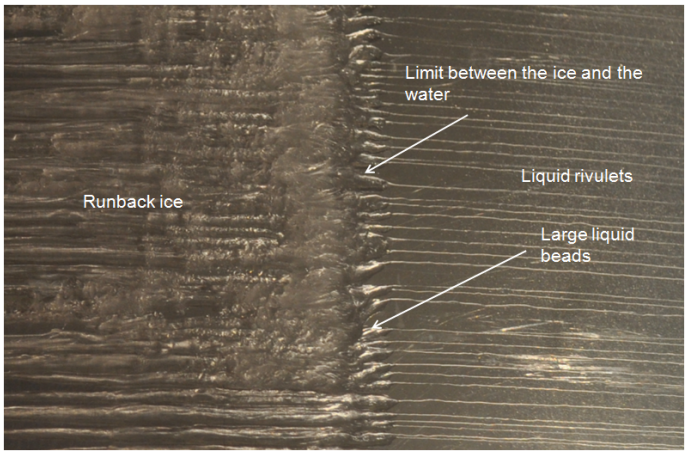

(a) Beads in front

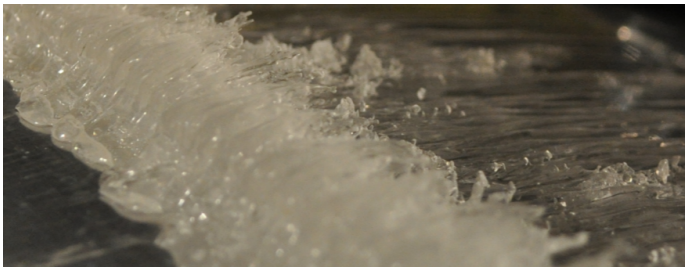

(b) Curved front face

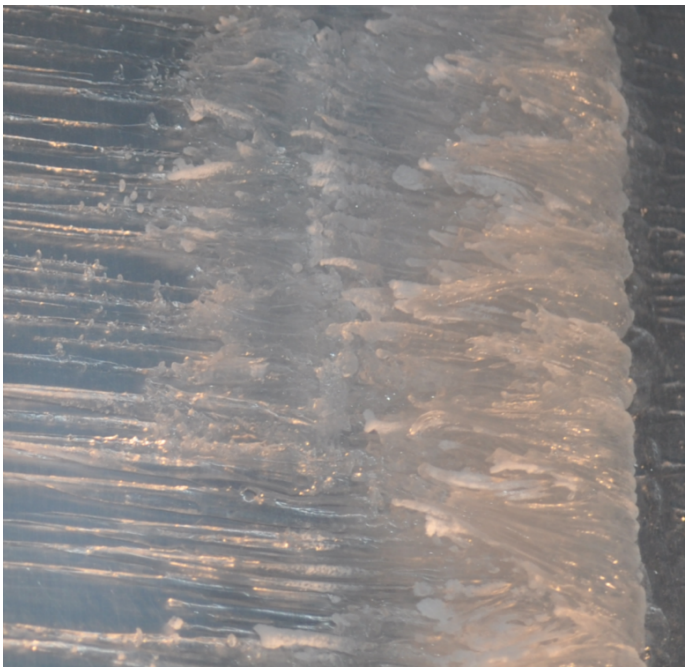

(c) Pattern of stacked rivulets and sawtooth at the back

Figure 5.16: *Close-up views of the ridge*

5.7.2 Influence of the LWC

In order to assess the impact of LWC, run 8-1 and run 10 are compared (case 1) as they all have the same heat input but different LWC. Likewise, run 2a-2 and run 2abis may be compared (case 2). Table 5.5 presents the conditions used for these runs. The heat input configurations are presented in Figure 5.17. Their corresponding temperature distributions are presented in Figure 5.18. The pictures of the runback ice shapes, associated with their 2D ice tracing, and a possible simplistic shape are presented in Figure 5.19 and Figure 5.20 for case 1 and Figure 5.21 and Figure 5.22 for case 2.

	Controlled parameters				
	Runs	Heat inpt config.	Total heat input (kW)	LWC (g/m^3)	Time of accretion (min)
case 1	8-1	H4	1.2	0.45	20
	10	H4	1.2	1.2	10
case 2	2a-2	H1	2.3	0.45	20
	2abis	H1	2.3	1.2	10

Table 5.5: *Characteristic of the runs used for the influence of the LWC on the runback ice*

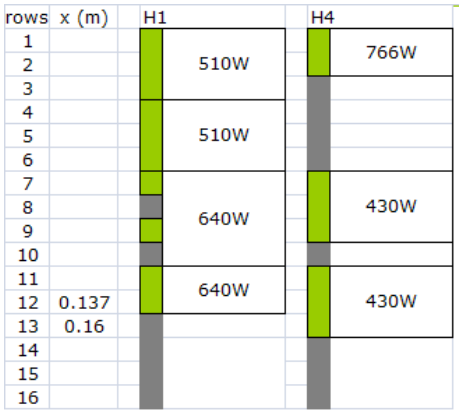

Figure 5.17: *Details of the heat input h1 and h4*

From Figure 5.18 we can see that the discrepancy between the surface temperautre distributions for high and low LWC is increasing until the end of the impingement zone ($\approx$ 0.06 m from the most front point). The discrepancy is maximum close to this position. The surface temperature for the high LWC runs (run 10 and run 2abis) is 3-4 °C lower than the surface temperature for the low LWC, at the end of the impingement zone. After this position the surface temperature distributions for the high and low LWC tend to match until they start to slighlty diverge.

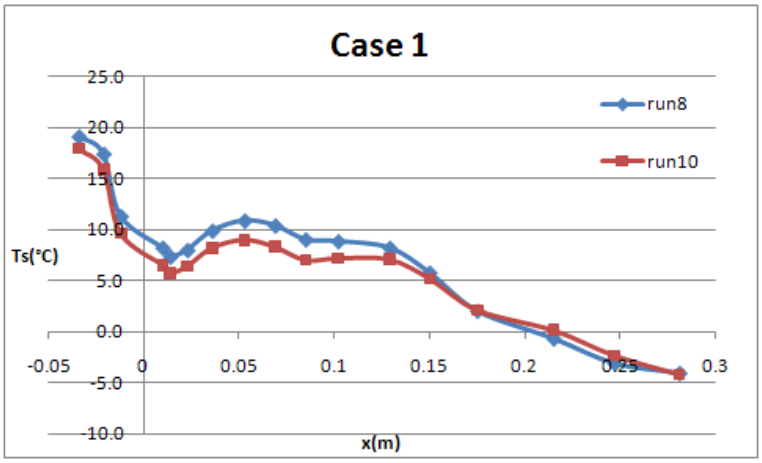

(a) Case 1

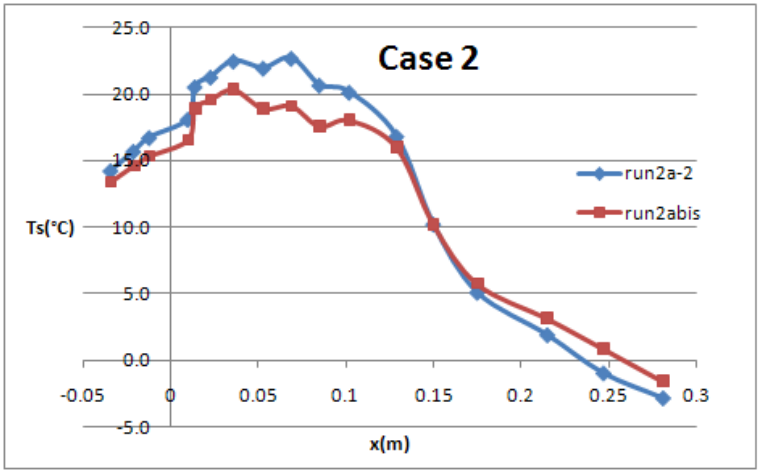

(b) Case 2

Figure 5.18: *Average wet surface temperature distributions*

It is not surprising that the surface temperature is decreased when the LWC is increased. A higher LWC increases the water impinging on the surface (M_{imp}

in Appendix B) and then there is more water running back on the airfoil surface. It makes the water film thicker that makes the surface temperature to cool down.

(a) Runback ice shape picture

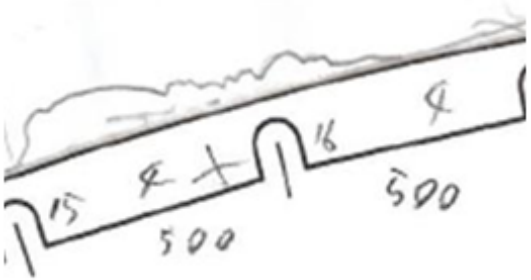

(b) Ice tracing

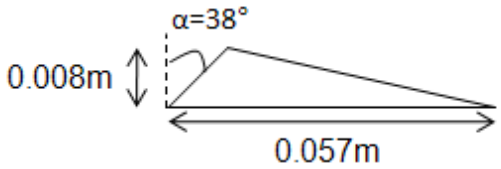

(c) Equivalent simplistic shape

Figure 5.19: *Case 1, run 8-1, H4 (total heat input 1.2 kW, limit of the heated zone x=0.16 m), LWC=0.42 g.m^{-3}, 20 min accretion*

(a) Runback ice shape picture

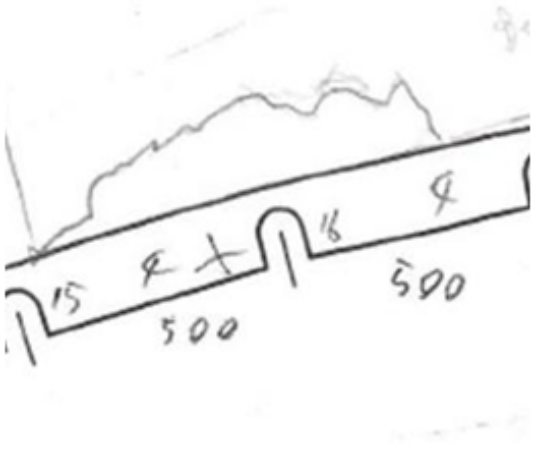

(b) Ice tracing

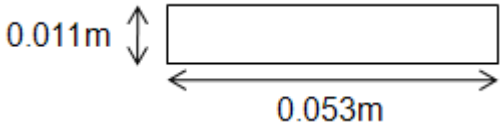

(c) Equivalent simplistic shape

Figure 5.20: *Case 1, run 10, H4 (total heat input 1.2 kW, limit of the heated zone x=0.16 m), LWC=1.2 g.m^{-3}, 10 min accretion*

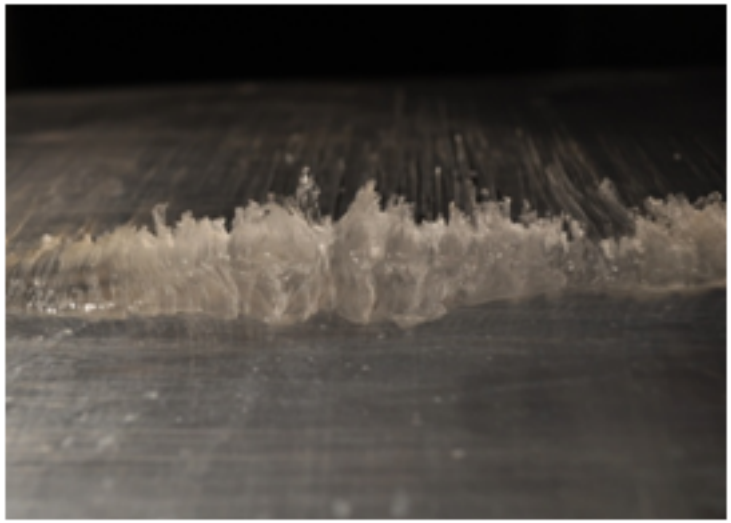

(a) Runback ice shape picture

(b) Ice tracing

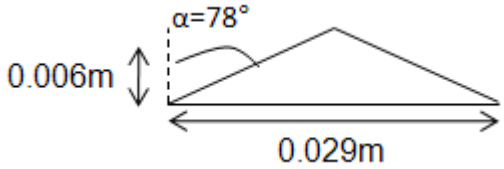

(c) Equivalent simplistic shape

Figure 5.21: *Case 2, run 2a-2, H1 (total heat input 2.3 kW, limit of the heated zone x=0.137 m), LWC=0.42 g.m^{-3}, 20 min accretion*

(a) Runback ice shape picture

(b) Ice tracing

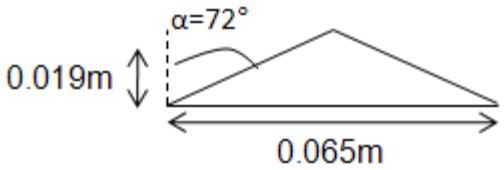

(c) Equivalent simplistic shape

Figure 5.22: *Case 2, run 2abis, H1 (total heat input 2.3 kW, limit of the heated zone x=0.137 m), LWC=1.2 g.m^{-3}, 10 min accretion*

Table 5.6 represents the runs characteristic, together with selected measured parameters. From Table 5.6 the distance D increases in both cases with the LWC but only by a small degree within the expected scatter. The change of α is different between case 1 and 2. It increases with the LWC in case 1 and it decreases with the LWC in case 2. The change in the heat input configuration (total heat input and limit of the heated zone) between case 1 and case 2 might be the reason for this result. The other characteristic dimensions of the ice shapes are presented in Figure 5.23. The trend for the distance in front of the ridge, a, and the ridge thickness, d, is clear for case 1 and case 2: a and d are increased when the LWC is increased. The length of the ridge, b, is more difficult to analyse. b is more than double in case 2 whereas in case 1, b is decreased by 8% when the LWC is increased.

	Controlled parameters					Measured parameters		
	Runs	Heat inpt config.	Total heat input (kW)	LWC (g/m^3)	Time of accretion (min)	D(m)	Average wet Ts(°C)	α(°)
case 1	8-1	H4	1.2	0.45	20	0.03	10.2	38
	10	H4	1.2	1.2	10	0.034	8.7	57
case 2	2a-2	H1	2.3	0.45	20	0.096	20.1	78
	2abis	H1	2.3	1.2	10	0.102	18.5	71

Table 5.6: *Characteristic of the runs used for the influence of the LWC on the runback ice, together with selected results*

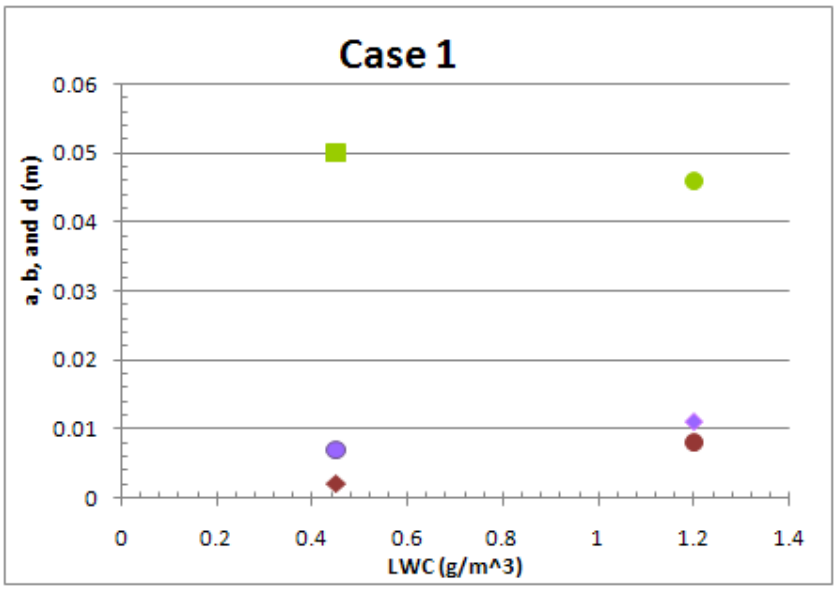

(a) case 1: H4 (total heat input 1.2 kW, limit of the heated zone x=0.16)

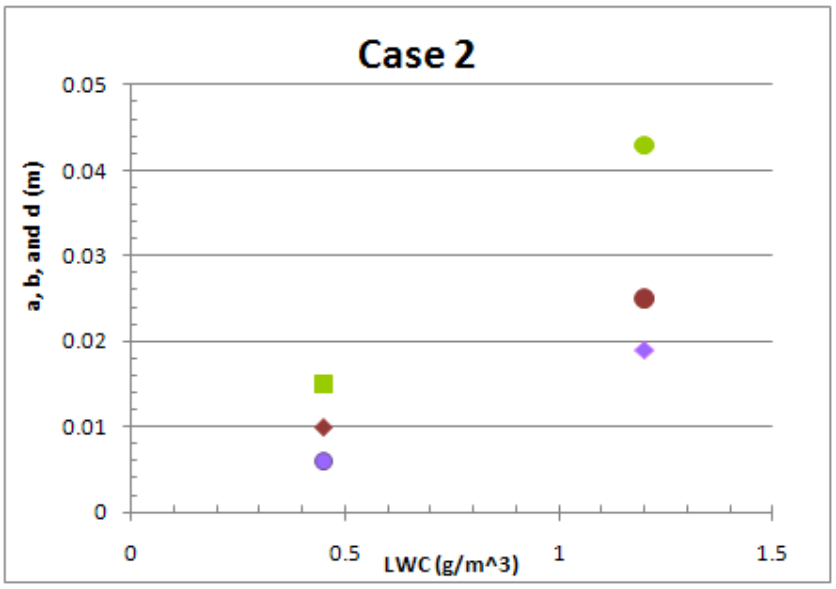

(b) case 2: H1 (total heat input 2.3kW, limit of the heated zone x=0.137 m)

Figure 5.23: *Characteristic dimensions of the ice tracing as function of the LWC (20 min accretion for LWC=0.42 g.m^{-3}and 10 min accretion for LWC=1.2 g.m^{-3}).*

As a reminder a is the distance in front of the ridge (red), b is the length of the ridge (green) and d represents the ridge thickness (purple).

The same trends can be visualized from the ice tracing and the numerous pictures in Figure 5.19 to Figure 5.22. The shapes look larger and thicker for high LWC. With low LWC the ridge is quite smooth with stream like shape on the surface. For the high LWC the ridge is rougher and numerous beads grow just after the ridge in the rivulets zone. We can see a difference in the shapes between case 1 and case 2. Between both cases, the differences come from the total heat input and the length of the heated zone. A difference in the length of the heated zone means that the positon of the shapes on the airfoil is different between the 2 cases. Hence, the heat input configuration has an influence on the shape. This is going to be studied in the next sections.

From these tracings it is possible to simplify the shapes in order to rank them with geometric features. In case 1, the low LWC shape looks like a triangle with its peak on the left hand side of its base (Figure 5.19). The reason for this is that, the maximum peak height is located at the front and then the ice thickness is decreasing gently. The high LWC run looks more like a rectangle with an almost uniform thickness and with steep slop forward and backward (Figure 5.20). For case 2, the ice is forming much downstream than for case 1. For both of the LWC (Figure 5.21 and Figure 5.22), the ice shapes look like isosceles triangles because the highest peak is roughly in the middle of the shape.

In summary, an increase of the LWC from continuous conditions to intermittent conditions produces an increase in the runback ice shape dimensions especially the thickness and its chordwise length. Also its surface is rougher. The surface temperature is decreasing of 2-3 °C when switching from low to high LWC. Some of the tracings are really close to those presented by Broeren et al. (2010c) (Figure 2.15).

5.7.3 Influence of the heat input

In order to assess the impact of the heat input, configurations H2, H3 and H4 are compared (case 3) as they all feature a common limit to the heated area. Likewise, configurations H6 and H7 may be compared (case 4). The details of the studied runs are presented in Table 5.7. The details of the heat input for case 3 and 4 are displayed in Figure 5.24. The average wet surface temperature distributions are displayed in Figure 5.25 for each cases. We can note that the main change in the heat input is made in the impingement zone. The pictures of the ice shapes, associated with their 2D tracing and a possible simplistic shapes are presented in Figure 5.26, Figure 5.27 and Figure 5.28 for case 3 and in Figure 5.29 and Figure 5.30 for case 4.

	Controlled parameters				
	Runs	Heat inpt config.	Total heat input (kW)	LWC (g/m^3)	Time of accretion (min)
case 3	run 2b-2	H2	1.9	0.45	20
	run 8	H4	1.2	0.45	20
	run 5-3	H3	1.13	0.45	20
case 4	run 3-2	H6	1.47	0.45	20
	run 6-2	H7	0.7	0.45	20

Table 5.7: *Characteristic of the runs used for the influence of the heat input on the runback ice*

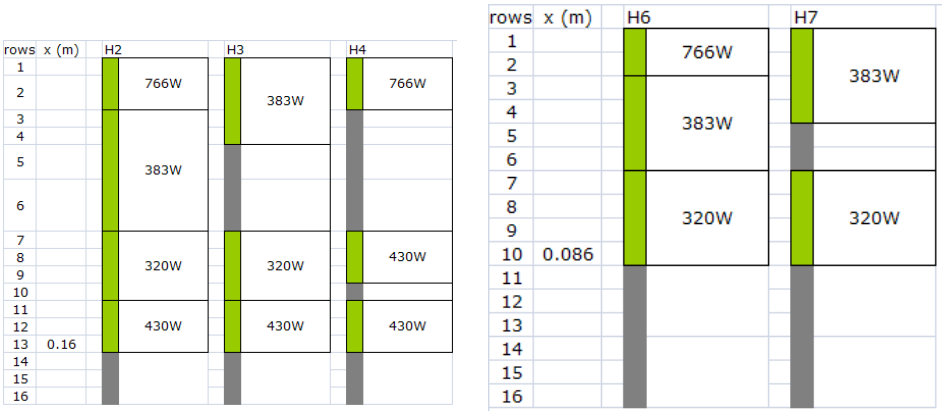

(a) Case 3 (b) Case 4

Figure 5.24: *Details of the heat input for the study of the influence of the heat input in the runback ice*

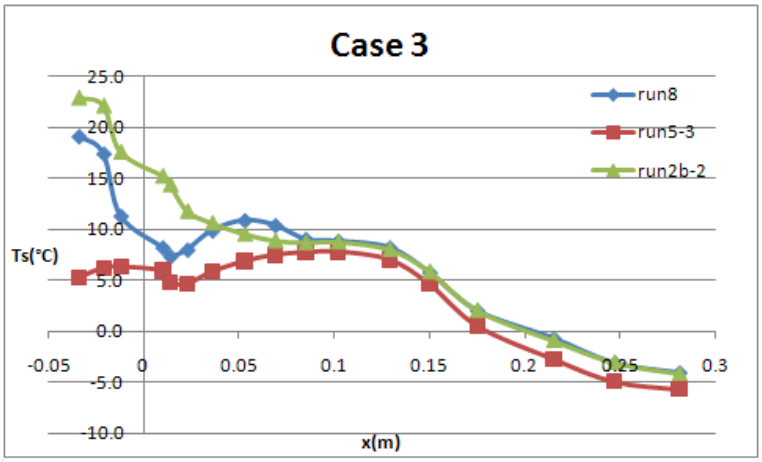

(a) Case 3

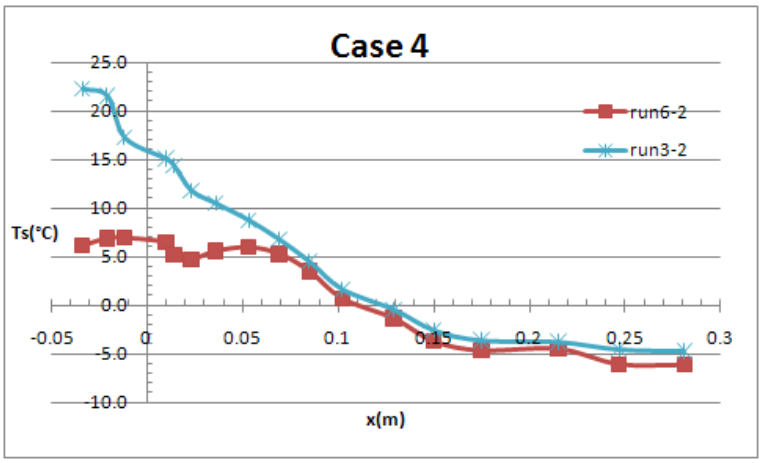

(b) Case 4

Figure 5.25: *Average wet surface temperature distributions*

(a) Runback ice shape picture

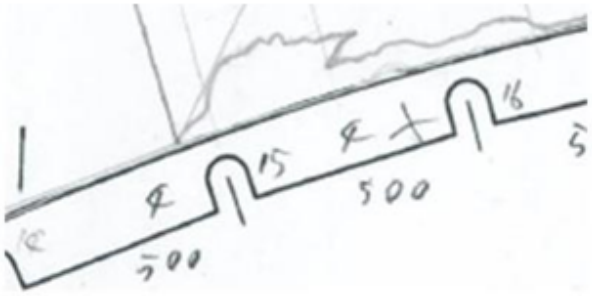

(b) Ice tracing

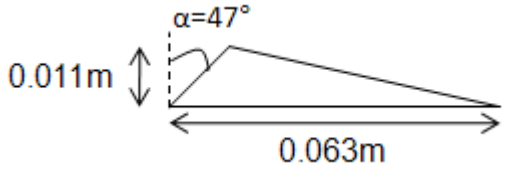

(c) Equivalent simplistic shape

Figure 5.26: *Case 3, run 2b-2, H2 (total heat input 1.9 kW, limit of the heated zone x=0.16 m), LWC=0.42 g.m^{-3}, 20 min accretion*

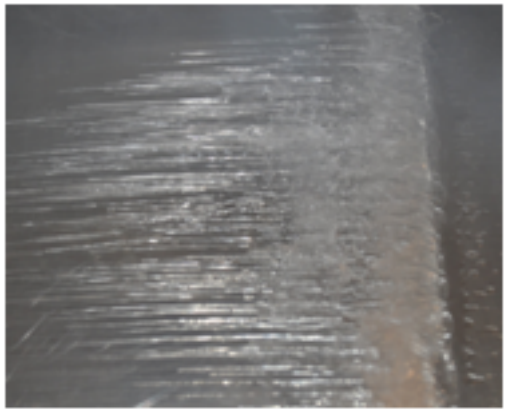

(a) Runback ice shape picture

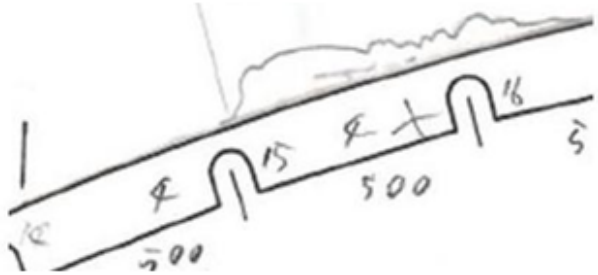

(b) Ice tracing

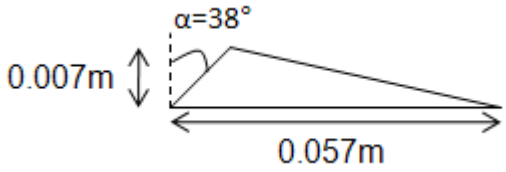

(c) Equivalent simplistic shape

Figure 5.27: *Case 3, run 8-1, H4 (total heat input 1.2 kW, limit of the heated zone x=0.16 m), LWC=0.42 g.m^{-3}, 20 min accretion*

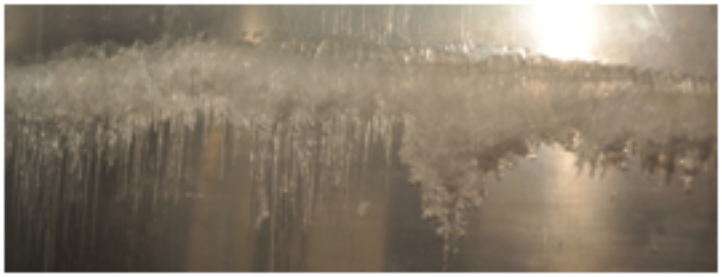

(a) Runback ice shape picture

(b) Ice tracing

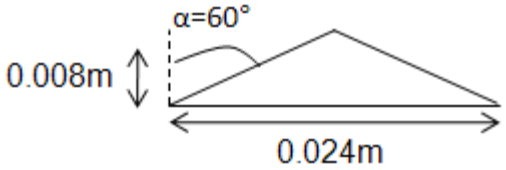

(c) Equivalent simplistic shape

Figure 5.28: *Case 3, run 5-3, H3 (total heat input 1.3 kW, limit of the heated zone x=0.16 m), LWC=0.42 g.m^{-3}, 20 min accretion*

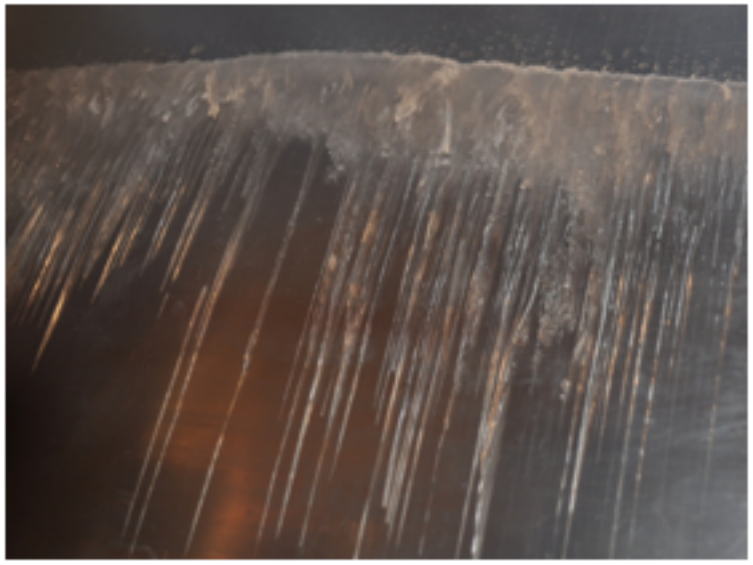

(a) Runback ice shape picture

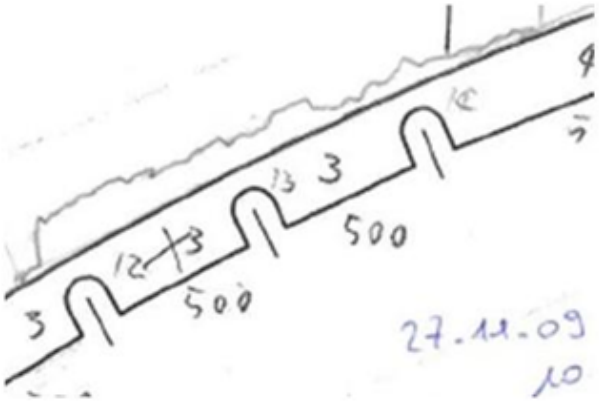

(b) Ice tracing

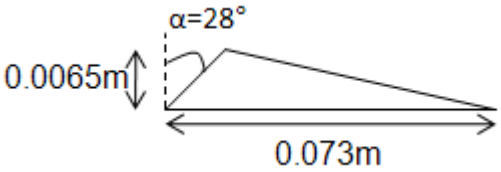

(c) Equivalent simplistic shape

Figure 5.29: *Case 4, run 3-2, H6 (total heat input 1.47 kW, limit of the heated zone x=0.086 m), LWC=0.42 g.m^{-3}, 20 min accretion*

(a) Runback ice shape picture

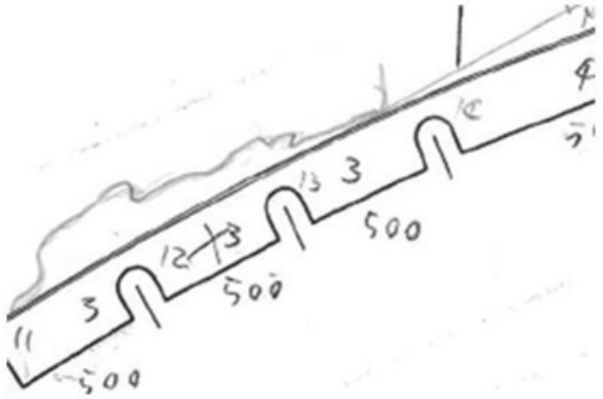

(b) Ice tracing

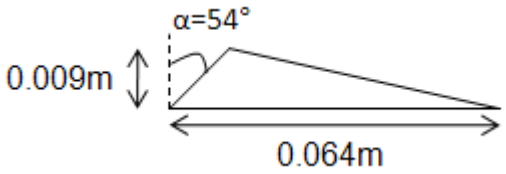

(c) Equivalent simplistic shape

Figure 5.30: *Case 4, run 6-2, H7 (total heat input 0.7 kW, limit of the heated zone x=0.086 m), LWC=0.42 g.m^{-3}, 20 min accretion*

The details of the studied runs are presented in Table 5.8, together with selected measured parameters.

	Controlled parameters					Measured parameters		
	Runs	Heat inpt config.	Total heat input (kW)	LWC (g/m^3)	Time of accretion (min)	D (m)	Average wet Ts(°C)	α(°)
case 3	run 2b-2	H2	1.9	0.45	20	0.028	12.1	47
	run 8	H4	1.2	0.45	20	0.03	10.2	38
	run 5-3	H3	1.13	0.45	20	0.015	6.4	60
case 4	run 3-2	H6	1.47	0.45	20	0.02	12.9	28
	run 6-2	H7	0.7	0.45	20	0.006	5.7	54

Table 5.8: *Characteristic of the runs used for the influence of the heat input on the runback ice*

As the evaporation is decreased when the heat input is decreased, it was expected to get larger ice shapes for run 8 and run 5-13 than for run 2b-2. Likewise it was expected that the shape of run 6-2 would be larger than the shape of run 3-2. From the ice shapes pictures of Figure 5.28, Figure 5.27 and Figure 5.26 we can see that the runback ice shapes of run 5-3 and run 8 are larger than for run 2b-2. This trend is not obvious when looking at the tracings. Run 5-3 and run 8 have shorter length and shorter thickness than run 2b-2 in regards to the tracings. From the pictures of Figure 5.29 and Figure 5.30, it seems that the shape of run 6-2 is bigger than the one of run 3-2. In case 4, the tracings of the shapes show that the ice shape of run 6-2 has a larger thickness than the one of run 3-2.

When looking at α and at the distance between the end of the heating system and the position of the shape, D, in Table 5.8, two trends appear. D is increased with the total heat input whereas α is decreased when the total heat input is increased. In case 3, when comparing run 2b-2 and 5-3 which found that the heat input increased by 68% which leads to an increase of 86% of D. In case 4, the heat input of run 3-2 is roughly 2 times the heat input of run 6-2 which leads to an increase of D of roughly 3 times is value for run 6-2. More trends appear when looking at Figure 5.31. The influence of the heat input on a and d are difficult to evaluate. This is not surprising as case 3 and 4 have very different limit of the heated zone. Hence the relationships between the total heat input and ice shapes size might be different if the limit of the heated zone play an important role in the ice shape features. For case 3, where the limit of the heated zone is the furthest downstream, the increase in the heat input does not affect a and d much. The trend for a is to decrease when the heat input is increased and d is slightly increased with respect to the heat input. For case 4, where the limit of the heated zone is the closest to the stagnation zone a and b are more influenced by the change of the heat

input: a is increased with the heat input while b is decreased with the heat input.

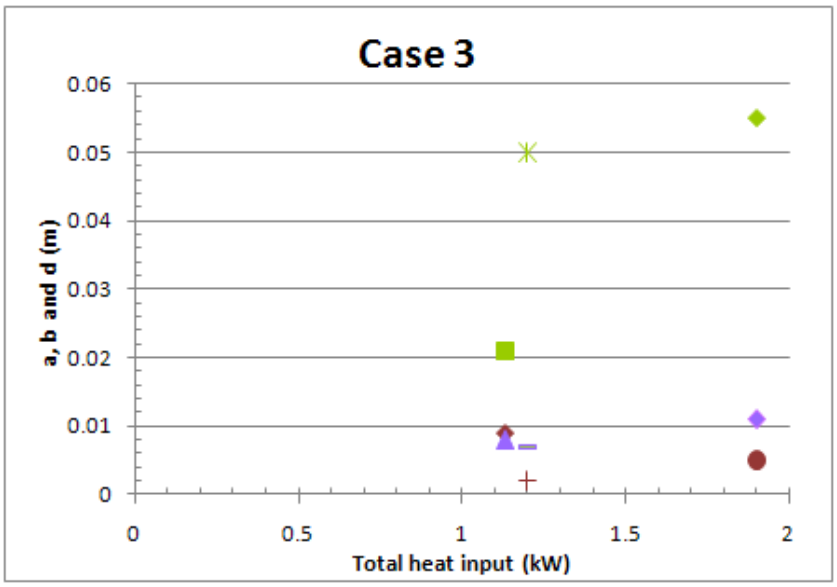

(a) Case 3: limit of the heated zone x=0.16 m

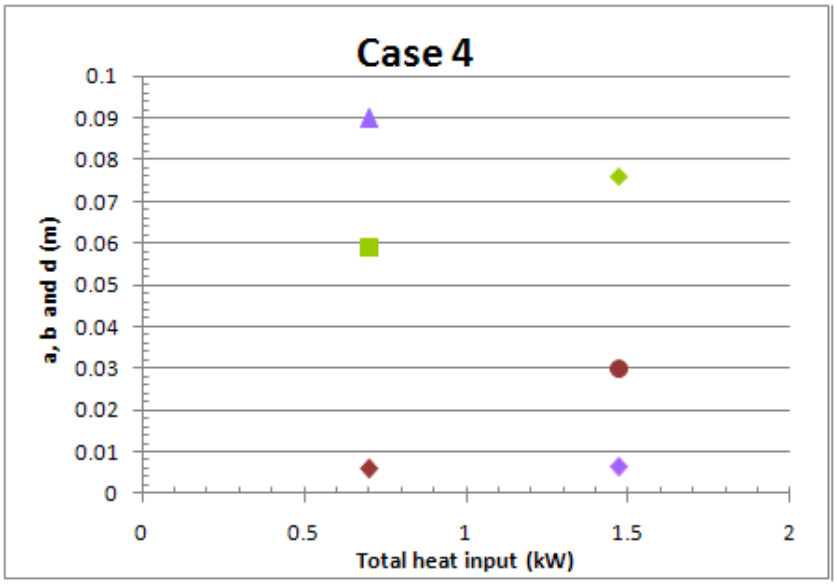

(b) Case 4: limit of the heated zone x=0.086 m

Figure 5.31: *Characteristic dimensions of the runback shapes as function of the total heat input, LWC=0.42 g.m^{-3}, 20 min accretion.*

As a reminder a is the distance in front of the ridge (red), b is the length of

the ridge (green) and d represents the ridge thickness (purple).

Simplistic shapes are associated with the 2D tracings (Figure 5.26 to Figure 5.30). These simplistic shapes are mainly triangles with the peak in front except for run 5-3 (Figure 5.28) which simplistic shapes is an isoceles triangle. The triangle with the peak in front are associated with a shape with a strong slope in front and a thickness which is decreasing gently, giving a smooth slope at the back. Run 5-3 has its maximum peak in the middle, which reminds of an isoceles triangle.

Particular attention is required for the runs with short heating zones and low heat inputs (case 4 run 6 for instance (Table 5.7)). For these runs, very large features pointing into the flow appear at low heat input at some positions along the span (Figure 5.32). These features join up to form a nearly continuous ridge when the LWC is increased (Figure 5.33). These horns are very sensitive to the icing conditions. For two runs with the same conditions (run 6-2 and run 6-3) the horn shape is changed (Figure 5.32 and Figure 5.33). It can be a large horn in the middle (Figure 5.32 b)) or several smaller horns (Figure 5.32 a)). In the case of high LWC (Figure 5.33), several horns are growing and after a while they are joining each other forming a massive obstacle for the flow all along the span. The growth rate of the horn is very fast. In a couple of minutes a horn can be several cm large. These features haven't been observed for the most downstream position (case 3, x=0.16 m) and/or for heat input which maintains the average wetted surface temperature above 10°C. It is likely that this phenomenon is triggered by a combination of two factors: the closeness of the ice to the stagnation zone and lower levels of evaporation (H7 and H8 in Table 5.2). The closeness to the stagnation point eases the development of a secondary impingement region. When a certain thickness is reached for the ice shape, droplet trajectories which do not normally impinge the clean model may impinge the ice shape. Lower level evaporation due to lower heat input thickens the water film on the surface. Then, the break-up of the droplets into the film may trigger splashing which may increase the secondary impingement. The full scale runback ice shape studied by Bragg et al. (2007) an a NACA 2312 (c=1.8 m) has similar horns feature (Figure 2.14). It is located close to the stagnation point (x/c=4%). No indication concerning the amount of heat input is available.

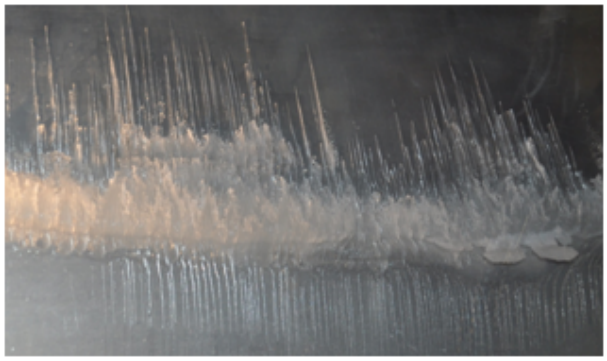

(a) Run 6-2

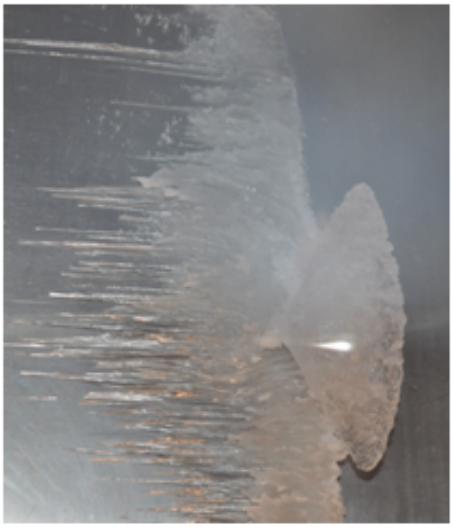

(b) Run 6-3

Figure 5.32: *H7 (total heat input 1.13 kW, limit of the heated zone x=0.086 m, wet T_S=5.70° C), LWC=0.42 g.m^{-3}, 20 min accretion.*

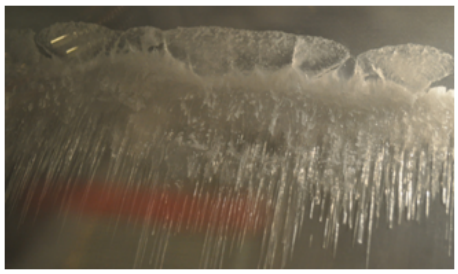

Figure 5.33: *run 9, H8 (total heat input 1.13 kW, limit of the heated zone x=0.073 m, wet T_S=8.70° C), LWC=1.2 g.m^{-3}, 10 min accretion.*

5.7.4 Influence of the limit of the heated zone

The comparison in this section has been done with a LWC of 0.42 $g.m^{-3}$for similar heating system configuration but with different spatial limits to the heated surface. The details of the studied runs are presented in Table 5.9. The heat input details are shown graphically in Figure 5.34. The surface temperature distributions are presented in Figure 5.35. The pictures of the ice shapes, associated with their 2D tracing and a possible simplistic shape are presented in Figure 5.36 and in Figure 5.37 for case 5 and in Figure 5.38 and in Figure 5.39 for case 6.

	Controlled parameters					
	Runs	Heat inpt config.	Total heat input (kW)	Limit of the heated zone (m)	LWC (g/m^3)	Time of accretion (min)
case 5	run 2a-2	H1	2.3	0.137	0.45	20
	run 1b-2	H5	1.66	0.073	0.45	20
case 6	run 5-3	H3	1.13	0.16	0.45	20
	run 6-2	H7	0.7	0.086	0.45	20

Table 5.9: *Characteristic of the runs used for the influence of the limit of the heated zone on the runback ice*

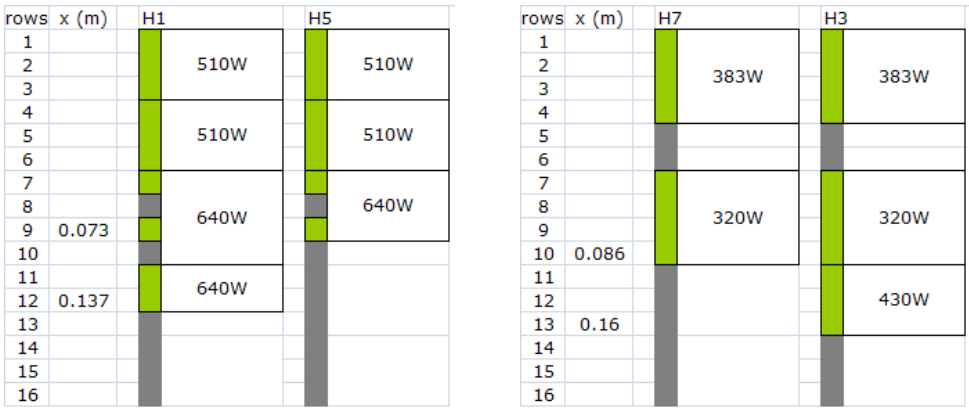

(a) Case 5 (b) Case 6

Figure 5.34: *Details of the heat input for the study of the influence of the limit of the heated zone in the runback ice*

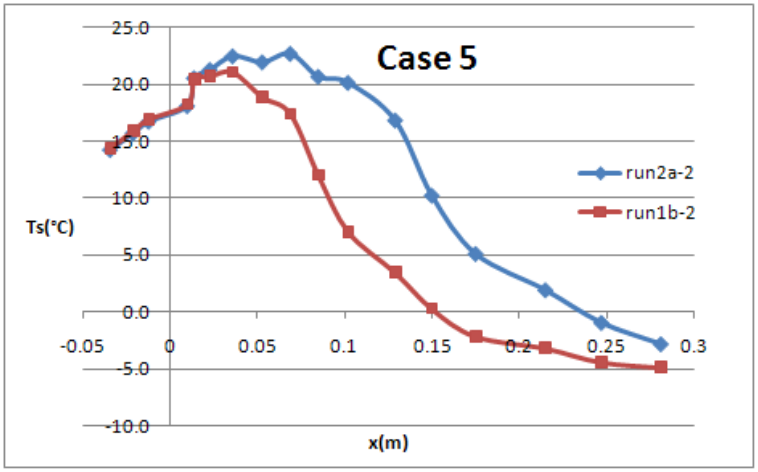

(a) Case 5

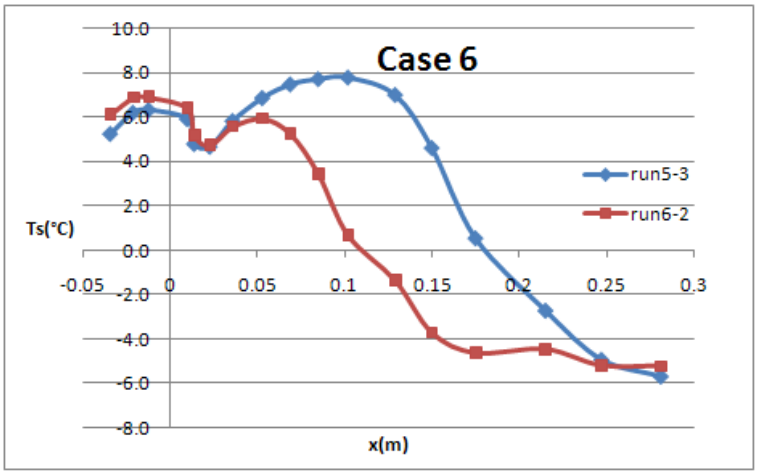

(b) Case 6

Figure 5.35: *Average wet surface temperature distributions*

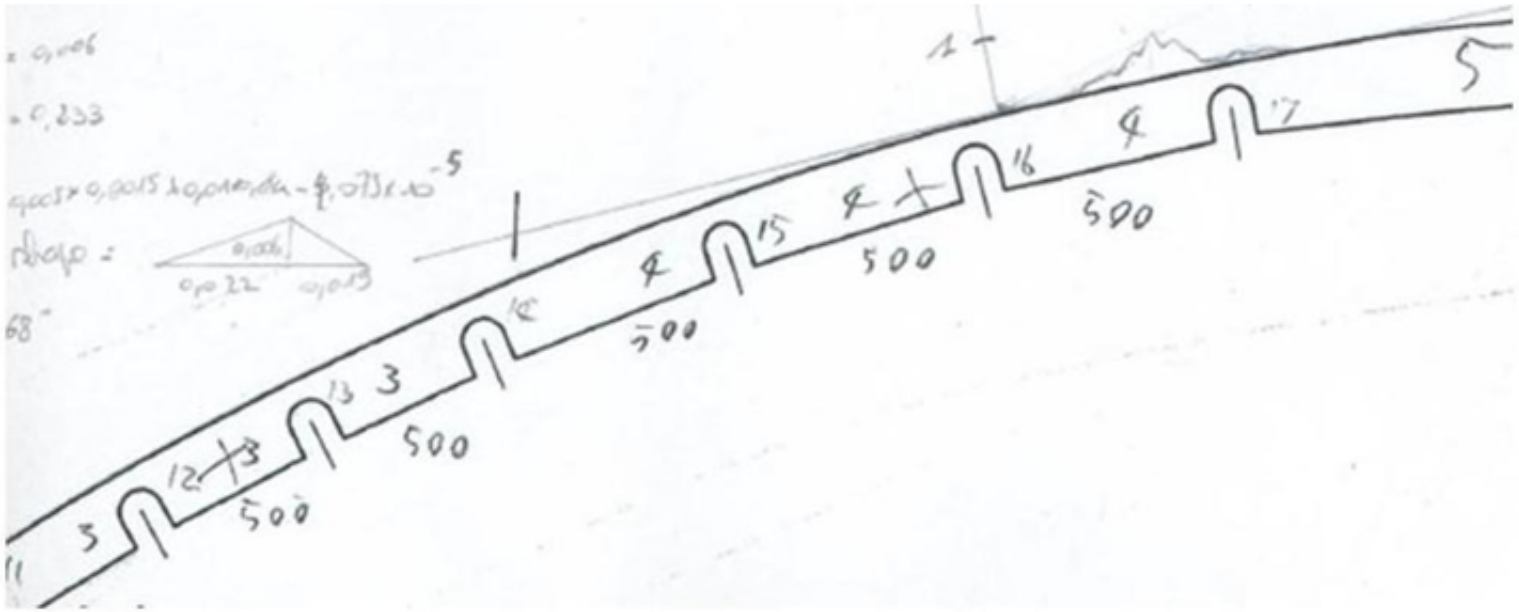

(a) Tracing

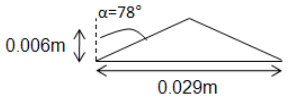

(b) Simplistic shape

Figure 5.36: *Case 5, run 2a-2, LWC=0.42 g.m^{-3}, H1 (limit of the heated zone x=0.137 m, total heat input 2.3 kw), 20 min accretion*

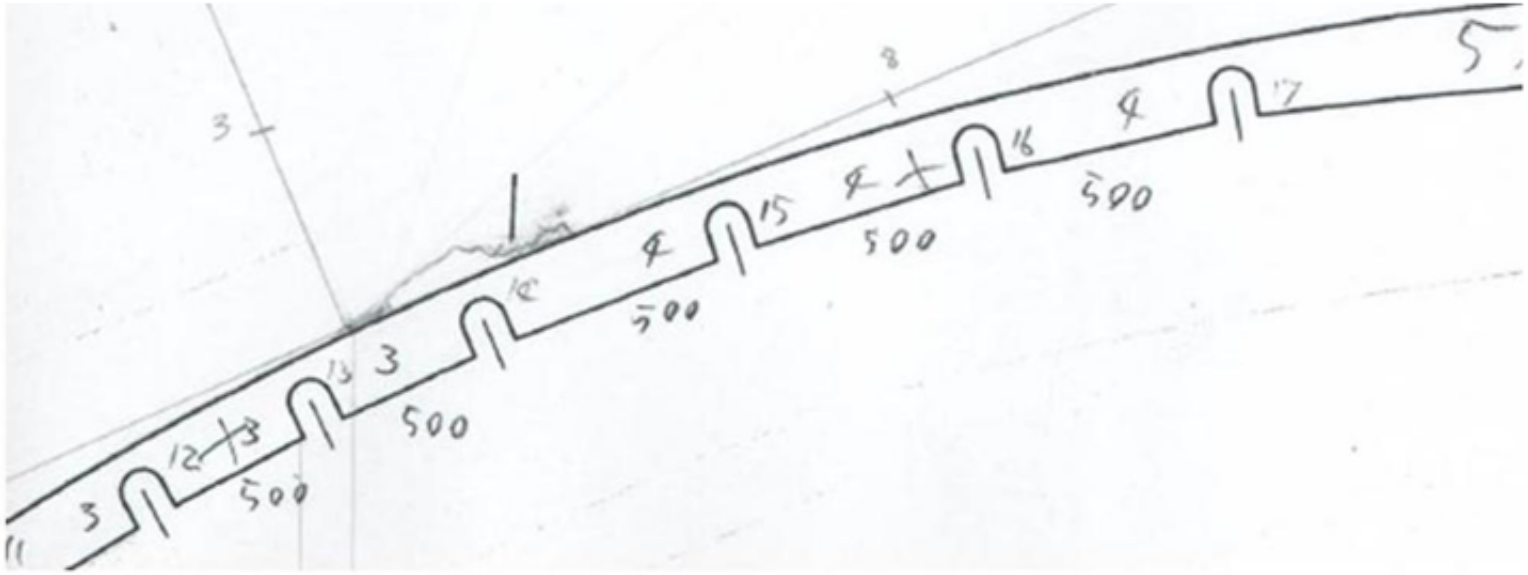

(a) Tracing

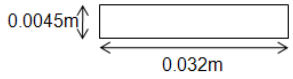

(b) Simplistic shape

Figure 5.37: *Case 5, run 1b-2, LWC=0.42 g.m^{-3}, H5 (limit of the heated zone x=0.073 m, total heat input 1.6 kw), 20 min accretion*

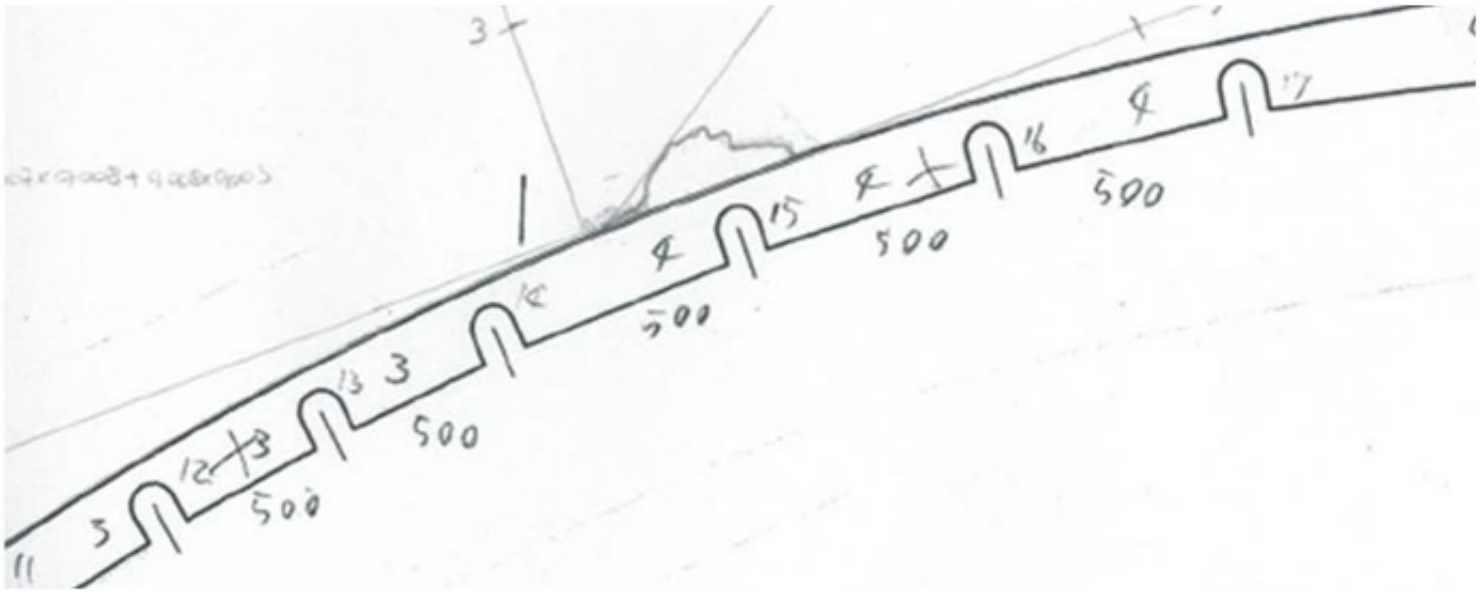

(a) Tracing

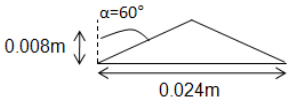

(b) Simplistic shape

Figure 5.38: *Case 6, run 5-3, LWC=0.42 g.m^{-3}, H3 (limit of the heated zone x=0.16 m, total heat input 1.13 kw), 20 min accretion*

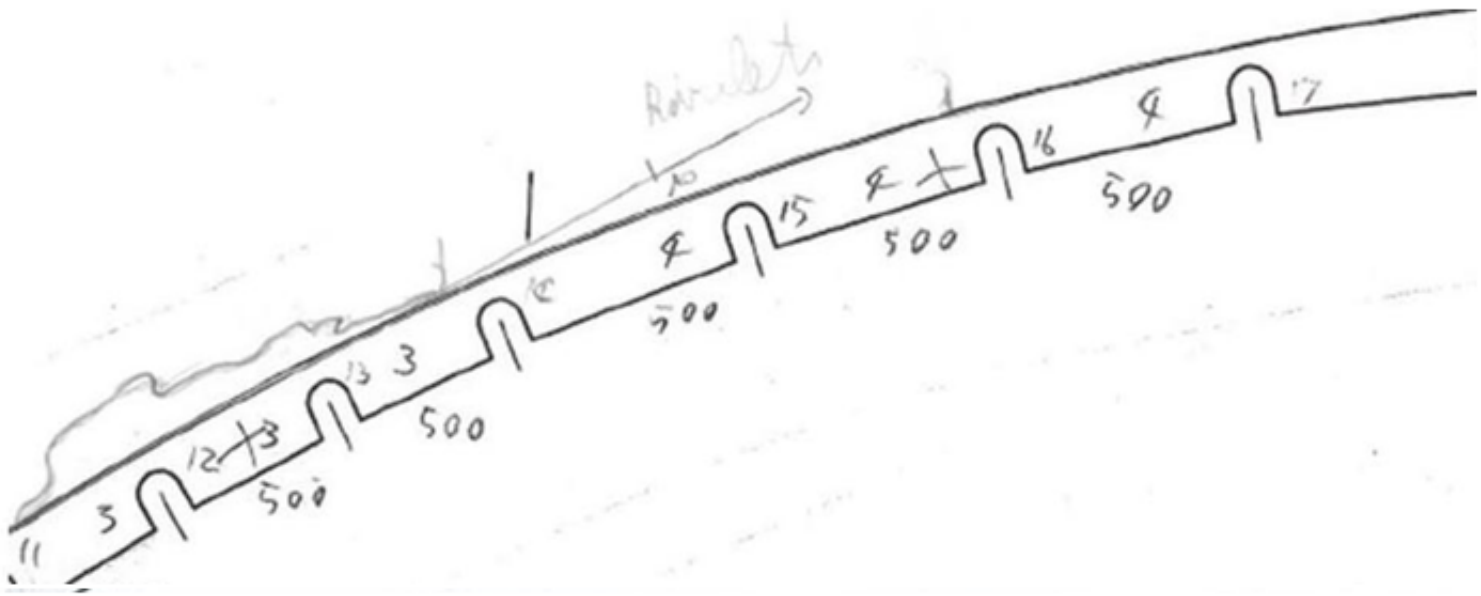

(a) Tracing

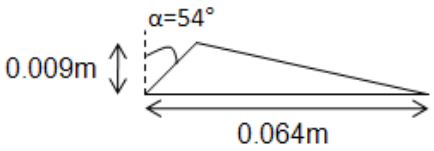

(b) Simplistic shape

Figure 5.39: *Case 6, run 6-2, LWC=0.42 g.m^{-3}, H7 (limit of the heated zone x=0.086 m, total heat input 0.7 kw), 20 min accretion*

From the tracings in Figure 5.36 and Figure 5.37 for case 5 and in Figure 5.38 and Figure 5.39 for case 6, the shift in the ice shape position in the chordwise position when the heated zone is changed, is well illustrated. From the pictures in Figure 5.36 to Figure 5.39, it seems that the ice shapes which are growing at an upstream position (run 1b-2 and run 6-2), result in larger ice shapes. This is quite logical as the input in run 1b-2 and run 6-2 is smaller than for run 2a-2 and run 5-3 respectively. As mentioned in the previous section (5.7.3), the combination of a lower heat input and a more foreward cut off of the heating allows for the develoment of horns in front. This is the reason why, a couple of horns appears on the right side of the accretion of run 6-2 (Figure 5.40) whereas no horns were grown for run 1b-2. The horns of run 6-2 doesn't appear on the tracing (Figure 5.39) as they were located at a different position spanwise.

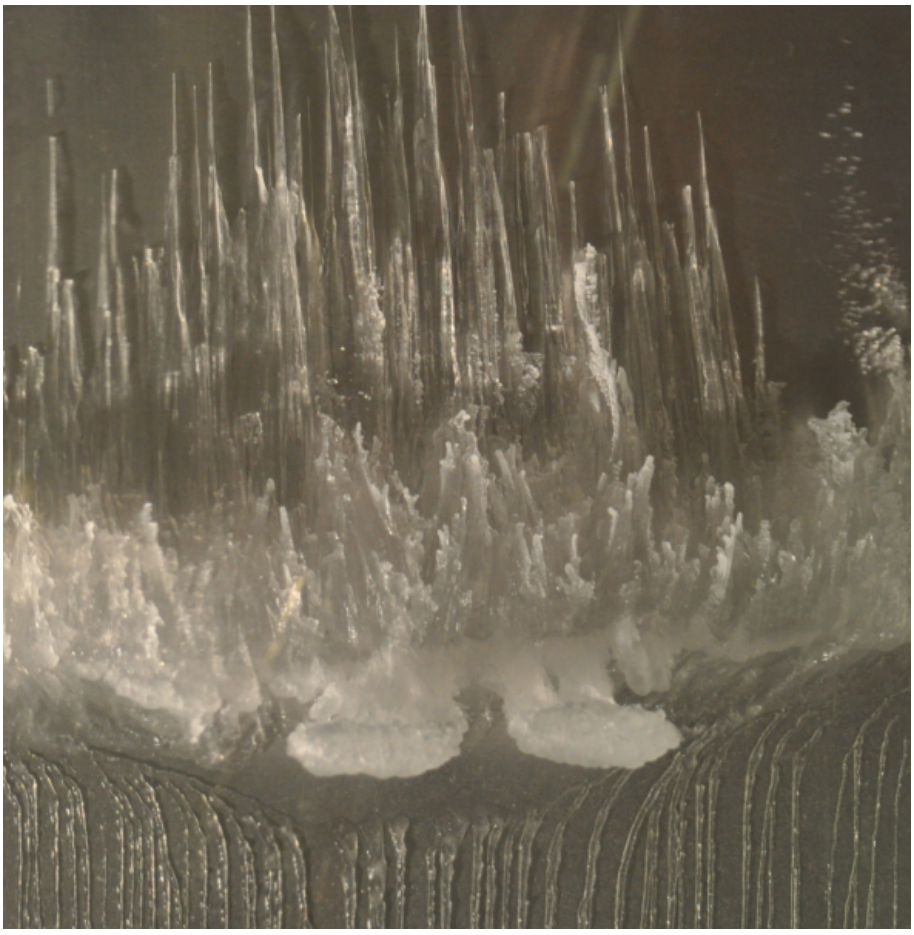

Figure 5.40: *Top view of the horns on the right hand side of the ridge of run 6-2*

The details of the studied runs are presented in Table 5.10, together with selected results.

	Controlled parameters						Measured parameters		
	Runs	Heat inpt config.	Total heat input (kW)	Limit of the heated zone (m)	LWC (g/m^3)	Time of accretion (min)	D(m)	Average wet Ts(°C)	α(°)
case 5	run 2a-2	H1	2.3	0.137	0.45	20	0.096	20.1	78
	run 1b-2	H5	1.66	0.073	0.45	20	0.071	15.7	46
case 6	run 5-3	H3	1.13	0.16	0.45	20	0.015	6.4	60
	run 6-2	H7	0.7	0.086	0.45	20	0.006	5.7	54

Table 5.10: *Characteristic of the runs used for the influence of the limit of the heated zone on the runback ice*

Table 5.9 summarises the limits of the heated zone. The zone is moved from 0.137 to 0.073 m in case 5 and from 0.16 to 0.086 m in case 6. The limit between the end of the heated zone and the ice shape, D, is increased with respect to the limit of the heated zone. It is likely that the increase in the heat input when the heated zone is longer, played a role in that increase. The angle α is increased when the limit of the heated zone is moved downstream. This increase may be linked with an increase of the speed chordwise up to the suction peak. In case 5 the ice shape is growing further downstream than in case 6 mainly because of a larger heat input. Though, α is larger in case 5 when the ice is forming downstream the most forward position. The other characteristic dimensions of the ice shapes as function of the limit of the heated zone are presented in Figure 5.41 for case 5 and case 6. The length of ice in front of the ridge is increased when the limit of the heating system is moved downstream. This increase is of 66% and 50% for case 5 and case 6 respectively. The reason could be the increase of the speed in the vicinity of the airfoil up to the suction peak. The length of the ridge, b, is decreased in both cases when the limit of the heat input is increased. The height of the ridge, d, is increased with respect to the limit of the heated zone in case 5 whereas in case 6 the change of limit of the heated zone does not influence much d.

To sum-up, the limit of the heated zone has an influence on the shape of the runback ice. It seems that when the shape is moved further downstream of the stagnation zone, the highest peak is moved backward. Thus the ice shapes tracings look more isoceles triangle (Figure 5.36 and Figure 5.38).

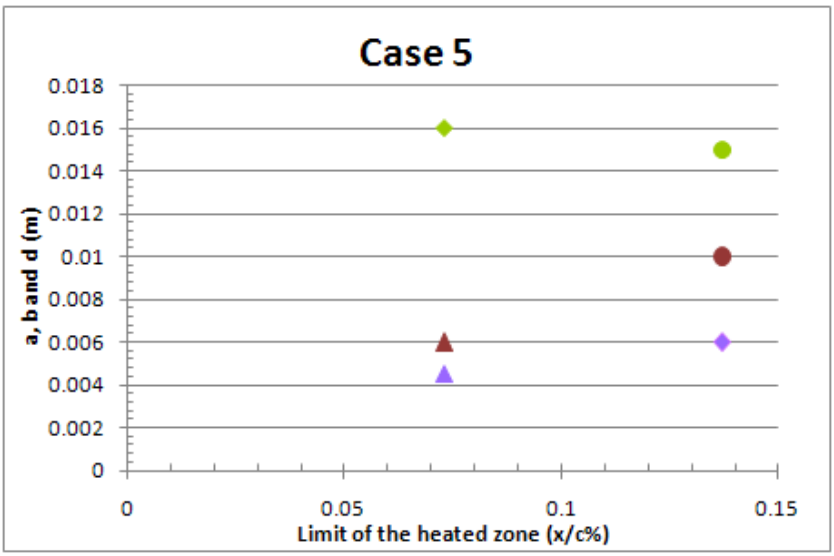

(a) Case 5

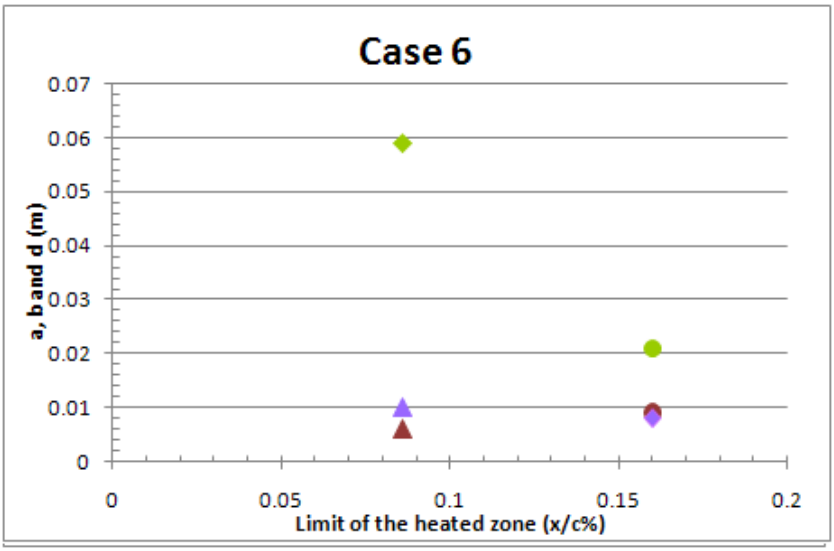

(b) Case 6

Figure 5.41: *Characteristic dimensions of the runback shapes as function of the limit of the heated zone, LWC=0.42 g.m^{-3}, 20 min accretion.*

As a reminder a is the distance in front of the ridge (red), b is the length of the ridge (green) and d represents the ridge thickness (purple).

5.7.5 Capture of full-scale runback ice shapes

After studying the influence of the LWC, heat input and the limit of the heated zone on the runback ice growth using an anti-icing system, some typical runs were re-run, moulded and cast. The list of the runs used for the moulding and the casting are presented in Table 5.11.

Date	Runs	Heating system config	Limit of the heated zone (m)	LWC (g/m^3)	Time of run (min)	Ttotal in the tunel (°C)	Upper limit of the runback ice (x/c)	Average wet heated Ts (°C)	Dry heated Ts (°C)
12/01/2010	run8-2	H4	0.16	0.45	20	-5	NA	10	18
11/01/2010	run2b-3	H2	0.16	0.45	20	-5	NA	12.8	23.2
20/11/2009	run5-2	H3	0.16	0.45	20	-5	NA	7.1	11.8
04/03/2010	run 5-4	H3	0.16	0.45	10	-5	NA	6.6	13.1
03/03/210	run6-8	H7	0.086	0.45	10	-5	NA	3.3	8.4
05/03/2010	run 1b-3	H4	0.073	0.45	12	-5	NA	17.5	32.1
08/03/2010	run 7-3	H3	0.16	1.2	5	-5	NA	5.6	12
09/03/2010	run 2a-3	H1	0.137	0.45	15	-5	NA	19.9	34.9
16/03/2010	run11-2	H9	0.16	0.45	11	-5	NA	17.8	29

Table 5.11: *Details of the runs used to do runback ice moulding using an anti-icing systems*

In order to scale the activity to the availabilities of the wind tunnel, three casts were selected from this group (purple highlighted in Table 5.11):

- Run 2b-3: Thick casts typical of continuous maximum conditions ($\approx$ 1cm thick and $\approx$ 5 cm long)
- Run 11-2: Thin casts typical of continuous maximum conditions ($\approx$ 4mm thick and $\approx$ 6.5 cm long)
- Run 7-3: Thin casts typical of intermittent maximum conditions ($\approx$ 5mm thick and $\approx$ 8.5 cm long). As this shape correspond to a high LWC, the height spanwise variation is bigger than for lower LWC.

It is important to note that even though run 2b-3 was grown in the same nominal conditions as run 2b-2 (Table 5.7 and Table 5.8), both runs can be slightly different and so can the shapes. The pictures of the cast for run 2b-3, run 11-2 and run 7-3 are presented in Figure 5.42, Figure 5.43 and Figure 5.44 respiectively. The differences between continuous and intermittent conditions are clear to see and match the tracings. Firstly for low LWC, the shape is shorter than for the high LWC run. For high LWC, the ridge and the rivulets zone are longer. Secondly, the ice shape from intermittent conditions is rougher than for continuous conditions.

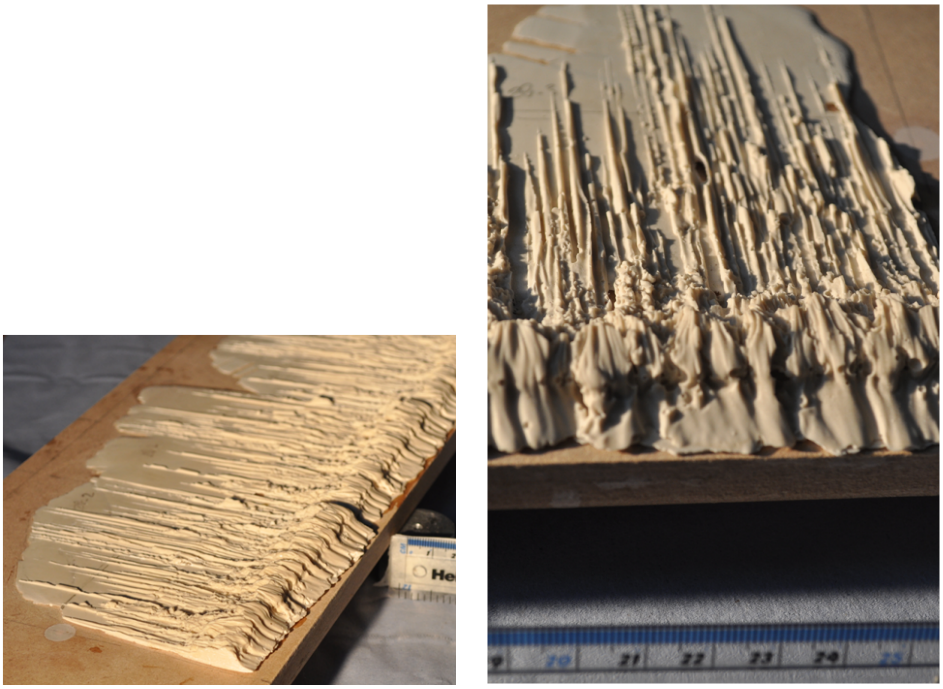

(a) Overall view (b) Close-up view

Figure 5.42: *Thick cast of typical runback ice shape for continuous maximum icing conditions (run 2b-3)*

(a) Top view (b) Lateral view

Figure 5.43: *Thin cast of typical runback ice shape for continuous maximum icing conditions (run 11-2)*

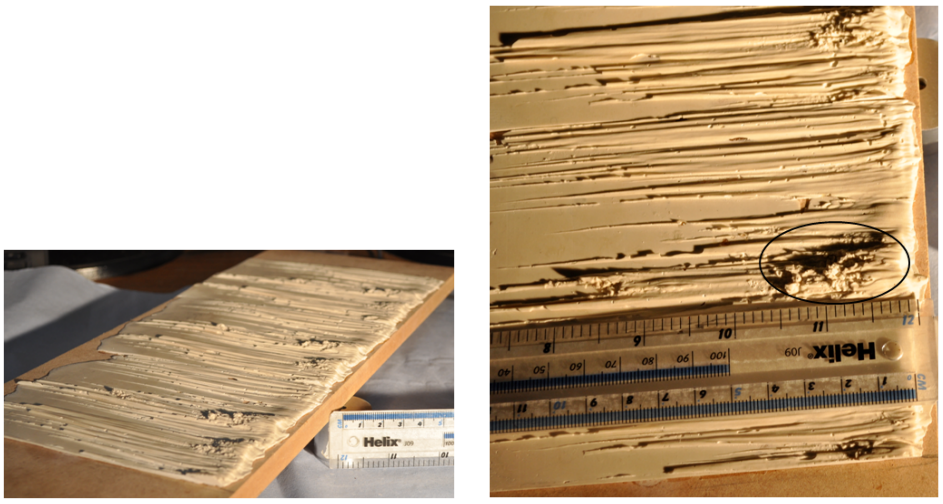

(a) Overall view (b) Close-up view

Figure 5.44: *Thin cast of typical runback ice shape for intermittent maximum icing conditions (run 7-3)*

Those high-fidelity 3D castings show some similarities with the only 3D high-fidelity runback ice shape cast (NG0671, Figure 2.17) found in the literature, even if they were grown for different conditions on a different airfoil (Whalen et al. (2005) and Broeren et al. (2010c)). The casting of Figure 2.17 is supposed to be "representative of flight in holding conditions for a full-scale aircraft equipped with a bleed-air, thermal ice protection system" (U_∞ =72 $m.s^{-1}$, AOA=1.1°, MVD=28 μm, LWC=0.91 $g.m^{-3}$, $T_t = -5.05$°C, $T_s = -7.66$°C and for a time of accretion of 22.5 min). For each casting there is a ridge in front with some rivulets at the back. The LWC used to grow the shape NG0671 is relatively high and close to the LWC used to grow the shape 7-3 for intermittent conditions. Both casts have some similar 3D features. These features are circled in Figure 2.17 and Figure 5.44. These similarities between the castings of the present study and full-scale cast from the literature highlight the fact that full-scale runback ice shape were successfully grown on the Hybrid airfoil in the CIT.

5.8 Runback ice growth with anti-icing system: conclusions

An analysis of the runback ice tracings allows us to quantify the influence of the LWC, heat input and the limit of the heated zone on the runback ice shapes dimensions and roughness:

- Influence of the LWC
  - For low LWC the runback ice is quite smooth with a ridge which looks like pile of frozen rivulets.
  - For high LWC the mass of ice is greater. The shape is thicker, longer and much rougher, the distance between the end of the heated zone and the ice is increased.
- Influence of the heat input: increase of the heat input
  - Increase of the length of the shape.
  - The length between the end of the heated zone and the ice shape is increased.
  - The ridge thickness is decreased.
  - The angle α is decreased.
- Influence of the limit of the heated zone combined with a heat input increase. It is important to note that the ice shape are always upstream of the suction peak in that study. When the limit of the heated zone is increased:
  - The mass of ice is decreased.
  - The length between the end of the heated zone and the ice shape is increased.
  - The iced zone in front of the ridge, a, is increased.
  - The angle α is increased .

From this study it is possible to make a ranking of the ice shapes in three main groups depending mainly on the heat input, LWC and chordwise positions (Figure 5.45). A triangle shape with its peak on the left hand side of its base is the most common shape for maximum continuous conditions. The angle α is in every cases studied greater than the 15°of the triangle used by the aircraft

manufacturers. When the LWC is increased (intermittent conditions) the shape tends to look more like a rectangle. If the shape is moved downstream closer to the suction peak, its peak will be shifted probably because of the increase of the speed close to the surface. Then the ice shapes looks like an isoceles triangle. A combination of high LWC with a most forward positions leads as well to an isosceles triangle shape. A CFD study would help to determine which simplistic shapes are worth testing compare to the castings during the wind tunnel testing campaign.

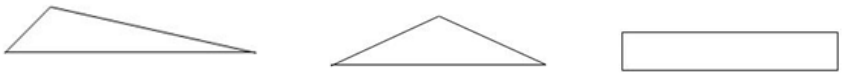

(a) Low LWC and position not close to the leading edge

(b) High LWC and position closer to the suction peak

(c) High LWC and position not close to the leading edge

Figure 5.45: *Typical simplistic shapes that were found following the study of runback ice tracings and casts using an anti-icing systems*

Three casts has been chosen for the wind tunnel study:

- Run 2b-3: thick shape for maximum continuous icing conditions, 20 min accretion
- Run 11-2: thin shape for makimum continuous icing conditions, 10 min accretion
- Run 7-3: thin shape for maximum intermittent icing conditions

5.9 Runback ice growth with de-icing system: results

It has been decided to present and discuss only two runs for the de-icing system experiments as it wasn't the main focus of the study (Table 5.12). The overall runs studied for a de-icing system are compiled on a DVD (see Appendix G). No ice castings were made for the de-icing system tests, because the runback ice grows close to the stagnation point which makes the moulding technique much more challenging to apply. Only close-up pictures of the ice and tracings were used to capture the runback ice shapes from a de-icing system.

The details of the heating system configuration are presented in Figure 5.46 and Figure 5.47. The energy required in each heated zone is higher than for the anti-icing configuration (Figure 5.7 and Table 5.2). However as there are periods where the de-icing system is fully off or where only certain zones are heated, the power required to use a de-icing system is less than for an anti-icing system. The surface temperature distribution for each run as function of the time is presented in Figure 5.48. On each figure, the three curves represent the central thermocouples of the first row of each heated zone. For instance, for run 14, in zone A, the first row is 2 (Figure 5.46) and its central thermocouple is T2 (Figure 5.6).

The main difference between both runs, is that for run 14 the stagnation zone is heated cyclically whereas for run 15-2, the stagnation zone is heated continuously. In run 14, as a result of this, there is some intercycle ice forming, whereas there is not any for run 15-2. For that reason no angle α or distance in front of the ridge can be defined for run 14 as it is difficult to see the limit between runback ice and intercycle ice.

Runs	Heating system config	Limit of the heated zone (m)	LWC (g/m^3)	Time of run (min)	Ttotal in the tunel (°C)	a(m)	b(m)	d(m)	α (°)
run14	H12	0.053	0.45	9min 56s (4 cycles)	-5	NA	0.067	0.009	NA
run15-2	H13	0.109	0.45	17min 43s (8 cycles)	-5	0	0.081	0.007	67

Table 5.12: *Details of the runs studied to capture runback ice shape from a de-icing systems*

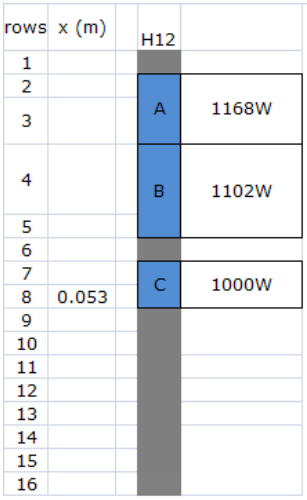

(a) Rows arrangement

Heated zone	A	B	C	off
Time (s)	18	15	20	96

(b) Cycle sequence

Figure 5.46: *Details of H12 heat configuration for de-icing system*

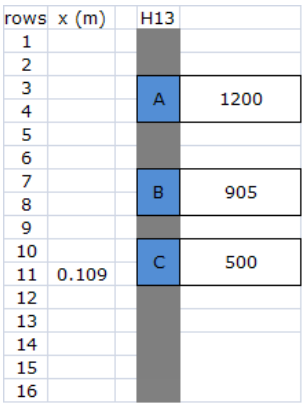

(a) Rows arrangement

Heated zone	A	B	C	off
Time (s)	on	15	20	96

(b) Cycle sequence (continuous heat at the stagnation zone

Figure 5.47: *Details of H13 heat configuration for de-icing system*

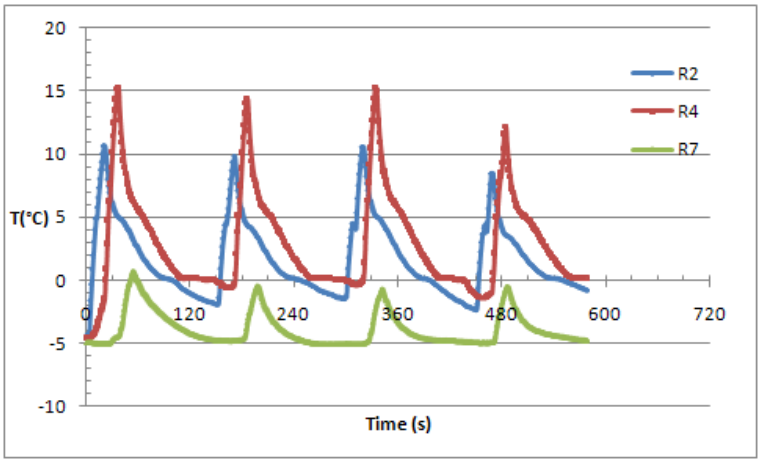

(a) Run 14 (H12 heat configuration, stagnation zone cyclically heated)

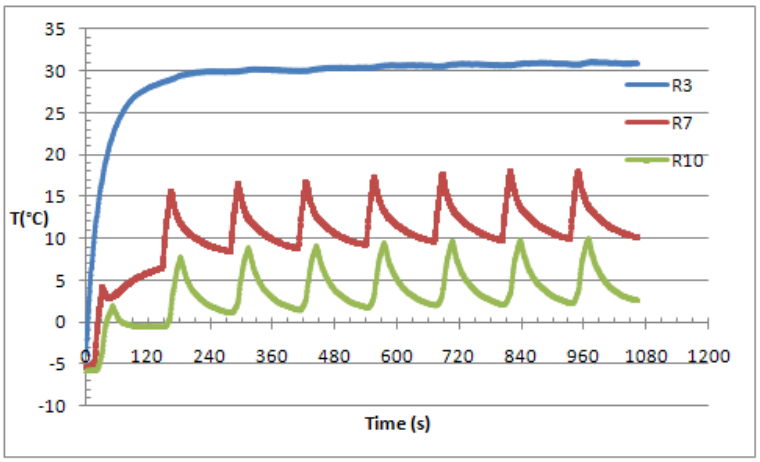

(b) Run 15-2 (H13 heat configuration, stagnation zone continuously heated)

Figure 5.48: *Central surface temperature for the first row of each zone of the heat configuration for de-icing system*

Pictures and tracings of run 14 and run 15-2 are presented in Figure 5.49 to Figure 5.51. The first remark is that on the tracing of run 14, the shape is not stoped at the front. This is because there was some intercycle ice that was too small to capture properly on the tracing. The second remark from the tracings is that for both runs the shape has a front ridge/horn, then there is a decrease of the ice thickness in the middle of the shape, and then at the end of the shape there is another ridge/horn feature. This double ridge configuration was found for all the runs studied. It is because the front ridge is cyclically shedded (cyclical runback ice) because it is located on the zone which is cyclically heated. The second ridge is not located on the heated zone, so there is always some runback ice if all the water is not evaporated by the heating system. Then the second ridge of the shape comes from two mechanisms of growth:

- Rivulets from the cloud impinging the model.
- Rivulets or film from the melting and the shedding of the first runback ice ridge.

This phenomenon of cyclical runback has been well captured by pictures. In Figure 5.51 the growth of the double ridge runback ice shape is well represented (b) as well as the first ridge shedding (a). The third remark is that, because the ice shapes form closer to the stagnation zone, after a while the droplets which normally miss the surface, do impact on the ice shape (Figure 5.50). That results in big features in front of the runback ice shape. These features are likely to be very dramatic for the aerodynamic of the flow.

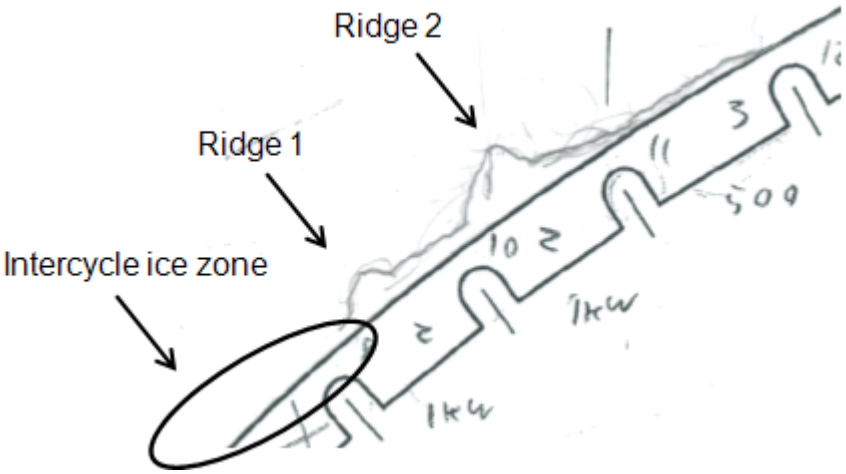

(a) Run 14: de-icing system with the leading edge cyclically heated

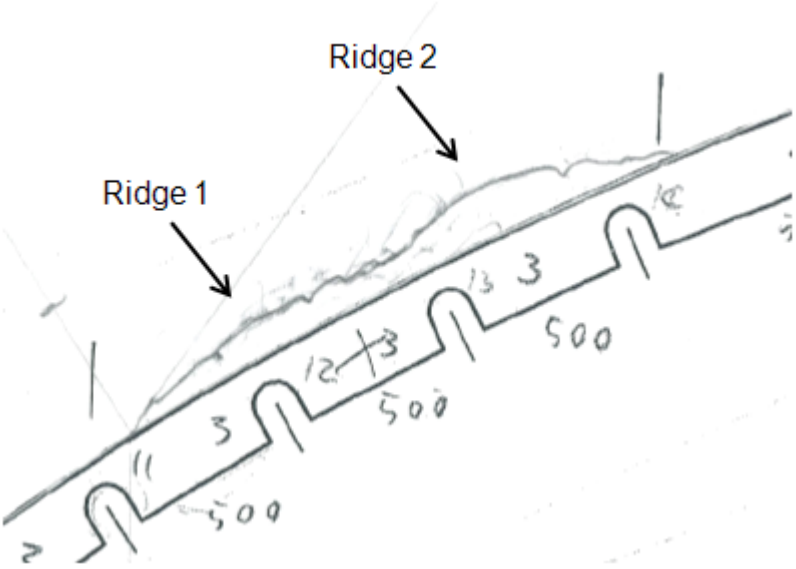

(b) Run 15-2: de-icing system with the leading edge continuously heated

Figure 5.49: *Ice tracings of runback ice*

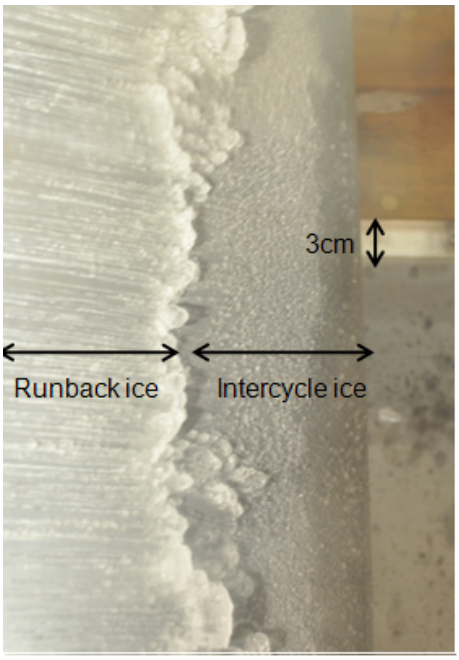

(a) Top view

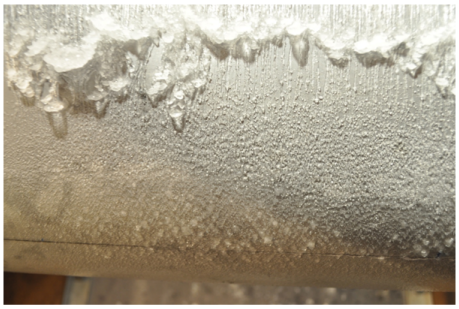

(b) Front view

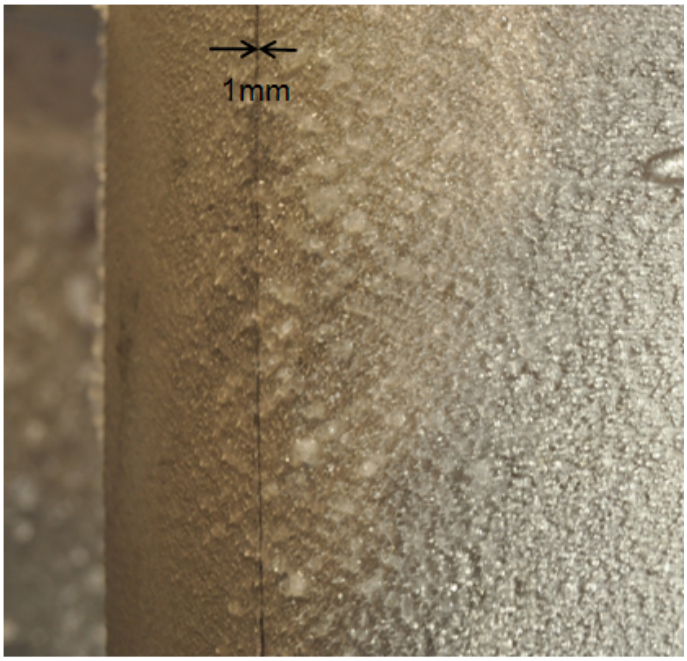

(c) Close-up view of intercycle ice

Figure 5.50: *Runback and intercycle ice at the end of run 14*

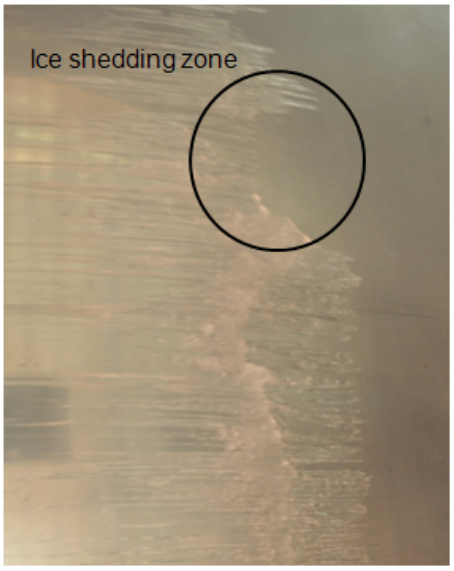

(a) Runback ice during the cycle sequence

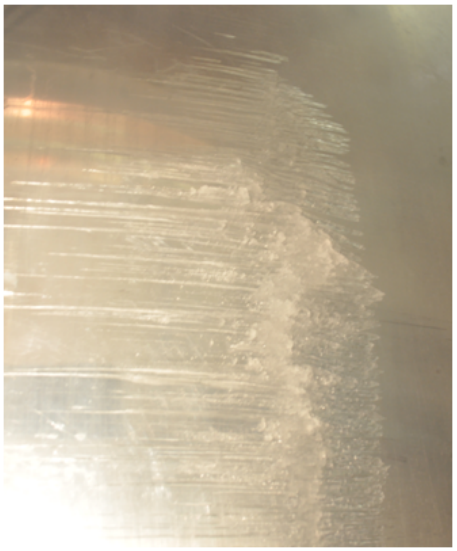

(b) Runback ice at the end of the run

(c) Close-up view of runback ice at the end of the run

Figure 5.51: *Runback ice pictures for run 15-2*

5.10 Runback ice growth with de-icing system: conclusions

Even if the runback ice growth from a de-icing system has not been studied extensively, it is possible to have some conclusions, based on the ice growth build-up observations. However, these conclusions are highly dependent on the heating system configuration (heat input and limit of the heated zone), so they may change in a different context.

- More energy is necessary for de-icing system than for anti-icing system. However less power is required for de-icing system than for an anti-icing system.
- The runback ice shape looks to be more dramatic for the flow because:
  - They are closer to the stagnation zone.
  - Massive feature are growing in front of the shapes after a while.
  - Double ridge feature.
  - The runback ice shapes look longer than when it is grown with an anti-icing system.

Chapter 6

Preliminary aerodynamic study

6.1 Introduction

The objective of the wind tunnel experiments is to compare the aerodynamics of simplistic shapes with the aerodynamics of full-scale high-fidelity ice shapes. Some preliminary work was necessary to decide which model is going to be used for the wind tunnel tests, pick the most relevant simplistic shapes to compare with the castings and decide which physical parameters can be used to compare the effects on the flow of the real shapes and of the simplistic shapes.

6.2 Boundary layer background

The boundary layer has been first introduced by Prandtl at the beginning of the 20th century. He introduced the concept of the non-slip condition of the fluid at the surface due to friction effect. He assumed that the friction was restricted to a zone close to the surface: the boundary layer. He highlighted that there are large shearing velocities through the boundary layer because of the slowdown of the flow close to the surface. Outside the boundary layer, the flow is not affected by the friction anymore. The boundary layer thickness tends to grow from the leading edge in the downstream direction. The definition of the boundary layer thickness is arbitrary. It is when the velocity in the boundary layer is very close to the local free stream velocity. In the present work the boundary layer is considered as fully developed when the velocity reaches 99.4% of the local free stream velocity. The local free stream velocity is defined by Houghton and Carpenter (2002) as the velocity that would exist at the surface with the flow being considered to be inviscid. Two others thicknesses are used to fully defined a boundary layer and remove

the uncertainties on the definition of the local free stream velocity. There is the displacement thickness, δ^* (equation (6.2.1)), which represents the length by which a surface would have to be displaced if the body was an inviscid flow to get the same mass flow as between the surface and the real fluid. It corresponds to a modification in the shape of the body. The displacement thickness represents graphically, the area underneath the velocity profile (Figure 6.1). As the velocity profile is asymptotic, the upper limit of the integral, δ (equation (6.2.1)), does not need to be known accurately as in that zone the area is very small. There is, as well, the momentum thickness, θ (equation (6.2.2)), which corresponds to the length by which a surface would have to be displaced if the body was an inviscid flow to get the same momentum as between the surface and the real fluid. Both thicknesses are calculated from velocity profiles:

$$\delta^* = \int_0^\delta 1 - \frac{u(y)}{U_e} dy \tag{6.2.1}$$

$$\theta = \int_0^\delta \frac{u(y)}{U_e} \left(1 - \frac{u(y)}{U_e}\right) dy \tag{6.2.2}$$

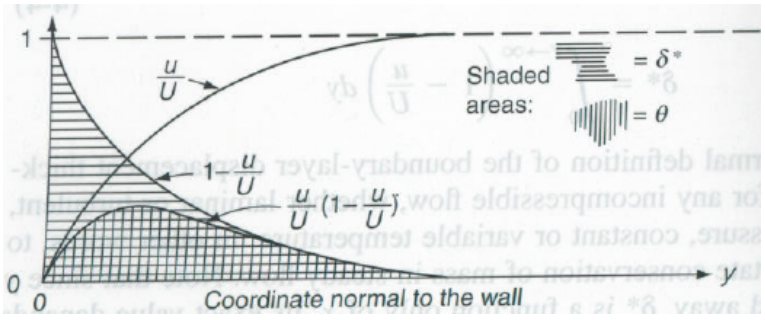

Figure 6.1: *Graphical representation of the displacement and momentum thickness White (2006)*

6.3 Choice of the model for the wind tunnel experiments

6.3.1 Introduction

To prepare for the wind tunnel experiments it was first necessary to decide what form of model is going to be used for the aerodynamic study. It is important to keep in mind, that the aerodynamic study is not directly focused on the aerodynamic performance loss induced by the ice shapes on an airfoil but on the relationship between the real shapes and the simplistic shapes. The most meaningful study would be to choose an airfoil and study the lift and drag coefficients when the airfoil is contaminated by real ice shapes and simplistic shapes. However, it was decided to focus on the study on the boundary layer characteristics instead, as it gives us some more flexibility on the choice of the model. The Cranfield 8 by 6 ft low speed wind tunnel has been chosen for the present study. It has been decided that the aerodynamic study would use the maximum speed allowed in the tunnel (45 $m.s^{-1}$). This speed corresponds to a Mach number of 0.13. This Mach number is included in the range of Mach number explored by Broeren et al. (2010c) and Broeren et al. (2010a). The authors concluded that there was little effect by the Mach number on the aerodynamic performance loss of an iced airfoil.

Three options have been investigated:

- Option 1: Hybrid model (c=1m, 45 $m.s^{-1}$)
- Option 2: Scaled B737/700 airfoil (c=0.6, 45 $m.s^{-1}$)
- Option 3: Flat plate (c=2m or more, 45 $m.s^{-1}$)

In order to decide which option was the most suitable for this study it was decided to study which option best fulfil the following key requirements:

- The meaningfulness of the measurements: Cl_{max} or the boundary layer characteristics
- The ability to use full scale ice shapes
- The manufacturing cost of the model
- The tunnel constraints: size (2.4m*1.8m) and speed limit (45 $m.s^{-1}$)

The pros and cons of all the options are discussed in the following sections.

6.3.2 Option 1: Full-scale Hybrid airfoil

There are two main advantages of using the full scale Hybrid model. First, the curvature of the model remains the same for the icing tunnel and for the wind tunnel test campaign. Second, there is no other model to design. However this airfoil is not really suitable for wind tunnel tests because it is not aerodynamically friendly. This was first highlighted when choosing the aerodynamic parameters for the icing tunnel tests as the flow was detached at the trailing edge of the Hybrid airfoil at a speed of 85 $m.s^{-1}$ (see section 4.5.1). There is no doubt that with the ice shape on the upper surface, the flow is going to detach and is not going to reattach. Actually, a picture (Figure 6.2) was taken during the icing tunnel tests while the air in the tunnel was above 0°, in order to remove the runback ice of the leading edge. The picture represents the upper surface of the airfoil from a point near the trailing edge. It shows that the flow is reversed in the zone downstream the full-scale leading edge. It makes the aerodynamic study of the airfoil meaningless. It is likely that whatever the kind of shapes that would be added to the surface, the flow would detach without reattaching.

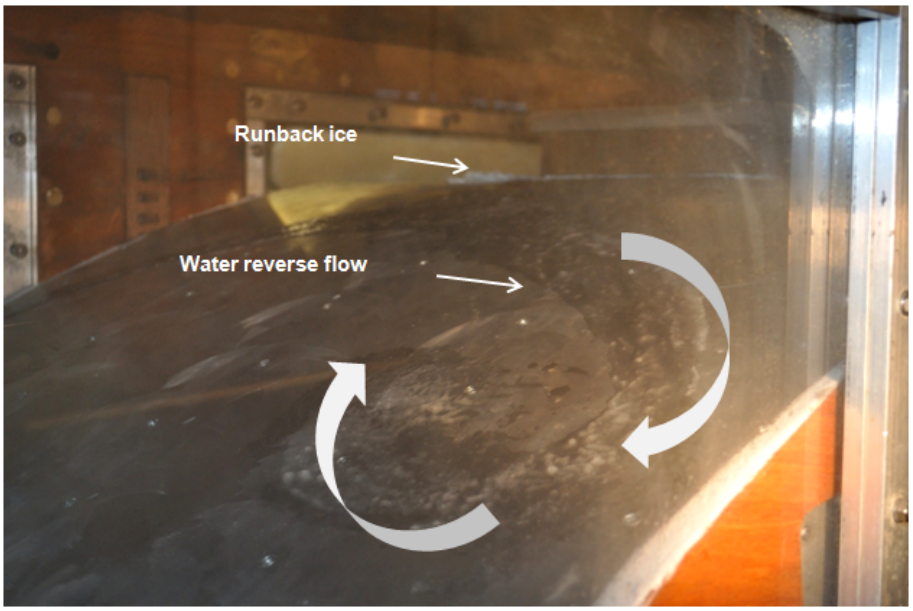

Figure 6.2: *Water reverse flow on the upper surface of the Hybrid airfoil downstream the full-scale leading edge*

6.3.3 Option 2: Sub-scale B737-700 airfoil

In order to get a more aerodynamically friendly airfoil the possibility of using the B737/700 airfoil was investigated. However as the airfoil is relatively big compared to the test section, the blockage effect might have a big influence on the aerodynamic measurements. It would mean that the airfoil need to be scaled. So would the ice shapes. Scaling ice shapes is a complex matter and out of the scope of this project. Moreover, the manufacturing costs of an airfoil are quite high.

6.3.4 Option 3: Flat surface

The use of a flat plate would avoid the problem of massive flow detachment and the boundary layer characteristics would be meaningful. However the use of a flat plate does raise some drawbacks: It would not allow the measurement of the lift coefficient, a plate would need to be manufactured and attached to the test section and the boundary layer would develop on a non pressure gradient surface. However, these drawbacks are not that dramatic in regards to the main aim of the project.

The main drawback of using a flat surface is the absence of pressure gradient. The length of the detached zone downstream the shapes is a function of the pressure gradient and of the size of the boundary layer where the ice shapes are embedded. This has been highlighted by the literature (see section 2.2, Calay et al. (1997) and Papadakis et al. (2004a)). Then the presence of pressure gradient or the closeness of the ice shapes to the suction peak could increase or decrease the length of the detached zone and then influence the effect of ice shapes on the aerodynamic of the flow. Some pressure gradient could be generated on the flat plate by changing the shape of the upper tunnel wall or by adding some incidence to the plate. Changing the tunnel upper wall would be a big project, which was out of the scope of this PhD. Adding some incidence to a flat plate would be easier to put in place, however it would have meant spend more time in the tunnel. Due to a very tight schedule in the 8*6 ft wind tunnel that was not possible. As the project is focused on a relative aerodynamic effect specifically, the correlation between real shapes and simplistic shapes, the pressure gradient was not considered in this instance. To avoid manufacturing a flat plate, it was decided to attache the ice shapes to the tunnel floor. This option raised the problem of the thickness of the boundary layer where the shapes would have to be embedded. To make sure that the study was relevant, the shapes had to be embedded in a thin boundary layer, typical of an airfoil leading edge. However, the boundary

layer on the floor of the test section is generally likely to be quite thick, well above the thickness targeted. To address this problem, the size of the boundary layer was adjusted using a suction device embedded in the floor of the 8*6 ft wind tunnel. Finally, instead of studying the maximum lift coefficient, the boundary layer characteristics was decided to be studied.

6.3.5 Conclusions

A flat plate model seems to be the best option in regards to the key requirements that were investigated to choose the model for the wind tunnel tests. So, even if the lift coefficient is not going to be measured and there won't be any pressure gradient on the surface, this solution is a good compromise to compare the boundary layer development downstream real ice shapes and simplistic shapes when the shapes are embedded in a relatively thin boundary layer. It was decided in collaboration with the sponsor, Airbus UK, to study the boundary layer characteristics such as the displacement thickness. However, it is has been highlighted through the literature review that the results of aerodynamic studies of runback ice are highly linked to the model on which the ice has grown (Lee and Bragg (1999) and Lee et al. (2000)) and to the position of the ice shape chordwise. So, the results of the present aerodynamic investigation have to be considered with care and kept in their context.

6.4 Preliminary CFD study of the simplistic shapes

6.4.1 Introduction

The objective of the wind tunnel testing is to compare the aerodynamic properties of 2D real ice shapes with their associated simplistic shapes by comparing the boundary layer development downstream the shapes. However, there are an infinite number of simplistic shapes that could be tested. Only the most releavant must be taken into account. Plus, it is vital to make the wind tunnel measurements at optimum positions in order to get the most useful data to analyse. This preliminary CFD study then, has to fulfil two objectives:

- Choose roughly the simplistic shapes which are worthwhile testing in the wind tunnel
- Decide on the positions of the velocity measurements in the wind tunnel in order to have the most valuable data.

6.4.2 Cases studied

To meet the objectives, a 2D ice profile from maximum continuous icing conditions has been considered in this preliminary study (Figure 6.3 and table 6.1). The 2D profile has been scanned and the coordinates has been extracted to an Excel spreadsheet using the GetData[1] software. From here it was easy to import the data into Gambit. This method is widely used in the literature to model high-fidelity 2D ice profile (Chi et al. (2002)).

Runs	LWC (g/m^3)	Time of run (min)	Ttotal in the tunel (°C)
run2b-2	0.45	20	-5

Table 6.1: *Details of the conditions for run2b-2*

[1]Free data recovery software www.getdata.com

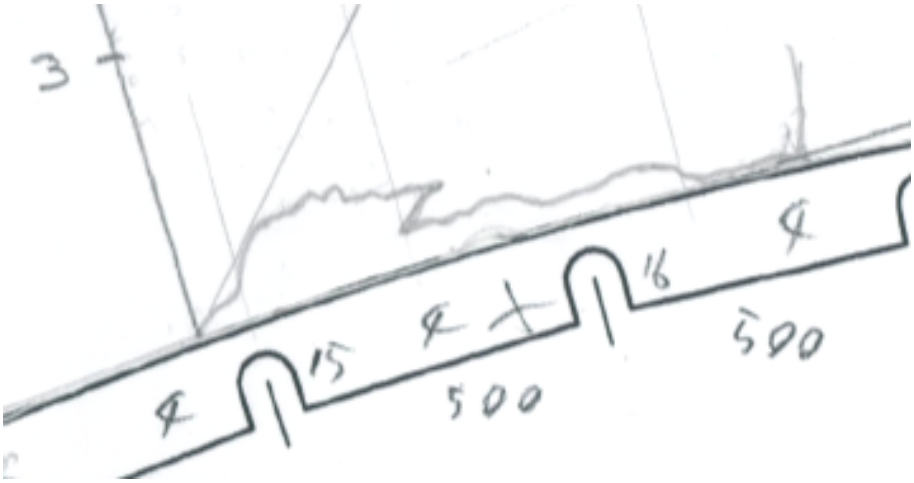

Figure 6.3: *Run2b-2 tracing*

The choice of the simplistic shapes was done based on three points:

- Well-known technique to simulate runback ice: For full-scale studies a sharp[2] triangle with a 15°angle in front is used. For the sub-scales tests in wind-tunnel ballotini strips can be used. They look like rectangles with smooth corners and roughness.
- Conclusions from the study of the tracings and casts that was done as part of that project (see section 5.8): It has been shown that the 2D ice profiles are similar in form to triangles and rectangles.
- Results from the literature show that simplistic shapes such as rectangle with or without roughness give encouraging results (Broeren et al. (2010c)).

For these reasons, a sharp triangle, with a 15° angle in front, and different rectangle types (round and sharp corner) were compared to the tracing. A triangle shape with the same front angle as the casting (α=47°) has been tested as well. The length of the simplistic shapes are either equal to the length of the tracing or half the length of the tracing in order to study the influence of the length of the simplistic shape on its aerodynamic performance loss. The height of the simplistic shapes is taken to be peak height of the 2D profile of the real ice shapes (Broeren et al. (2010c)). Seven simplistic shapes have been compared to the ice profile (Figure 6.4 and Table 6.2):

[2]Sharp is used to specify that the corner on the upstream face of the shape is not rounded

- Rectangle
- Triangle
- Sharp triangle
- Half rectangle
- Half triangle
- Front rounded rectangle
- Rear and front rounded rectangle

Runs	a(m)	b(m)	d(m)	α(°)
run2b-2	0.003	0.006	0.011	47
rectangle	NA	0.006	0.011	0
triangle 47°	NA	0.006	0.011	47
triangle 15°	NA	0.006	0.011	15
half rectangle	NA	0.006	0.011	0
half triangle	NA	0.006	0.011	47
front rounded corner rectangle	NA	0.006	0.011	0
rear and front rounded corner rectangle	NA	0.006	0.011	0

Table 6.2: *Geometric details of the 2D profile and its corresponding simplistic shapes*

As a reminder, a, b and d correspond respectively to the length in front of the ridge, the length of the ridge and the maximum thickness of the ridge.

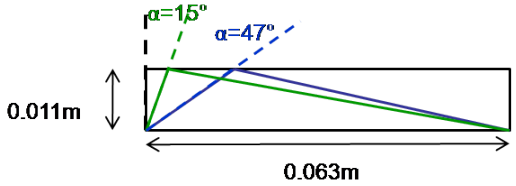

(a) Superimposed artificial shapes: rectangle (black), triangle with front angle close to the one of the profile (blue) and triangle used by aircraft manufacturers (green)

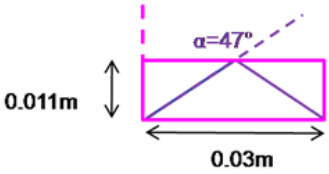

(b) Superimposed artificial shapes: half rectangle and half triangle

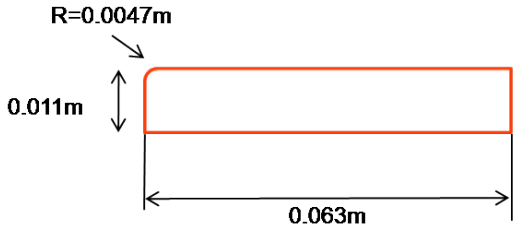

(c) Rectangle with a rounded corner at the front

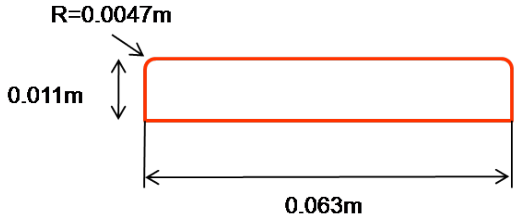

(d) Rectangle with a rounded corner at the front and rear

Figure 6.4: *Simplistic shapes corresponding to the 2D profile of the thick maximum continuous icing conditions shape 2b-3*

6.4.3 Meshing and numerical set-up

The shape is positioned on a 2m long plate. A wall has been built 1.8m above the plate, to simulate the wind tunnel roof. The free stream velocity is 45m/s. The Reynolds number based on the length of the shape chordwise (6 cm long) is $Re = 1.7*10^5$. By the time this study was made, the experimental set-up was not known. Then the position of the shapes on the flat plate was decided arbitrarily. All the studied shapes were positioned at 10 cm from the plate leading edge. At this position the boundary layer thickness is 3.07 mm according to the Schlichting formula (equation (7.6.4)) over a turbulent flat plate. Velocity profiles were captured at 5, 10 , 20 and 50 cm from the front of the tracing and they were compared with the one downstream the simplistic shapes. The displacement thickness is not calculated in this section, as it is a preliminery study and the level of understanding of the flow required is not very high.

The objective of the simulation is to capture the recirculation zone properly. For this, the mesh must be fine in the vicinity of the shapes and downstream of the shapes. A multi-block strategy was used for the mesh in order to make a fine mesh close to the surface and to remove streaks with high aspect ratio cells (Chi et al. (2002)). The region in the vicinity of the shape is meshed with triangular cells. A size function is linked to the shape of the surface in order to get the first cell thickness equal to 0.0006 mm. The y^+ targeted is 1, or at worst, below 5. Outside that zone a structured grid is applied. A second order algorithm was used. A pressure-based solver is used and the pressure-velocity coupling is done using the SIMPLE[3] algorithm. The simulation was considered as converged once the drag coefficient remained unchanged between two iterations with residuals reasonably low (at least 10^{-3} -10^{-4} for the continuity equation) and constant. The discretization errors were controled by doing a grid independance study. It was done for different mesh sizes for an ice profile similar to the one from profile 2b-3 (Table 6.3). The reason for this is that the grid independance was checked before the final selection of the shapes for the wind tunnel experiments was made. The mid sized grid has been chosen for the study of the 2b-2 profile and its equivalent artificial shapes. An overall view of the midfine grid for a 2D ice profile is presented in Figure 6.5. Close-up views of the midfine grid for the 2b-2 profile are presented in Figure 6.6. Finally, a double precision solver was chosen to reduce the round-off error.

Velocity inlet and pressure outlet boundary conditions were applied to the input and the output of the model respectively. The realizable k-ϵ turbulence

[3]Semi-Implicit Method for Pressure Linkage Equation

model associated with the enhanced wall treatment was used. This turbulence model has been chosen for the preliminary study because it proved to predict correctly the flow detachement downstream a backward facing step (Tu et al. (2008)).

Grid	Number of nodes	Drag coefficient
coarse	24418	0.045
mid	246557	0.042
fine	383813	0.042

Table 6.3: *List of the grid densities used for the grid independence study and the corresponding drag coefficient.*

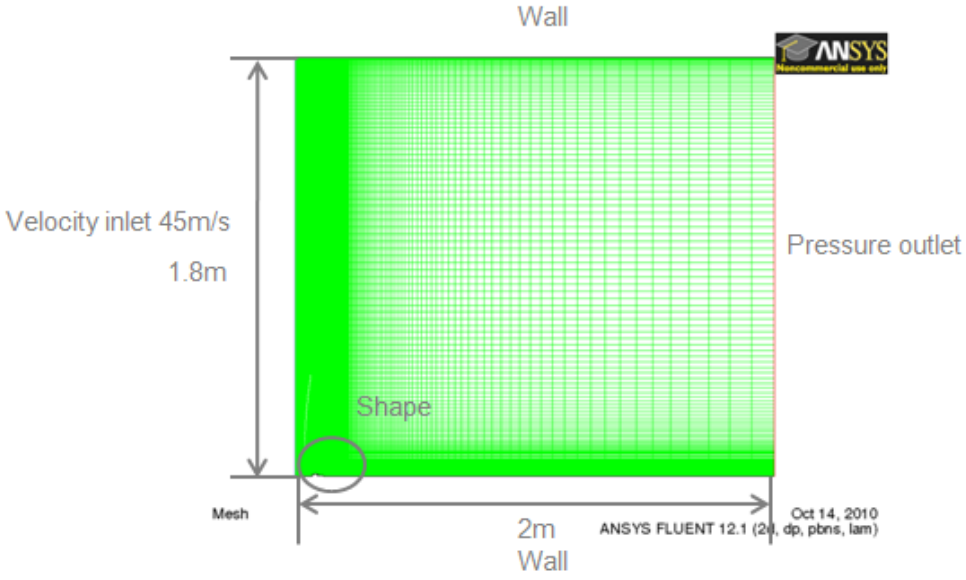

Figure 6.5: *Midfine mesh*

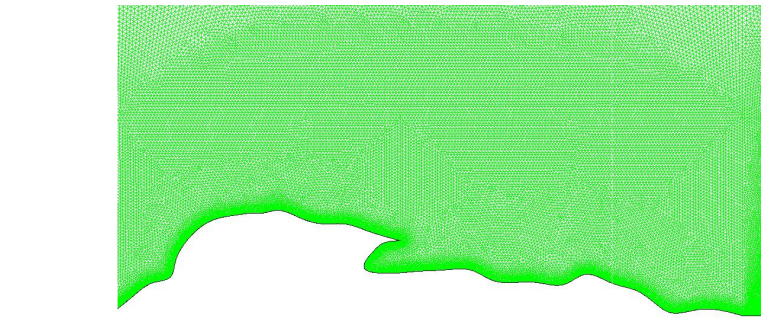

(a)

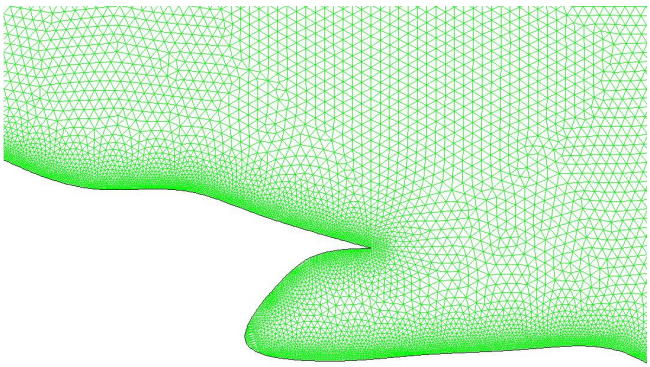

(b)

Figure 6.6: *Close-up views of the midfine grid in the vicinity of the ice shape profile from cast 2b-3*

6.4.4 Results and discussion

The velocity profiles downstream of the shapes have been captured 5, 10, 20 and 50 cm from the front of the shape (Figure 6.7 to Figure 6.10). A general remark, when looking at the pictures, concerns the differences between the velocity profiles of the shapes as function of the position of the measurements. These differences are big for the first three positions, but for the fourth position, 50 cm domnstream the front of the shapes, the discrepancies between the shapes are small as the flow is recovering. Between the positions 10 cm and 20 cm downstream the simplistic shapes the flow is reattaching for all the shapes. This is something that must be taken into account during the wind tunnel tests. The velocity measurements have to be done in a zone relatively close to the shapes in order to see the differencies between the shape the most clearly as possible. However, this zone has to be not too close to the shape in order to be out of the detached zone.

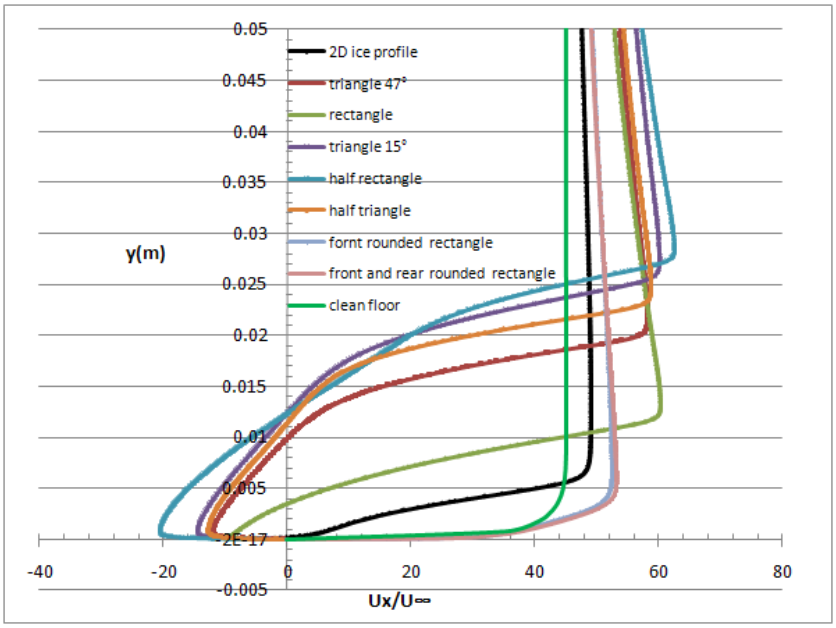

Figure 6.7: *Velocity profiles 5cm downstream the front of the tracing and the simplistic shapes*

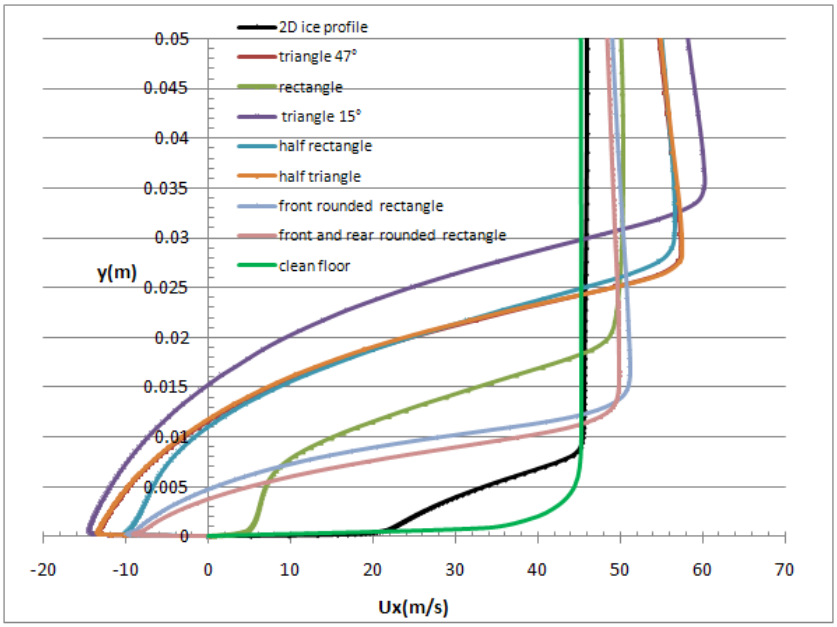

Figure 6.8: *Velocity profiles 10cm downstream the front of the tracing and the simplistic shapes*

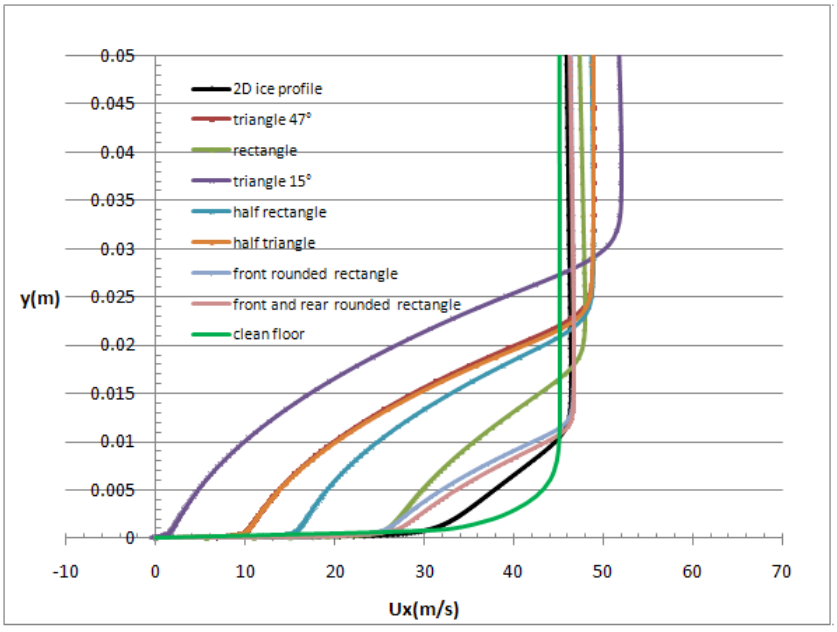

Figure 6.9: *Velocity profiles 20cm downstream the front of the tracing and the simplistic shapes*

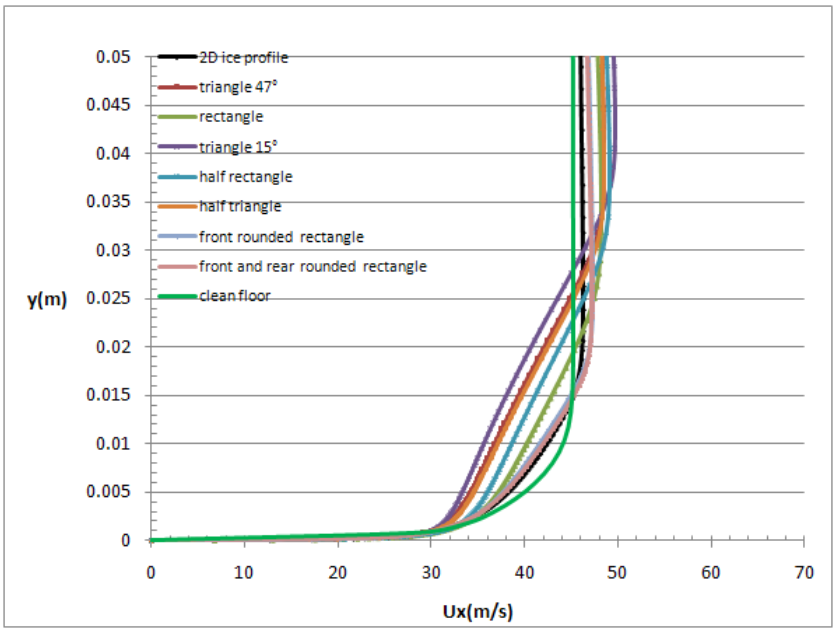

Figure 6.10: *Velocity profiles 50cm downstream the front of the tracing and the simplistic shapes*

For all the positions except 5 cm downstream the shapes, the triangle shapes are much worse for the flow than the 2D ice profile. The boundary layer downstream the triangles is thicker and the length of the detached bubble is longer than for the other shapes. The triangle used by the aircraft manufacturers, with a 15°angle in front, is the worst of the triangles for the flow. The rectangles seem to be the closest to the real ice shape. For instance, at the position 10 cm downstream the 2D ice profile (Figure 6.8, black curve), the flow is reattached. The flow downstream the rectangle (light green curve) is just reattached at 10 cm downstream the shape. All the other simplistic shapes have a detached flow at this position.

Concerning the difference between the shapes with the rounded corners and the ones with the sharp corner, it seems that, this small change in geometry, makes a big change on the aerodynamics of the flow. For instance, 20 cm downstream of the front of the shapes (Figure 6.9), the sharp triangle is still the worst in terms of aerodynamic disturbance. Both rectangles with the rounded front angle and the one with the rounded front and rear angle are getting close to the velocity profile of the tracing. Fifty cm downstream the shapes (Figure 6.10), the two rounded rectangles have equivalent velocity profile compare to the tracing. It is interesting to note that the flow is attached on the top of the rectangle with the front rounded whereas the flow

is massively detached on the top of the rectangle with a sharp corner (Figure 6.13, 6.14 and Figure6.15). For all the positions studied, the sharp corner rectangle is worse for the flow than the rounded corner rectangle. The difference between the rectangle with the front corner rounded and the one with both, the rear and front corner rounded, is small. The front and rear rounded corner rectangle tends to slightly decrease the detached zone.

Concerning the difference between the triangle with a 15° angle in front and the triangle with an angle similar to the one from the 2D ice profile, it seems that the 15° angle is worse for the flow in comparison to the other triangle and to the 2D tracing. However, it has been highlighted during the icing tunnel experiments that the angle between the front of the ridge and the normal to the surface was dependant on the LWC and on the ice position along the chord. So, it is meaningless to find a single angle which would be close to the real ice shapes as the real angle varies. The chosen angle has to be conservative.

Concerning the influence of the length of the shapes, the results are different depending if we consider the triangles or the rectangles. For the triangles, the short one is worse for the flow, 5 cm downstream of the shape. For the other positions, the effect of the short and long triangles are similar. This can be explained by the fact that the slope of the backward face of the triangle is higher for the short one than for the long one. This greater slope has a more adverse effect on the flow. The velocity contours in the vicinity of the triangle are presented in Figure 6.11 and Figure 6.12.
For the rectangles, whatever the position considered, it seems that the short one is more adverse for the flow. For the long rectangles, the flow is not detached on the top of the rounded rectangles but it is detached on the top of the sharp rectangle. However, in the case of the sharp long rectangle, the flow tends to reattach before the end on the shape (Figure 6.15). In the case of the short rectangle the flow can't reattach and then a very long and thick bublle is created from the front of the shape to several cm downstream the shape (Figure 6.16). This is the reason for such a difference between both sizes. It is likely that the length of the rectangle shape won't have a big influence, as long as the shape is long enough to let the flow reattach on the top surface of the rectangle. The ice tracing technique allows to capture the runback ice ridge, and sometime, if the rivulets are thick enough, the front of the rivulets at the back of the ridge. It has been found in 5.7.1 that downstream the ridge the rivulets were very dense. Hence, the length of the simplistic shape could the length of the runback ice shape up to the point were the rivulets are covering less than 80% of the surface.

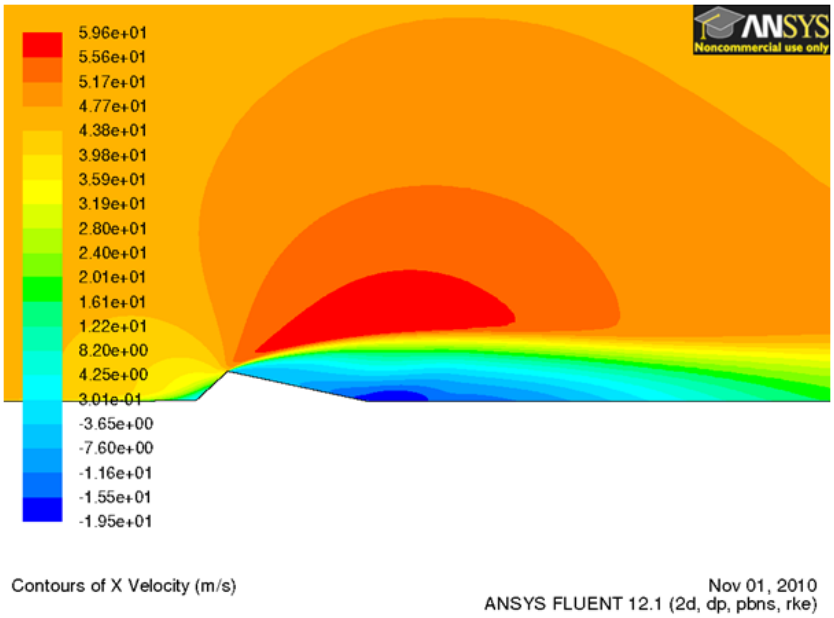

Figure 6.11: *Velocity contours in the vicinity of the triangle*

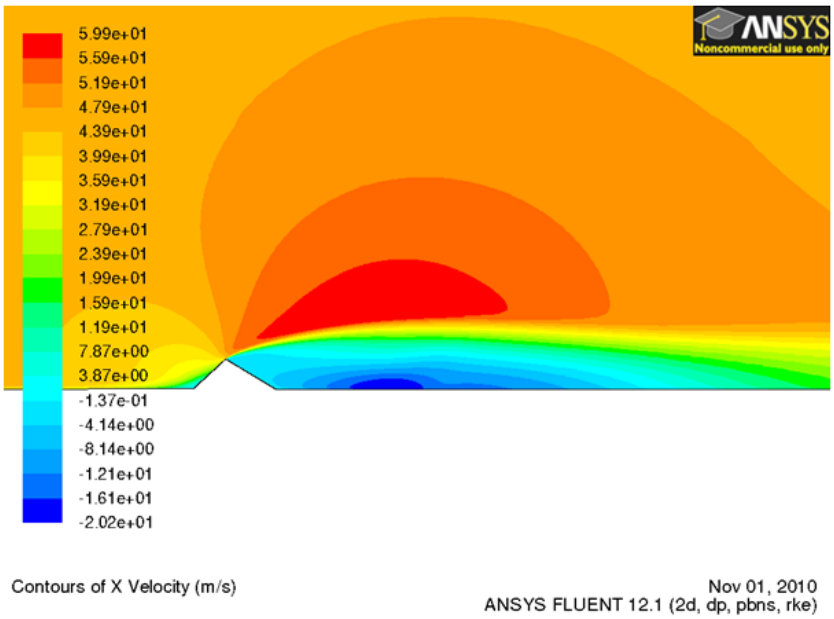

Figure 6.12: *Velocity contours in the vicinity of the half-triangle*

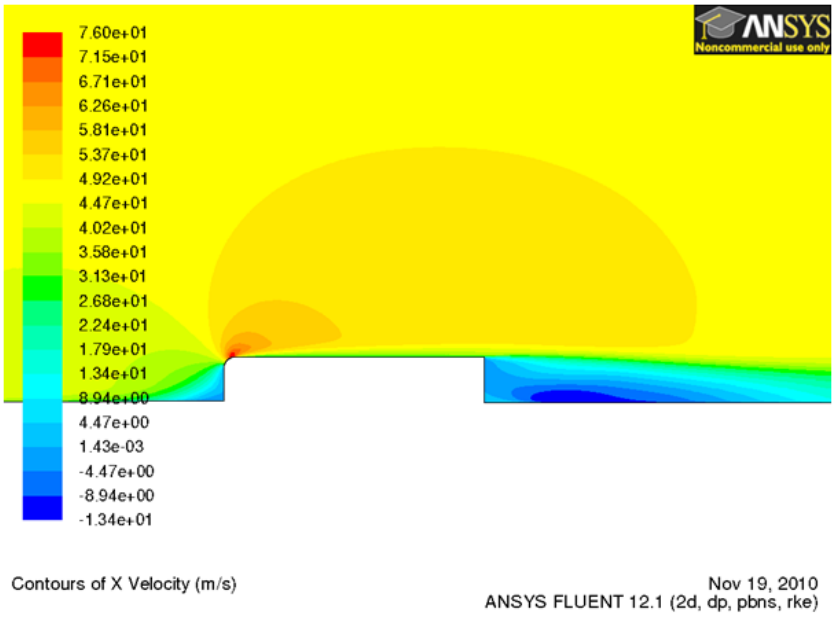

Figure 6.13: *Velocity contours in the vicinity of the front rounded rectangle*

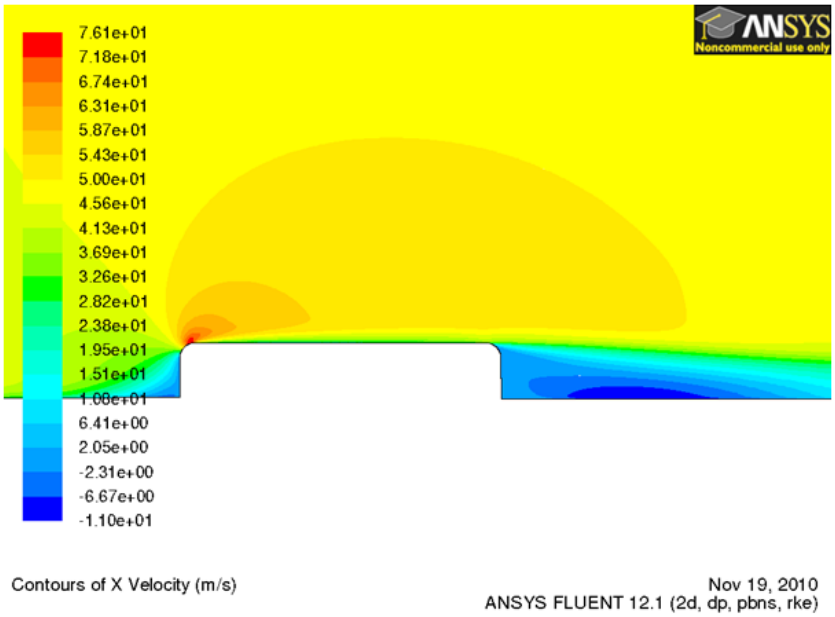

Figure 6.14: *Velocity contours in the vicinity of the front and rear rounded rectangle*

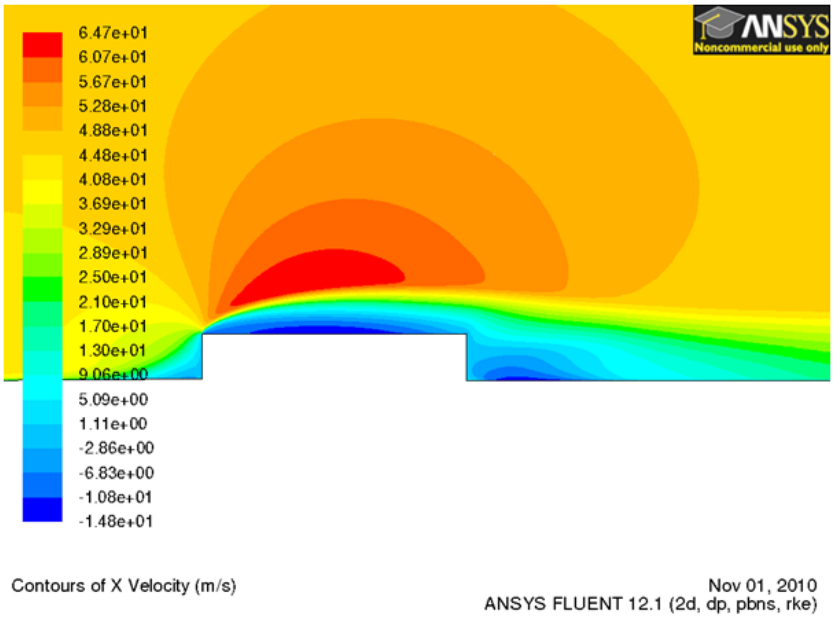

Figure 6.15: *Velocity contours in the vicinity of the rectangle shape*

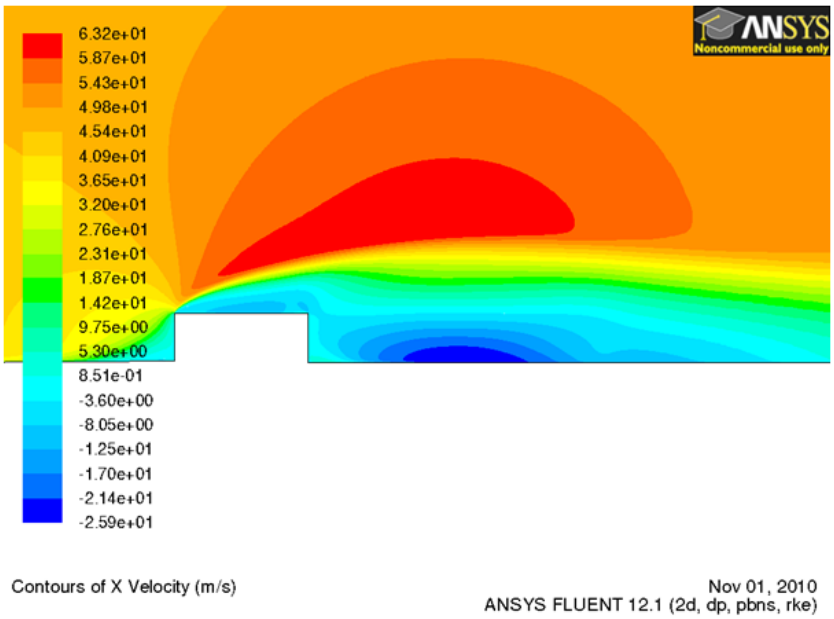

Figure 6.16: *Velocity contours in the vicinity of the half-rectangle*

6.4.5 Conclusion

According to these Fluent simulations, the sharp triangle is the simplistic shape which is the most adverse compared to the ice tracing for the aerodynamic of the flow. It is the most conservative shape. Rounded corners on the upstream face of the simplistic shapes reduces the flow detachement induced to the shape. The rectangle with the rounded corners (upstream face or upstream and downstream faces) is the one which matches the best the 2D ice profile in terms of boundary layer. Following these results it is possible to draft a methodology for the wind tunnel experiments:

- Rounded corners rectangles are the main simplistic shapes which are going to be studied as they seem to be the closest to the aerodynamics of real ice shapes. However, triangles (rounded or not) are going to be tested as well, as it is a reference for the aeronautics manufacturers. As the real angles varies for the real shapes, it is decided to choose the conservative angle used by the aircraft manufacturers. The triangles will be manufactured with an angle of 15° between the upstream face and the normal to the surface.

- The length of the simplistic shapes for the castings that are going to be studied in the wind tunnel (run2b-3, run11-2 and run7-3) are going to be determined arbitrarily in order to take into account the zone where the rivulets are relativaly dense: it is the length from the front of the shape to the end of the zone where the rivulets are covering 80% of the surface.

- The height of the simplistic shapes will be the maximum height of the 2D ice profiles.

- The positions for the velocities measurements have to be made in a zone between the detached flow and a position where any differencies in the velocity profile between the shapes investigated are too small to be measured, as the flow recovers. As no flow vizualisation was planned for the testing because of a lack of time, the length of the detached zone was based on these CFD results. It is decided to measure the velocity profiles at 15, 20 and 25 cm downstream the front of the shape.

Chapter 7

Wind tunnel experiments

7.1 Objectives

The objective of these experiments is to compare the boundary layer displacement thickness downstream ice castings and simplistic ice shapes on a flat surface. The runback ice is considered as an obstacle for the flow. Its influence on the boundary downstream the shape will give some hints on its effect on the aerodynamic performance loss.

7.2 Experimental set-up

The experiments were conducted in the 8 by 6 foot Cranfield wind tunnel. This is a closed loop tunnel, with a test section length of 5.18m, a width of 2.43m and a height of 1.82m. The turbulence intensity on the working section center line at 40m/s is 0.09%. The test section is rectangular with corner fillets. The corner fillets help in keeping the pressure gradient negligible in the test section. The suction device of the tunnel was used to thin the boundary layer in front of the ice shapes (Duncan et al. (1960)). The suction was used at its maximum speed.

The speed used during the tests was 45 $m.s^{-1}$ which is the maximum speed in the tunnel. The ice shapes were mounted flush with the flloor of the test section, downstream of the suction device to reduce the boundary layer thickness in front of the shapes. The objective was to get the boundary layer thickness reasonably thin (between 1 and 2 mm) in front of the shape which would correspond to the boundary layer thickness in front of an ice shape on a full scale airfoil at a position between 7 to 20 cm from the leading edge. For this reason, it was decided to put the shapes as close as possible to the point of

the suction. The closest position where it was possible to attach the shape to the floor was 70 mm downstream the suction. The ice shapes were glued onto some inserts which fit into the floor. In order to reduce the possible 3D tip effects, 3 identical castings were glued side by side on the insert.

7.3 Instrumentation

A preliminary study of the tunnel boundary layer was made using a Pitot tube mounted on a micrometer (Figure 7.1). The objective was to assess the nature of the boundary layer downstream the suction. The results have been compared with the Schlichting formula, for a fully developed flat plate (Schlichting (1955)). The velocity profile measurements, downstream the shapes, were captured using 3 Pitot tube rakes of 10 tubes each (Figure 7.1).

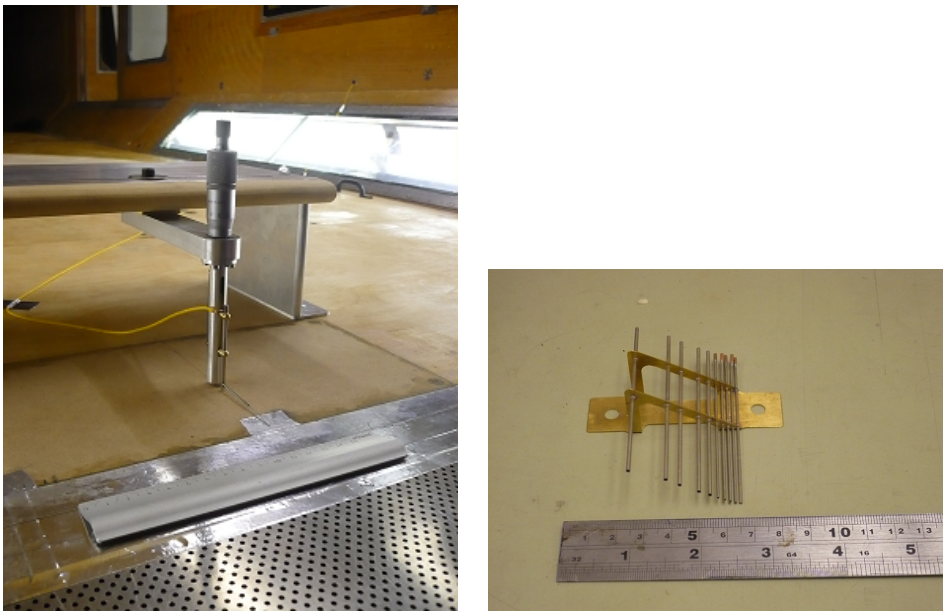

(a) Calibration probe (b) Pitot probe rake

Figure 7.1: *Pitot probes used for the experiments*

Each rake is spread horizontally as the space required between each tube close to the floor is smaller than the tubes themselves. It allows to have Pitot tubes more densely clustered close to the wall. The three rakes are placed side by side to capture the 3D characteristics of the boundary layer. The pitot tip for all but the bottom tube on each rake were cut square. The tube the closest to the floor was flattened to allow measurement closer to the floor. The

rakes are parallel to the flow. The static pressure was measured using a probe embedded in one of the walls of the tunnel. Then the dynamic pressure was measured with a differential pressure transducer. The velocity profiles were captured at 3 positions downstream of the shapes (15, 20 and 25 cm from the front of the shapes or for x=220, 270 and 320 mm according the abscissa origin which is situated just downstream the end of the suction) except for the maximum intermittent conditions because the corresponding casting was longer than the first velocity measurement position at 15 cm from the ridge.

It was decided to design removable side pieces for the inserts in order to have several measurements in the y direction (spanwise). Different lengths were used for the side pieces as these allowed us to slide the insert in the y direction. This was done to avoid moving the measurement device in this direction. It was possible to slide the shapes by 5cm with an increment of 1 cm on each side. For the position "0", the middle rake was positioned in order to have the middle of the casting between tubes 5 and 6. Actually, only this rake was used for the data analysis as no big change in the boundary layer characteristics was observed for the other two rakes. Figure 7.2 gives a general view of the test section with the experimental set-up.

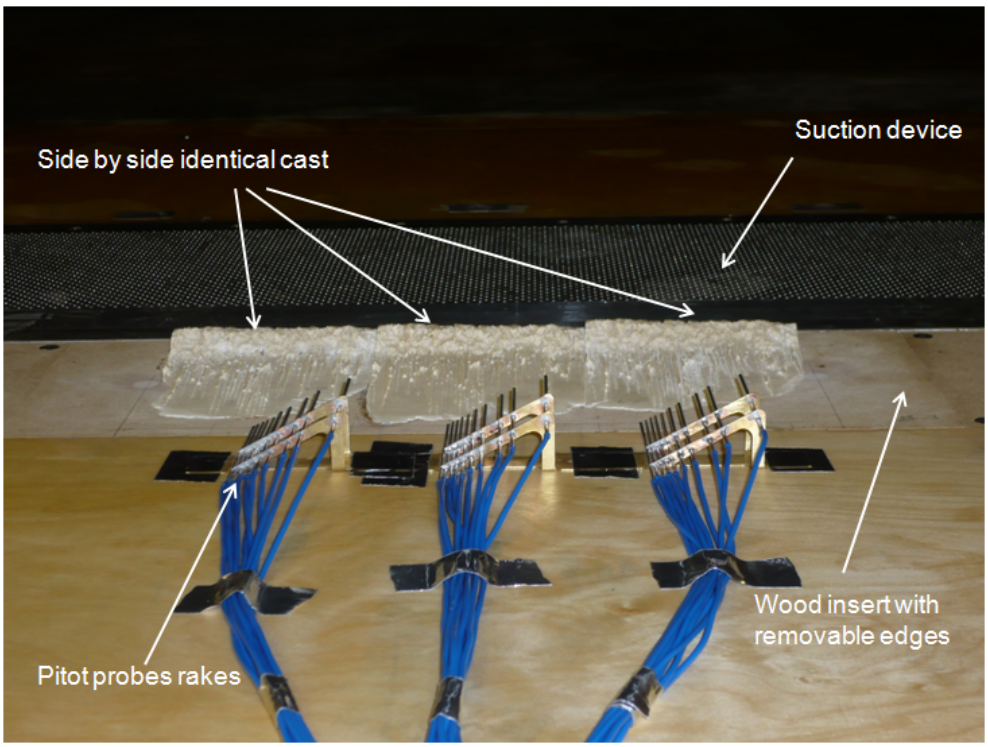

Figure 7.2: *Test section with the ice shape and the instrumentation set-up*

7.4 Cases studied

Following the icing tunnel experiments, it has been decided to study the aerodynamics of three castings that are typical of maximum continuous and intermittent icing (see section 5.7.5). The chordwise lengths of the castings are abitrary: it is the length from the front of the shape to the point were the surface is covering 80% of the surface. The thickness of the casting correspond to the peak height. Following the conclusions of a preliminary CFD study (see section 6.4), the simplistic shapes corresponding to each casting were defined (Table 7.1).

runs	shape description	Total length (m)	Thickness (m)	Roughness (mm)	α (°)
2b-3	2b-3 casting	NA	0.01	NA	56
2b-31	sharp triangle	0.05	0.01	NA	15
2b-32	rounded rectangle	0.05	0.01	NA	0
2b-33	rounded triangle	0.05	0.01	NA	15
2b-34	rounded rectangle with ballotini	0.05	0.01	1	0
11-2	11-2 casting	NA	0.004	NA	80
11-21	rounded rectangle	0.065	0.004	NA	0
11-22	ballotini	0.08	NA	1	NA
11-23	ballotini	0.08	NA	2	NA
11-24	rectangle with ballotini	0.065	0.004	1	NA
7-3	7-3 casting	NA	0.005	NA	43
7-31	rounded rectangle	0.085	0.005	NA	0
7-32	rounded rectangle with ballotini	0.085	0.005	1	0

Table 7.1: *Ice shapes castings associated with their simplistic shapes for the wind tunnel tests*

The simplistic shapes are made of medium fibre wood, ballotini or medium fibre wood + ballotini. On the top of some of them, ballotini were glued to simulate significant roughness. Some of the simplistic shapes have been rounded. This means that the corners are not sharp. It can be noted on Table 7.1, that the length of the simplistic shapes for the 11-2 casting, made of ballotini only (shape 11-22 and 11-23) are 1.5cm longer than the other simplitic shapes for the 11-2 casting. The reason for this, is that it was assumed that as there was no thickness but just roughness, the length should be increased in order to be closer to the geometry of cast 11-2.

The pictures of the castings and the simplistic shapes for run 2b-3, run 11-2 and run 7-3 are presented in Figure 7.4, Figure 7.5 and Figure 7.6 respectively. A close-up view of the ballotini is presented in Figure 7.3

Figure 7.3: *Close-up picture of 2 mm ballotini glued on the floor as used for the simplistic shapes associated with the thin casting*

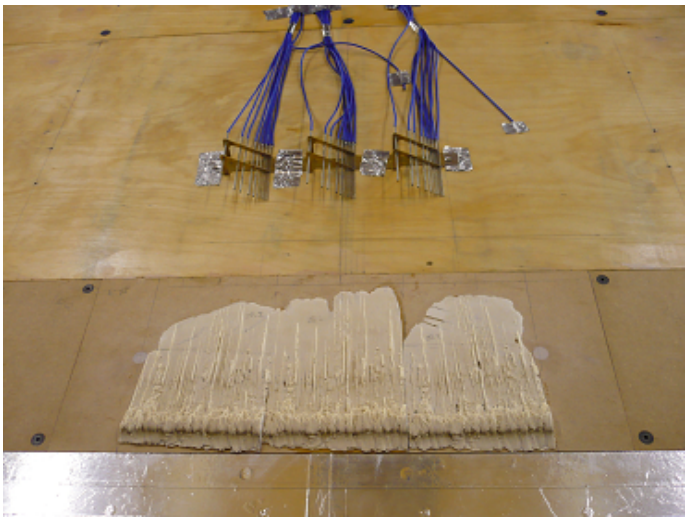

(a) 3 identical castings side by side (2b-3)

(b) Sharp triangle (2b-31)

(c) 3 identical castings side by side lateral view (2b-3)

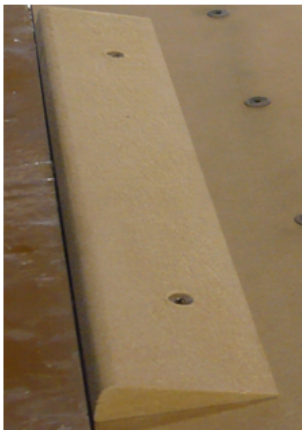

(d) Rounded triangle (2b-33)

(e) Rounded rectangle (2b-32)

(f) Rounded rectangle with 1 mm ballotini (2b-34)

Figure 7.4: *Thick casting (2b-3) and its simplistic ice shapes for maximum continuous conditions*

(a) 3 identical castings side by side (11-2)

(b) Rounded rectangle (11-21)

(c) 1 mm ballotini (11-22)

(d) 2 mm ballotini (11-23)

(e) Rectangle with 1 mm balotine (11-24)

Figure 7.5: *Thin casting and its simplistic ice shapes for maximum continuous conditions*

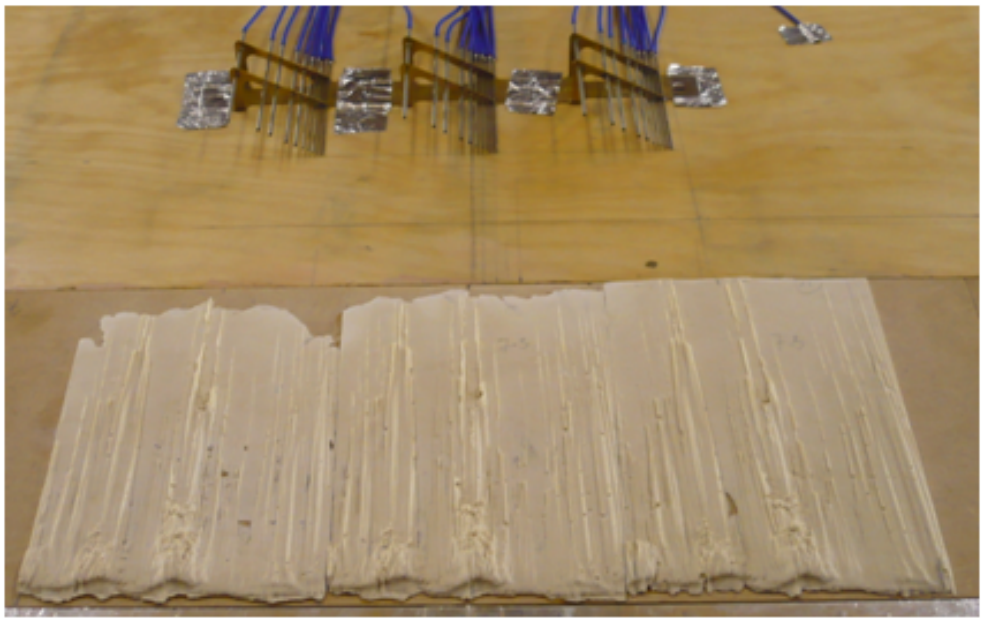

(a) 3 identical castings side by side (7-3)

(b) Rounded rectangle (7-31)

(c) Rounded rectangle with 1 mm ballotini (7-32)

Figure 7.6: *Thin casting and its simplistic ice shapes for maximum intermittent conditions*

7.5 Repeatability and uncertainties

The repeatability of the experiments has been studied to quantify random errors caused by instrument fluctuations. The same run was repeated 3 times (run 147, 148 and 149 in Appendix F). The run was for velocity measurement 15 cm downstream of cast 11-2. The panel was kept in place for these 3 runs. The velocity profiles of these three runs are presented in Figure 7.7. The boundary layer characteristics and their average, standard deviation of the mean and relative error are presented in Table 7.2 for a confidence level of 99% (Taylor (1982), Birch (2001) and Bell (2001)).

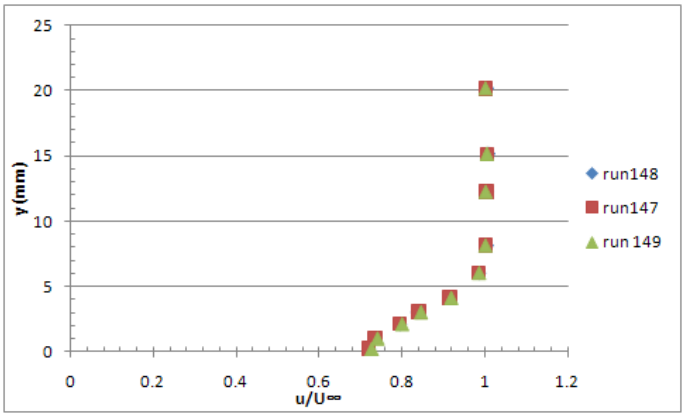

Figure 7.7: *Velocity profile for 3 repeated runs*

	run 147	run 148	run 149	average (mm)	σmean (mm)	Relative error (%)
δ*(mm)	1.05	1.04	1.01	**1.04**	**0.03**	**3.10**
δ(mm)	7.14	7.11	7.02	**7.09**	**0.10**	**1.34**

Table 7.2: *Boundary layer characteristics for 3 repeated runs*

We can see that the three runs give very similar δ and δ^* measurements. The biggest difference between each run occurs for the measurements close to the floor. It is due to the wall interferences. The other changes in the repeated runs are due to the fluctuations which are captured by the pitot rake. The relative error for a confidence level of 99% is then of $\pm$ 1.3% for δ and $\pm$ 3.1% for δ^*. However, δ is calculated using a linear interpolation and δ^* is calculated using a a trapezoidal intagration method. Both, the linear interpolation and the trapezoidal integration generate some errors. To quantify this error, it has been compared to a higher order numerical integration method: the cubic spline. The result from the higher order numerical integration is

considered as the true value. By this method, Dittmar (2010) found for the present data that δ is $\pm$ 4.9% of the true value and δ^* is $\pm$ 1.1% of the true value.

The sources of uncertainties in the pressure measurements are:

- Free stream dynamic pressure: accuracy of the differential pressure transducer kit $\pm$ 0.5%
- Local dynamic pressure: accuracy of the differential pressure transducer kit $\pm$ 2Pa or $\pm$0.2%
- Static pressure on the wall is not at the same chordwise positions as the dynamic probe. It is a very small error as the pressure drop through the working sections is negligible
- The air temperature which is taken into account to change the air density in the tunnel is measured with an uncertainties of $\pm$ 0.1°C.

The propagation of the random error within the velocity profile measurements for the highest tube of the middle rake is calculated as follow for the ratio R_u of dynamic pressure P_d, free stream and local or for the ratio of local and free strem speed : $R_u = \sqrt{\frac{P_d}{P_{d\,\infty}}} = \frac{u}{U_\infty}$:

$$\frac{\delta R_u}{\overline{R_u}} = \sqrt{\left(K_1 \frac{\delta_{P_d}}{P_d}\right)^2 + \left(K_2 \frac{\delta_{P_{d\infty}}}{P_{d_\infty}}\right)^2} \tag{7.5.1}$$

$$K_1 = \frac{P_d}{R_u} * \frac{\partial R_u}{\partial P_d} = 0.5 \tag{7.5.2}$$

$$K_2 = \frac{P_{d_\infty}}{R_u} * \frac{\partial R_u}{\partial P_{d_\infty}} = 0.5 \tag{7.5.3}$$

Then the absolute random error in the velocity ratio measurement, δR_u, is $\pm$0.5% for a confidence level of 99%. This value is small compared to the error that was found during the repeatability tests (Table 7.2). Finally the total error for δ and δ^* in taking into account the error from the repeatability, the error from the numerical calculation and the error from the total pressure measurement and its propagation in the velocity profile, is:

$$\epsilon_\delta = \pm 5.1\% \tag{7.5.4}$$

$$\epsilon^*_\delta = \pm 3.3\% \tag{7.5.5}$$

The sources of uncertainties in the position of the rake are:

- For the calibration probe only: the height where the probe is touching the floor depends on the operator. The smallest graduation of the micrometer was 0.01mm. It was estimated that the accuracy to measure the point were the probe was touching the floor is $\pm$0.005mm
- The orientation of the rake rake in the direction of the flow (yaw angle) $\pm$ 1°(by eye)
- Horizontal position of the rake is $\pm$ 0.5mm.

The other classical sources of errors were neglected because they are very small in regards to the other source of errors:

- Buoyancy: no buoyancy effect as the model is embedded into the tunnel floor
- Solid and wake blockage: the model is tiny compared to the working section
- Stream line curvature: the walls are relatively far away the model.

7.6 Characteristics of the tunnel boundary layer

The objective of this section is to assess the nature of the boundary layer downstream the suction. To achieve this, the boundary layer characteristics on the clean wind tunnel floor downstream the suction device has been measured (run 1 to 6 in Appendix F) and compared with the well known Schlichting formula (Figure 7.8). The formulas used to calculate the turbulent boundary layer characteristics from Schlichting are (Schlichting (1955)):

$$\delta = 0.383 * x * Re_x^{-1/5} \tag{7.6.1}$$

$$\delta^* = 0.125 * \delta \tag{7.6.2}$$

$$\theta = \frac{7}{72} * \delta \tag{7.6.3}$$

The displacement thickness and momentum thickness from the experimental velocity profiles are calculated using a trapezoidal integration in Excel. Knowing δ (equation (7.6.4)) and δ^* (equation (7.6.5)), the shape factor, H, can be calculated (equation (7.6.6)):

$$\delta^* = \int_0^\delta 1 - \frac{u(y)}{U_e} dy \tag{7.6.4}$$

$$\theta = \int_0^\delta \frac{u(y)}{U_e} \left(1 - \frac{u(y)}{U_e}\right) dy \tag{7.6.5}$$

$$H = \frac{\delta^*}{\theta} \tag{7.6.6}$$

The displacement and momentum thicknesses measured on the floor downstream the suction are slightly bigger than for the Schlichting formula for a turbulent flat plate (Figure 7.8). However, they are quite close to each other. The nature of the boundary layer downstream of the suction can also be determined by the shape factor (Figure 7.8). Just downstream of the suction, the experimental shape factor is below the typical value for a turbulent flat plate (H$\approx$ 1.3 and H$\approx$ 2.6 for a laminer boundary layer over a flat plate). Further downstream, from x=250mm, the shape factor is getting closer to H=1.3. It means that in the zone where the velocity profiles are going to be measured, the suction as little effect on the boundary layer development. I t is considered that the experimental set-up is acceptable because it generates a boundary layer with characteristics relatively close to the one of a turbulent flat plate.

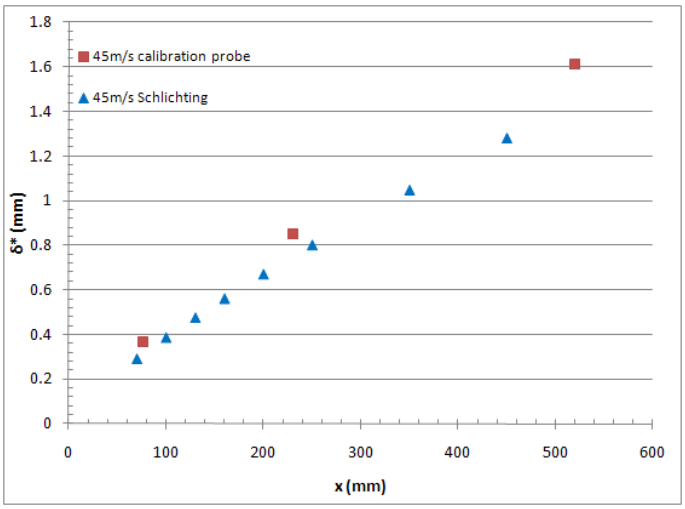

(a) Displacement thickness

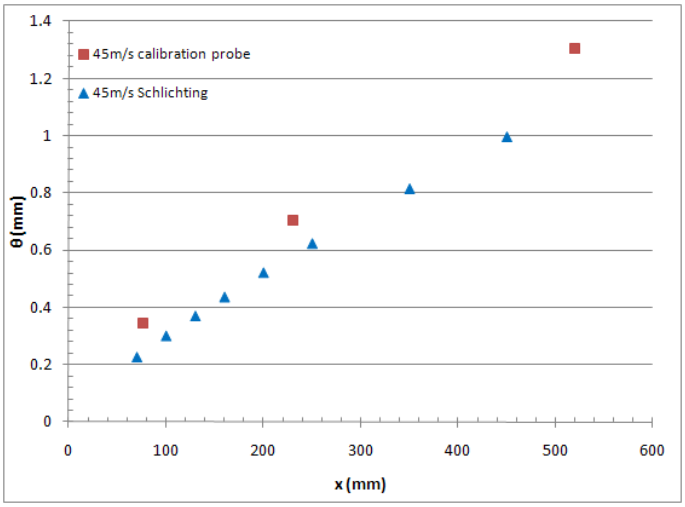

(b) Momentum thickness

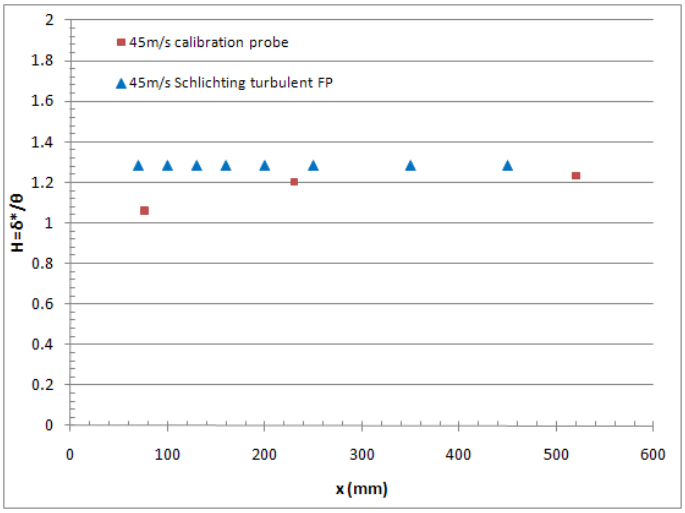

(c) Shape factor

Figure 7.8: *Boundary characteritcs comparison between experiments and the Schlichting formula for a fully turbulent flat plate*

7.7 Results

7.7.1 The 3D effects

The castings don't have a uniform shape. They have 3D geometrical features. Therefore, some 3D effects may occur in the flow. In Figure 7.9, the velocity profiles for the middle rake are recorded for all the spanwise positions. The "0" position corresponds to the position where tubes number 5 and 6 of the middle rake are in the middle of the castings. Then, the insert where the castings are glued are slide 10 mm by 10 mm, on both sides spanwise. We can see that the velocity profiles are dependant on the spanwise position, but that this dependance is quite small. Therefore, it has been decided not to take into account the spanwise positions, to have time to study more shapes in the given test slot. Only the "0" position of the middle rake was used to capture the boundary layer characteristics in this study (see section 7.7.2 and section 7.7.3). The 3D effects will need further investigations.

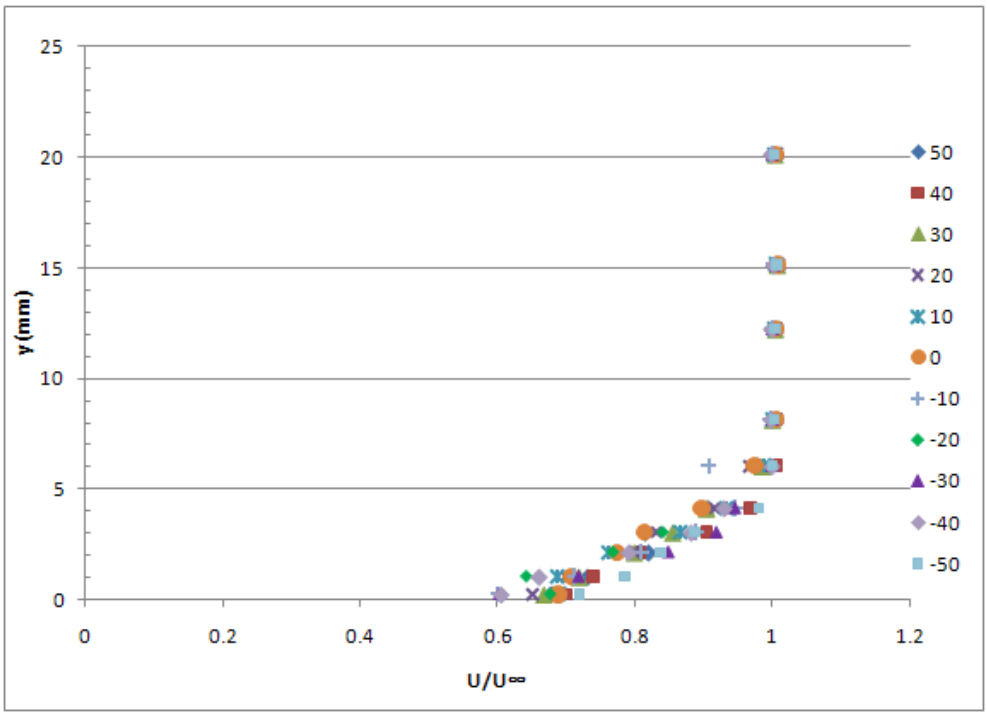

Figure 7.9: *Velocity profiles for the casting 11-2 (thin shape for maximum continuous icing conditions), 220mm downstream the suction for all the spanwise positions for the middle rake*

7.7.2 Ice castings from maximum continuous icing conditions

The boundary layer characteristics are presented for the thin (run 11-2) and thick (run 2b-3) shapes for maximum continuous icing conditions in Figure 7.10 and Figure 7.11 respectively. The percentage difference between δ and δ^* for the ice castings and the simplistic shapes, has been has calculated in Table 7.3 and Table 7.4 using the following formula:

$$\%\delta = \frac{(\delta_{simplistic\ shape} - \delta_{ice\ casting})}{\delta_{ice\ casting}} * 100 \tag{7.7.1}$$

$$\%\delta^* = \frac{(\delta^*_{simplistic\ shape} - \delta^*_{ice\ casting})}{\delta^*_{ice\ casting}} * 100 \tag{7.7.2}$$

Before analysing the data in detail, two remarks can be made. First of all, as the displacement thickness gives more valuable information than the boundary layer thickness, the focus is on δ^*. However, the boundary layer thickness remains an interesting parameter. Second of all, a noticeable behavior of δ^* can be seen in Figure 7.10 and Figure 7.11. Sometimes, δ^* is decreasing as the chordwise position is increasing. The reason for this phenomenon is not completly clear. However, a couple of arguments can justify this behavior. The first one is that the flow is still recovering from the detached flow. In this zone the flow is still massively disturbed and it tends to recover to an equilibrium flow with a thinner δ^*. The second one is that it could be a side effect due to the suction device. However this second argument is unlikely as it was found that the boundary layer downstream of the suction on the clean floor was close to the Schlichting turbulent boundary layer.

	%δ			%δ*		
	x=220	x=270	x=320	x=220	x=270	x=320
rounded rectangle	7	32	23	-16	-11	-15
1mm ballotini	-1	1	6	4	-1	-8
2mm ballotini	16	32	20	16	13	3
rectangle + 1mm ballotini	66	73	56	107	95	49

Table 7.3: *Difference in δ and δ^* expressed in % between the thin ice casting 11-2 and its corresponding simplistic shapes*

From Figure 7.10 and Table 7.3, we can see that the displacement thickness for the 1 mm ballotini simplistic shape matches perfectly the curve of the

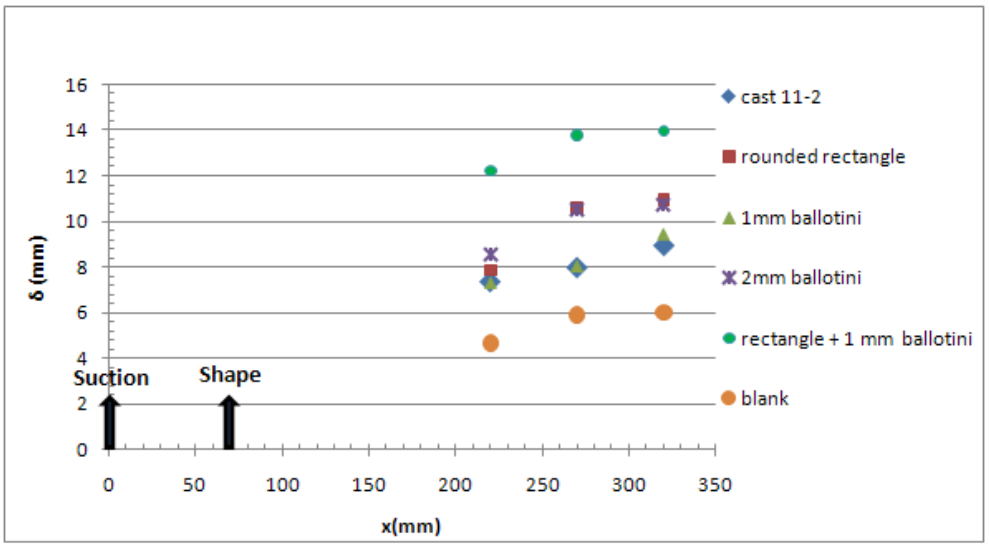

(a) Boundary layer thickness

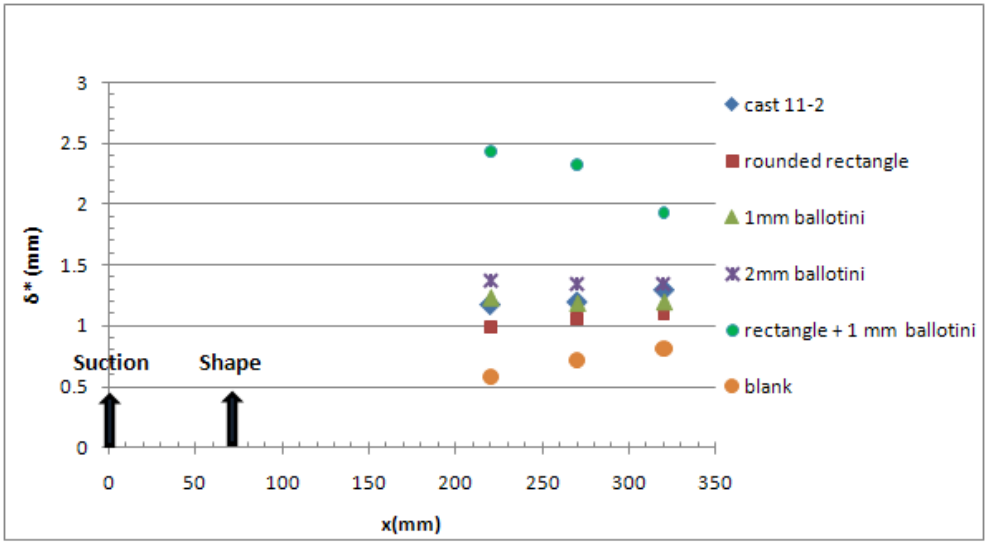

(b) Displacement thickness

Figure 7.10: *Boundary layer characteristics for the thin ice casting 11-2 (4 mm, maximum continuous icing conditions, LWC=0.42g.m^{-3}, 16µm≤MVD≤18µm) and its corresponding simplistic shapes*

casting 11-2. The difference between both δ^* is less than 10 %. The curve from the 2mm ballotini is slightly above the one from the casting 11-2 whereas the one from the rounded rectangle is slightly below the one from the casting. The rectangle with 1mm ballotini has a more dramatic effect on the flow due

to its sharp corner. Dittmar (2010) has extended this study to other simplistic shapes based on 4mm heigh beads. The beads were actually pins. She studied how the distribution and density of the beads may affect the flow and how it can be compared to the ice casting 11-2 which has a maximum thickness of 4 mm. However, none of the distributions tried by Dittmar (2010) give results as close to the casting as the 1mm ballotini.

For the thick shape (Table 7.4 and Figure 7.11), the first remark is that it is much more dramatic in terms of boundary layer disturbance than the thin shape.

	%δ			%δ*		
	x=220	x=270	x=320	x=220	x=270	x=320
rounded rectangle	-14	-12	-8	-17	-28	-16
rounded rectangle +1mm ballotini	3	4	7	27	11	18
rounded triangle	46	51	97	75	39	74

Table 7.4: *Difference in δ and δ^* expressed in % between the ice casting 2b-3 and its corresponding simplistic shapes*

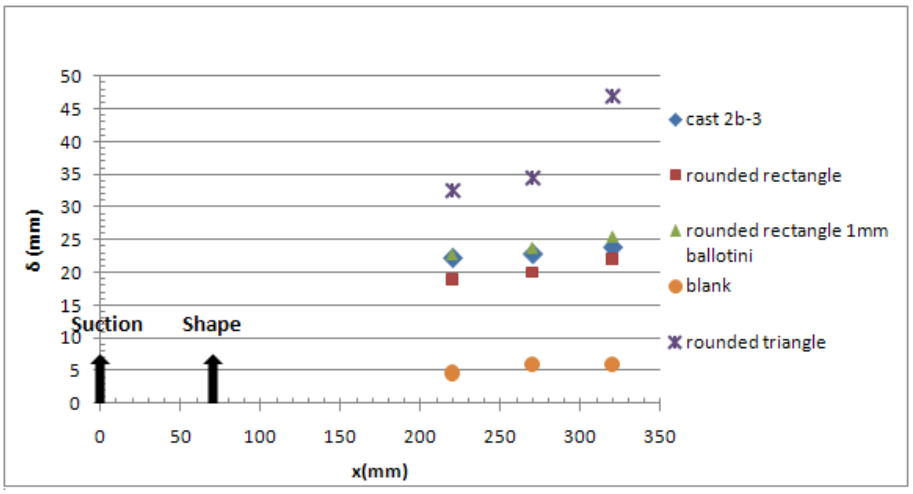

(a) Boundary layer thickness

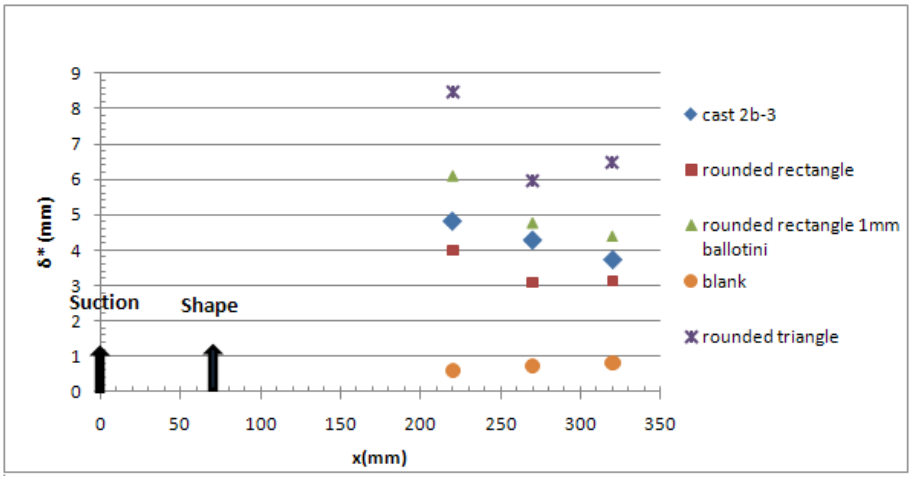

(b) Displacement thickness

Figure 7.11: *Boundary layer characteristics for the thick ice casting 2b-3 (10 mm, maximum continuous icing conditions, LWC=0.42g.m^{-3}, 16µm≤MVD≤18µm) and its simplistic shapes*

The boundary layer thickness for the thick cast 2b-3 is almost 5 times bigger than the one of the clean plate, whereas with the thin cast 11-2, the boundary layer is not even double in comparison with the clean flat plate. The triangle used by aircraft manufacturers (sharp corner) give detached flow in the zone where the velocity profiles were captured. For this reason it doesn't appear in Figure 7.11. The rounded triangle is a bit less disruptive for the flow (less conservative) and the flow is reattaching in the zone were the velocity profiles are measured. However, the boundary layer is so thick, that the rakes didn't

capture the upper part of the boundary layer (Figure 7.12). In this case the velocity profile were interpolated up to $\frac{u}{U_\infty} = 1$ to calculate the boundary layer characteristics. This, will introduce some further errors into the δ and δ^* values. However, this doesn't much affect δ^* which is more valuable than δ, as it is a small area.

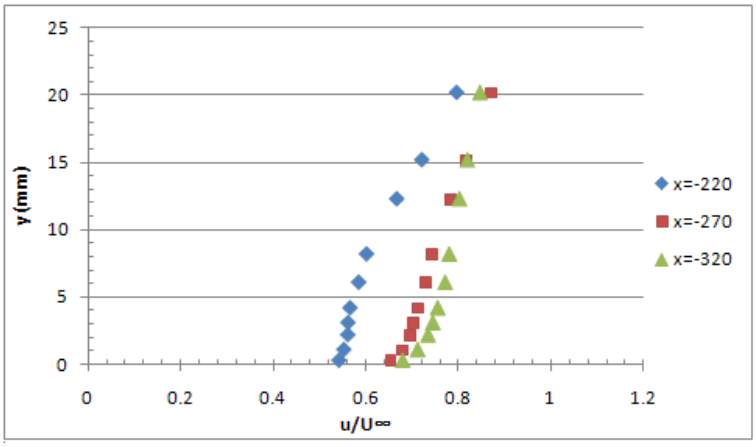

Figure 7.12: *Velocity profiles for the mooth triangle corresponding to the thick cast 2b-3*

Concerning the other simplistic shapes, the rounded rectangle with 1 mm ballotini is slightly more dramatic for the flow than the casting whereas the rounded rectangle with no additional roughness is slightly less dramatic. Once again, δ^* is decreasing, probably because the boundary layer is still recovering after the reattachment. This phenomenon can be seen when looking at the velocity profiles, for instance in Figure 7.12. The velocity profile becomes fuller when the position is moved further downstream. As δ^* represents the area underneath the velocity profile, the area is decreased when the velocity profile becomes fuller. It makes δ^* decrease.

7.7.3 Ice castings for maximum intermittent icing conditions

The casting 7-3 for the maximum intermittent conditions has more 3D features than the other two. The results are presented in Table 7.5 and Figure 7.13. Only 2 pressure measurements downstream of the shape are given as the flow was detached at x=220mm.

The velocty measurements at x=270 mm for the rounded rectangle gives some weird results. At this position, the rounded rectangle has a displacement thickness almost 600% thicker than the casting. The velocity profiles downstream of the rounded rectangle are displayed in Figure 7.13. The profile at x=270 mm is less full than the one for the following position at x=320 mm. An error of measurement during the test could be one of the reasons. At x=320 mm, δ^* of the rounded rectangle is 8% thinner than for the casting. This results makes more sense than the one for x=270mm. Concerning the rounded rectangle with 1mm ballotini on the surface, it seems to produce a displacement thickness at least 50% thicker than for the casting.

	%δ			%δ*		
	x=220	x=270	x=320	x=220	x=270	x=320
smooth rectangle	NA	232	61	NA	580	-8
smooth rectangle + 1mm ballotini	NA	57	79	NA	70	52

Table 7.5: *Difference in % between the ice casting 7-3 and its corresponding simplistic shapes*

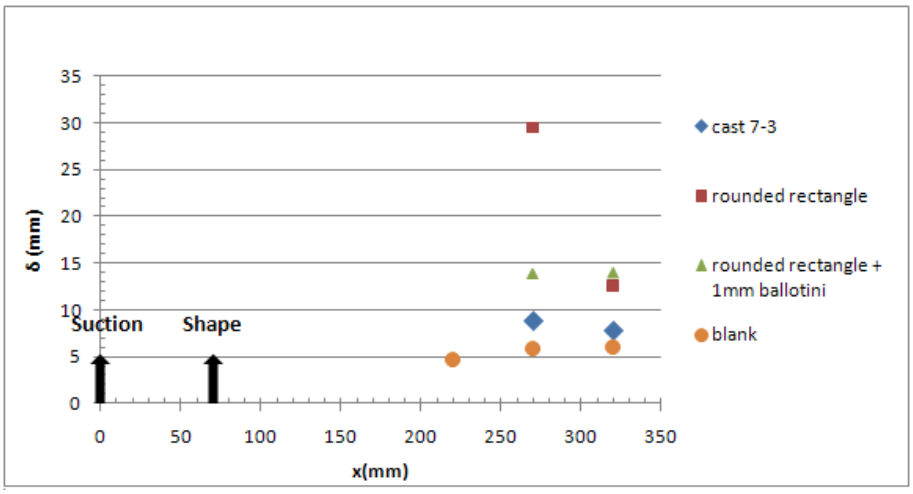

(a) Boundary layer thickness

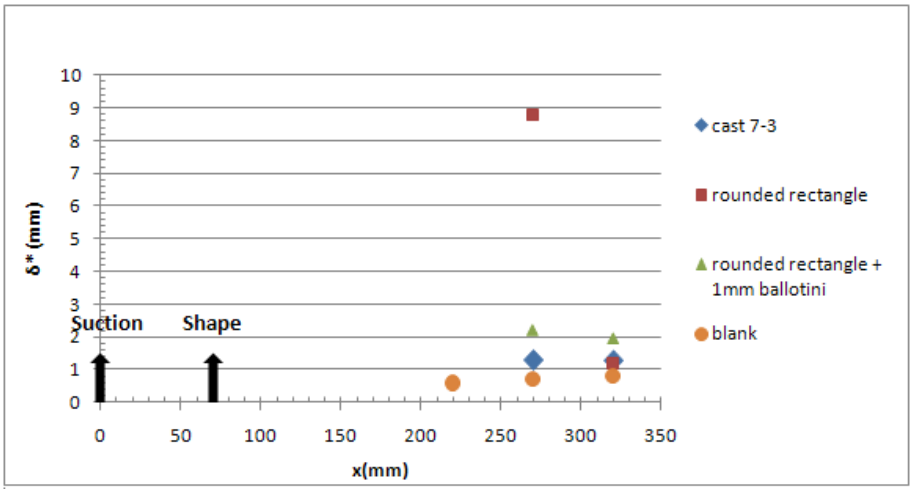

(b) Displacement thickness

Figure 7.13: *Boundary layer characteristics for the ice casting 7-3 (5mm, maximum intermittent icing conditions, LWC=1.2g.m^{-3}, 16µm≤MVD≤18µm)*

It is difficult to draw conclusions from for this case because of several reasons. First of all, only 2 simplistic shapes were tested. Second of all, instead of getting pressure measurements downstream the shapes, only 2 measurements are taken into account. The last reason is that the result of the rounded rectangle at x=270 seems wrong. However, it is possible to conclude that the simplistic shape substrate associated with ballotini is much worse for the flow than the casting. It seems that the rounded rectangle is closer to the casting than the rounded rectangle with 1mm ballotini.

7.8 Discussion

In the present study it is found that the effect on the flow of a 10 mm thick runback ice (cast 2b-3) is in between the effect of a rounded rectangle and the effect of a rounded rectangle with 1mm ballotini on it. For the thin runback ice shape (run 11-2, 4 mm thick) studied in the present work, the casting has an effect on the flow which is in between the effect of the rounded rectangle and the rectangle with 1 mm ballotini on it but with sharp corner. These results are similar to the ones from Broeren et al. (2010c) who studied the aerodynamic performance loss of full-scale runback ice and sub-scale simplistic shapes on a NACA 2312 airfoil (see section 2.2). The authors found that a simple ridge is relatively close to a full-scale iced airfoil from the aerodynamic perspective except for stall and that a simple ridge associated with some roughness on the upper surface (k_s/c=0.0008) resulted in larger performance degradation (in lift and drag) than for the full-scale casting. The authors don't mention if the ridge used to simulate full-scale runback ice has rounded corner or not. This study from Broeren et al. (2010c) is the only one which compares runback ice casting with simplistic shapes.

Dittmar (2010) led experiments in the 8*6 ft wind tunnel, using the same set-up as the present study. The author studied the boundary layer displacement thickness downstream circular pins of 4 mm height. It is interesting to see how close to the 4 mm roughness from Dittmar (2010), cast 11-2, cast 2b-3 and cast 7-3 are. To do so, the displacement thicknesses downstream the castings were compared with the displacement thickness downstream the 4 mm roughness used by Dittmar (2010):

- 4mm pins used by Dittmar (2010) (12 cm long chordwise)
- 4mm pins used by Dittmar (2010) (6.5 cm long chordwise)

The results are presented in Figure 7.14. The 4 mm roughness is much worse for the flow than the cast 11-2. It is clear that roughness of the same height of the ice shape does not reproduce the aerodynamics of the real ice shape. The cast 2b-3 is worse for the flow than the 4 mm roughness. Larger pins should be tested in order to see if a coarse roughness could have the same effect on the flow than the cast 2b-3. For the cast 7-3, the 4 mm pins are very conservative as downstream the pins the boundary layer thickness is twice the size as the boundary layer thickness downstream the casting. The curves

of δ^* of cast 7-3 and cast 11-2 match. Then the cast 7-3 is equivalent to 2 mm ballotini.

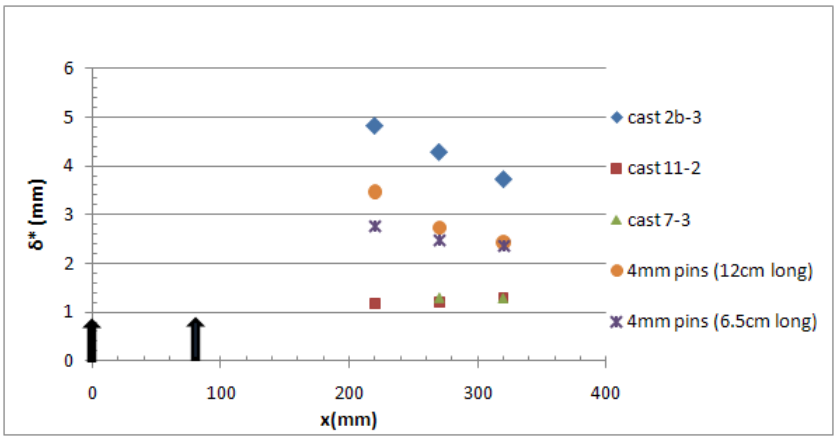

Figure 7.14: *Boundary layer displacement thickness for the casting 7-3 and its corresponding simplistic shapes*

7.9 Conclusions

- The triangle used by the aircraft manufacturers is very conservative. It is the most conservative simplistic shape tested in the present study.
- Rounded corners greatly improve the aerodynamics of the simplistic shapes such as triangle or rectangle.
- The difference between 1 mm ballotini and 2 mm ballotini is small in regards to the displacement thickness generated downstream the ballotini beads.
- 1 mm ballotini and 2 mm ballotini have a similar influence on the boundary layer as the thin cast (d $\approx$ 4 mm) for maximum continuous conditions.
- 2 mm ballotini have the same influence on the boundary layer as the thin cast (d $\approx$ 5 mm) for intermittent continuous conditions.
- Rounded rectangle of 10 mm with 1 mm ballotini on the surface has the same influence on the boundary layers as the thick cast (d $\approx$ 10 mm) for maximum continuous conditions.
- The errors are not large enough to interfere with the results.

Chapter 8

Overall conclusions

An aerodynamic study of full-scale high-fidelity runback ice was necessary in order to help Airbus to enhance their knowledge on this topic with an objective in mind: improve their approach to runback ice in order to make their design of icing systems and their icing policy as reliable and competitive as possible. So far very little knowledge on the aerodynamics and thermodynamics of full-scale runback ice is available in the open literature. Thus the aim of this project was to improve the full-scale runback ice knowledge and find a correlation between real runback ice shapes and simplistic shapes in order to improve the aerodynamic simulation of runback ice. The results of the three years work on runback ice have delivered conclusions directly related with the objectives of this PhD:

- The thermodynamics of the runback ice accretion has been investigated. A spreadsheet has been built which can predict roughly the heat and mass fluxes involved in the runback ice accretion mechanism.

- The geometrical aspects (shape, roughness) of full-scale runback ice shapes has been studied by growing full-scale high-fidelity runback ice shapes in the Cranfield Icing Tunnel. Due to a relatively small section compared to the model, the aerodynamic (speed, AOA) and icing (MVD, LWC) conditions were adapted to be close to full-scale in-flight conditions.

  - It has been possible to get somewhere near to full-scale conditions for the leading edge part of a mid span Boeing 737/700 wing for U_∞=85 $m.s^{-1}$, T_t=−5°C, AOA=8°, MVD=17 μm and LWC=0.42 $g.m^{-3}$or 1.2 $g.m^{-3}$.

  - An electrical heating system has been developed and used for this project. It can be used in an anti-icing mode or a de-icing mode. The heated zone and the heat intensity may be changed easily. The range of wetted surface temperature explored was between 5°C and 20°C.
  - It was possible to grow full-scale runback ice as a function of the heat input intensity, the heat input distribution and the LWC.

- An innovative silicone rubber based ice moulding technique has been developed giving the opportunity to capture multiple planarised castings of a single ice accretion.

- Rectangles, triangles and roughness were selected as simplistic shapes able to simulate full-scale runback ice shapes with different degree of conservatism.

- Relationships between full-scale ice shapes and simplistic shapes were established following low speed (45 $m.s^{-1}$) wind tunnel tests on a flat surface. The ice shapes were embedded in a boundary layer which has a thickness similar to the one on an airfoil leading edge. The velocity profiles downstream the ice shapes were measured to calculate the displacement thickness:

  - 2 mm ballotini simulates a similar boundary layer as runback ice accretions of 4 - 5 mm from continuous and intermittent maximum icing conditions.
  - Rectangle with rounded corner and 1 mm ballotini on the surface simulates with little conservatism runback ice shape of $\approx$ 10 mm from continuous maximum icing conditions.
  - The triangle shape widely used by the aircraft manufacturers is very conservative in terms of aerodynamic performance loss compared to the real ice shape. Actually it is the most conservative shape tested in this study.
  - Rounded corners improve a lot the aerodynamic of the simplistic shapes.

This PhD fully matches the aim and objectives of Airbus. The knowledge of full-scale runback ice shapes geometry has been enhanced. A relationship between full-scale high-fidelity runback ice shapes and simplistic shapes has been found for continuous and intermittent icing conditions. Even if some

simplifications were applied to the work, due mainly to experimental devices limitations, the ice shape of this study are considered as full-scale. The icing tunnel and wind tunnel results are going to be very useful for Airbus in the close future:

- The runback ice shapes which have been recorded during the icing tunnel tests are going to be used for icing code validation purposes
- The aerodynamic results can be used in different ways by Airbus:
  - Simplest and lowest risk is to use the data just to demonstrate that the standard triangle is conservative
  - Going slightly further, the data could be used to justify that a small radius may be added to the standard triangle, instead of having a sharp corner, thereby reducing the aerodynamic penalty due to the triangular simulated runback ice shape
  - Going further still, the data could possibly be used to support an argument that the runback ice shape definition should be changed to a smooth triangle without roughness.

Chapter 9

Future work

Even if the conclusions of this project bring a large contribution to the knowledge of the full-scale runback ice from a thermodynamic and aerodynamic point of view, many improvements can be made in order to make the study all the more valuable in an industrial context.

- Some improvements in the icing tunnel tests are required:
  - The runback ice from a de-icing system requires further study. More runs based on times cycle normally used in industry are necessary to fully understand the runback ice growth for a de-icing system. The moulding technique used for the capture of the runback ice from an anti-icing system may be improved in order to capture ice shape very close to the stagnation zone.
  - Even if many surface temperature configurations were tested, more temperature gradients should be tested. The temperature gradients achieved in the present study may not be representative of the temperature gradient which is produced by a Picolo tube heating system. What's more, some more work is required to study the gradient at the end of the heated zone in regards to experimental data and not in regards to numerical results.
  - Investigate the sensitivity of the runback ice formation to the tunnel speed, to determine if the skin friction and resulting speed of the water film/rivulets affects how quickly they freezes.
- Some improvements in the wind tunnel tests are required:
  - Some more work is required to conduct aerodynamic tests on an airfoil instead of a flat plate to assess if the relationship between the castings and the simplistic shapes remains the same. If a full-scale

airfoil remains too complex to test in the 8*6 feet wind tunnel, changing the design of the upper wall of the tunnel would allow the creation of some pressure gradient on the floor of the tunnel. Hence, the shapes could be attached to the floor and some pressure gradient would be applied to them.

- The behaviour of the aircraft manouevring with some ice on the wings has not been considered. The AOA used in the present study is characteristic of hold conditions. It means that other AOA should be investigated to see how the present results are affected by the other phase of flight (climb, descent).
- Get maximum lift coefficient measurements which is a more meaningful information in terms of aerodynamic performance loss or understand how the measured boundary layer displacement thickness can be linked to Cl_{max} loss.
- Study the aerodynamic effect of runback ice on a swept wing.
- Perform an aerodynamic study for a full-scale or higher Reynolds number.
- Study the aerodynamic effect of runback ice in a pressurised tunnel.
- Flow visualization might improve our knowledge on how the boundary layer downstream the shapes (vorteces detachment, flow recirculation, reattachement point, etc).
- Understand better the sensitivity of the aerodynamic effects to the radius applied to the corner of the simplified shapes.
- Test other types of simplified shapes.
- The 3D effects haven't been investigated in this study. More work is required to determine how the 3D features of the ice affect the aerodynamic performance loss. The 3D effects may be separated in two categories: large and small scale. Large features may appear on runback ice that may produce large effect on the boundary layer. For small features it is more difficult to analyse. Is it roughness? Is it shape? Some more testing is required around a small piece of ice accretion to study the shear stress, heat transfer, etc.

Bibliography

E Achenbach. Effect of surface roughness on the heat transfer from a circular cylinder to the cross flow of air. *International Journal of Heat and Mass Transfer*, vol. 20(4):359–369, 1977.

K. M. Al-Khalil, T. G. Keith, and K. J. De Witt. Development of an anti-icing runback model. Technical Report 0759, AIAA, 1990.

K. M. Al-Khalil, T. G. Keith, and K. J. De Witt. New concept in runback water modeling for anti-iced aircraft surfaces. *Journal of Aircraft*, 30(1): 41–49, 1993.

K. M. Al-Khalil, C. Horvath, D. R. Miller, and W. B. Wright. Validation of nasa thermal ice protection computer codes, part 3 - the validation of antice. 0051, AIAA, 1997.

N. Almendaroglu, A. Feo, W. Gent, C. Golia, D. Guffond, D. W. Hammond, J. Van Hengest, R. Kind, and S. Meyer. Ice accretion simulation. AR 1997, AGARD, 1997.

S. Bell. A beginner's guide to uncertainty of measurements. *NPL Measurement Good Practice Guide*, 11(2), 2001.

K. Birch. Estimating uncertainties in testing. *NPL Measurement Good Practice Guide*, 36, 2001.

M. B. Bragg and A. Khodadoust. Study of the droplet spray characteristics of a subsonic wind tunnel. *Journal of Aircraft*, 32(1):199–204, 1995.

M. B. Bragg and S. L. Wells. Effect of wind tunnel walls on airfoil droplet impingement. *Journal of Aircraft*, 31(1):175–180, 1994.

M. B. Bragg, M. Kerlo, and M. Cummings. Airfoil boundary layer due to large leading edge ice accretion roughness. *AIAA Journal*, 35(1):75–84, 1995.

M. B. Bragg, M. Cummings, and C. M. Henze. Boundary layer and heat transfer measurements on an airfoil with simulated ice roughness. Technical Report 0866, AIAA, 1996.

M. B. Bragg, A. P. Broeren, and L. A. Blumenthal. Iced airfoil aerodynamics. *Progress in Aerospace Sciences*, 41:323–362, 2005.

M. B. Bragg, A. P. Broeren, H. Addy, M. Potapczuk, D. Guffond, and E. Montreuil. Airfoil ice accretion aerodynamics simulation. In AIAA, editor, *45th Aerospace Sciences Meeting and Exhibit*, volume 2, Jan 8-11 2007.

A. P. Broeren and M. B. Bragg. Effect of residual and inercycle ice accretions on airfoil performance. Technical Report 02/68, FAA, 2002.

A. P. Broeren, G. T. Busch, and M. B. Bragg. Aerodynamic fidelity of ice accretion simulation on a subscale model. In SAE, editor, *SAE 2007 Aircraft and Engine Icing*, Sevilla, Spain, 24-27 Sept 2007.

A. P. Broeren, M. B. Bragg, H. E. Addy, S. Lee, F. Moens, and D. Guffond. Effect of high-fidelity ice accretion simulations on full scale airfoil performance. *Journal of Aircraft*, 47(1):240–254, 2010a.

A. P. Broeren, M. B. Bragg, H. E. Addy, S. Lee, F. Moens, and D. Guffond. Effect of high-fidelity ice accretion simulations on the performance of a full-scale airfoil model. TM 216344, NASA, 2010b.

A. P. Broeren, E. A. Whalen, G. T. Busch, and M. B. Bragg. Aerodynamic simulation of runback ice accretion. TM 215676, NASA, 2010c.

R. K. Calay, A. E. Holdo, P. Mayman, and I. Lun. Experimental simulation of runback ice. *Journal of Aircraft*, 34(2):206–212, 1997.

D. Cassou De Salle, A. Gilliot, C. Geiler, J. C. Monnier, A. P. Broeren, and H. E. Addy. Experimental investigation of simulated ice accretions at high reynolds numbers in the onera f1 wind tunnel. In *1st AIAA Atmospheric and Space Environments Conference*, San Antonio, Texas, Jun 22-25 2009. AIAA.

X. Chi, B. Zhu, T. Shih, J. W. Slater, H. E. Addy, and Y. K. Choo. Computing aerodynamic performance of a 2d iced airfoil: Blocking topology and grid generation. Technical Report 0381, AIAA, 2002.

X. Chi, H. Li, Y. Chen, H. E. Addy, Y. K. Choo, and T. Shih. A comparative study using cfd to predict iced airfoil aerodynamics. Technical Report 1371, AIAA, 2005.

J. J. Chung and H. E. Addy. A numerical evaluation of icing effects on a natural laminar flow airfoil. Technical Report 0096, AIAA, 2000.

S. G. Cober and G. A. Isaac. Estimating maximum aircraft icing environments using a large data base of in-situ observations. In AIAA, editor, *44th Aerospace Sciences Meeting and Exhibit*, volume 5, page 3268, Jan 9-12 2006.

M. E. Crawford, W. M. Kays, and B. Weigand. *Convective Heat and Mass Transfer*. Mcgraw-Hill Series in Mechanical Engineering, 4th edition, 2005.

G. Croce, H. Beaugendre, and W. G. Habashi. Cht3d: Fensap ice conjugate heat transfer computations with droplet impingement and runback effects. Technical report, AIAA, 2002.

R. A. Da Silveira, C. R. Maliska, D. A. Estivam, and R. Mendes. Evaluation of collection efficiency analysis methods for icing analysis. In *17th International Congress of Mechanical Engineering*, Nov 10-14 2003.

K. Dittmar. Runback ice simulation. Master's thesis, Cranfield University, 2010.

N. Dukhan, K. J. De Witt, K. C. Masiulaniec, and G. J. Van Fossen. Experimental frossling numbers for ice roughened naca 0012 airfoils. *Journal of Aircraft*, 40(6):1161–1167, 2003.

W. J. Duncan, A. S. Thom, and A. D. Young. *An Elementary Treatise on the Mechanics of Fluids*. Edward Arnold LTD., 1960.

T. A. Dunn, E. Loth, and M. B. Bragg. Computational investigation of simulated large droplet ice shapes on airfoil aerodynamics. *Journal of Aircraft*, 35(6):836, 1999.

Fluent. Fluent 6.3 user's guide. URL www.fluent.com.

G. Fortin, J. Laforte, and A. Ilinca. Heat and mass transfer during ice accretion on aircraft wings with an improved roughness model. *International Journal of Thermal Sciences*, 45(6):595–606, 2006.

T. F. Gelder and J. P. Lewis. Comparison of heat transfer from airfoil in natural and simulated icing conditions. TN 2480, NACA, 1951.

T. F. Gelder, J. P. Lewis, and S. L. Koutz. Icing protection for a turbojet transport airplane: Heating requirements, methods of protection and performance penalties. TN 2866, NACA, 1953.

R. W. Gent. Trajice2-a combined water droplet trajectory and ice accretion prediction program for aerofoils. TR 90054, Defence Research Agency RAE, 1990.

R. W. Gent, N. P. Dart, and J. T. Cansdale. Aircraft icing. *Philosophical Transaction of the Royal Society: Mathematical, Physical and Engineering Sciences*, 358(1776):2873–2911, 2000.

V. H. Gray and U. H. Von Glahn. Effect of ice and frost formations on drag of naca 65-212 airfoil for various modes of thermal ice protection. TN 2962, NACA, 1953.

S. D. Green. A study of a u.s. inflight icing accidents and incidents, 1978 to 2002. In AIAA, editor, *44th AIAA Aerospace Sciences Meeting and Exhibit*, volume 2, Jan 9-12 2006.

D. W. Hammond and G. Luxford. The cranfield university icing tunnel. In *41st AIAA Aerospace Sciences Meeting and Exhibit*, Jan 6-9 2003.

R. J. Hansman Jr. Droplet size distribution effects on aircraft ice accretion. *Journal of Aircraft*, 22(6):503–508, 1985.

R. J. Hansman Jr and S. R. Turnock. Investigation of surface water behavior during glaze ice accretion. *Journal of Aircraft*, 26(2):140–147, 1989.

P. V. Hobbs. *Ice Physics*. Oxford University Press, 1974.

E. L. Houghton and P. W. Carpenter. *Aerodynamics for Engineering Students*. Butterworth-Heinemann, 5 edition, 2002.

J. Hua, F. Kong, and H. H. T. Liu. Unsteady thermodynamic computational fluid dynamics simulations of aircraft wing anti-icing operation. *Journal of Aircraft*, 44(4), July-August 2007.

R. F. Ide and D. W. Sheldon. 2006 icing cloud calibration of the nasa glenn icing research tunnel. TM 211577, NASA, 2008.

R. K. Jeck. Icing design envelopes (14 cfr parts 25 and 29, appendix c) converted to a distance-based format. Technical Report DOT/FAA/AR-00/30, FAA, 2002.

H. W. Jentink. Supercooled large droplets in icing conditions. TP 98216, National Aerospace Laboratory of the Netherlands NLR, 2001.

L. E. Kollar, M. Farzaneh, and Karev; A. R. Modeling droplet collision and coalescence in an icing wind tunnel and the influence of these process on droplet size distribution. *International Journal of Multiphase Flow*, 31(1): 69–92, 2005.

A. V. Korolev, G. A. Isaac, and J. W. Strapp. Aircraft escape strategy from supercooled cloud layers. In AIAA, editor, *44th AIAA Aerospace Sciences Meeting and Exhibit*, volume 5, Reno, Nevada, Jan 9-12 2006.

S. Lee and M. B. Bragg. Effect of simulated spanwise ice shapes on airfoils: Experimental investigation. Technical Report 0092, AIAA, 1999.

S. Lee, H. S. Kim, and M. B. Bragg. Investigation of factors that influence iced airfoil aerodynamics. Technical Report 0099, AIAA, 2000.

G. Li, E. J. Gutmark, R. T. Ruggieri, and J. H. Mabe. Correlation of local heat transfer coefficients and pressure on an airfoil. Technical Report 4202, AIAA, 2003.

G. A. Lima da Silva, O. M. Silvares, and E. J G. J. Zerbini. Airfoil anti-ice system modeling and simulation. Technical Report 734, AIAA, 2003.

G. A. Lima da Silva, O. M. Silvares, and E. J G. J. Zerbini. Simulation of an airfoil electro-thermal anti-ice system operating in running wet regime. In AIAA, editor, *43rd AIAA Conference Aerospace Sciences Meeting and Exhibit*, Reno, Nevada, Jan 10-13 2005.

G. A. Lima da Silva, O. M. Silvares, and E. J G. J. Zerbini. Numerical simulation of airfoil thermal anti-ice operation part 1: Mathematical modeling. *Journal of Aircraft*, 44(2):627–634, 2007a.

G. A. Lima da Silva, O. M. Silvares, and E. J G. J. Zerbini. Numerical simulation of airfoil thermal anti-ice operation part 2: Implementation and results. *Journal of Aircraft*, 44(2):635–641, 2007b.

P. Louchez, G. Fortin, G. Mingione, and V. Brandi. Beads and rivulets modelling in ice accretion on a wing. Technical Report 0489, AIAA, 1998.

B. J. Mason. *Physics of Clouds*. Oxford Classic Texts in the Physical Sciences, 1971.

B. L. Messinger. Equilibrium temperature of an unheated icing surface as a function of air speed. *Journal of the Aeronautical Sciences*, 20(1):29–42, 1953.

M. Milanez and G. F. Naterer. Eulerian cross-phase diffusive effects on impinging droplets and phase change heat transfer. *International Communications in Heat and Mass Transfer*, 32(3-4):286–295, 2005.

T. G. Myers. Extension to the messinger model for aircraft icing. *AIAA Journal*, 39(2):211–218, 2001.

T. G. Myers and J. P. F Charpin. A mathematical model for atmospheric ice accretion and water flow on a cold surface. *International Journal of Heat and Mass Transfer*, 47(25):5483–5500, 2004.

T. G. Myers and D. W. Hammond. Ice and water film growth from incoming supercooled droplets. *International Journal of Heat and Mass Transfer*, 42 (12):2233–2242, 2004.

K. E. Noll and M. J. Pilat. Inertial impaction of particles upon rectangular bodies. *Journal of Colloid and Interface Sciences*, 33(2):197–207, 1970.

NTSB. Aircraft accident report. Technical Report PB96-91040I, National Transportation Safety Board, Washington, D.C. 20594, 1996.

S. O'Rourke. Icecremo ii project - validation report. Foreground Data 77740, Airbus, 2006.

A. A. Ozalp and H. Umur. An experimental investigation of the combined effects of surface curvature and streamwise pressure gradients both in laminar and turbulent flows. *Heat and Mass Transfer*, 39(10):869–876, 2003.

J. Pan, E. Loth, and M. B. Bragg. Rans simulation of airfoils with ice shapes. Technical Report 729, AIAA, 2003.

M. Papadakis, A. Rachman, S. Wong, H. Yeong, K. E. Hung, and C. S. Bidewell. Water impingement experiments on a naca 2312 airfoil with simulated glaze ice shapes. In AIAA, editor, *42nd AIAA Conference Aerospace Sciences Meeting and Exhibit*, Reno, Nevada, Jan 5-8 2004a.

M. Papadakis, H. Yeong, and S. Wong. Aerodynamic performance of a swept wing with simulated ice shapes. In *42nd AIAA Conference Aerospace Sciences Meeting and Exhibit*, Reno, Nevada, Jan 5-8 2004b.

M. Papadakis, S. H. Wong, H. W. Yeong, S. C. Wong, and G. T. Vu. Icing tunnel experiments with a hot-air anti-icing system. Technical Report 444, AIAA, 2008.

M. K. Politovich. Predicting glaze or rime ice growth on airfoils. *Journal of Aircraft*, 37(1):117–121, 2000.

A. Ragni, B. Esposito, M. Marazzo, M. Bellucci, and L. Vecchione. Calibration of the cira iwt in the high speed configuration. Technical Report 471, AIAA, 2005.

A. L. Reehorst and G. P. Richter. New methods and materials for molding and casting ice formation. TM 100126, NASA, 1987.

G. A. Ruff and B. M. Berkowitz. User manual for the nasa lewis ice accretion code (lewice). CR 185129, NASA, 1990.

F. Saeed, Selig M. S., and M. B. Bragg. Design of a subscale airfoil with full-scale leading edges for ice accretion testing. *Journal of Aircraft*, 34(1): 94–100, 1997.

F. Saeed, Selig M. S., M. B. Bragg, and H. E. Addy. Experimental validation of the hybrid airfoil desigb procedure for full-scale ice accretion simulation. Technical Report 0199, AIAA, 1998.

J. Sancho. *Runback Ice Modeling: Development of an Experimental Test Rig*. Msc, Cranfield University, 2008.

H. Schlichting. *Boundary Layer Theory*. Pergamon Press Ltd, 1955.

J. Shin. Characteristics of surface roughness associated with leading edge ice accretion. *Journal of Aircraft*, 33(2):316–321, 1996.

R. Stanfield. *Influence of the Flight-Path Variability of Conditions Upon In-Flight Icing*. PhD thesis, Cranfield University, 2008.

NASA STI. Scientific and technical information. URL http://sti.nasa.gov.

J. R. Taylor. *An Introduction to Error Analysis*. University Sciences Books, 1982.

J. Tu, G. H. Yeo, and C. Liu. *Computational Fluid Dynamicd: A Practical Approach*. Elsevier Inc, 2008.

A. B. Turner, S. E. Hubbe-Walker, and F. J. Bayley. Fluid flow and heat transfer over straight and curved rough surfaces. *International Journal of Heat and Mass Transfer*, 43(2):251–262, 2000.

UIUC. Uiuc airfoil data site. URL www.ae.illinois.edu/m-selig/ads/coord_database.

M. Vargas, J. C. Tsao, and A. P. Rothmayer. Review of role of icing feathers in ice accretion formation. Technical Report 01-3294, SAE, 2007.

T. Wang and T. W. Simon. Heat transfer and fluid mechanics measurement in transitional boundary layers on convex curved surfaces. *Journal of Turbomachinery*, 109(3):443–452, 1987.

E. A. Whalen, A. P. Broeren, M. B. Bragg, and S. Lee. Characteristics of runback ice accretions on airfoils and their aerodynamic effects. In AIAA, editor, *43rd AIAA Conference Aerospace Sciences Meeting and Exhibit*, Reno, Nevada, Jan 10-13 2005.

E. A. Whalen, A. P. Broeren, and M. B. Bragg. Consideration for aerodynamic testing of scaled runback ice accretions. In *44th AIAA Aerospace Sciences Meeting and Exhibit*, Reno, Nevada, Jan 9-12 2006.

F. M. White. *Viscous Fluid Flow, 3rd Edition.* Mc Grow Hill International Edition, 2006.

S. Wirogo and S. Srirambhatla. An eulerian method to calculate the collection efficiency on two and three dimensional bodies. Technical Report 1073, AIAA, 2003.

W. B. Wright. Users manual for the improved nasa lewis ice accretion code lewice 1.6. CR 198355, NASA, 1995.

W. B. Wright. Validation methods and results for a two-dimensional ice accretion code. *Journal of Aircraft*, 36(5):827–835, 1999.

W. B. Wright. An evaluation of jet impingement heat transfer correlations for piccolo tube applications. In AIAA, editor, *42nd AIAA Conference Aerospace Sciences Meeting and Exhibit*, Reno, Nevada, Jan 5-8 2004.

W. B. Wright. Validation results for lewice 3.0. In AIAA, editor, *43rd AIAA Conference Aerospace Sciences Meeting and Exhibit*, Reno, Nevada, Jan 10-13 2005.

Alec Tiranti Ltd Edge Impact Consulting Ltd. www.tiranti.co.uk. URL http://www.tiranti.co.uk/.

B. Zhu, X. Chi, T. I-P. Shih, and J. W. Slater. Computing aerodynamic performance of a 2d iced airfoil: Blocking strategy and convergence rate. Technical Report 3049, AIAA, 2002.

B. Zhu, X. Chi, T. I-P. Shih, J. W. Slater, H. E. Addy, and Y. K. Choo. Computing aerodynamic performance of a 2d airfoils with structured grids. Technical Report 1071, AIAA, 2003.

Appendix A

Appendix C of FAA FAR Part 25

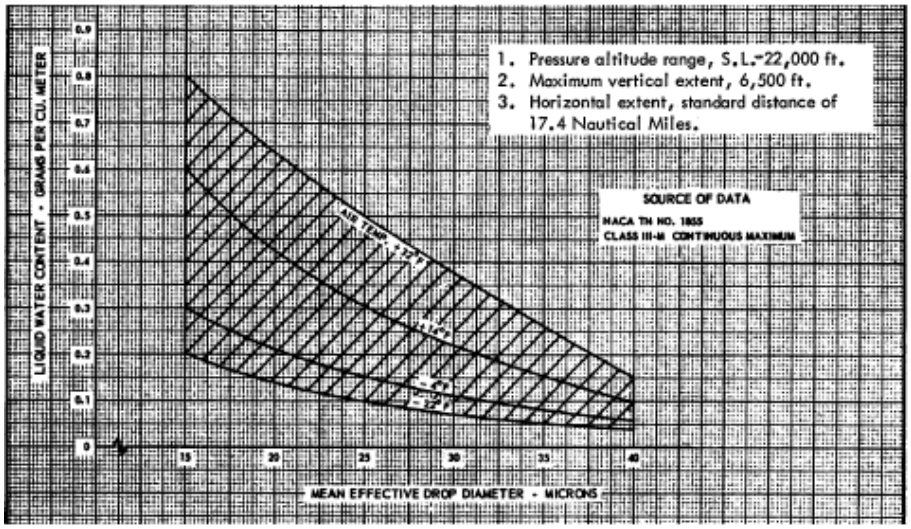

Figure A.1: *Continuous maximum conditions, LWC vs MVD (Jeck (2002))*

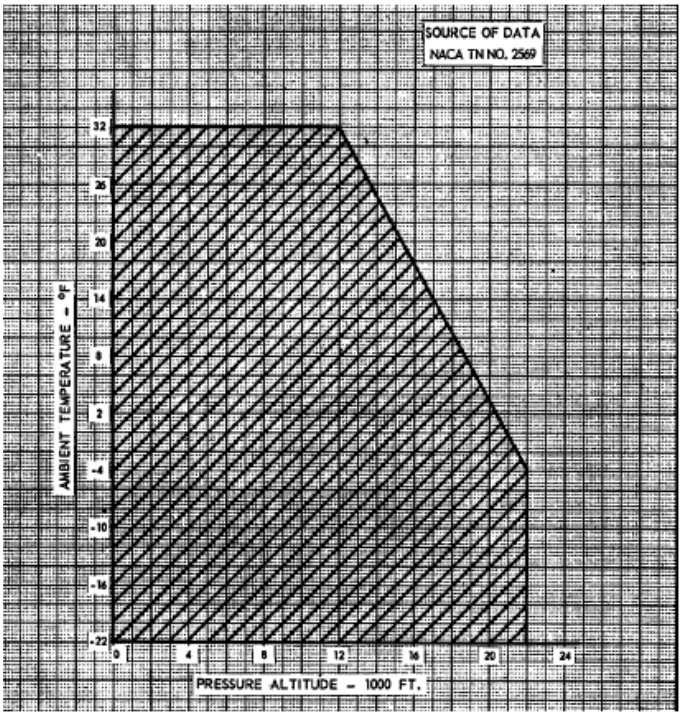

Figure A.2: *Continuous maximum conditions, ambient temperature vs ambient pressure (Jeck (2002))*

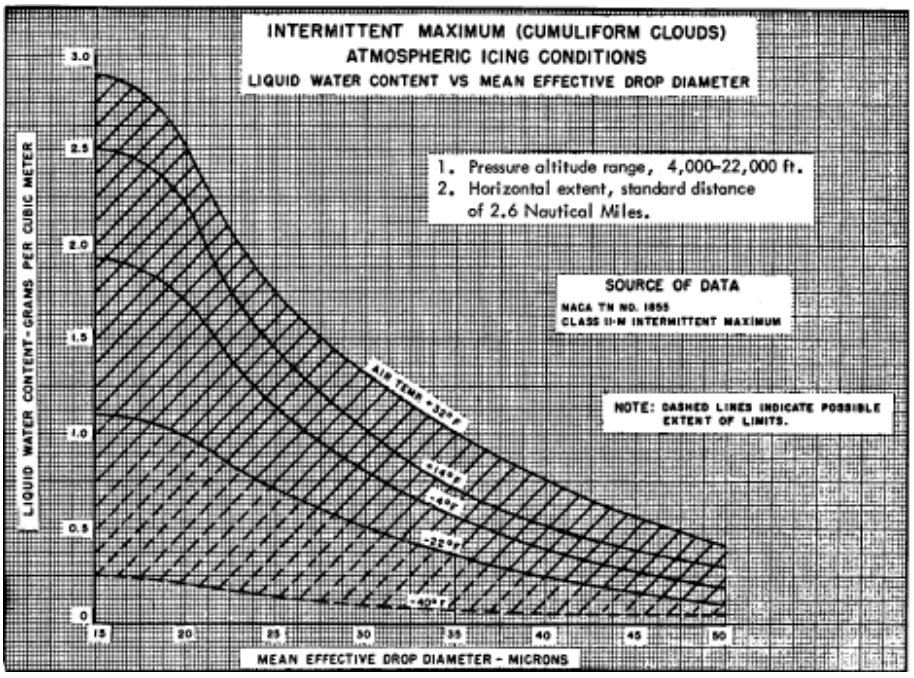

Figure A.3: *Intermittent maximum conditions, LWC vs MVD (Jeck (2002))*

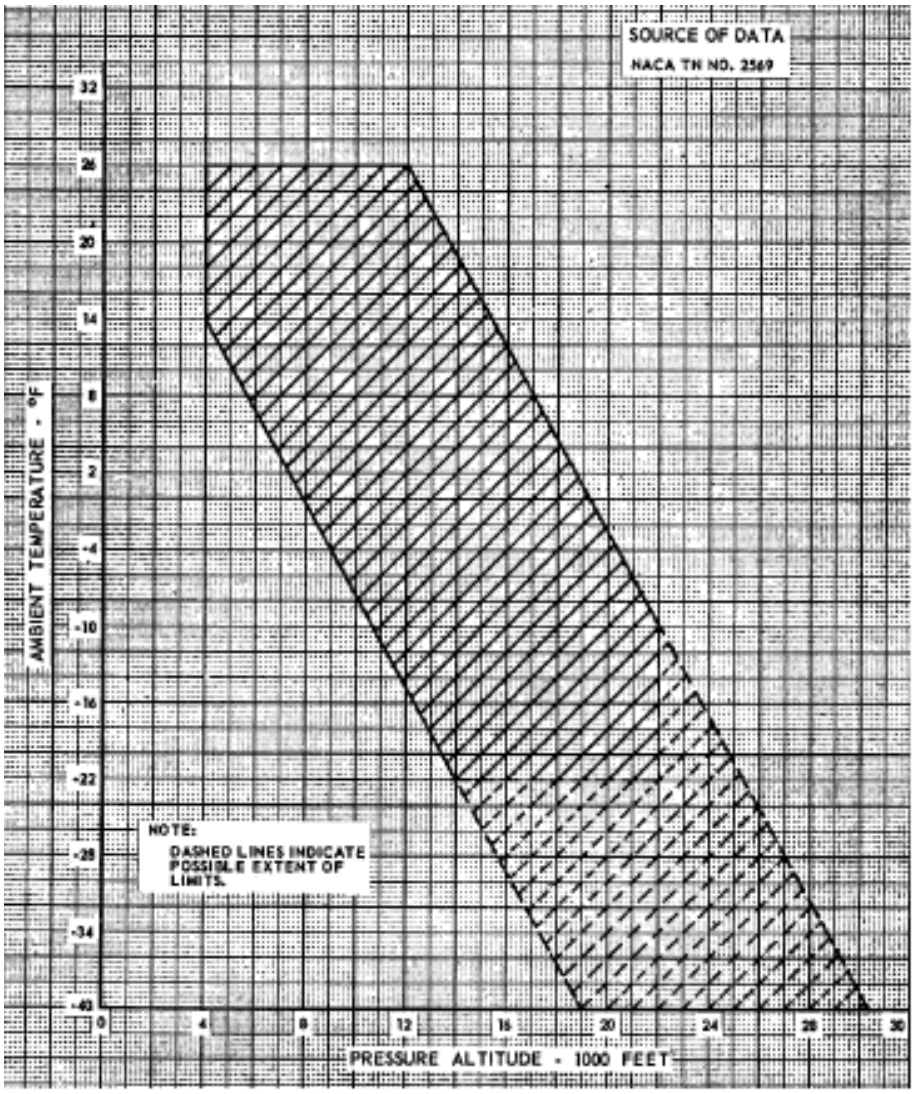

Figure A.4: *Intermittent maximum conditions, ambient temperature vs ambient pressure (Jeck (2002))*

Appendix B

Details of the heat and mass transfer calculation in the 1D model

The details of the calculation comes from Messinger (1953) and Hansman Jr and Turnock (1989) , except the evaporative flux formulations which come from Hansman Jr and Turnock (1989) and O'Rourke (2006). The reason for testing different evaporative flux formulations is because evaporation is one of the main heat loss in the system and its formulation is slightly changed between the authors.

The energy terms which are included in the system are:

- Heat from the anti-icing system (Wm^{-2})

$$\dot{Q}''_{anti} = \begin{cases} \dot{Q}''_{anti} & \text{if within the heated zone} \\ 0 & \text{if not} \end{cases} \tag{B.0.1}$$

- Latent heat of fusion released as the droplet freeze downstream the heating system (Wm^{-2})

$$\dot{Q}''_{freezing} = \begin{cases} 0 & \text{if within the heated zone} \\ M''_{freeze}\left(L_f + C_i\left(273 - T_S\right)\right) & \text{if not} \end{cases} \tag{B.0.2}$$

- Aerodynamic heating due to the viscous effects in the boundary layer (Wm^{-2})

$$\dot{Q}''_{\text{aero heating}} = \frac{rhU_\infty^2}{2C_p} \tag{B.0.3}$$

- Kinetic energy of the droplet impacting the surface (Wm^{-2})

$$\dot{Q}''_{\text{drop kinetic energy}} = \frac{M_{imp}U_\infty^2}{2} \tag{B.0.4}$$

The energy terms which are removed from the system are:

- Convection heat (Wm^{-2})

$$\dot{Q}''_{conv} = h\left(T_S - T_\infty\right) \tag{B.0.5}$$

- Evaporative heat (Wm^{-2})
  - Hansman Jr and Turnock (1989)

$$\dot{Q}''_{evap} = \frac{hD_wL_v}{k_a}(\rho_{vsurf} - \rho_{v\infty}) = M_{evap}L_v \tag{B.0.6}$$

  - O'Rourke (2006)

$$\begin{aligned}\dot{Q}''_{evap} &= \frac{0.622hL_v}{c_pP_tL_e^{2/3}}\left(e_s\frac{T_t}{T_S}\left(\frac{P_l}{P_t}\right)^{-\frac{1}{\gamma}} - R_he_\infty\frac{P_t}{P_\infty}\right) \\ &= M_{evap}L_v\end{aligned} \tag{B.0.7}$$

- Heat absorbed from the surface as supercooled droplet impinge and warm to the recovery temperature in the heated zone°C (Wm^{-2})

$$\dot{Q}''_{\text{drop warming}} = \dot{M}_{imp}c_w\left(T_S - T_\infty\right) \tag{B.0.8}$$

Then at the steady state the balance equations between the heat fluxes are:

- In the impingement zone within the heated zone

$$\begin{aligned}\dot{Q}''_{\text{aero heating}} + \dot{Q}''_{\text{drop kineic energy}} + \dot{Q}''_{anti} = \dot{Q}''_{conv} + \dot{Q}''_{evap} \\ + \dot{Q}''_{\text{drop warming}}\end{aligned} \tag{B.0.9}$$

- Outisde the impingement zone within the heated zone

$$\dot{Q}''_{\text{aero heating}} + \dot{Q}''_{anti} = \dot{Q}''_{conv} + \dot{Q}''_{evap} \tag{B.0.10}$$

- Downstream the heated zone

$$\dot{Q}''_{\text{aero heating}} + \dot{Q}''_{freeze} = \dot{Q}''_{conv} + \dot{Q}''_{sub} \tag{B.0.11}$$

M''_{imp}, M''_{freeze} and M''_{evap} can be found easily:

$$M''_{imp} = \beta\, LWC\, U_\infty \left(kgm^{-2}s\right) \tag{B.0.12}$$

$$M''_{evap} = \frac{\dot{Q}_{evap}}{L_v} \left(kgm^{-2}s\right) \tag{B.0.13}$$

Finally the mass balance allow us to calculate the runback water mass flux:

- At the stagnation zone which is the first control volume:

$$A\, M''_{imp,0} = 2M_{out,0} + A\, M''_{evap,0} \tag{B.0.14}$$

- Downstream the stagnation zone and within the impingement zone and the heated zone the mass balance in CV_i:

$$A\, M''_{imp,i} + M_{out,i-1} = M_{out,i} + A\, M''_{evap,i} \tag{B.0.15}$$

- Downstream the impingement zone and within the heated zone the mass balance in CV_i:

$$M_{out,i-1} = M_{out,i} + A\, M''_{evap,i} \tag{B.0.16}$$

- Downstream the heated zone the mass balance in CV_i:

$$M_{out,i-1} = M_{out,i} + A\, M''_{freeze,i} \tag{B.0.17}$$

The control volume where we stop the calculation depend on the limit of the heated zone.

Appendix C

Icing tunnel calibration

C.1 Background

An icing tunnel is quite useful and very rare testing facility. The main ones, are the one from NASA in the US and from CIRA in Italy. The Cranfield Icing Tunnel is the only one of this kind within university environment. Even if the CIT is not as big as the main ones, it is very convenient tunnel to study aircraft icing and all different kinds of phenomena linked to icing.

The CIT (Figure C.1, Hammond and Luxford (2003)) has a choice of different working section. The one used in the present work is a rectangular section of $760 * 760$ mm. It has a gentle contraction for better cooling, distribution and acceleration of larger droplets. The Mach number range is 0.1 to 0.5. The total air temperature range is from - 30°C to + 30°C and the droplet sizes from 15 to 80 μm. The LWC range is from 0.05 to 3 $g.m^{-3}$. However, the limits of each range of conditions can not be reached simultaneously. The cloud is monitored by the spray rake upstream the test section made from 6 horizontal bars with nozzles (Figure C.2). The bars constitute a double pipe. One is for the water jet which is coming out the nozzle and the other one is for the air jet which is cuting the water jet and which is monitoring the droplet size. By changing the air and water pressure it is possible to change the droplets size and the LWC. The nozzles can be closed or opened and it is possible to add pipe underneath or above a part of the bar in order to help the cloud mixing.

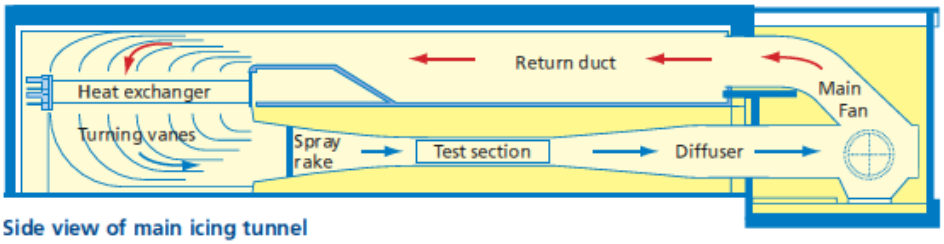

Figure C.1: *Cranfield icing tunnel facility*

Figure C.2: *Spray in the CIT, configuration with all the nozzles blocked*

To monitor the icing conditions a calibration of the tunnel is necessary to make the link between the nozzles water pressure, the nozzles air pressure, the droplets diameter and the LWC required for the experiments (Ragni et al. (2005) and Ide and Sheldon (2008)). To find an uniform cloud the nozzles configuration has to be changed several times before finding the one which gives a cloud as uniform as possible with the required droplets diameter and LWC. A family of curves which link the water pressure and air pressure to the volumetric median droplet diameter is used to get all the information necessary to set up the droplet MVD into the cloud (Figure C.3). It is not a matter of getting a uniform cloud and never change it again. The requirements for the cloud are different for each model tested and conditions.
The method used to do the cloud calibration is the icing blade method. The technique, though labour intensive, is easy to implement and gives satisfactory results for a large range of conditions (Ide and Sheldon (2008)). First of all, values of water pressure and air pressure are read on Figure C.3 for

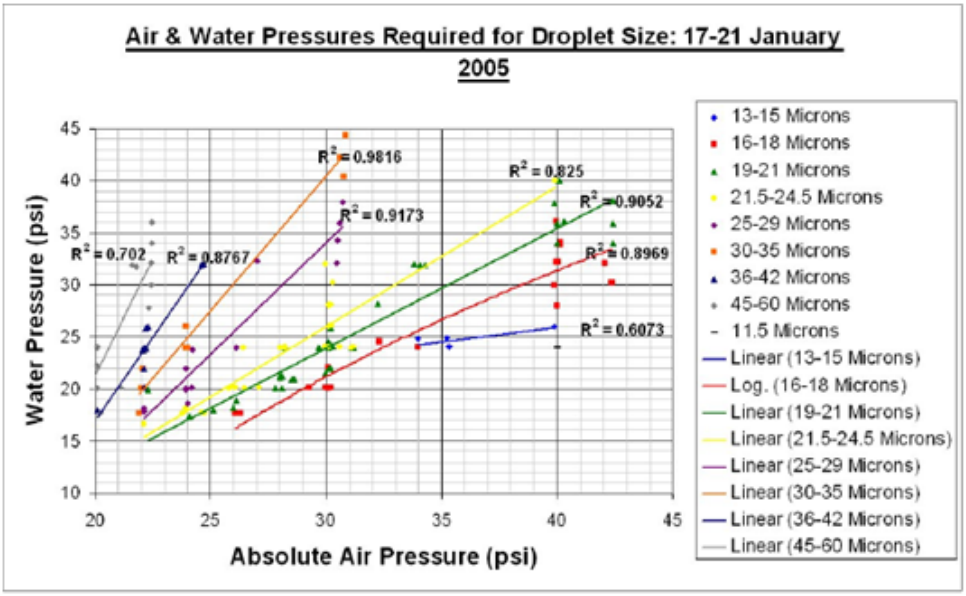

Figure C.3: *Data captured during the CIT droplet size calibration that allows determination of system air pressure according to system water pressure for different droplet size ranges.*

the required droplet diameter range. Then a metal blade is introduced into the tunnel during a certain time step for the chosen water pressure and air pressure. By measuring the thickness of the ice on the blade using a chilled micrometer, we can get the LWC. The formula used to get the LWC is:

$$LWC = \frac{i\rho_i}{tU_\infty B} \tag{C.1.1}$$

with ρ_i the ice density: $\rho_i = 0.9 g.cm^{-3}$.

The global catch efficiency is assumed to be 1 for the icing blade. It is then possible to study the cloud uniformity by changing the nozzles configuration until the correct LWC distribution is reached. The objective for the present study is to get a LWC of $\pm 10\%$ of the mean value in a zone of 10-15 cm width situated in the middle of the span to reduce the wall effect. Before studying the cloud uniformity a study of the droplets trajectories in front of the model has to be made in order to decide at which distance in front of the model the icing blade test needs to be done (see Appendix D). The study of the droplets trajectories in front of the model is not always necessary. For small models for instance, such study is not required. However, when it comes to large model this preliminary work is necessary to ensure that the LWC measured is not

in a zone where the model has an influence on the droplets trajectories. It was decided to do the icing blade test 25 cm from the Hybrid model leading edge at 8 vertical position with an increment of 2 cm between each position (Figure C.4).

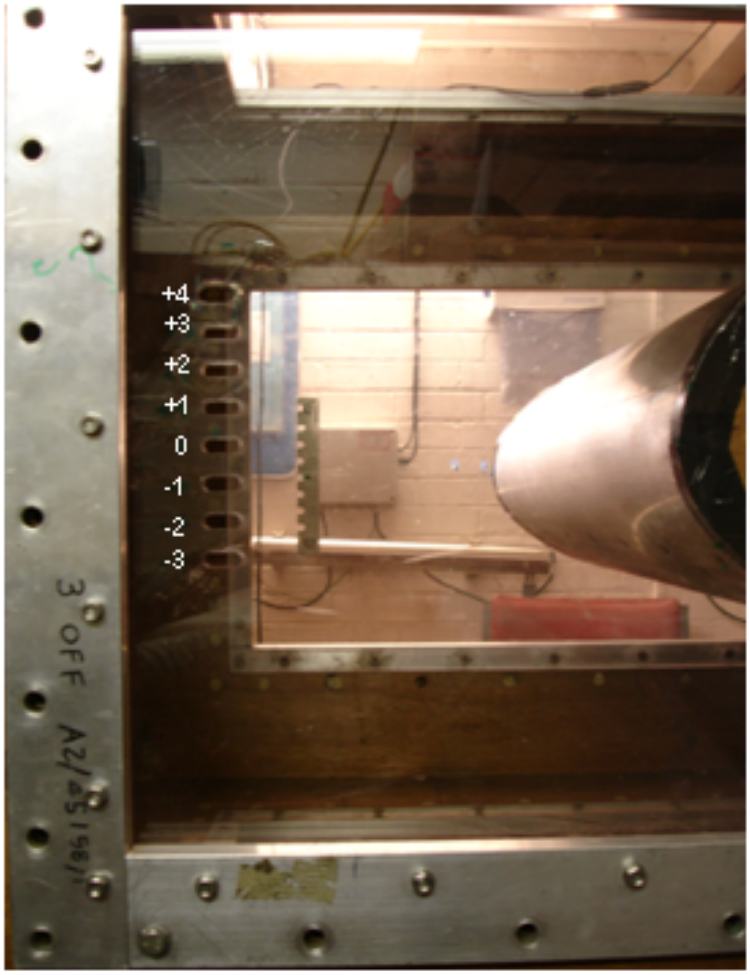

Figure C.4: *Position of the icing blade 25 cm in front of the model*

C.2 Calibration

The calibration was done with a static temperature of -15°C, a free stream velocity of 85 $m.s^{-1}$ and 16 μm≤MVD≤18 μm. The time of the spraying for each icing blade position was 30 s. The final nozzles configuration is presented in Figure C.5. The Figure represents the nozzles which are opened or blocked. The measurement of the ice thickness along the blade is made every each 5 cm. A map of the ice thickness along the blade for the 8 vertical positions is presented in Figure C.6. In Figure C.6, the position 4 is 40 cm from the left hand side when looking in front if the model and so on for the other positons. From the previous picture, it has been decided that the width of the studied zone will be between the positions 3 and4. The mean LWC in that zone is 0.42 $g.m^{-3}$within the ± 10% scatter. The front and top view of the cloud shows the uniform zone centred in the middle of the span (Figure C.7).

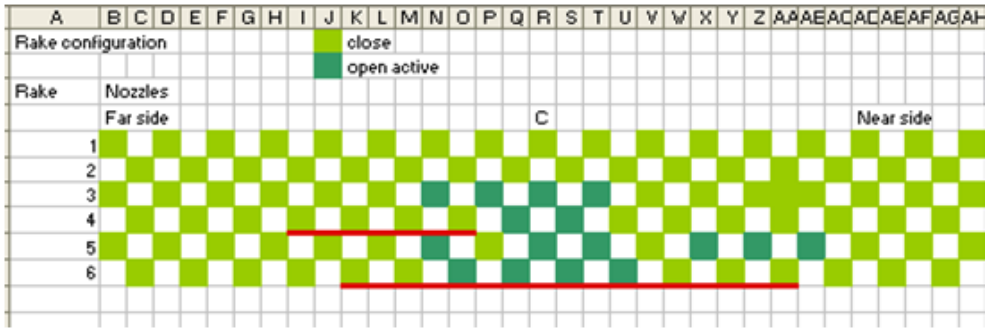

Figure C.5: *Final cloud configuration*

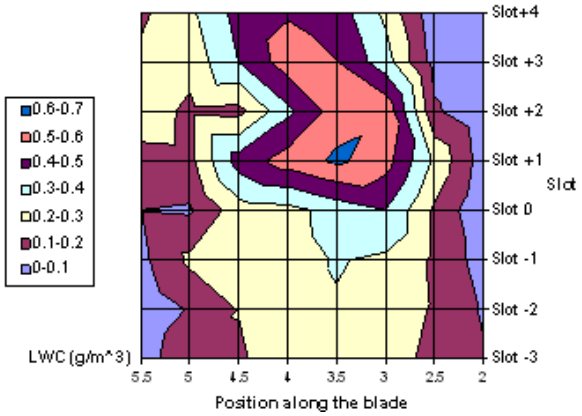

Figure C.6: *Final cloud LWC distribution*

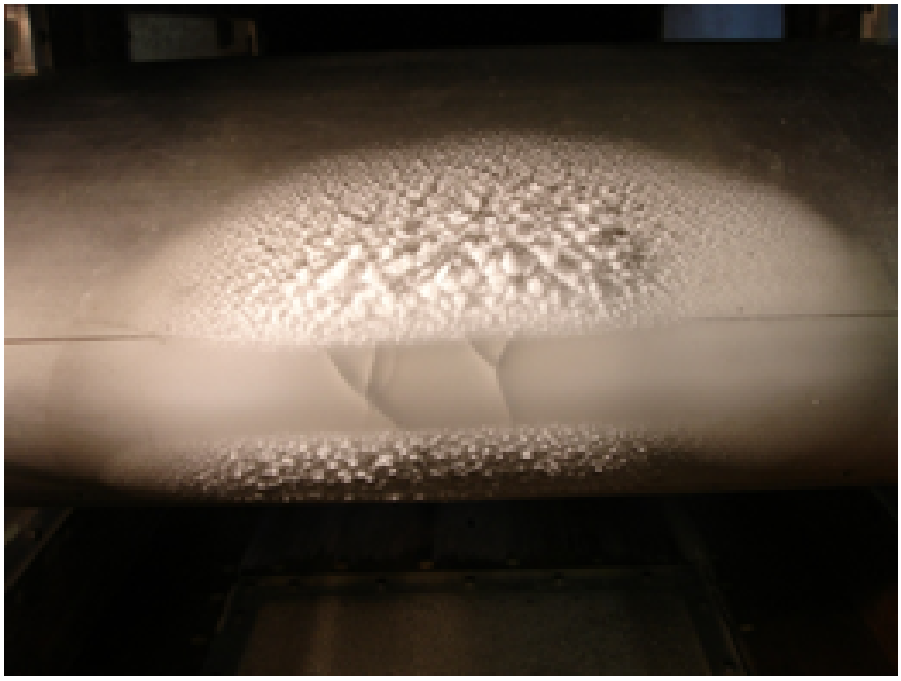

(a) Front view

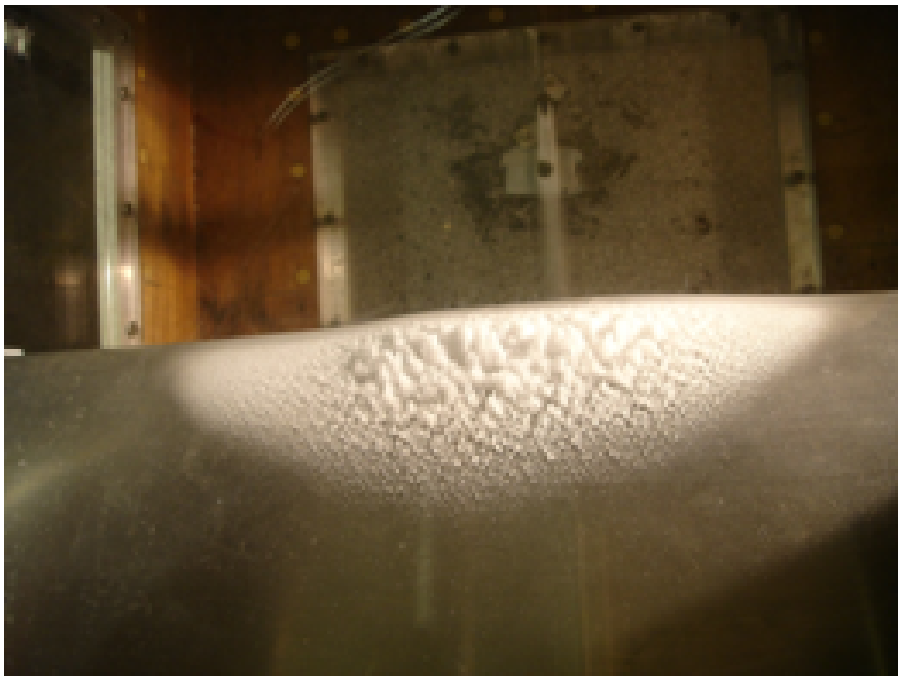

(b) Top view

Figure C.7: *Final cloud after 7 min and 30 s of impingement ($U\infty$ =85 $m.s^{-1}$, 16 $\mu m \leq MVD \leq 18$ μm, LWC=0.42 $g.m^{-3}$, Ts=- 15° C)*

The curve of the LWC as function of the water pressure was determined (Figure C.8 and Table C.1). The result is a smooth curve which tends to reach plateau for water pressure above 25psi. It seems that the intermittent LWC of 2.2 $g.m^{-3}$can not be reach with such speed, airfoil and cloud configuration. Then, it has been decided to use a LWC of 1.2 $g.m^{-3}$ for the intermittent conditions. The atmospheric pressure during the time of the calibration was 990 mbar (14.37 psi). It has to be taken into account to set up the water and air pressure. If the atmospheric pressure of the day of testing is different from the one of the calibration it means that the water and air pressure are different as well.

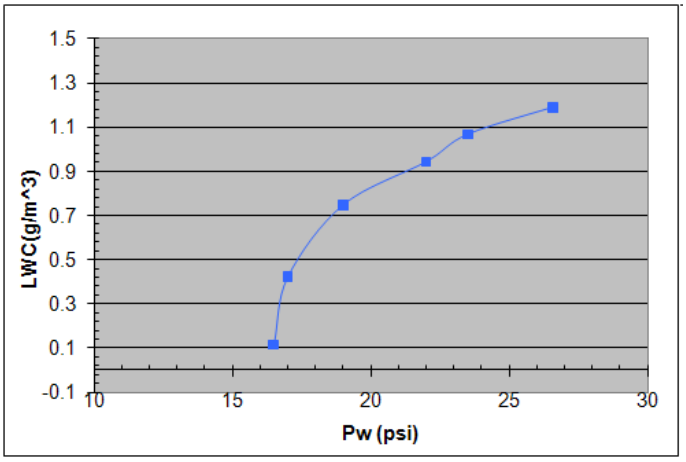

Figure C.8: *LWC as function of the warer pressure for 16 $\mu m \leq MVD \leq 18$ μm*

	Pw (psi)	Pa (psi)	LWC(g/m^3)
Continuous conditions	17	26.7	0.42
Intermittent conditiosn	26.6	35	1.19

Table C.1: *Spray conditions for the icing tunnel experiments*

Following the CIT calibration, the LWC for the continuous and intermittent conditions has been changed. The final conditions for the icing tunnel tests are:

Aerodynamic conditions		Icing conditions				
AOA (°)	Speed (m/s)	T∞(°C)	Conditions	Time of exposure (min)	LWC(g/m^3)	Droplet diamter (μm)
8	85	-9	continuous	NA	0.42	17
8	85	-9	intermittent	NA	1.2	17

Table C.2: *Final conditions for the Hybrid airfoil in the CIT*

C.3 The uncertainties

The uncertainties study is based on the guidance of the British Measurement and testing Association (Taylor (1982), Birch (2001) and Bell (2001)). The uncertainties on the LWC has been studied for three ice thickness measurements on the icing blade in the zero position for Pw=17 psi and Pa=26.7 psi. The value of the LWC in taking into account the uncertainties is the LWC best estimate (average value of LWC, equation (C.3.1)) plus or minus the random error (standard deviation of the mean, equation (C.3.3)) which occurs during the LWC measurement. The uncertainties are then multipled by a factor of 2.58 to get a confidence level of 99%:

$$\bar{x} = \frac{1}{N}\sum_{k=1}^{N} x_k \tag{C.3.1}$$

$$\sigma = \sqrt{\frac{1}{N-1}\sum_{k=1}^{N}(x_i - \bar{x})} \tag{C.3.2}$$

$$\sigma_{mean} = \delta_x = \frac{\sigma}{\sqrt{N}} * 2.58 \tag{C.3.3}$$

With $\bar{x}$ the average value of a parameter x, σ the standard deviation and σ_{mean} the mean standard deviation or the random error with a confidence level of 99%. Hence:

$$LWC = \overline{LWC} + \delta_{LWC} \tag{C.3.4}$$

The LWC is a function of the ice thickness i, the time of accretion and the free stream speed, U_∞ (equation (C.1.1)). The propagation of the random error is calculated as follow:

$$\frac{\delta LWC}{\overline{LWC}} = \sqrt{\left(K1\,\frac{\delta_i}{\bar{i}}\right)^2 + \left(K2\,\frac{\delta_t}{\bar{t}}\right)^2 + \left(K3\,\frac{\delta U_\infty}{\overline{U_\infty}}\right)^2} \tag{C.3.5}$$

$$K_1 = \frac{i}{LWC} * \frac{\partial LWC}{\partial i} = 1 \tag{C.3.6}$$

$$K_2 = \frac{t}{LWC} * \frac{\partial LWC}{\partial t} = -1 \tag{C.3.7}$$

$$K_2 = \frac{U_\infty}{LWC} * \frac{\partial U_\infty}{\partial LWC} = -1 \tag{C.3.8}$$

Following the calculation of the $\overline{LWC}$ and δ_{LWC} it is found that LWC=0.42 $\pm$0.11 $g.m^{-3}$for a confidence level of 99%.

The uncertainty in the droplet diameter size has been estimated to be 1.2 μm during the first calibration of the CIT (Stanfield (2008)). By estimating the water and air pressures fluctations during a run it is possible to see on Figure C.3 how these fluctuations affect the MVD. For the low LWC, it has been found that 16.8 psi$\leq$ P_w = 17 $\leq$17.2 psi and 26.2 psi$\leq$ P_a = 26.7 $\leq$27.2 psi. This lead to an uncertainty of $\pm$1 μm. Hence, this uncertainty and the uncertainty found in the droplets size during the first calibration lead to MVD=17$\pm$ 2.2 μm for a LWC of 0.42 $g.m^{-3}$. For LWC of 1.2 $g.m^{-3}$, the water and air pressures are fluctuating more which leads to MVD=17$\pm$ 3.2 μm.

To finish the random error in the in free stream temperature is estimated to be $\pm$0.5°C.

Appendix D

Position of the icing blade

It is likely that the cloud is going to be changed significantly close to the model as the blockage effect is big for the present experiments. Hence, to calibrate the cloud it is necessary to measure the LWC at a position in front the model, where the droplets trajectories are not disturb by the airfoil in the test section. The objective of this study is to find a position for the icing blade where the distance between 2 droplets, Δy, is the same as free stream and if possible, a position which remains in the test section. The test section walls are made of plexiglass windows which can be changed whereas the tunnels walls outside the test section are made of wood. It would be more convinient to mount the the icing blades within the plexiglass than within the wood in order not to damage permanently the main body of the tunnel. The farthest distance to the model where the icing blade could be attached, until the and of the plexiglass window, is 25 cm. This position was then investigated in order to assees if the droplets trajectories were influenced by the Hybrid airfoil downstream the test section. The numerical set up is the one used in the preliminary CFD study for the Hybrid airfoil mounted in the icing tunnem (see 4.3).

In figure D.1 the trajectories of the last hitting droplets against the Hybrid model in the tunnel are plotted for three diameters: 15μm, 25μm and 30μm. It is obvious that the cloud is shifted up in front of the airfoil and this trend is all the more important that the droplets diameter is small.

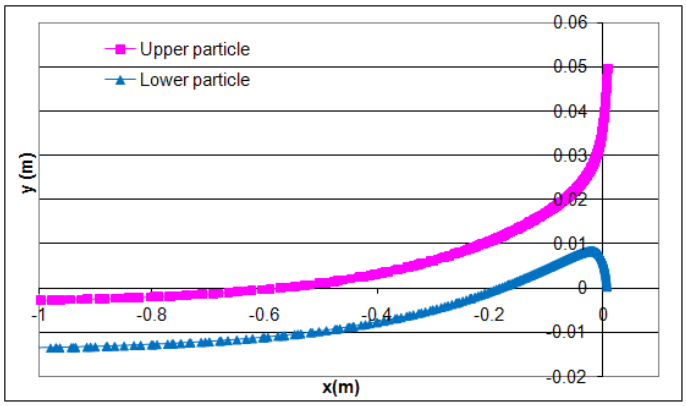

(a) 15μm

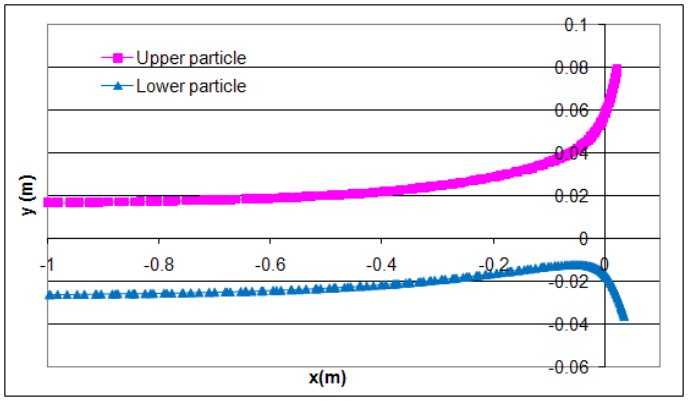

(b) 25μm

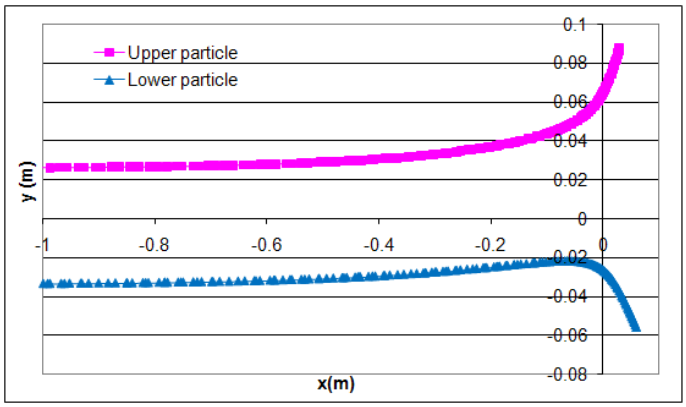

(c) 30μm

Figure D.1: *Trajectories of the last hitting droplets on the Hybrid model, for different droplets diameters*

To quantify the shift of the cloud, 3 significant distances as been defined (Figure D.2) and calculated as follow:

$$\%\Delta y = \frac{\Delta y_{x=-6} - \Delta y_{x=-0.25}}{\Delta y_{x=-6}} \tag{D.0.1}$$

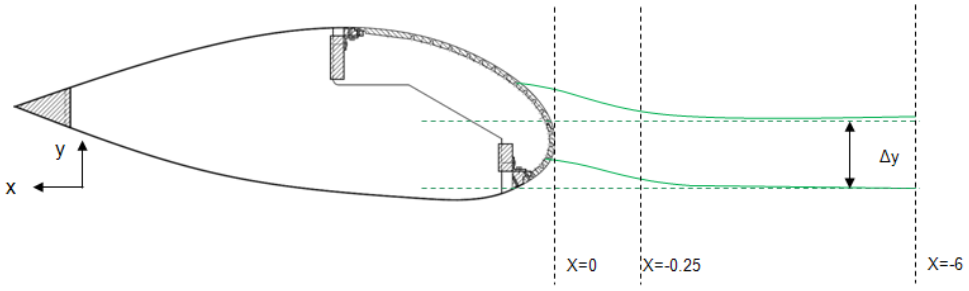

Figure D.2: *Significant distance for the droplet trajectories study*

All the results are compiled in Table D.1. The distance between the droplets trajectories remains very close at a position 6 m or 25 cm upstream the model. The lower and upper trajectories are shifted up of by keeping the same distance as the difference between the 2 positions is less than 2% (Table D.1). This result means that the icing blade test can be made 25 cm in front of the model.

Droplet diameter (µm)	Δy(x=-6) (m)	Δy(x=-0.25) (m)	%Δy
15 µm	0.0109	0.0111	-1.76
25 µm	0.0437	0.0443	-1.37
30 µm	0.0605	0.0613	-1.32

Table D.1: *Significant distance for the droplet trajectories study*

As the model is large, a large cloud is required in order to be sure that the impingement is maximum, especially in the vertical direction. If the cloud was not thick enough, the risk would be that no droples would pass above the model and then the impingement limits on the Hybrid airfoil might not maximum. It has been decided that 8 vertical positions with an increment of 2 cm are used for the icing blade calibration technique. As the cloud tends to be shifted up between the icing blade position and the model, it was interesting to study the trajectories of a droplet from each vertical position of the icing blade to the model. The objective is to find out which icing blades position is the most important for the calibration. Hence, the droplet trajectories from the icing blade positions to the model have been computed for different droplet diameters (Figure D.3) .

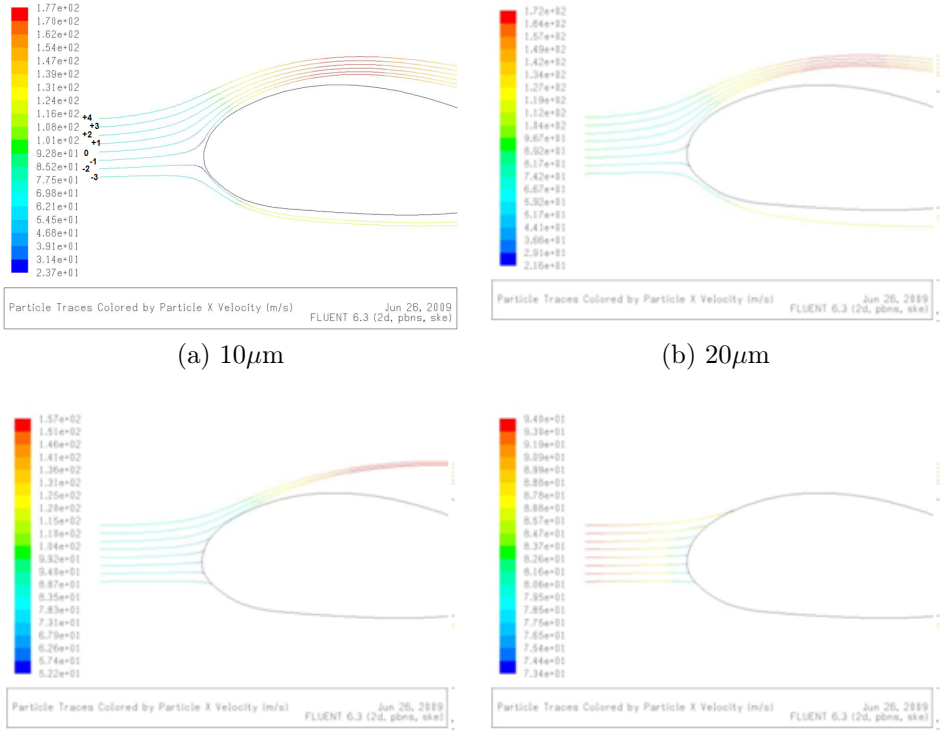

(a) 10μm (b) 20μm

(c) 50μm (d) 100μm

Figure D.3: *Droplets trojectories computed with the DPM in Fluent in front of the Hybrid model in the tunnel*

From Figure D.3, it is a reasonable assumption to consider that the positions which contribute to the main impingement on the upper surface, are from position -1 to +2, at least for the droplets diameters which have the main contribution in the droplets diameters distribution (Figure 3.4). Even though the ice thickness will be measured on the icing blade for all positions in order to get a complete map of the LWC in front of the airfoil, the calibration is focused on the icing blade positions -1, 0, +1 and +2 for the tunnel calibration.

Appendix E

List of the run details for the icing tunnel tests

Anti-icing runs	Heating system config	Limit of the heated zone (m)	LWC (g/m^3)	Time of run (min)	Ttotal in the tunel (°C)	Upper limit of the runback ice (x/c)	Wet heated Ts (°C)	Dry heated Ts (°C)	Cast
run1b-2	H5	0.073	0.45	20	-5	0.144	15.7	27.8	no
run 1b-3	H4	0.073	0.45	12	-5	NA	17.5	32.1	yes
run2a-2	H1	0.137	0.45	20	-5	0.233	20.1	33.3	no
run 2a-3	H1	0.137	0.45	15	-5	NA	19.9	34.9	yes
run2b-2	H2	0.16	0.45	20	-5	0.188	12.1	21.4	no
run2b-3	H2	0.16	0.45	20	-5	NA	12.8	23.2	yes
run2abis	H1	0.137	1.2	10	-5	0.239	18.5	36.2	no
run3-2	H6	0.086	0.45	20	-5	0.106	12.9	25.1	no
run5-3	H3	0.16	0.45	20	-5	0.175	6.4	11.9	no
run6-2	H7	0.086	0.45	20	-5	0.092	5.7	11.2	no
run6-3	H7	0.086	0.45	20	-5	0.092	5.1	10.3	no
run6-4	H7	0.086	0.45	20	-5	0.0915	4.9	10.2	no
run6-5	H7	0.086	0.45	20	-5	0.085	5.4	10.7	no
run6-8	H7	0.086	0.45	10	-5	NA	3.3	8.4	yes
run 7-3	H3	0.16	1.2	5	-5	NA	5.6	12	yes
run8-1	H4	0.16	0.45	20	-5	0.19	10.2	18.7	no
run9	H8	0.073	0.45	20	-5	0.082	8.7	18.7	no
run10	H4	0.16	1.2	10	-5	0.194	8.7	18.4	no
run11-2	H9	0.16	0.45	11	-5	NA	17.8	29	yes

Table E.1: *Details of the runs for the the anti-icing experiments*

De-icing runs	Heating system config	Limit of the heated zone (m)	LWC (g/m^3)	Time of run (min)	Ttotal in the tunel (°C)
run14	H12	0.053	0.45	9min 56s (4 cycles)	-5
run15-2	H13	0.109	0.45	17min 43s (8 cycles)	-5

Table E.2: *Details of the runs for the the de-icing experiments*

Appendix F

List of the run details for the wind tunnel tests

runs	x position (mm)	y position (mm)	probe	ice shapes	Speed (m/s)
1	-6	0	pitot probe	blank	25,30,35,40,45
2	-6	-150	pitot probe	blank	25,30,35,40,45
3	-6	150	pitot probe	blank	25,30,35,40,45
4	-320	0	pitot probe	blank	25,30,35,40,45
5	-610	0	pitot probe	blank	25,30,35,40,45
6	-320	-150	pitot probe	blank	25,30,35,40,45
8	-150	0	3 pitot rakes	2b-3	25,30,35,40,45
9	-150	-10	3 pitot rakes	2b-3	25,30,35,40,45
10	-150	-20	3 pitot rakes	2b-3	25,30,35,40,45
11	-150	-30	3 pitot rakes	2b-3	25,30,35,40,45
12	-150	-40	3 pitot rakes	2b-3	25,30,35,40,45
13	-150	-50	3 pitot rakes	2b-3	25,30,35,40,45
14	-150	10	3 pitot rakes	2b-3	25,30,35,40,45
15	-150	20	3 pitot rakes	2b-3	25,30,35,40,45
16	-150	30	3 pitot rakes	2b-3	25,30,35,40,45
17	-150	40	3 pitot rakes	2b-3	25,30,35,40,45
18	-150	50	3 pitot rakes	2b-3	25,30,35,40,45
19	-150	50	3 pitot rakes	blank	25,30,35,40,45
20	-150	50	3 pitot rakes	11-2	25,30,35,40,45
21	-150	40	3 pitot rakes	11-2	25,30,35,40,45
22	-150	30	3 pitot rakes	11-2	25,30,35,40,45
23	-150	20	3 pitot rakes	11-2	25,30,35,40,45
24	-150	10	3 pitot rakes	11-2	25,30,35,40,45
25	-150	0	3 pitot rakes	11-2	25,30,35,40,45

26	-150	-10	3 pitot rakes	11-2	25,30,35,40,45
27	-150	-20	3 pitot rakes	11-2	25,30,35,40,45
28	-150	-30	3 pitot rakes	11-2	25,30,35,40,45
29	-150	-40	3 pitot rakes	11-2	25,30,35,40,45
30	-150	-50	3 pitot rakes	11-2	25,30,35,40,45
31	-200	-50	3 pitot rakes	7-3	25,30,35,40,45
32	-200	-40	3 pitot rakes	7-3	25,30,35,40,45
33	-200	-30	3 pitot rakes	7-3	25,30,35,40,45
34	-200	-20	3 pitot rakes	7-3	25,30,35,40,45
35	-200	-10	3 pitot rakes	7-3	25,30,35,40,45
36	-200	0	3 pitot rakes	7-3	25,30,35,40,45
37	-200	10	3 pitot rakes	7-3	25,30,35,40,45
38	-200	20	3 pitot rakes	7-3	25,30,35,40,45
39	-200	30	3 pitot rakes	7-3	25,30,35,40,45
40	-200	40	3 pitot rakes	7-3	25,30,35,40,45
41	-200	50	3 pitot rakes	7-3	25,30,35,40,45
42	-200	0	3 pitot rakes	2b-3	25,30,35,40,45
44	-200	0	3 pitot rakes	11-2	25,30,35,40,45
45	-200	-10	3 pitot rakes	11-2	25,30,35,40,45
46	-200	-20	3 pitot rakes	11-2	25,30,35,40,45
47	-200	-30	3 pitot rakes	11-2	25,30,35,40,45
48	-200	-40	3 pitot rakes	11-2	25,30,35,40,45
49	-200	-50	3 pitot rakes	11-2	25,30,35,40,45
50	-200	50	3 pitot rakes	11-2	25,30,35,40,45
51	-200	40	3 pitot rakes	11-2	25,30,35,40,45
52	-200	30	3 pitot rakes	11-2	25,30,35,40,45
53	-200	20	3 pitot rakes	11-2	25,30,35,40,45
54	-200	10	3 pitot rakes	11-2	25,30,35,40,45
55	-200	0	3 pitot rakes	2b-33	45
56	-200	0	3 pitot rakes	11-21	45
57	-200	0	3 pitot rakes	2b-32	45
58	-200	0	3 pitot rakes	2b-31	45
59	-200	0	3 pitot rakes	7-31	45
61	-200	0	3 pitot rakes	blank	45
62	-200	0	3 pitot rakes	2b-34	45
63	-200	0	3 pitot rakes	11-24	45
64	-200	0	3 pitot rakes	7-32	45
65	-200	0	3 pitot rakes	11-22	45
66	-200	0	3 pitot rakes	11-23	45

73	-150	0	3 pitot rakes	11-23	45
74	-150	0	3 pitot rakes	11-22	45
75	-150	0	3 pitot rakes	7-32	45
76	-150	0	3 pitot rakes	2b-34	45
77	-150	0	3 pitot rakes	2b-31	45
78	-150	0	3 pitot rakes	2b-33	45
79	-150	0	3 pitot rakes	2b-32	45
80	-150	0	3 pitot rakes	7-31	45
81	-150	0	3 pitot rakes	11-21	45
82	-150	0	3 pitot rakes	11-24	45
85	-250	0	3 pitot rakes	11-2	45
86	-250	-10	3 pitot rakes	11-2	45
87	-250	-20	3 pitot rakes	11-2	45
88	-250	-30	3 pitot rakes	11-2	45
90	-250	-40	3 pitot rakes	11-2	45
91	-250	-50	3 pitot rakes	11-2	45
93	-250	10	3 pitot rakes	11-2	45
94	-250	20	3 pitot rakes	11-2	45
95	-250	30	3 pitot rakes	11-2	45
97	-250	40	3 pitot rakes	11-2	25,30,35,40,45
98	-250	50	3 pitot rakes	11-2	25,30,35,40,45
99	-250	0	3 pitot rakes	11-22	45
101	-250	0	3 pitot rakes	11-23	25,30,35,40,45
102	-250	0	3 pitot rakes	11-24	45
103	-250	0	3 pitot rakes	blank	45
106	-250	0	3 pitot rakes	2b-34	45
108	-250	0	3 pitot rakes	7-32	45
109	-250	0	3 pitot rakes	7-31	45
110	-250	0	3 pitot rakes	11-21	45
111	-250	0	3 pitot rakes	2b-31	45
112	-250	0	3 pitot rakes	2b-32	45
113	-250	0	3 pitot rakes	2b-33	45
117	-250	0	3 pitot rakes	7-3	45
118	-250	-10	3 pitot rakes	7-3	45
119	-250	-30	3 pitot rakes	7-3	45
120	-250	-50	3 pitot rakes	7-3	45
121	-250	50	3 pitot rakes	7-3	45
122	-250	30	3 pitot rakes	7-3	45
123	-250	10	3 pitot rakes	7-3	45

125	-250	0	3 pitot rakes	2b-3	45
126	-250	-10	3 pitot rakes	2b-3	45
127	-250	-30	3 pitot rakes	2b-3	45
128	-250	-50	3 pitot rakes	2b-3	45
130	-250	50	3 pitot rakes	2b-3	45
131	-250	30	3 pitot rakes	2b-3	45
132	-250	10	3 pitot rakes	2b-3	45
135	-200	-10	3 pitot rakes	2b-3	45
136	-200	-30	3 pitot rakes	2b-3	45
137	-200	-50	3 pitot rakes	2b-3	45
139	-200	10	3 pitot rakes	2b-3	45
140	-200	30	3 pitot rakes	2b-3	45
142	-200	50	3 pitot rakes	2b-3	45
147	-150	0	3 pitot rakes	11-2	45
148	-150	0	3 pitot rakes	11-2	45
149	-150	0	3 pitot rakes	11-2	45

Table F.1: *Details of the runs for the the wind tunnel experiments*

Appendix G

DVDs

The experimental data, spreadsheets, pictures and Fluent case and data files have been compiled on DVDs. For any information on these DVDs, it is advised to contact Dr. Hammond from the Power and Propulsion departement in the School of Engineering.

- DVD 1: Recording of the intercycle runs, run 15, run 16 and run 17 in the CIT (chapter 7)
- DVD 2: CIT experimental data 1 (chapter 5 and chapter 7)
  - List of the anti-icing and intercycle runs in the CIT (Runback ice experiments-Cranfield Uni.xlsb)
  - Runback ice shapes catalogue (Runback ice shapes catalogue-Cranfield University.docx)
  - Pictures of the heating system (Heating system pictures Cranfield University.docx)
  - Pictures and coordinates of the ice tracings
  - Pictures of the castings
  - Pictures and tunnel data for the intercycle runs
  - Industrial drawings
  - Spreadsheets for the 1D runback ice model applied to the B737 fres stream and to the Hybrid airfoil
  - Preliminary CFD study for the CIT experiments (airfoils coordinates, B737 free stream, Hybrid airfoil free stream, Hybrid airfoil in the tunnel)

- DVD 3: CIT experimental data 2 (pictures and tunnel data for the anti-icing runs classified by date (chapter 7))
  - Runback 11-11-09
  - Runback 12-11-09
  - Runback 13-11-09
  - Runback 17-11-09
  - Runback 18-11-09
  - Runback 19-11-09
  - Runback 20-11-09
  - Runback 25-11-09
  - Runback 26-11-09
  - Runback 27-11-09
  - Runback 08-01-10
  - Runback 11-01-10
  - Runback 12-01-10
  - Runback 08-01-10
  - Runback 03-03-10
  - Runback 04-03-10
  - Runback 05-03-10
  - Runback 08-03-10
  - Runback 09-03-10
  - Runback 16-03-10
  - Runback 17-03-10
- DVD 4: Aerodynamic study
  - Preliminary CFD study (chapter 8)
  - Aerodynamic CFD study to compare with wind tunnel results (chapter 10)
  - Wind tunnel data (runs, pictures) and analysis (chapter 9)